



Développement de matériaux composites thermoplastiques pour des applications de blindage électromagnétique : modélisation, formulation, procédés et propriétés

Hubert Lecocq

► To cite this version:

Hubert Lecocq. Développement de matériaux composites thermoplastiques pour des applications de blindage électromagnétique : modélisation, formulation, procédés et propriétés. Polymères. Université de Lyon, 2021. Français. NNT : 2021LYSE1063 . tel-03736462

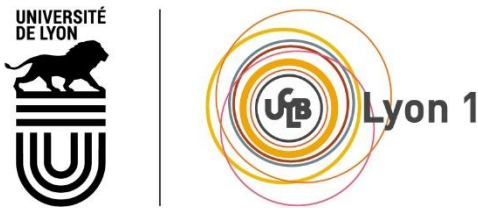
HAL Id: tel-03736462

<https://theses.hal.science/tel-03736462v1>

Submitted on 22 Jul 2022

HAL is a multi-disciplinary open access archive for the deposit and dissemination of scientific research documents, whether they are published or not. The documents may come from teaching and research institutions in France or abroad, or from public or private research centers.

L'archive ouverte pluridisciplinaire **HAL**, est destinée au dépôt et à la diffusion de documents scientifiques de niveau recherche, publiés ou non, émanant des établissements d'enseignement et de recherche français ou étrangers, des laboratoires publics ou privés.



THÈSE de DOCTORAT DE L'UNIVERSITÉ DE LYON
opérée au sein de
I'Université Claude Bernard Lyon 1

École Doctorale ED 34
École Doctorale Matériaux de Lyon

Spécialité de doctorat : Physique des matériaux
Discipline : Matériaux polymères & composites

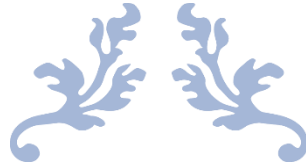
Soutenue publiquement le 26/03/2021, par :
Hubert Lecocq

Développement de matériaux composites thermoplastiques pour des applications de blindage électromagnétique : modélisation, formulation, procédés et propriétés

Devant le jury composé de :

Prof. Elianne Espuche	Université de Lyon 1 – IMP@Lyon1	Examinateuse
Prof. Paula Moldenaers	Katholieke Universiteit Leuven – Soft Matter, Rheology and Technology	Rapporteure
Dr. François Lequeux	ESPCI Paris – SIMM	Rapporteur
Dr. Olivier Lhost	Total Research and Technology – Polymer Materials Department	Examinateur
Dr. Edith Peuvrel-Disdier	Mines ParisTech – CEMEF	Examinateuse
Prof. Philippe Cassagnau	Université de Lyon 1 – IMP@Lyon1	Directeur de thèse
Dr. Anatoli Serghei	Université de Lyon 1 – IMP@Lyon1	Co-directeur de thèse
Dr. Philippe-Franck Girard	Total SA Paris – Direction scientifique	Invité
Dr. Nicolas Garois	Hutchinson SA CRI – Département R&D Polymères thermoplastiques	Invité
Dr. Yves Trolez	Total Research and Technology – Polymer Materials Department	Invité

- DOCTORALE THESIS -



**Development of thermoplastic composite materials for
applications of electromagnetic interference shielding**

Modeling, formulation, process and properties



Hubert Lecocq

Lyon Doctoral School of Materials ED 34
University Claude Bernard Lyon 1
Lyon, France

Supervision
Prof. Philippe Cassagnau
Dr. Anatoli Serghei

Defended on 26th March 2021

« La créativité se situe à la rencontre de la discipline et de l'esprit enfantin. »

-- **Robert Greene**

Les smartphones 5G sont là ...



REMERCIEMENTS

Je souhaite remercier tout d'abord mes directeurs de thèse, Philippe Cassagnau et Anatoli Serghei, pour m'avoir guidé, conseillé et encouragé tout au long de ce projet de thèse. Leur expérience respective dans les domaines de la physique des polymères, des matériaux diélectriques et surtout de la rédaction de publications scientifiques m'a été très précieuse. Je les remercie pour leur enthousiasme par rapport aux bons résultats, mais également aux moins bons !

Je remercie également mes encadrants industriels, Olivier Lhost, Yves Trolez, Nicolas Garois, Philippe-Franck Girard et Cathy Vix, pour le suivi de ce projet industriel, leur enthousiasme et les nombreux conseils et encouragements qu'ils m'ont donnés. Je remercie tout particulièrement Philippe-Franck Girard qui à l'origine de projet de thèse, Nicolas Garois qui est à l'origine de mon recrutement et Olivier Lhost pour sa participation majeure dans le dépôt d'un brevet concernant mes travaux de thèse (et son humour belge bien trempé !). Je remercie le groupe Total d'avoir financé mon projet de thèse. Mener ce projet de recherche au sein de ce grand groupe fut une expérience très enrichissante d'un point de vue scientifique, professionnel et personnel. Je remercie Jean-Michel Brusson pour son suivi des doctorants dépendant du siège social et pour son organisation des évènements d'échanges conviviaux entre doctorants.

Je souhaite remercier Pierre Alcouffe pour son aide très très précieuse dans la préparation et l'observation d'échantillons optique et de microscopie électronique. Sa sympathie, son engagement et son expertise sont ce que le laboratoire IMP a de plus précieux ! Je remercie également Guillaume Sudre pour son aide en spectroscopie et microscopie infrarouge, Adrien Tauleigne et Karim Delage pour leur aide en hall d'extrusion ainsi que tout le personnel technique de l'IMP.

Je remercie René Fulchiron et Véronique Bounor-Legare pour leur bienveillance et leurs précieux conseils en mise en œuvre et en rhéologie.

Je remercie Sylvie Novat-Tomatis et Corinne Menant pour leur sympathie et leur aide précieuse dans l'organisation de déplacements nationaux et internationaux, ainsi que dans la commande de matière première.

Je remercie tout particulièrement les membres et ex-membres de mon bureau à l'IMP (428, the best) pour la bonne ambiance permanente et les très bons moments passés en leur compagnie : Mamoudou, Thomas, Renaud, Thibaut, Léa, Clémentine et Mathurin (le p'tit dernier). Je remercie de

même tous les doctorants de l'IMP qui font de ce laboratoire un second chez-soi où il fait bon travailler et où la bonne ambiance nous aide à traverser les moments plus compliqués d'une thèse.

Je remercie mes parents, mes deux frères, ma famille de Bretagne, du nord de la France et d'ailleurs. Je remercie mes amis, mes potos de Bretagne (la team !) et mes potes de promo de PC !

Je remercie enfin ma compagne, ma chérie Marie-Françoise qui m'a soutenu tout au long de ce projet. Je la remercie d'avoir partagé avec moi les bons moments de ces trois dernières années et de m'avoir supporté et encouragé dans les moments les plus difficiles.

ABSTRACT

In this work we present the development of a polyolefin composite material with electromagnetic interference (EMI) shielding properties. The project objective is set to a shielding effectiveness of at least 40 dB (99.99% of the wave power blocked) for a film thickness of 1mm over a broad frequency range spanning from 100 MHz to 10 GHz that includes many applications that can be found in consumer electronics or connected cars for instance. Composite material density and mechanical properties are expected to remain as close as possible to the pure polymer matrix. No study found in the literature complies with all these specifications, highlighting the challenge of such a research project. Understanding the physical mechanisms of EMI shielding in polymer composite materials is also an issue of this work.

In the project, we first focused on the study of carbon nanotubes-based composite materials that displayed good but not satisfying EMI shielding properties due to limited electrical conductivity. Development of a first theoretical model enabled us to identify the relevant composite properties for shielding and oriented our attention on composites filled with metal fillers. The high density of this kind of fillers however required a low concentration in the composite materials and strategies to lower filler percolation. Liquid metal revealed to be incompatible with molten polymer because of high values of interfacial tension and viscosity ratio. The hybrid silver-coated glass fibers of moderate density but high metal conductivity were found to be the best candidate. The addition of stearic acid led to improved shielding properties that reached and surpassed the set objectives. The unexpected effect of the fatty acid on material morphology was identified and explained. Finally, the shielding properties of these composite materials could be theoretically modeled considering the self-inductance of metal filler and adding an inductive component to the composite electrical conductivity. The model was also found to correctly predict shielding properties of composite materials filled with metal fillers from the literature. Thus, this work has significantly contributed to the development of novel polymer composite materials for EMI shielding, to the processing of these materials and to the understanding of EMI shielding physics.

Key words: Electromagnetic shielding, Composite materials, Carbon nanotubes, Polypropylene, Stearic acid, Rheology, Electrical conductivity

RÉSUMÉ

Ces travaux portent sur le développement d'un matériau composite polyoléfine aux propriétés de blindage électromagnétique (EM). L'objectif du projet est fixé à une valeur d'efficacité de blindage de 40 dB (99,99% de la puissance d'une onde incidente bloquée) à 1mm d'épaisseur dans une large gamme de fréquence s'étendant de 100 MHz à 10 GHz incluant de nombreuses applications dans l'électronique nomade ou les voitures connectées par exemple. La densité du matériau et ses propriétés mécaniques doivent demeurer proches de celles de la matrice pure. Aucune étude de la littérature ne remplit toutes ces conditions à la fois, soulignant le défi posé par ce projet de recherche. Comprendre la physique du blindage EM des matériaux composites est également une problématique importante de ces travaux.

Le début de ces travaux s'est concentré sur l'étude de composites à base de nanotubes de carbone qui ont présenté de bonnes propriétés de blindage mais insuffisantes pour le projet en raison de leur conductivité électrique limitée. Le développement parallèle d'un premier modèle théorique nous a permis d'identifier les paramètres pertinents au blindage EM et nous a ainsi orienté vers l'étude de composites à base de charges métalliques de plus grande conductivité. La densité élevée de ce type de charges nécessite cependant de limiter leur concentration dans le matériau et donc de développer des stratégies pour abaisser leur seuil de percolation électrique. Le métal à l'état liquide s'est avéré incompatible avec le polymère fondu en raison des valeurs trop importantes de tension interfaciale et de rapport de viscosité. Le meilleur candidat est une charge hybride : des fibres de verre recouvertes d'argent, de densité modérée et de haute conductivité métallique. L'ajout d'acide stéarique, dont l'effet inattendu sur la morphologie du composite a été identifié et expliqué, a été associé à une augmentation des propriétés de blindage du composite atteignant et dépassant les objectifs fixés. Le comportement en blindage EM de ces composites a été modélisé en considérant l'auto-inductance des charges métalliques et donc en ajoutant une composante inductive à la conductivité du composite. Ce modèle s'est également avéré capable de prédire le blindage de matériaux composites chargés en particules métalliques issus de la littérature. Ainsi, ces travaux contribuent de façon significative au développement de nouveaux matériaux composites polymères aux propriétés de blindage et à leur mise en œuvre, ainsi qu'à la compréhension de la physique et des mécanismes du blindage EM dans les matériaux composites.

Mots clefs : Blindage électromagnétique, Matériaux composites, Nanotubes de carbone, Polypropylène, Acide stéarique, Rhéologie, Conductivité électrique.

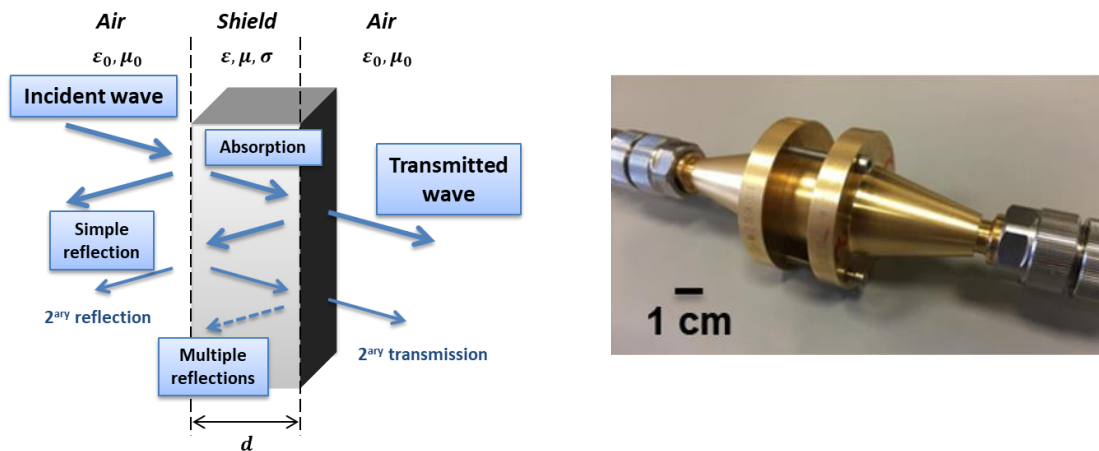
PRÉSENTATION SYNTHÉTIQUE DES TRAVAUX

Depuis la découverte des ondes électromagnétiques (EM) par le physicien allemand Heinrich Rudolf Hertz en 1886, leur utilisation dans les télécommunications, la diffusion et les radars s'est développée de façon exponentielle. Cette croissance continue est actuellement portée par la demande pour ces technologies dans les pays en voie de développement et l'arrivée progressive de la 5G. Une des conséquences néfastes de la multiplication des usages des ondes EM est l'augmentation de la pollution électromagnétique de l'environnement, qui peut gêner les moyens de communication à distance (en augmentant le niveau de bruit) et peut potentiellement être très préoccupante quand les communications concernées sont vitales (par exemple avec les systèmes de guidage d'un avion). Les avancées récentes concernant les systèmes connectés (comme les voitures connectées) nécessitent souvent l'accumulation de multiples appareils électroniques, chacun ayant un rôle précis, dans un espace confiné. Ceci constitue un terrain idéal pour le développement d'interférences électromagnétiques entre ces différents appareils qui peuvent porter atteinte au fonctionnement du système global voire provoquer une panne. Lors de la conception de systèmes embarqués et/ou connectés, il est ainsi nécessaire de considérer ces interférences et, le cas échéant, utiliser des écrans de blindage électromagnétique afin de protéger un dispositif sensible des perturbations extérieures ou d'isoler un dispositif fortement rayonnant de ses voisins.

Les matériaux métalliques, sous forme de plaques, de revêtement ou de grilles, sont souvent utilisés pour des applications de blindage EM grâce à leur haute conductivité électrique. Cependant, ces derniers présentent souvent une densité élevée, une sensibilité à la corrosion, un prix potentiellement important et nécessitent beaucoup d'énergie pour leur production et leur mise en forme. Une alternative aux matériaux métalliques pour des applications de blindage EM ne présentant pas ces défauts sont les matériaux composites polymères conducteurs. Il s'agit de l'association d'une matrice polymère de faible densité, mais isolante, avec une charge conductrice lui conférant des propriétés de conductivité électrique et de blindage EM. Le marché du blindage EM est important et en constante croissance depuis une décennie (6,4 milliards de dollars US en 2019, estimation à 10 milliards de dollars US en 2025) avec de forts investissements dans la R&D. Ceci combiné avec la volonté d'allègement des structures et de réduction des émissions de gaz à effet de serre justifie l'intérêt croissant envers les matériaux composites polymères pour des applications de blindage EM.

L'objectif de ce projet de recherche est le développement d'un matériau composite polyoléfine présentant une efficacité de blindage d'au moins 40 dB (au moins 99,99% de la puissance d'une onde EM incidente bloquée) pour un écran de 1 mm d'épaisseur et à des fréquences s'étalant

de 100 MHz à 10 GHz, recouvrant ainsi des applications que l'on peut retrouver dans l'aéronautique ou dans une voiture connectée : ondes radio et téléphone, 4G, 5G, Wi-Fi, Bluetooth, et ondes radars civils. La densité du matériau composite doit rester inférieure à 1500 kg.m^{-3} et ses propriétés mécaniques (en traction) et de mise en œuvre les plus proches possibles de la résine polymère pure. Les problématiques du projet sont les suivantes : quelles charges conductrices dispersées dans une matrice PP permettent d'obtenir les meilleures propriétés de blindage EM tout en limitant la densité du matériaux composite et les changements de propriétés mécaniques et de mise en œuvre comparées à la matrice PP pure ? A une concentration en charge fixe, comment peut-on améliorer les propriétés de blindage EM du matériau composite ? Comment modéliser les propriétés de blindage du composite en fonction des propriétés intrinsèques des charges et de la matrice polymère ?



Gauche : Représentation schématique des mécanismes du blindage EM. Droite : cellule de mesure coaxiale du blindage EM

Dans le premier chapitre la littérature scientifique est passée en revue. Le cadre théorique de l'étude du blindage EM des matériaux composites polymères est mis en place et les paramètres importants du blindage et différents modèles théoriques issus de la littérature sont présentés. Les charges conductrices les plus intéressantes pour des applications de blindage EM avec des composites polymères sont identifiées. Il s'agit des charges carbonées, telles que le noir de carbone, le graphène et les nanotubes de carbone (NTC ou CNT) ; les polymères conducteurs comme le polyaniline ; les charges métalliques, telles que les nanofils de cuivre ; des charges hybrides métalliques telles que les fibres de polymère ou de verre recouvertes d'argent ; des charges magnétiques, telles que la magnétite et le nickel ; et des MXenes, à base de carbures, nitrures et carbonitrides de métaux de transition. Un paramètre important à considérer est le seuil de percolation électrique, la concentration en charge au-delà de laquelle le matériau composite devient conducteur et peut alors présenter des

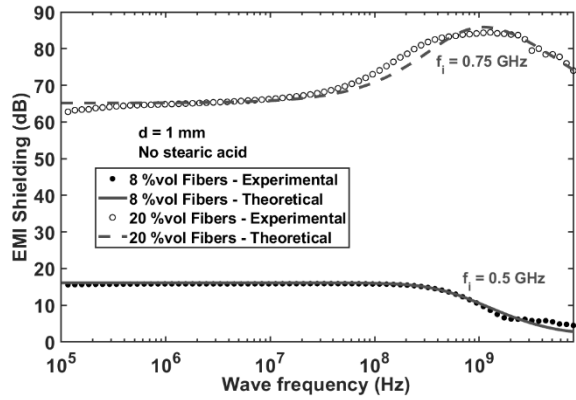
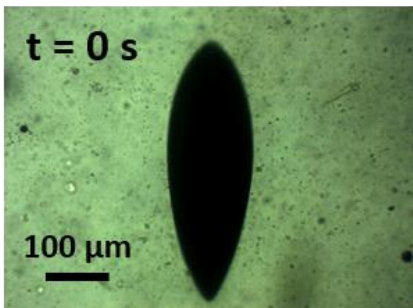
propriétés de blindage EM. Il faut préférablement que ce seuil soit faible afin de limiter la concentration en charges conductrices nécessaire pour obtenir des propriétés de blindage et ainsi limiter leur impact sur la densité et les propriétés mécaniques et de mise en œuvre du matériau composite. Le seuil de percolation dépend des propriétés des charges (leur facteur de forme) et de leur dispersion et distribution au sein de la matrice polymère. Pour atteindre les objectifs du projet, un intérêt particulier est porté aux charges conductrices de haut rapport d'aspect et de densité modérée, soit les nanotubes de carbone et les fibres de verre recouvertes d'argent.

Le second chapitre de ce manuscrit présente les matériaux utilisés lors de ces travaux, ainsi que les méthodes de fabrication, de mise en forme et de caractérisation des propriétés des matériaux composites polymères. Le développement des méthodes de mesure de la conductivité électrique et des propriétés de blindage EM réalisé durant ce projet et l'étude de l'influence des méthodes de mise en forme des échantillons sur ses propriétés sont présentés en détail.

Le chapitre III présente l'étude théorique et expérimentale de composites PP à base de NTC. Le développement d'un modèle théorique du blindage électromagnétique concernant les matériaux homogènes, isotropes et dont les propriétés sont constantes avec la fréquence de l'onde incidente a permis d'identifier les mécanismes du blindage EM (la réflexion simple, l'absorption et les réflexions internes multiples) et les paramètres ayant une influence sur l'efficacité de blindage (la fréquence de l'onde, l'épaisseur et la conductivité électrique de l'écran de blindage). A partir d'une mesure de conductivité DC des composites PP – CNT étudiés mais également de composites issus de nombreuses études de la littérature scientifique, ce modèle est capable de prédire de façon exacte les propriétés de blindage de ces composites. Les composites PP – CNT étudiés présentent un seuil de percolation remarquablement bas (0,4 % volumique) et le composite à 10 %vol de NTC atteint les objectifs fixés en termes de blindage. Cependant, ce dernier présente des modifications de propriétés mécaniques par rapport à la matrice PP pure très importantes et sa mise en forme (presse à chaud, injection) s'est avérée difficile. Ces composites sont limités par la conductivité intrinsèque des NTC, orientant la suite de nos travaux vers des charges de conductivité métallique.

Le chapitre IV s'intéresse à une charge conductrice de conductivité métallique pouvant potentiellement mener à un composite présentant des propriétés de blindage EM plus importantes que les NTC : le métal liquide. La densité élevée des charges métalliques requiert la mise en place de stratégies afin d'abaisser le seuil de percolation de ces charges et obtenir des matériaux composites conducteurs pouvant posséder des propriétés de blindage pour de faibles concentrations en charges, d'où l'étude de métaux mélangés à l'état liquide avec le polymère fondu. Les deux liquides se sont cependant avérés incompatibles : une démixtion totale est observée avant leur solidification.

L'utilisation d'une phase solide percolée supplémentaire de haute tension de surface (ferrite ou magnésite), afin d'avoir une interaction plus favorable avec le métal liquide et mener à sa percolation au sein du matériau, n'a pas non plus été concluante. Une étude rhéologique de la relaxation de gouttelettes d'étain ou d'alliage eutectique SnAgCu liquide dans une matrice de PP fondu a cependant permis de mesurer pour la première fois (aucune autre étude ne rapporte cette mesure) la tension interfaciale entre le liquide organique et métallique. Une valeur importante de 350 mN.m^{-1} est obtenue entre le PP et l'alliage eutectique SnAgCu à 230°C qui, combinée à un rapport de viscosité inférieur à 10^{-6} , explique l'incompatibilité et les phénomènes de démixtion observés entre les deux liquides. L'influence de la viscoélasticité de la matrice PP et de l'oxydation en surface du métal liquide ont été analysées afin de déterminer les conditions optimales pour mesurer la tension interfaciale entre le polymère et le métal liquide. Par trempe thermique sous cisaillement continu des gouttelettes de métal fondu, des ellipsoïdes solides ont été obtenues dont la taille caractéristique est limitée par le paramètre de déformation critique défini par Taylor. Ces particules solides de facteurs de forme supérieurs à 1 peuvent potentiellement conduire à une percolation électrique et donc à un matériau composite conducteur. Notre attention se porte donc désormais sur des matériaux composites chargés en charges métalliques solides.



Gauche : Gouttelette de SnAgCu liquide déformée par cisaillement dans PP fondu. Son temps caractéristique de relaxation permet de mesurer la tension interfaciale entre les deux liquides.

Droite : Efficacité de blindage EM en fonction de la fréquence de composites à base de fibres de verre argentées, épaisseur 1 mm, avec prédition théorique du modèle à composante inductive.

Le chapitre V s'intéresse ainsi à l'étude de composites PP à base de particules métalliques solides : des microparticules d'étain et des microfibres de verre recouvertes d'argent. Les fibres argentées, charges hybrides métalliques, se sont avérées très efficaces dans l'obtention de composites à forte efficacité de blindage EM. L'ajout d'acide stéarique aux composites à base de particules ou de fibres a également montré une amélioration importante et inattendue de leurs propriétés de blindage.

Ainsi, le composite chargé à 10 %vol en fibres de verre argentées et 3 %vol d'acide stéarique surpassé largement les objectifs fixés avec une efficacité de blindage de 50 dB à 1 MHz, 70 dB à 8 GHz (1 mm d'épaisseur) et une densité de 1090 kg.m⁻³. L'effet de l'acide stéarique a été étudié et a été lié à une modification de la morphologie du composite avec la formation de structures ségrégées des charges abaissant leur seuil de percolation et augmentant la conductivité électrique et les propriétés de blindage EM des matériaux composites à base de charges métalliques. Des analyses physicochimiques de la surface des charges métalliques et de la répartition de l'acide gras dans le volume du composite ont également permis de déterminer le mécanisme impliqué. Ainsi, dans le polymère fondu, l'acide stéarique réagit et se lie de façon covalente avec la surface des charges métalliques, puis forme des domaines fortement concentrés en charges et en acide gras. Ces domaines s'agrègent ensuite, menant à la formation de la structure ségrégée et percolée des charges dans le composite liée à l'amélioration de ses propriétés électriques et de blindage électromagnétiques.

Le sixième et dernier chapitre de ce manuscrit de thèse est dédié à la modélisation des propriétés de blindage EM des composites à base de charges métalliques étudiées précédemment, les particules d'étain et les fibres de verre argentées. Le modèle théorique développé avec les composites à base de NTC s'est en effet avéré incapable de prédire de façon précise l'efficacité de blindage des composites à base de charges métalliques. Ce modèle prédit une augmentation du blindage avec la fréquence alors que le blindage mesuré expérimentalement des composites basés sur des charges métalliques, issus de nos travaux et de la littérature scientifique, diminue avec la fréquence. Les propriétés d'auto-inductance des charges métalliques ont donc été considérées et une composante inductive a été ajoutée à la conductivité électrique du composite, induisant une chute du blindage EM au-dessus d'une fréquence inductive caractéristique. Ce modèle avec composante inductive s'est révélé capable de prédire avec exactitude l'efficacité de blindage des matériaux composites à base de charges métalliques issus de nos travaux et de nombreuses études de la littérature scientifique.

Les études menées lors de ce projet de thèse ont ainsi conduit à l'élaboration d'un matériau composite répondant au cahier des charges : un composite PP chargé en microfibres de verre recouvertes d'argent et en acide stéarique satisfaisant les exigences de blindage EM, de densité, de propriétés mécaniques et de propriétés de mise en forme. Pour chaque type de composite étudié, à base de NTC ou de charges métalliques, un modèle théorique prédisant efficacement les propriétés de blindage EM a pu être développé en se basant sur les propriétés intrinsèques des charges conductrices et de la matrice polymère. Ces travaux apportent donc une contribution significative au développement de nouveaux matériaux composites polymères de faible densité pour des applications de blindage EM et au développement de la modélisation des propriétés de blindage des matériaux

composites. Les perspectives du projet sont l'industrialisation des composites PP – Fibres de verre argentées – Acide stéarique et l'étude éventuelle de l'influence des procédés de mise en œuvre et de mise en forme de ces composites sur leurs propriétés de blindage. L'amélioration du modèle théorique du blindage EM est également possible avec l'ajout de nouvelles composantes dans le but d'affiner ses prédictions (capacitive, effet de grille). Ce projet de thèse répond ainsi à certains des grands défis d'aujourd'hui : le développement du blindage EM face à la multiplication de l'usage des ondes EM et la demande pour des matériaux légers visant à des économies d'énergie et des réductions des émissions de gaz à effet de serre.

TABLE OF CONTENTS

REMERCIEMENTS	i
ABSTRACT.....	iii
RÉSUMÉ.....	iv
PRÉSENTATION SYNTHÉTIQUE DES TRAVAUX.....	v
TABLE OF CONTENTS.....	1
GENERAL INTRODUCTION	7
CHAPITRE I. REVUE DE LA LITTERATURE SCIENTIFIQUE.....	11
1. Introduction au blindage électromagnétique et ses domaines d'application	11
a. Origines et inconvénients des interférences électromagnétiques (EMI)	11
b. Champ proche ou lointain : blindage électrique, magnétique et électromagnétique	14
c. Fréquences et domaines d'application.....	16
d. Marchés et importance économique du blindage électromagnétique.....	18
2. Théorie du blindage d'interférences électromagnétiques.....	19
a. Introduction succincte à la théorie de l'électromagnétisme	19
b. Un premier modèle théorique simple du blindage électromagnétique dans un matériau linéaire, homogène et isotrope	23
i. <i>Mécanismes et efficacité de blindage</i>	23
ii. <i>Expressions simplifiées de l'efficacité de blindage</i>	26
i. <i>Formule basse fréquence</i>	27
ii. <i>Avantages et inconvénients de ce modèle simple de blindage : défis de la modélisation des composites</i>	28
c. Autres modèles théoriques du blindage électromagnétique des matériaux composites	29
i. <i>Une approche matricielle pour les matériaux multicouches</i>	30
ii. <i>Moyenne logarithmique des propriétés d'un matériau composite</i>	30
iii. <i>Théorie des milieux effectifs</i>	32
3. Matériaux composites appliqués au blindage EM	33
a. Les matériaux composites : composition générale.....	33
i. <i>La matrice polymère</i>	34
ii. <i>Les charges fonctionnelles</i>	34
i. <i>Agents de dispersion et de compatibilisation polymère/charge</i>	37
b. Propriétés électromagnétiques des matériaux composites polymères	38
i. <i>Conductivité électrique des matériaux composites</i>	38

<i>ii.</i> <i>Les techniques de mesure du blindage électromagnétique</i>	44
<i>iii.</i> <i>Valeurs de blindage électromagnétique de matériaux composites polymères rapportées dans la littérature</i>	47
1- Le choix de la charge conductrice	47
2- Effets de synergie entre les charges conductrices	51
3- Effet de la structuration et de la morphologie d'un matériau composite sur ses propriétés de blindage EM.....	52
4. Conclusion de cette revue de littérature.....	55
a. Résumé des études antérieures de la littérature	55
b. Problématiques et orientations du projet de thèse.....	56
Références	58
CHAPTER II. MATERIALS AND METHODS: PROCESSING AND PROPERTIES MEASUREMENT OF POLYMER COMPOSITE MATERIALS	63
1. Introduction	63
2. Raw materials and composite materials fabrication methods	63
a. Polymer matrices and conductive fillers.....	63
b. Composite materials processing and sample fabrication	66
<i>i.</i> <i>Internal batch mixer</i>	66
<i>ii.</i> <i>Twin-screw extruder</i>	68
<i>iii.</i> <i>Samples hot compression molding</i>	68
<i>iv.</i> <i>Samples injection molding</i>	69
3. Properties characterization of studied composite materials.....	70
a. Electrical contacts metallization and conductivity measurement	70
b. Composite materials EMI shielding effectiveness measurements.....	72
<i>i.</i> <i>Coaxial cell measurement</i>	74
<i>ii.</i> <i>Waveguide cells measurement</i>	76
<i>iii.</i> <i>Electromagnetic properties of injected samples</i>	78
c. Optical and scanning electron microscopy observations of studied composite materials ...	81
<i>i.</i> <i>Sample preparation</i>	81
<i>ii.</i> <i>Observations.....</i>	82
d. Molten polymers, composite materials and liquid metals rheological measurements	83
e. Measurement of tensile mechanical properties of composite materials	85
f. Surface property measurement: water drop contact angle	86
g. Chemical analysis of fillers and composite materials	87
References	89

CHAPTER III. EXPERIMENTAL AND THEORETICAL STUDY OF EMI SHIELDING PROPERTIES OF CARBON NANOTUBES-BASED COMPOSITE MATERIALS 91

Abstract.....	91
1. Introduction	92
2. EMI shielding theoretical model.....	94
3. Materials and methods.....	99
a. Materials	99
b. Fabrication of PP — CNT polymer composites	100
c. Scanning Electron Microscopy.....	100
d. Electrical characterization of PP — CNT polymer composites	100
e. EMI shielding measurements of PP — CNT polymer composites	100
4. Results and discussions	102
a. Electrical conductivity of PP—CNT composites	102
b. EMI shielding effectiveness of PP—CNT composites in coaxial cell.....	104
c. EMI shielding effectiveness of PP—CNT composites in waveguide cells	107
d. SEM of PP/CNT composites	109
e. Advantages and limits of our theoretical model.....	109
5. Conclusion.....	113
References	115
Supplementary Information.....	120

CHAPTER IV. STUDY OF LIQUID METAL AS A POTENTIAL CANDIDATE FOR HIGHLY CONDUCTIVE COMPOSITE FILLER 125

Context.....	125
Abstract.....	126
1. Introduction	127
2. Retraction of deformed drop theoretical models.....	129
3. Materials and methods.....	132
a. Materials	132
b. Rheological measurements	132
c. Determination of interfacial tension by RDDM	134
4. Results and discussion	136
a. Rheology of liquid tin and eutectic SnAgCu alloy.....	136
b. Interfacial tension measurement by RDDM	138
c. Dynamic morphology freezing by temperature quenching	144
5. Conclusion.....	147
References	148

CHAPTER V. EFFECTS OF STEARIC ACID ADDITION ON SHIELDING PROPERTIES OF METAL FILLERS-BASED COMPOSITE MATERIALS	153
Abstract.....	153
1. Introduction	154
2. Materials and methods.....	156
a. Materials	156
b. Fabrication of PP – tin microparticles and Ag-coated glass microfibers composites	157
c. Electrical characterization of composites	158
d. Broadband EMI shielding measurements of composites.....	158
e. Optical microscopy	161
f. Transmission Infrared spectroscopy on filler – stearic acid mixes.....	161
g. Contact angle measurement on filler – stearic acid mixes	161
h. Transmission infrared microscopy on PP – filler composites.....	162
3. Results and discussion	162
a. Electrical conductivity of PP composites	162
b. EMI shielding properties of PP composites measured in coaxial cell.....	167
c. EMI shielding properties of PP composites measured in waveguides	171
d. Morphology of composites.....	174
e. Mechanism of stearic acid action on composite morphology and properties	176
f. IR spectroscopy of tin particles or silver-coated glass fibers mixes with stearic acid	177
g. Metal fillers surface properties modification with stearic acid	178
h. Interf. tension theoretical analysis of the tertiary PP–metal filler–stearic acid mixes.....	180
i. Infrared transmission microscopy on composites	181
4. Conclusion.....	184
References	185
Supplementary information.....	190

CHAPTER VI. THEORETICAL MODELING OF EMI SHIELDING PROPERTIES OF COMPOSITE MATERIALS FILLED WITH METAL FILLERS	195
Abstract.....	195
1. Introduction	196
2. EMI shielding theoretical model with an inductive component of conductivity.....	198
a. Frequency dependance of metal material conductivity	198
b. EMI shielding theoretical model and parameters influence on shielding effectiveness	200

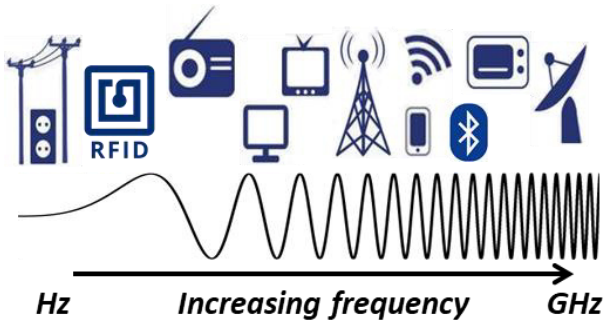
3. Application of the inductive component theoretical model to metal filler-based composite materials	205
a. Modeling of shielding effectiveness of studied tin particles and Ag-coated glass fibers PP composites	205
b. Fitting of metal-filler based composite shielding from the literature	206
4. Theoretical model limits and development perspectives	209
5. Conclusion.....	211
References	212
GENERAL CONCLUSION AND OUTLOOKS	215
ANNEXE: LIST OF ABBREVIATIONS AND SYMBOLS.....	219

General Introduction

GENERAL INTRODUCTION

Since the discovery of electromagnetic (EM) waves by the German physicist Heinrich Rudolf Hertz in 1886, its use in telecommunication, broadcasting and radar detection has grown exponentially. This growth is expected to continue with the demand of developing countries for these technologies and the upcoming arrival of 5G networks. One consequence is the increase of environmental electromagnetic pollution that hampers the same remote communications (by increasing the noise to signal ratio for instance) and can cause serious problems when these communications are vital (like a plane guidance system for example). The recent advances in connected systems – such as connected cars – require the reunion of multiple electronic devices, each completing a particular task, in a confined space. Such an accumulation of different working frequencies and power systems, EM wave emitters and receptors can lead to mutual hindrance leading to a reduced functionality or even a breakdown of the global connected system. These phenomena are called electromagnetic interferences (EMI) and are capital to consider while designing in-vehicle systems. The use of shields is then required to protecting a sensitive device from external perturbations or isolating a radiating device from its close neighbors. The use of metal plaques and meshes is common as metals are known as good EMI shielding materials (faradization) but they exhibit a high density, a sensitivity to corrosion, a potential high cost and a high processing and shaping required temperature (with cost and safety issues associated). Materials displaying similar EMI shielding properties to metals but without the cited drawbacks are conductive polymer composite materials. Associating a polymer matrix of low density but insulating with conductive fillers leads to composite materials exhibiting tunable shielding properties. The EMI shielding market represented in 2019 6.4 billions US dollars and is expected to reach almost 10 billion US dollars in 2025 with a constant gross. Combined to the need for lighter structures and lower greenhouse gas emissions, this highlights the interest for investing in the development of polymer composite materials for EMI shielding applications.

The objectives of the current research project are the development of a polyolefin polymer composite displaying a shielding effectiveness of at least 40 dB (99.99% of incident wave power blocked) for a shield thickness of 1mm over the broad frequency range of 100 MHz to 10 GHz including applications such as radio and phone waves, Wi-Fi, Bluetooth, 4G, 5G and radar waves. Density of the composite material must remain inferior to 1500 kg.m^{-3} and its mechanical (tensile) and processing properties as close as possible to the ones of the pure polymer resin.



Some applications of electromagnetic waves: Radio frequency identification, radio, TV and phone waves, 4G, 5G, Wi-Fi, Bluetooth, microwave ovens, and radars

The first chapter of this study concerning the literature review and analysis is written in French. The following chapters concerning materials and methods, and the carried-out research are all written in English. Questions that we will strive to bring answers to in our studies are: what conductive fillers dispersed in PP resin lead to the best composite EMI shielding properties while minimizing the composite material density and the changes in the material mechanical properties compared to the pure PP resin? At a given conductive filler concentration, how can we improve composite EMI shielding properties? How can we model a composite material shielding properties according to intrinsic properties of fillers and polymer matrix?

Study of the literature dealing with EMI shielding properties first oriented our works on the study of polypropylene – carbon nanotubes (CNT) composite materials. The project objectives (40 dB) were reached for a CNT concentration of 10 vol%, but this nanofiller concentration led to processing and shaping difficulties, as well as large changes in composite material mechanical properties compared to the pure PP. A shielding theoretical model corresponding to homogeneous and isotropic materials was developed and found to correctly predict the studied material properties. Three parameters relevant to shielding properties were identified and their influence studied: wave frequency, sample thickness and DC electrical conductivity (all easily measurable). CNT-based composites are limited by the intrinsic conductivity of the fillers, which then pushed us toward the study of fillers of higher intrinsic conductivity: metal materials. The density of such fillers requires finding new strategies to lower the filler percolation threshold in order to minimize the composite filler concentration.

Combining molten polymer (PP) with liquid metal (eutectic SnAgCu alloy) was one of these strategies but revealed to be challenging. The measurement of the interfacial tension between the molten state organic and metal material, never done before in the scientific literature, pointed out a

value as large as 350 mN.m^{-1} . Combined with the low viscosity ratio close to 10^{-6} , these parameters indicated the impossibility of effectively dispersing or percolating liquid metal drops in a polymer matrix. Obtaining solid ellipsoids of metal, whose size is limited by the capillary number and critical Taylor deformation, in the polymer matrix was however possible by temperature quenching and could potentially lead to lower metal particles percolation thresholds. Attention was thus brought to solid metal fillers.

Our study then focused on PP composites filled with tin microparticles and hybrid fillers: silver-coated glass microfibers of moderate density compared to pure metals but of high metal conductivity. The use of these metal fillers proved to be efficient in getting a high shielding effectiveness composite material. Besides, adding stearic acid to these two composite types led to a large and quite unexpected increase in the shielding properties. Thus, the composite filled with 10 vol% Ag-coated glass fibers and 3 vol% stearic acid surpassed the set project goals with an EMI shielding effectiveness of 50 dB at 1 MHz and 70 dB at 8 GHz (1mm thickness). The role of stearic acid was investigated and found to influence the composite morphology with the appearance of filler segregated structures. Physicochemical analyses helped us to uncover the involved mechanism: in molten polymer, stearic acid reacts on metal filler surface and forms domains of high filler and fatty acid concentration. Those domains then aggregate, leading to the formation of the percolated segregated structure of enhanced electrical conductivity and EMI shielding properties.

The last part of this study is dedicated to the theoretical modeling of EMI shielding properties of the two previous metal filler-based composite materials. The model developed with the CNT-based composite was found to be unable to correctly predict the shielding effectiveness of those materials. Indeed, while the model predicts an increase of shielding when wave frequency increases, experimental shielding effectiveness of metal filler-based materials, including from studies from the literature, was observed to drop with increasing frequency. Based on the self-inductance properties of the metal fillers, an inductive component was added to the composite conductivity, implying a drop of this parameter above a characteristic inductance frequency parameter. The theoretical model was found to correctly predict EMI shielding properties of metal filler-based materials from our works and from studies from the literature.

The presented works thus are thus a significant contribution to polymer composite materials and EMI shielding science and engineering. Combining a critical view on the obtained experimental results and from the literature, and a theoretical approach of EMI shielding, we could orient our research efforts on the most promising composite types. A PP composite material based on silver-

coated glass fibers and stearic acid was found to be the best candidate to fulfill and surpass the set project objectives.

This project is the results of the collaboration between the laboratory Ingénierie des Matériaux Polymères (IMP) in Lyon, the Feluy, Belgium Total research center, the Total SA holding in Paris and the Hutchinson Centre de Recherche et Innovation (CRI) in Montargis.

Chapitre I. Revue de la littérature scientifique

Chapitre I. Revue de la littérature scientifique

Théorie du blindage électromagnétique, conductivité et blindage des matériaux composites polymères

1. Introduction au blindage électromagnétique et ses domaines d'application

a. Origines et inconvénients des interférences électromagnétiques (EMI)

Les interférences électromagnétiques (Electromagnetic Interference, EMI en anglais) sont issues d'ondes électriques, magnétiques ou électromagnétiques (EM) émises par rayonnement ou conduites par un dispositif électronique en fonctionnement et sont des signaux parasites pouvant endommager ou perturber le fonctionnement d'autres dispositifs électroniques, environnants ou non. Ces ondes parasites peuvent également, lorsqu'elles sont de forte puissance, endommager les tissus des êtres vivants. Ces dernières décennies ont vu un développement exponentiel des dispositifs électroniques et des communications à distance par moyen d'ondes électromagnétiques. Sans surprise, les problèmes d'EMI se sont également multipliés avec des signaux parasites lors des communications à distance (exemple classique du téléphone portable induisant des interférences électriques dans un haut-parleur) et la forte augmentation de la pollution électromagnétique des zones à forte densité de population pouvant porter atteinte au fonctionnement de dispositifs électroniques sensibles non protégés. Les EMI peuvent s'avérer dangereuses lorsqu'elles concernent le disfonctionnement des systèmes de pilotage des avions, des dispositifs de sécurité des voitures et des dispositifs médicaux indispensables au maintien en vie d'un patient. Un premier exemple est l'interdiction d'utilisation de dispositifs électroniques émetteurs d'onde (téléphone, ordinateur portable avec le wifi) pour les passagers lors du décollage et de l'atterrissement d'un avion. Ces dispositifs sont susceptibles d'interférer avec les systèmes de communication et de guidage de l'avion. Un autre exemple est le défibrillateur cardiaque : l'électronique pilotant le fonctionnement de l'appareil doit être protégée des décharges électriques intenses générées par l'appareil et destinées au patient. Les forts champs magnétiques générés par des passages de courants intenses, comme dans les batteries de voiture, peuvent également fortement perturber le fonctionnement des dispositifs électroniques.

environnements. Ce problème est d'autant plus d'actualité par le fort développement des voitures électriques et/ou connectées. Ces exemples sont illustrés en Figure 1.

L'électronique de grande consommation et les dispositifs nomades de plus en plus petits imposent aux fabricants de rassembler dans le même boîtier ou même sur une même carte électronique tous les dispositifs nécessaires au fonctionnement du produit : batterie, transformateur de courant, antenne wifi et GPS, microprocesseur, carte graphique, etc. La proximité de tous ces dispositifs électroniques en fonctionnement combinée aux perturbations des champs EM extérieurs est un terrain idéal pour le développement d'EMI portant irrémédiablement atteinte au bon fonctionnement du produit. La mise en place de stratégies de blindage EM est donc indispensable pour isoler les dispositifs des perturbations de ses voisins et de celles extérieures. Cela peut se faire par une organisation spatiale réfléchie des composants électroniques et la mise en place d'écrans de blindage EM.

Les ondes EM et les interférences EM sont également susceptibles d'entraîner des accumulations de charges sur des matériaux isolants, peu conducteurs ou non reliés à la terre. La conséquence de ces charges accumulées est l'apparition d'un champ électrique (et donc un nouveau champ parasite) et la possible décharge brutale de ces charges accumulées. Pour les dispositifs électroniques très sensibles ou lorsque les ondes EM sont de grandes amplitudes et impliquent une forte accumulation de charges, une décharge peut fortement endommager le dispositif. Dans l'industrie et la recherche où des champs EM forts peuvent être utilisés, les décharges peuvent également blesser gravement un opérateur.

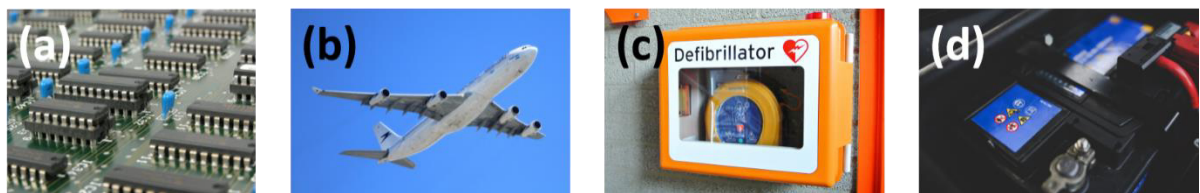
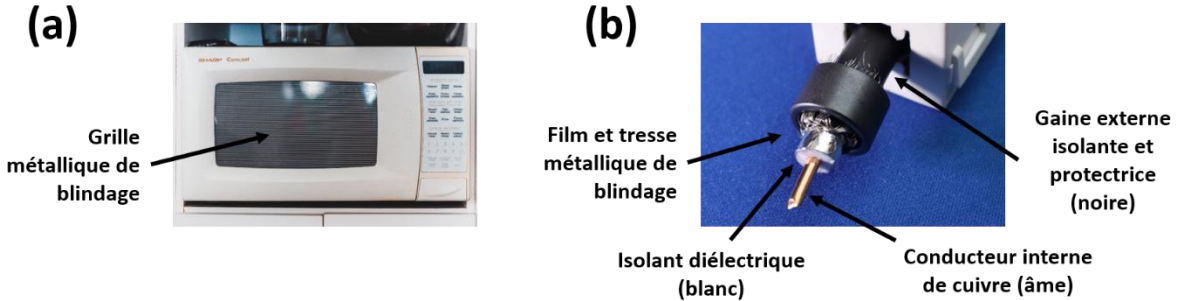


Figure I - 1 : Systèmes soumis aux EMI nécessitant un blindage. Les cartes microélectroniques (a), les systèmes de guidage et de communication d'un avion (b), les défibrillateurs cardiaques (c) et l'environnement d'une batterie de voiture (d) sont des systèmes susceptibles d'être perturbés par les EMI.

La dangerosité des ondes EM et interférences EM pour l'homme dans le cas d'émissions de faibles intensités comme avec les téléphones portables, les petites antennes et instruments de communication à distance n'a pas encore été prouvée scientifiquement. La nocivité des champs EM de grandes amplitudes a en revanche été démontrée [1]. Une exposition prolongée à un champ magnétique statique supérieur à 2 Tesla peut entraîner des nausées, vertiges, une sensation de goût métallique dans la bouche et une perte momentanée de certaines fonctions cognitives. Ce peut être le cas au voisinage d'une IRM 3T. Un autre effet indirect dangereux de ce fort magnétisme est l'attraction ou la projection d'objets métalliques sur l'appareil due au champ magnétique (matériel médical mais également implant médical contenant un matériau ferromagnétique !). Une exposition à un champ magnétique basse fréquence de 1 à 400 Hz peut entraîner des phosphènes rétiniens (magnétophosphènes). Les champs électriques et magnétiques de basses fréquences (1 Hz à 10 MHz) et de fortes intensités peuvent perturber le système nerveux central ou périphérique. Pour les plus hautes fréquences, de 100 kHz à 300 GHz, une exposition à un champ électrique, magnétique ou EM entraîne un échauffement des tissus (en surface au-dessus de 6 GHz, en profondeur en-dessous de 6 GHz). Lorsque l'intensité de ces champs est importante, une exposition prolongée ou non peut entraîner de graves brûlures. Enfin, un dernier effet notable sur l'homme est l'apparition d'un « clic » auditif lors de l'exposition à un champ EM impulsif de grande amplitude de fréquence entre 300 MHz et 6 GHz. Ce peut être le cas au voisinage de certains radars. Il est donc clair que dans le cadre industriel et de la recherche, où des champs EM de fortes intensités peuvent être utilisés, il est impératif de protéger les opérateurs des risques induits par ces champs en utilisant un blindage EM par exemple.

Une solution simple pour s'affranchir des EMI est soit d'enfermer la source des interférences dans une boîte de blindage pour protéger l'environnement alentour, soit, si les perturbations sont extérieures, protéger le dispositif sensible par cette même boîte. Cette boîte, souvent métallique, aux parois pleines ou sous forme de grille, est souvent appelée cage de Faraday, et le processus de protection est appelé faradisation. En fait, tout matériau possédant une conductivité électrique suffisante peut potentiellement être utilisé pour faire du blindage EM, c'est-à-dire que lorsque le matériau forme une boîte bien fermée, il empêche toute onde EM de rentrer dans la boîte et également toute onde générée dans la boîte d'en sortir. Lorsqu'une onde électromagnétique, soit un champ électrique et un champ magnétique couplés, pénètre dans un matériau conducteur, le champ électrique exerce une force sur les électrons libres dans le matériau. Cette force induit alors l'apparition de courants dans le volume du matériau. Ces derniers entraînent l'apparition d'un champ magnétique induit dans le matériau qui s'oppose à la propagation de l'onde électromagnétique dans

le matériau. Le choix du matériau est important pour obtenir un bon blindage EM : les matériaux présentant une forte conductivité électrique sont les plus adaptés. C'est la raison pour laquelle les métaux sont des matériaux de choix pour réaliser des faradisations. Des exemples simples d'emploi des métaux dans les applications de blindage EM sont : dans les câbles coaxiaux, le conducteur interne et l'isolant diélectrique sont enveloppés d'un film ou d'une tresse métallique (ou les deux) qui protège le fil central, vecteur des informations, des perturbations extérieures. Les fours à micro-ondes sont équipés sur leur hublot d'une grille métallique qui protège les utilisateurs des micro-ondes émises à l'intérieur du four pour réchauffer les aliments. Ces exemples sont illustrés en Figure 2. L'épaisseur de l'écran de blindage est également très importante : un écran constitué d'un matériau conducteur bloquera d'autant plus une onde EM incidente qu'il est épais. C'est un simple effet de volume car il y a alors plus d'électrons libres participant au blindage.



*Figure I - 2 : Exemples d'emploi des matériaux métalliques dans des applications de blindage EM :
(a) Un four à micro-onde et (b) un câble coaxial.*

b. Champ proche ou lointain : blindage électrique, magnétique et électromagnétique

Une onde électromagnétique est caractérisée par trois grandeurs fondamentales : sa vitesse de propagation, égale à la vitesse de la lumière dans le milieu de propagation, sa fréquence, le nombre d'oscillation du champ par seconde, et la longueur d'onde associée. Ces trois grandeurs sont reliées par l'expression suivante :

$$\lambda = \frac{c}{f} \quad (1)$$

λ est la longueur d'onde, f la fréquence et c la vitesse de la lumière égale à 3.10^8 m.s^{-1} dans le vide (la même valeur de vitesse dans l'air est admise). A partir d'une source de champ électromagnétique, une

onde peut se propager dans le vide, l'air ou n'importe quel milieu qui le lui permet grâce au couplage des champs électriques et magnétiques de l'onde.

Lorsqu'une onde EM plane progressive monochromatique se propage dans un milieu donné (assez loin de la source), le rapport des amplitudes des champs électrique et magnétique est constant. Ce rapport est appelé impédance d'onde Z et dépend du milieu de propagation [2]. Dans le cas du vide, l'impédance caractéristique du vide est égale à :

$$Z_0 = 377 \Omega \quad (2)$$

Lorsque la source des EMI (circuit électronique, fil électrique, antenne) et l'entité à protéger (circuit électronique, on l'appellera l'observateur) ont été identifiées, la distance entre les deux ainsi que la nature de la source de champ sont des paramètres importants à considérer car ils caractérisent le type de champ EM dans lequel l'observateur est plongé. La source peut émettre un champ électrique statique (charge fixe, condensateur chargé de façon permanente, courant continu) ou un champ magnétique fixe (aimant) ; dans ce cas il n'y a pas de champ EM, l'observateur est plongé soit dans un champ électrique statique soit dans un champ magnétique statique. Si la source émet un champ électrique ou magnétique oscillant et que la distance source/observateur est supérieure à la longueur $\lambda/2\pi$ alors on considère que l'on est dans le cas d'un champ lointain et l'observateur est plongé dans un champ électromagnétique. Le champ électrique E et magnétique H sont couplés, le rapport E/H est constant égal à l'impédance d'onde dans le milieu de propagation. Si la distance source/observateur est inférieure à la longueur précédente, la situation est plus complexe. Au voisinage d'une source de champ électrique (générateur, condensateur), on se retrouve souvent à devoir blinder un champ électrique. Au voisinage de courants alternatifs (fils électriques, solénoïde, antenne, batterie, fils haute tension) peuvent être présents à la fois des champs électriques et magnétiques non couplés et donc dont les amplitudes ne sont pas reliées [3]. Une stratégie de blindage électrique et magnétique doit alors être mise en place pour se protéger des deux champs différents. Ces différents cas de figure sont schématisés en Figure 3.

Ainsi, en fonction de la nature de la source, de la fréquence des EMI et de la distance entre le dispositif à protéger et la source, des stratégies différentes doivent être employées : blindage électrique, magnétique ou électromagnétique.

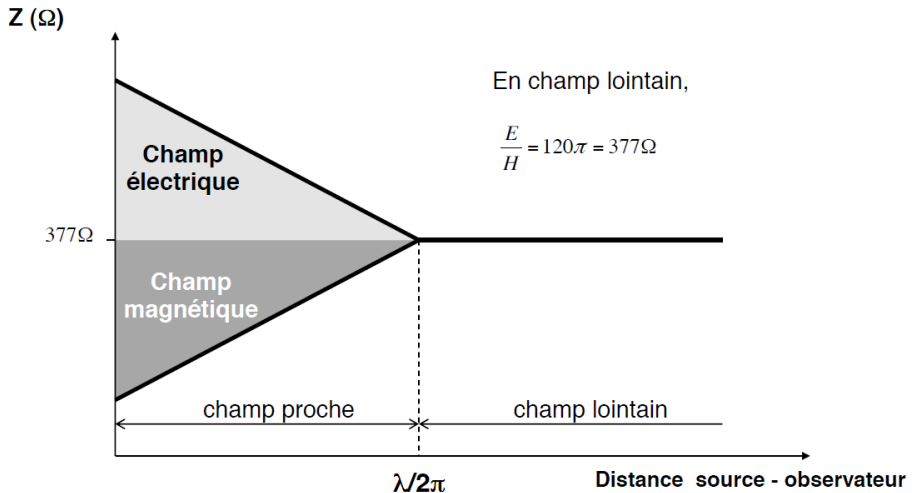


Figure I - 3 : Impédance d'onde en fonction de la distance entre la source et l'observateur.

c. Fréquences et domaines d'application

Un schéma du spectre EM est représenté en Figure 4. En fonction de la fréquence d'une onde EM, les applications sont très diverses. En commençant par les Très Basses Fréquences (TBF) et les Extrêmement Basses Fréquences (EBF), on trouve des ondes EM naturelles tels que le champ magnétique terrestre ou les champs électriques générés dans l'atmosphère (orage, foudre). Dans ces catégories peuvent également être rangés les courants DC, la fréquence du secteur électrique à 50 Hz, la magnétoscopie, les démagnétiseurs industriels et l'induction métallique dans les forges [4]. Dans le domaine basses fréquences (BF), on peut trouver des applications telles que la radiodiffusion commerciales/amateurs et les canaux de communication radiofréquence (talkie-walkie, radio à bord des bateaux ou des avions). Les applications d'Identification RadioFréquence (RFID) se trouvent également dans cette gamme mais s'étalent également dans les micro-ondes avec des fréquences allant de 125 kHz à 6 GHz. C'est une technologie utilisée par exemple dans les portiques de magasin, dans les badges d'accès, les puces d'identification (animaux domestiques ou sauvages par exemple) et les paiements sans contact. Au-delà des 100 MHz on va trouver les ondes de télévisions (TNT), la téléphonie mobile, les téléphones sans fil et de nombreux canaux de radiocommunications. Au-dessus de 1 GHz sont situés encore des canaux de téléphonie mobile, la 4G, la 5G, la Wi-Fi, le Bluetooth. Les applications radars (militaires ou civils, positionnement et/ou mesure de vitesse) sont divisées en plusieurs bandes de fréquence qui s'étalent entre 3 et 100 GHz. Des exemples plus précis de fréquences associées à des applications concrètes sont listés en Tableau 1.

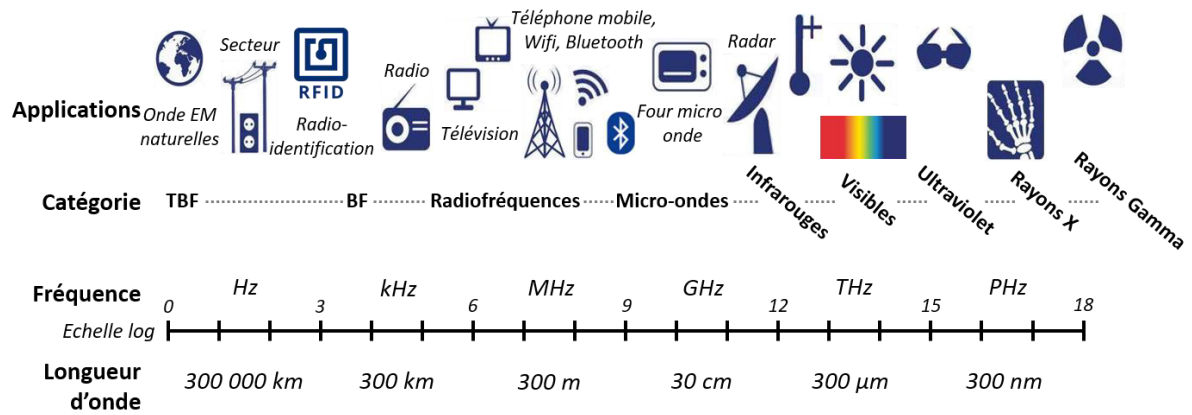


Figure I - 4 : Spectre électromagnétique. Fréquences avec longueurs d'onde, catégories d'onde et applications correspondantes.

Tableau I - 1 : Exemples d'application des ondes EM et les fréquences associées

Application	Fréquences
Induction forge	1 Hz – 1 kHz
Portique antivol	6,25 kHz
Badge d'accès	121,5 kHz
Identification animale	134,2 kHz
Paiement sans contact, passeport	13,56 MHz
Radio FM	87,5 – 108 MHz
Badge transport en commun	900 MHz
Téléphonie mobile (GSM)	890 – 960 MHz
GPS civil	1,575 GHz
4G	700 MHz – 2,6 GHz
Bluetooth	2,4 GHz
Wifi	2,4 & 5 GHz
Four à micro-onde (alimentaire)	2,45 GHz
Télépeage autoroutier	5,8 GHz
5G	6 & >24 GHz
Radar routier (civil)	8 – 40 GHz

Ainsi les ondes EM concernées par les applications de blindage EM ont des fréquences allant du courant continu (DC) à des fréquences de 100 GHz. Au-dessus de ces fréquences se trouvent les ondes infrarouges, le spectre visible et les ultraviolets, et à plus haute fréquence les rayons X et gamma. Les longueurs d'onde, inférieures au micron, et les énergies associées, suffisantes pour interférer avec les électrons gravitant autour des noyaux atomiques, ne nous intéressent pas dans ce projet car elles ne rentrent pas dans la catégorie d'ondes visées par le blindage électromagnétique.

d. Marchés et importance économique du blindage électromagnétique

Le marché du blindage électromagnétique a représenté en 2019 environ 6,4 milliards de dollar US. Il est en croissance constante puisqu'il représentait 6 milliards de dollars US en 2018 (+ 7%) et il est estimé qu'il atteindra un total de 6,8 milliards de dollars US en 2020 (+ 6%). Les projections économiques attribuent à ce marché un taux de croissance annuel de 6,3%, si bien qu'il devrait atteindre une valeur de 7,3 milliards de dollars US en 2021 et 9,2 milliards de dollars US en 2025 [5]. Cette telle croissance est majoritairement portée par le développement et l'arrivée de la 5G en Europe, Asie et Amérique du nord, et par les normes de plus en plus contraignantes concernant les EMI. Ce marché comprend les rubans et stratifiés de blindage EMI, les peintures et revêtements EMI, les pièces métalliques EMI, les composites polymères EMI et les filtres EMI. Les peintures et revêtements conducteurs représentent la plus grosse part du marché (viennent ensuite les rubans et stratifiés, les métaux et les composites) pour des applications majoritairement radiatives (moyennes et hautes fréquences) en opposition aux applications de blindage électrique basse fréquence (pas d'onde EM). Les applications représentant les ventes les plus importantes sont, de la plus importante à la moins importante, l'électronique grand public (surtout les smartphones), les technologies de l'information et de la communication (Telecom), le secteur automobile, la santé connectée, la défense et l'aéronautique. Ce marché est majoritairement situé dans les pays développés avec la zone Asie-Pacifique représentant 40% du marché, l'Amérique du nord 30% et l'Europe presque 25%. Parmi les cinq entreprises leaders des produits de blindage EM on trouve trois américaines (Parker-Hannifin, PPG Industries and RTP Company), une anglaise (Laird Performance UK) et une allemande (Henkel). Ces entreprises ainsi que d'autres entreprises du domaine du blindage EM investissent massivement dans la R&D, le leader anglais du marché y investissant par exemple 10% de son chiffre d'affaire.

Le marché des composites polymères conducteurs appliqués au blindage EM suit cette même tendance de forte croissance. L'intérêt pour ces matériaux stimule de forts et nombreux investissements dans la recherche et leur développement, à l'instar de ce projet de thèse.

2. Théorie du blindage d'interférences électromagnétiques

Dans cette partie vont être développés les aspects théoriques du blindage EM. Une compréhension théorique des mécanismes du blindage et des paramètres pouvant l'influencer est indispensable pour le développement éclairé d'un nouveau matériau présentant des propriétés de blindage. Après une introduction succincte de la théorie de l'électromagnétisme sera présenté un modèle théorique simple mais pertinent du blindage EM, modèle qui sera souvent utilisé dans la suite du projet. Suivront la présentation d'autres modèles théoriques présents dans la littérature témoignant de l'importance de la modélisation dans l'étude des phénomènes de blindage EM.

a. Introduction succincte à la théorie de l'électromagnétisme

Un champ électrique est issu d'un gradient spatial de charge. Il peut être créé par une différence de potentiel électrique (dans un circuit électrique par exemple, différence de concentration d'ions de part et d'autre d'une membrane) ou par une accumulation de charges (condensateur chargé, charges statiques sur un isolant). Un champ magnétique est lui créé par le mouvement de particules chargées (courant électrique) ou généré par des matériaux magnétiques (aimants).

L'unité du champ électrique E est $V.m^{-1}$ ou $kg.m.A^{-1}.s^{-3}$, et celle du champ magnétique H est T (tesla) ou $kg.A^{-1}.s^{-2}$.

Une onde électromagnétique résulte du couplage entre un champ électrique \vec{E} et un champ magnétique \vec{H} . Les lettres H et B peuvent être utilisées pour désigner le champ magnétique bien que B soit plus souvent utilisée pour le champ magnétique induit. Une onde EM se propage dans le vide, l'air ou tout matériau le lui permettant. Le couplage entre le champ électrique et magnétique, ainsi que leurs propriétés respectives sont théorisés par les équations de Maxwell [3] :

$$\vec{\nabla} \cdot \vec{E} = \frac{\rho_c}{\epsilon_0} \quad (1)$$

$$\vec{\nabla} \cdot \vec{H} = 0 \quad (2)$$

$$\vec{\nabla} \times \vec{E} = -\frac{\partial \vec{H}}{\partial t} \quad (3)$$

$$\vec{\nabla} \times \vec{H} = \mu_0 \vec{J} + \mu_0 \epsilon_0 \frac{\partial \vec{E}}{\partial t} \quad (4)$$

La densité volumique de charges fixes est ρ_c et les mouvements de charges (comme le courant électrique) sont décrits par le vecteur densité de courant \vec{j} . ϵ_0 et μ_0 sont respectivement la permittivité diélectrique et la perméabilité magnétique du vide. Les opérateurs $\vec{\nabla}.$ et $\vec{\nabla} \times$ sont respectivement la divergence et le rotationnel.

L'équation 1 (Maxwell-Gauss) décrit l'apparition d'un champ électrique en présence de charges électriques. L'équation 2 (Maxwell-Thomson ou Maxwell-flux) traduit le fait que, contrairement aux charges électriques, il n'existe pas de monopôles magnétiques. L'équation 3 (Maxwell-Faraday) décrit le phénomène d'induction électromagnétique où la variation d'un champ magnétique entraîne l'apparition d'un champ électrique. Enfin, l'équation 4 (Maxwell-Ampère) décrit l'apparition d'un champ magnétique en présence d'un mouvement de charge et/ou de la variation d'un champ électrique.

De ces équations, on peut déduire l'équation de propagation d'une onde EM dans le vide ou l'air, espace dénué de charges fixes et de courants ($\rho = 0$ et $\vec{j} = \vec{0}$) :

$$\frac{\partial^2 \vec{E}}{\partial t^2} - c^2 \vec{\Delta}(\vec{E}) = \vec{0} \quad (5)$$

$$c = \frac{1}{\sqrt{\mu_0 \epsilon_0}} \quad (6)$$

La vitesse de la lumière dans le vide est c , égale à environ $3 \times 10^8 \text{ m.s}^{-1}$. L'opérateur $\vec{\Delta}(.)$ est la dérivée Laplacienne tridimensionnelle. L'équation 5 est aussi valable pour le champ magnétique H en le substituant à E . Le passage d'une équation à l'autre peut se faire avec les équations de Maxwell.

Une solution (parmi d'autres) de l'équation 5 est l'onde plane progressive harmonique monochromatique :

$$\vec{E}(\vec{r}, t) = \vec{E}_0 \exp(\vec{k} \cdot \vec{r} - \omega t + \varphi_0) \quad (7)$$

\vec{r} est le vecteur position, ω la pulsation de l'onde ($\omega = 2\pi f$ avec f la fréquence de l'onde), φ_0 une constante correspondant à la phase de l'onde, $|\vec{E}_0|$ l'amplitude de l'onde supposée constante pour une onde plane et \vec{k} est le vecteur d'onde caractéristique de la direction de propagation de l'onde. La relation de dispersion, obtenue avec les équations de Maxwell, relie ce vecteur à la pulsation en fonction des caractéristiques du milieu de propagation :

$$\omega = \frac{c}{n(\omega)} \|\vec{k}\| \quad (8)$$

$\|\cdot\|$ est la norme vectorielle et $n(\omega)$ est l'indice caractéristique du milieu de propagation. Il est constant pour un milieu non dispersif mais peut dépendre de la fréquence de l'onde pour les milieux dispersifs.

Pour cette onde plane, les champs électriques et magnétiques sont couplés. De l'équation 3 on peut obtenir :

$$\vec{H} = \frac{\vec{k} \times \vec{E}}{\omega} = \frac{n(\omega)}{c} \cdot \vec{x} \times \vec{E} \quad (9)$$

\vec{x} est un vecteur unitaire parallèle à la direction de propagation de l'onde (et donc parallèle à \vec{k}) et \times est le produit vectoriel entre deux vecteurs. La solution d'onde plane progressive est en général valable loin de la source de l'onde ($\|\vec{r}\| \gg \lambda$) où l'amplitude de l'onde varie peu, soit en champ lointain.

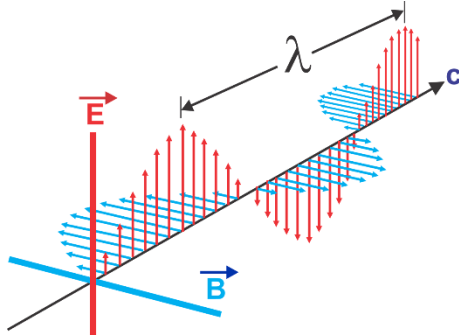


Figure I - 5 : Champ électrique E et champ magnétique B couplés d'une onde EM de longueur d'onde λ se propageant dans le vide à la vitesse c .

La puissance P d'une onde électromagnétique (en W) peut être définie à travers l'expression du vecteur de Poynting \vec{P} et son flux à travers une surface S :

$$\vec{P} = \frac{\vec{E} \times \vec{H}}{\mu_0} \quad (10)$$

$$P = \iint_S \vec{P} \cdot d\vec{S} \quad (11)$$

L'amplitude du champ électrique étant proportionnelle à celle du champ magnétique (Eq. 9), l'équation 11 nous indique que la puissance d'une onde EM est proportionnelle au carré de l'amplitude de son champ électrique ou magnétique.

Les ondes EM étudiées dans ce projet ne sont pas des ondes libres mais des ondes guidées à l'intérieur soit d'une cellule de mesure coaxiale, soit d'une cellule de mesure de type guide d'onde. Dans une cellule coaxiale, l'onde est de type progressive mais dans un guide d'onde elle est de type stationnaire due aux réflexions des ondes progressives entraînant la formation de maxima et minima d'amplitude d'onde à l'intérieur du guide. Dans les deux cas, il est commode de caractériser la propagation d'une onde EM à travers un milieu donné par l'impédance d'onde Z dépendant des propriétés physiques de ce milieu. Cette définition est analogue à l'impédance de ligne sans perte reliant le potentiel d'un dipôle au courant qui le traverse, et relié à l'inductance L et à la capacité C linéaire de la ligne :

$$Z_{\text{ligne}} = \sqrt{\frac{L}{C}} \quad (12)$$

$$Z_{\text{onde}} = \frac{E}{H} \quad (13)$$

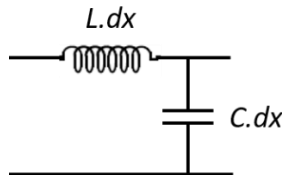


Figure I - 6 : Schéma d'un morceau de longueur dx de ligne coaxiale sans perte avec inductance linéaire L et capacité linéaire C .

L'impédance d'onde est alors définie comme le rapport du champ électrique et du champ magnétique couplés se propageant dans le milieu considéré. Pour un milieu linéaire, homogène et isotrope, l'impédance d'onde prend alors l'expression :

$$Z = \sqrt{\frac{\mu^*}{\epsilon^*}} = \sqrt{\frac{j\omega\mu'}{\sigma+j\omega\epsilon'}} \quad (14)$$

L'impédance d'onde Z est un nombre complexe.

Pour un milieu diélectrique conducteur et magnétique, l'expression de sa permittivité diélectrique ϵ^* caractérisant les charges liées et mobiles, et de sa perméabilité magnétique μ^* caractérisant les dipôles magnétiques sont :

$$\epsilon^* = \epsilon' - j\omega\epsilon'' = \epsilon' - j\frac{\sigma}{\omega} \quad (15)$$

$$\boldsymbol{\mu}^* = \boldsymbol{\mu}' - j\omega\boldsymbol{\mu}'' \quad (16)$$

Ces deux grandeurs sont des nombres complexes. La partie réelle de la permittivité diélectrique correspond à la permittivité mesurée sur les matériaux isolants et caractérise les charges liées entraînant une polarisation électrique sous l'effet d'un champ électrique extérieur. La partie imaginaire caractérise les charges mobiles dans un matériau conducteur et est reliée à la conductivité électrique du matériau. La partie imaginaire de la perméabilité magnétique est communément négligée pour les matériaux magnétiques classiques.

b. Un premier modèle théorique simple du blindage électromagnétique dans un matériau linéaire, homogène et isotrope

i. Mécanismes et efficacité de blindage

L'efficacité de blindage (Shielding Effectiveness) d'un écran est définie comme suit :

$$SE = 10 \cdot \log_{10} \left(\frac{P_t}{P_i} \right) = 20 \cdot \log_{10} \left(\left| \frac{E_t}{E_i} \right| \right) = 20 \cdot \log_{10} \left(\left| \frac{B_t}{B_i} \right| \right) \quad (17)$$

P, E et B sont la puissance de l'onde, l'amplitude de son champ électrique et magnétique, respectivement. Les indices i et t désignent respectivement l'onde incidente à l'écran de blindage et l'onde transmise à travers cet écran. Les facteurs différents devant les logarithmes découlent de la relation quadratique entre puissance et amplitude (Eq. 10 & 11). $|.|$ est le module complexe car les amplitudes des champs électriques et magnétiques sont des grandeurs complexes (Eq. 7 et 14).

Une onde se propageant dans un matériau donné présente une impédance d'onde donnée Z dépendant des caractéristiques du milieu (Eq. 14). Une onde se propageant dans le vide ou l'air présente une impédance caractéristique Z_0 définie comme :

$$Z_0 = \sqrt{\frac{\mu_0}{\epsilon_0}} \approx 377 \Omega \quad (18)$$

Les interfaces entre l'air et le matériau composant l'écran de blindage constituent une discontinuité des propriétés physiques des milieux de propagation : permittivité diélectrique, perméabilité magnétique et conductivité électrique, et a fortiori impédance d'onde Z. Cette discontinuité entraîne la réflexion et transmission partielle de l'onde EM à cette interface. Pour une

incidence normale à la surface de l'écran de blindage, les coefficients de réflexion r_{01} et transmission t_{01} en amplitude sont égaux à [6] :

$$r_{01} = \frac{Z_1 - Z_0}{Z_1 + Z_0} \quad (19)$$

$$t_{01} = \frac{2Z_1}{Z_1 + Z_0} \quad (20)$$

L'air est défini comme milieu 0 et le matériau de blindage comme milieu 1 d'impédance d'onde Z_1 . On peut noter que $r_{01} = -r_{10}$. Un schéma du trajet de l'onde à travers l'écran de blindage d'épaisseur d est présenté en Figure 7. Comme évoqué, l'onde EM incidente est partiellement réfléchie à la 1^{ère} interface air-écran. L'onde transmise traversant le matériau sur son épaisseur subit des phénomènes d'absorption diminuant son amplitude. L'origine de ces phénomènes de dissipation en énergie thermique sont multiples : dissipations de courants induits, polarisations diélectriques, polarisations interfaciales, dissipations par courants de Foucault (ou « Eddy currents »), pertes par hystérésis ou pertes par résonnances magnétiques [7]. L'effet de ces phénomènes d'absorption est réduit en un facteur d'absorption α :

$$\alpha = e^{-d/\delta} \quad (21)$$

$$\delta = \sqrt{\frac{2}{\mu' \cdot \omega \cdot \sigma}} = \sqrt{\frac{1}{\mu' \cdot \pi \cdot f \cdot \sigma}} \quad (22)$$

$$f_c = \frac{1}{\mu' \cdot \pi \cdot \sigma \cdot d^2} \quad (23)$$

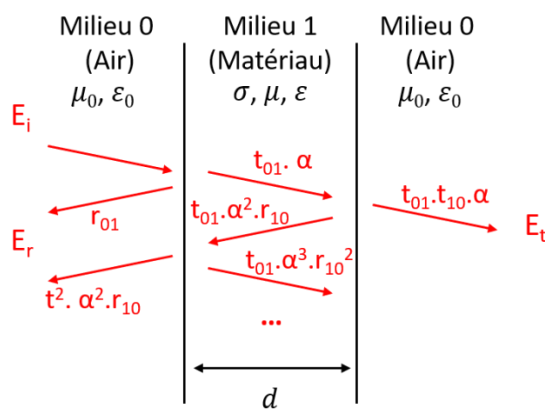


Figure 1 - 7 : Schéma du trajet de l'onde dans un écran de blindage. Les indices au-dessus des flèches désignent les facteurs multipliant l'amplitude de l'onde initiale.

Une longueur et une fréquence caractéristique sont associées à ce facteur d'absorption. Lorsqu'une onde EM parcours une longueur caractéristique δ , également appelée épaisseur de peau, elle perd 63% de son amplitude. La fréquence caractéristique f_c liée aux propriétés de l'écran de blindage délimite les zones de fréquences où l'absorption est minime voire nulle (en-dessous de cette fréquence) et celles où l'absorption devient importante (au-dessus de cette fréquence).

En arrivant sur la 2^{ème} interface écran-air, l'onde EM subit à nouveau une transmission ainsi qu'une réflexion. L'onde transmise est mesurée. L'onde réfléchie revient vers la 1^{ère} interface, subit une absorption en chemin et à nouveau une transmission/réflexion à la 1^{ère} interface matériau/air. S'ensuit une onde transmise dans la direction de la source, considérée comme réflexion secondaire, et une onde réfléchie qui repart vers la 2^{ème} interface. L'onde peut alors effectuer de multiples aller-retours, son amplitude diminuant au fur et à mesure alors qu'elle est absorbée et réfléchie. Ce phénomène est appelé réflexions internes multiples.

Le rapport de l'amplitude de l'onde (champ électrique, le champ magnétique est proportionnel) transmise et incidente peut alors être calculé en considérant tous ces phénomènes (Fig. 7) :

$$\begin{aligned} \frac{E_t}{E_i} &= t_{01} \cdot t_{10} \cdot \alpha + t_{01} \cdot t_{10} \cdot r_{10}^2 \cdot \alpha^3 + t_{01} \cdot t_{10} \cdot r_{10}^4 \cdot \alpha^5 + \dots \\ &= \alpha \cdot t_{01} \cdot t_{10} \cdot \sum_{n=0}^{+\infty} (r_{10} \cdot \alpha)^{2n} = \alpha \cdot t_{01} \cdot t_{10} \cdot \frac{1}{1 - (r_{10} \cdot \alpha)^2} \end{aligned} \quad (24)$$

En combinant les Eq. 17 et 24, l'expression du blindage devient :

$$SE = 20 \cdot \frac{d}{\delta} \cdot \log_{10}(e) - 20 \cdot \log_{10} \left(\left| \frac{4 \cdot Z_0 \cdot Z_1}{(Z_1 + Z_0)^2} \right| \right) + 20 \cdot \log_{10} \left(\left| 1 - \left(e^{-d/\delta} \frac{Z_1 - Z_0}{Z_1 + Z_0} \right)^2 \right| \right) \quad (25)$$

Le grand avantage de cette équation est qu'elle est divisée en trois termes et chacun d'eux correspond exactement à un des mécanismes du blindage décrit précédemment. Le 1^{er} terme concerne l'absorption que l'onde subie lors de sa 1^{ère} traversée de l'écran de blindage. Le 2^{ème} terme correspond à la première réflexion, ou réflexion simple, que l'onde incidente subie lorsque qu'elle entre en contact pour la première fois avec l'écran de blindage. Le dernier terme est relié aux réflexions internes multiples.

Le détail de ce modèle et l'influence des paramètres physiques (épaisseur de l'écran, conductivité électrique, permittivité diélectrique, perméabilité magnétique du matériau et fréquence de l'onde incidente) sur l'efficacité de blindage seront traités au Chapitre III.

ii. Expressions simplifiées de l'efficacité de blindage

L'équation 25 peut être simplifiée selon les paramètres d'une expérience de mesure de blindage et les caractéristiques de l'écran de blindage. Le 3^{ème} terme de réflexions multiples internes peut être négligé si le terme d'absorption est suffisamment important. En effet, ces multiples réflexions font intervenir plusieurs fois l'absorption (à chaque aller-retour). Ainsi, une absorption conséquente sur un seul trajet va grandement réduire l'importance des réflexions internes multiples dont l'amplitude devient très rapidement négligeable. Il est souvent considéré que les réflexions multiples peuvent être négligées si le terme d'absorption (absorption sur un seul trajet) vaut plus que 10 dB [6]. Cette condition est en générale remplie dans les hautes fréquences pour un échantillon conducteur (au-dessus de f_c).

Les meilleurs matériaux pour des applications de blindage sont les matériaux conducteurs. Une simplification du 2^{ème} terme (réflexion simple) peut s'obtenir en prenant l'approximation du bon conducteur :

$$\sigma \gg \omega \epsilon' \quad (26)$$

Cette approximation revient à négliger l'importance des charges liées par rapport à celles libres, une approximation correcte pour les bons conducteurs. Pour un matériau non ou faiblement magnétique, cette approximation entraîne $Z_1 \ll Z_0$ (Eq. 14). Ces approximations permettent rapidement d'obtenir les expressions simplifiées suivantes :

$$SE_T = SE_R + SE_A + SE_M \quad (27)$$

$$SE_R = 39.5 + 10 \cdot \log_{10} \left(\frac{\sigma}{2\pi f \mu'} \right) \quad (28)$$

$$SE_A = 8.7 \cdot d \cdot \sqrt{\pi \cdot f \cdot \mu' \cdot \sigma} \quad (29)$$

$$SE_M = 0 \text{ si } SE_A > 10 \text{ dB} \quad (30)$$

Selon ces expressions simplifiées du blindage pour un matériau linéaire (grandeur constantes avec la fréquence), homogène, isotrope et bon conducteur, l'efficacité de blindage ne dépend que de l'épaisseur de l'écran, sa conductivité, sa perméabilité magnétique et la fréquence de l'onde incidente.

Toutes ces simplifications ne peuvent cependant se faire que dans des cas bien précis. Il est nécessaire que le phénomène d'absorption soit suffisamment important pour pouvoir ignorer les réflexions multiples. Ceci implique d'avoir un échantillon bon conducteur pour que f_c ne soit pas trop

grande (l'absorption peut alors être présente dans la gamme de mesure) et de se placer dans le domaine des hautes fréquences, au-dessus de f_c . Ces simplifications ne sont donc en général valables que pour les matériaux bon conducteurs dans les hautes fréquences ($f > f_c$).

Nasouri et al. ont testé ces expressions théoriques simplifiées sur des composites PVP/MWCNT [8]. Leurs résultats expérimentaux et théoriques sont présentés en Figure 8. Le modèle théorique concorde bien avec les données expérimentales et des coefficients de détermination R^2 compris entre 0.92 et 1 ont été calculés. La conductivité utilisée dans le modèle est la conductivité DC.

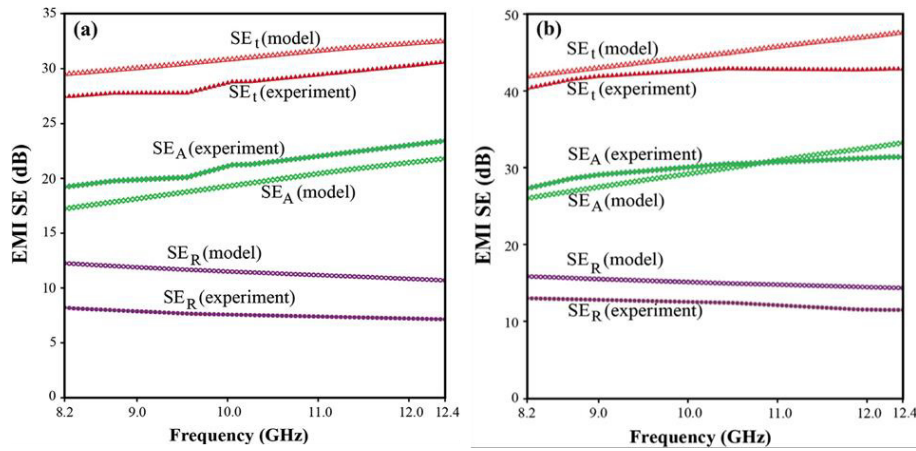


Figure 1 - 8 : Blindage théorique et expérimental dans la bande de fréquence X sur composite PVP/MWCNT chargé à 7.5 %m (a) et 10 %m (b). Epaisseur 1mm. Extrait de Nasouri et al. [8]

i. Formule basse fréquence

Il est possible de simplifier ces expressions (Eqs. 27-30) encore davantage en se plaçant dans le domaine des basses fréquences où il n'y a pas de phénomènes d'absorptions [9], ce qui est vérifié si :

$$f \ll f_c \quad \text{soit} \quad d \ll \delta \quad (31)$$

On peut alors raisonner sur un circuit électrique simple sans effets capacitif ou inductifs. Dans le cas de la cellule coaxial qui couvre ce domaine des basses fréquences (en général kHz-MHz), on a alors juste un câble coaxial avec comme charge l'échantillon.

A partir du schéma de la Figure 9, on peut calculer l'efficacité de blindage en basses fréquences avec un câble coaxial d'impédance caractéristique 50Ω :

$$SE_{BF} = 20 \cdot \log_{10} \left(\frac{V}{V_0} \right) = 20 \cdot \log_{10} \left(1 + \frac{R_0}{R} \right) = 20 \cdot \log_{10} \left(1 + \frac{50}{R} \right) \quad (32)$$

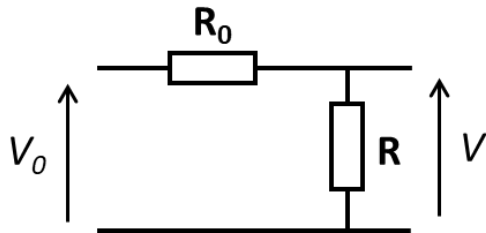


Figure I - 9 : Schéma de la cellule coaxiale avec un échantillon dans le domaine des basses fréquences. R est la résistance de l'échantillon, R_0 est l'impédance caractéristique du câble (50Ω).

Le blindage en basse fréquence ne dépend que de la résistance de l'échantillon, elle-même reliée à la conductivité et l'épaisseur de celui-ci. On ne peut pas relier cette expression aux formules simplifiées précédente (Eqs. 27-30) car les hypothèses ne sont pas compatibles. Ce modèle est destiné pour tout échantillon dans le domaine des basses fréquences ($f \ll f_c$, pas d'effets capacitifs et inductifs).

ii. Avantages et inconvénients de ce modèle simple de blindage : défis de la modélisation des composites

L'avantage incontestable du modèle décrit par l'Eq. 25 et simplifié en Eqs. 27 – 30 est sa facilité d'utilisation. Pour un matériau métallique ou composite non magnétique, en connaissant simplement l'épaisseur de l'écran de blindage, sa conductivité facilement mesurable avec des instruments communs et la fréquence de l'onde à blinder, il est possible de rapidement prédire l'efficacité de blindage de l'écran. Pour un matériau possédant en plus des propriétés magnétiques, il suffit également de connaître sa perméabilité magnétique. Ce modèle théorique est large bande : il peut prédire le blindage d'un matériau des fréquences basses, ou en DC, aux plus hautes fréquences (THz) avec comme limite théorique les rayonnements infrarouges impliquant des mécanismes physiques de réflexion/absorption différents.

Le principal inconvénient de ce modèle vient de ses hypothèses de matériau linéaire, homogène et isotrope. En fonction du matériau utilisé pour l'écran de blindage, la linéarité de ses propriétés physiques peut ne pas être vérifiée avec par exemple une permittivité électrique, une perméabilité magnétique ou une conductivité pouvant varier avec la fréquence. Par exemple, la perméabilité magnétique de certains matériaux ferromagnétiques est fonction de la fréquence de l'onde excitatrice [10]. Dans un matériau composite, l'hypothèse d'homogénéité, soit le fait que les hétérogénéités du matériau doivent être bien plus petites que la longueur d'onde, peut également ne pas être vérifiée. Ce phénomène est d'autant plus important aux hautes fréquences où la longueur d'onde peut être de l'ordre de grandeur de l'épaisseur des échantillons ou plus faible : à 100 GHz, la longueur d'onde est par exemple égale à 3 mm. Dans les matériaux composites à base de charges métalliques, la formation de boucles de courant à l'intérieur du composite peut avoir des conséquences sur sa conductivité par des phénomènes d'inductance, remettant en cause l'hypothèse de linéarité [11]. Toujours dans le domaine des composites, la mise en forme des pièces et des échantillons par des méthodes induisant de forts phénomènes de cisaillements, comme la mise en forme par injection, peut induire une dispersion de charges non homogène dans l'échantillon ainsi qu'une orientation des charges ou des agrégats de charges [12]. Les hypothèses d'homogénéité et d'isotropie peuvent alors ne pas être vérifiées.

La modélisation des propriétés de blindage électromagnétique des matériaux composites peut donc s'avérer plus compliquée que l'utilisation du précédent modèle simple. La nature même du composite, le mélange de deux ou plusieurs composés différents avec des propriétés physiques différentes, peut nécessiter une stratégie de modélisation différente puisque les hypothèses d'homogénéité, de linéarité et d'isotropie du matériau ne sont pas forcément vérifiées. Chaque matériau composite peut alors demander une approche différente en fonction de ses composants, faisant de la modélisation de ces matériaux un véritable défi.

c. Autres modèles théoriques du blindage électromagnétique des matériaux composites

L'intérêt croissant de l'utilisation de matériaux composites légers, peu chers et présentant de bonnes propriétés de blindage EM a accentué le besoin de pouvoir modéliser de façon fiable leurs propriétés. Les grands avantages de la modélisation théorique sont le gain de temps et la réduction des coûts. Avec un modèle théorique fiable, la rapidité de calcul d'un ordinateur permet de connaître

quasiment instantanément l'efficacité de blindage d'un écran de taille et de géométrie données dans des conditions de fonctionnement données, sans avoir à fabriquer la pièce et à la mesurer. Le gain de temps est très conséquent, ainsi que l'économie des coûts relatifs à la fabrication et aux tests sur la pièce.

Quelques modèles théoriques issus de la littérature scientifique sont présentés.

i. Une approche matricielle pour les matériaux multicouches

Hoang et al. ont proposé une approche matricielle du calcul du blindage afin de pouvoir modéliser le blindage de matériaux multicouches, constitués de plusieurs couches d'épaisseurs données de matériaux linéaires, homogènes et isotropes [13]. Chaque couche est de perméabilité magnétique μ_i , de permittivité diélectrique ϵ_i , de conductivité électrique σ_i , d'impédance d'onde Z_i et d'épaisseur d_i . La matrice caractéristique de la couche est définie comme :

$$[\mathbf{M}_i] = \begin{bmatrix} \cos(k_i d_i) & -j \cdot Z_i \cdot \sin(k_i d_i) \\ -\frac{j}{Z_i} \cdot \sin(k_i d_i) & \cos(k_i d_i) \end{bmatrix} \quad (33)$$

$$k_i = \frac{2\pi}{\lambda} \sqrt{\epsilon'_i + \frac{\sigma_i}{j\epsilon_0 \omega}} \quad (34)$$

La multiplication matricielle des différentes couches permet d'obtenir une matrice pour le matériau multicouche. Les coefficients de réflexion, transmission et l'efficacité de blindage peuvent ensuite être calculés à partir des coefficients de cette matrice.

Les auteurs ont appliqué ce modèle à un matériau multicouche à base de composite PVP – polyaniline (conducteur) et de Kapton (isolant). La modélisation de ces résultats expérimentaux est présentée en Figure 10. Un bon accord entre le blindage mesuré et celui prédit peut être observé.

ii. Moyenne logarithmique des propriétés d'un matériau composite

Un modèle théorique idéal serait un modèle capable de prédire le blindage EM d'un composite directement à partir des propriétés intrinsèques de la matrice (ou des matrices si mélanges de polymères) et des charges que l'on y incorpore. Peng et al. ont proposé une prédition théorique de la conductivité et permittivité complexes d'un matériau composite à partir de la moyenne logarithmique

de ses composants pondérée de leur fraction volumique [14]. Cette conception s'inspire de la résistance/capacitance équivalente d'un réseau (Figure 11). Ainsi, la conductivité complexe théorique σ^* d'un matériau composite (formule identique pour la permittivité ϵ^*) est fonction de celle σ_n^* de ces composants n de fraction volumique f_n :

$$\sigma^* = \prod_n (\sigma_n^*)^{f_n} \quad (35)$$

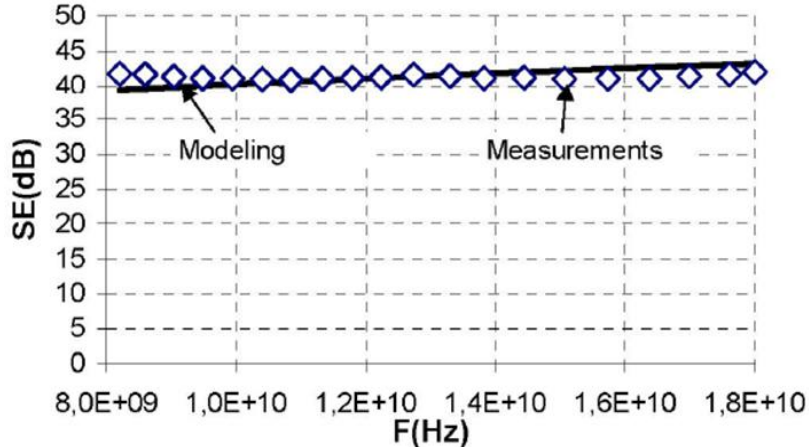


Figure I - 10 : Blindage dans la bande X d'un film multicouche Pani8.8/PU (93µm) – Kapton (125µm) - Pani8.8/PU (360µm). Extrait de Hoang et al. [13]

Pour un composite constitué d'une matrice isolante (indice m) et d'une charge conductrice (indice c), la conductivité complexe théorique prédict par ce modèle est :

$$\sigma^* = [j\omega\epsilon_0(\epsilon'_m - j\epsilon''_m)]^{f_m} \cdot \left[j\omega\epsilon_0 \left(\epsilon'_c - j\frac{\sigma_c}{\omega\epsilon_0} \right) \right]^{1-f_m} \quad (36)$$

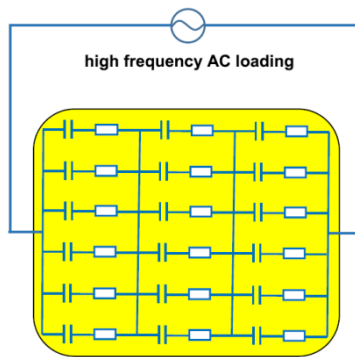


Figure I - 11 : Représentation schématique d'un matériau composite comme un réseau d'éléments capacitance-résistance. Extrait de Xia et al. [15]

Les auteurs peuvent ensuite prédire l'évolution des parties réelles et imaginaires de la permittivité et de la conductivité de composites PMMA / SWCNT en fonction de la fréquence et du taux de nanotubes de carbone. Ces paramètres pourraient ensuite potentiellement être utilisés pour prédire l'efficacité de blindage EM du même matériau composite.

iii. Théorie des milieux effectifs

D'autres modèles théoriques permettent d'estimer les propriétés macroscopiques d'un matériau composite à partir des propriétés locales de ses constituants. Les théories des milieux effectifs développées par Mossoti, Maxwell, Poisson et Lorentz sont ainsi souvent utilisées pour la modélisation des propriétés des matériaux composites. Xia et al. ont utilisé ces théories des milieux effectifs pour modéliser la conductivité électrique et le blindage EM de composites époxy ou PS chargés en graphène ou CNT, solides ou sous forme de mousses [15,16].

D'autres effets et phénomènes ont également été pris en compte dans ce modèle : le contact électrique imparfait entre les charges avec l'ajout d'une résistance de contact, la conductivité par effet tunnel et la formation d'un réseau de nano-capacités en complément de cette interface imparfaite (Figure 11), ainsi que des phénomènes de sauts électroniques de Dyre et de relaxations électroniques de Debye. Les auteurs ont ainsi pu modéliser les propriétés de leurs composites à partir de toutes ces grandeurs physiques. La comparaison de leur modèle théorique aux résultats expérimentaux est présentée en Figure 12. Les auteurs constatent que les mécanismes précédents pris séparément ne conduisent pas aux bonnes prédictions mais leur combinaison permet de correctement prédire la conductivité et le blindage EM de leurs composites. Cependant, ce modèle possède 19 paramètres dont une grande partie sont des paramètres ajustables. Il reflète la complexité de la modélisation des matériaux composites.

Le modèle théorique privilégié dans ce projet est le modèle théorique simple « non simplifié » (Eq. 25) car il est facile d'utilisation. En effet, il n'est nécessaire de ne connaître que trois paramètres simples à mesurer expérimentalement : la fréquence de l'onde incidente, l'épaisseur et la conductivité du matériau de blindage (simples à mesurer). De plus, ce modèle est large bande car il permet de modéliser l'efficacité de blindage d'un composite sur toute la gamme de fréquence (DC – 100 GHz), et il est connu pour sa fiabilité et sa précision de prédition dans la littérature. Ce modèle théorique requiert cependant un matériau homogène (hétérogénéités plus petites que la longueur d'onde),

linéaire (paramètres physiques constants avec la fréquence) et isotrope (pas de direction privilégiée de propagation de l'onde EM) pour des prédictions fiables et précises.

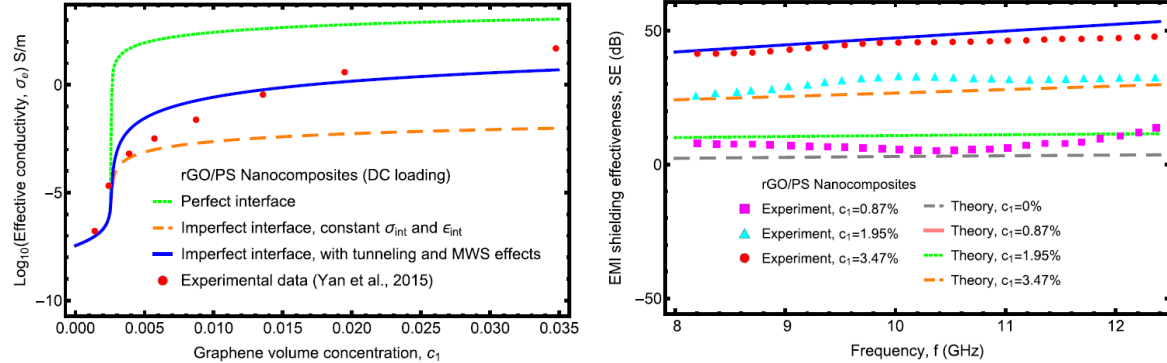


Figure I - 12 : Résultats expérimentaux de composites PS/rGO et prédictions théoriques à partir du modèle des milieux effectifs : conductivité en fonction de la fraction de graphène (gauche) et blindage en fonction de la fréquence (droite). Extrait de Xia et al. [15]

3. Matériaux composites appliqués au blindage EM

a. Les matériaux composites : composition générale

Un matériau composite polymère est un mélange de plusieurs composés, miscibles ou non. L'avantage d'un matériau composite est l'obtention, à partir de composés aux propriétés physiques et chimiques différentes, d'un nouveau matériau aux propriétés nouvelles. Par exemple, une matrice polymère isolante du courant et ne présentant pas de blindage EM (la majorité des polymères) peut être mélangée avec des charges conductrices pour obtenir un composite conducteur avec des propriétés de blindage. L'avantage d'utiliser un matériau composite par rapport aux charges seules peut être un gain en densité du matériau si les charges sont denses (en les mélangeant avec le polymère de faible densité), des propriétés de résistance mécaniques améliorées si les charges sont fragiles ou friables (elles sont alors fixées/figées et protégées dans la matrice polymère) et une mise en œuvre ainsi qu'une mise en forme de pièces facilitées grâce aux propriétés thermoplastiques des polymères par exemple.

i. La matrice polymère

La base d'un matériau composite est la ou les matrices polymères le constituant. Il peut s'agir d'un seul polymère ou d'un mélange de polymères. Ce dernier apporte en général de la complexité au composite due à la comptabilisation requise entre les différents polymères et la répartition des charges différente dans les différentes matrices. Deux grandes catégories de polymères sont en général utilisées dans l'industrie. Il y a les résines thermoplastiques comme le polypropylène (PP), le polyéthylène (PE), le polyamide (PA), le polystyrène (PS), le polycarbonate (PC) ou le poly(fluorure de vinylidène) (PVDF) par exemple. L'intérêt des matériaux thermoplastiques est leur recyclabilité moyennant toutefois le développement de nouvelles formulations. Les matériaux thermodurcissables sont légèrement différents, ils sont en général issus d'une réaction chimique induisant la réticulation de leurs chaînes polymères. Des exemples de résines thermodurcissables sont les résines époxy, le polyuréthane (PU), le polydiméthylsiloxane (PDMS) ou les caoutchoucs (naturel, butyl ou butyl-styrène). Cependant, ils ne sont pas recyclables du fait de leur nature réticulée.

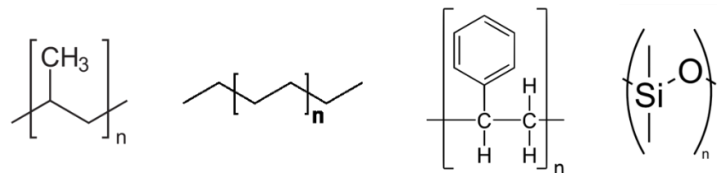


Figure I - 13 : structure chimique de quelques polymères communs. De gauche à droite : PP, PE, PS, PDMS.

ii. Les charges fonctionnelles

L'autre composant principal d'un matériau composite polymère est la ou les charges apportant les nouvelles propriétés au composite comparé au polymère seul. Les charges introduites dans les matrices polymères sont très diverses. En fait, la viscosité réduite des matrices polymères fondues (ou pré-réticulation pour les thermodurcissables) permet d'y incorporer n'importe quelle charge solide de taille millimétrique, micrométrique ou nanométrique.

Afin d'obtenir un matériau composite présentant des propriétés de blindage EM, des charges conductrices ou magnétiques doivent être incorporées dans une matrice polymère comme expliqué

dans la partie théorique précédente. De nombreux matériaux possèdent des propriétés de conduction électronique. Les grandes catégories de charges conductrices sont présentées :

- **Les charges carbonées** : grâce aux très nombreuses insaturations présentes sur un réseau d'atomes de carbone, la bande de conduction d'un matériau carboné peut être accessible aux électrons mobiles et le doter de propriétés de conduction électronique. Parmi ces matériaux, on trouve les noirs de carbone (CB) [17], le graphène [18,19], les nanotubes de carbones CNT (mono-paroi ou multi-paroi) [20,21] (Figure 14) et tout matériau organique ayant subis une carbonisation [22]. Leur avantage est de présenter de bonnes conductivités électriques et de faibles densités grâce à leur nature carbonée.

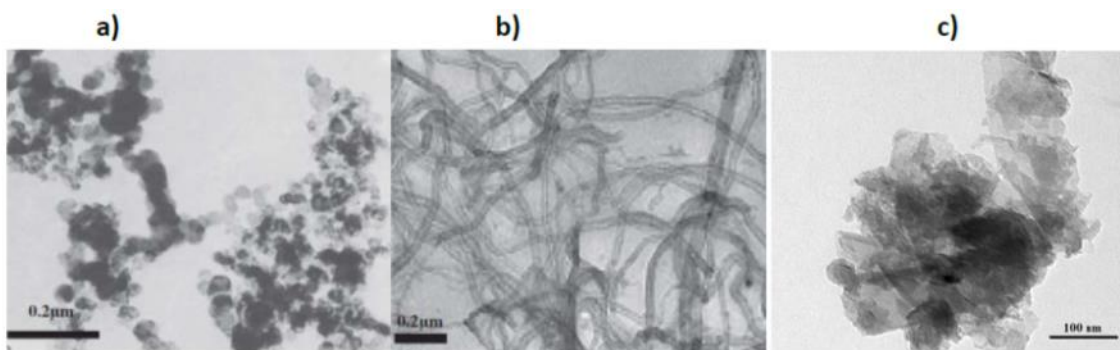


Figure I - 14 : Clichés de microscopie électronique par transmission de charges carbonées. (a) Noir de carbone, (b) Nanotubes de carbone, tirés de Dang et al. [23]. (c) Graphène, tiré de Mehrali et al. [24].

- **Les polymères conducteurs** : des polymères possédant des insaturations conjuguées tout au long de leurs chaînes peuvent posséder des propriétés de conduction électronique. En général, l'utilisation d'un dopant permet de fortement augmenter cette conductivité. Des exemples de polymères conducteurs sont le polyacétylène (la meilleure conductivité mais très instable), le polyaniline (PANI), le polypyrrole, le polythiophene et ses dérivés P3HT et P3MT [25,26]. Une difficulté majeure d'incorporation de ces polymères dans une autre matrice polymère est que leur température de fusion est en général plus grande que leur température de dégradation. Les polymères présentant des propriétés de conduction ionique ne présentent pas de propriétés de blindage EM à cause de la très faible interaction des ions avec les ondes EM lorsque la fréquence dépasse les kHz.
- **Les charges métalliques** : les matériaux présentant les meilleures conductivités sont évidemment les matériaux métalliques. Leur incorporation est fréquente dans les composites pour le blindage EM, ce qui leur permet d'atteindre de fortes valeurs d'efficacité de blindage. Un défaut inhérent des charges métalliques est cependant leur forte densité intrinsèque et

leur sensibilité à la corrosion. Cette dernière peut être atténuée une fois les charges dispersées dans le polymère. Les métaux les plus utilisés sont souvent les plus communs (ceux dont le prix du marché est raisonnable) comme le fer/acier, l'argent, le cuivre, le nickel et l'aluminium. Ils peuvent être présents sous forme de particules [27], de fibres [28], de nanofibres [29,30] ou alors en revêtement (« coating ») sur des matériaux plus légers telles que des fibres textiles ou de verre [31,32], ou sur des particules de polymère par exemple [33].

- **Les charges magnétiques :** la majorité des matériaux avec des propriétés magnétiques sont d'origine métallique et possèdent donc les mêmes avantages et inconvénients. Leurs propriétés magnétiques peuvent, en plus de leur éventuelle conductivité, apporter de l'efficacité de blindage supplémentaire. Les charges magnétiques les plus couramment utilisées sont l'oxyde de fer (magnétite Fe_3O_4) et le nickel [34]. Quelques alliages métalliques possèdent également des propriétés magnétiques exceptionnelles tel que le mu-métal et le permalloy, alliage à base de fer et de nickel avec un peu de cuivre, de molybdène et de manganèse [35]. Ces derniers peuvent atteindre des perméabilités magnétiques relatives à température ambiante de 10^5 quand le nickel atteint 600.
- **Les charges MXenes :** les Mxenes sont des matériaux constitués de quelques couches atomiques de carbures, nitrures et carbonitrides de métaux de transition. Parmi ces métaux on retrouve souvent le titane, le gallium, le molybdène et l'aluminium. Un intérêt récent a été porté sur ces charges de densité moyenne et de conductivité métallique, avec potentiellement des propriétés magnétiques. Des exemples de Mxenes utilisés pour le blindage EM sont le Ti_2AlC , le Ti_3AlC_2 et le $\text{Ti}_3\text{C}_2\text{T}_x$ avec T les terminaisons de surface (-OH, =O, -F) [36–38].

L'introduction de charges dans une matrice polymère peut se faire de plusieurs manières. Les trois principales sont le mélange à l'état fondu, le mélange en solvant et la polymérisation in-situ [39,40]. La première manière est la plus simple et la plus répandue dans l'industrie de la mise en œuvre et mise en forme des matériaux polymères. Cette technique est très utilisée pour les résines thermoplastiques telles que le PP et le PE. La seconde manière consiste à disperser les charges dans un solvant, à y dissoudre le polymère (le solvant choisi doit être un bon solvant pour le polymère) et à évaporer le solvant, souvent directement dans un moule pour obtenir l'échantillon final. Cette technique permet de contourner la montée en température du mélange à l'état fondu susceptible d'endommager ou de dégrader certains polymères. Enfin, la dernière méthode consiste à disperser les charges directement dans le monomère ou oligomère à partir duquel est fabriqué le polymère. L'échantillon final est obtenu par polymérisation directement dans un moule. Cette dernière technique

est souvent employée pour les composites à base de résine époxy ou de PDMS par exemple. Ces méthodes sont schématisées en Figure 15.

i. Agents de dispersion et de compatibilisation polymère/charge

Lors de la fabrication de matériaux composites polymères, quelle que soit la méthode de fabrication, de petites molécules peuvent être utilisées pour faciliter la dispersion des charges. Ces composés peuvent parfois être cruciaux pour la mise en œuvre du matériau ou pour l'obtention de caractéristiques physiques particulières telles qu'une bonne dispersion des charges ou la stabilité d'un mélange de deux polymères immiscibles. Dans la mise en œuvre à l'état fondu, la technique de fabrication utilisée dans ce projet, on peut distinguer les agents de dispersion et/ou de compatibilisation. Les charges dispersées dans une matrice polymère, et en particulier les nanocharges, ont souvent tendance à s'agrégner en raison des forces de Van der Waals et de leur possible faible affinité avec la matrice. Pour casser ces agrégats (mélange dispersif) et arriver à une meilleure dispersion des charges, de petites molécules sont souvent utilisées. Elles sont choisies de telle sorte qu'elles ont une bonne affinité à la fois avec les charges et avec la matrice polymère, et peuvent même réagir et s'adsorber à la surface des charges. Le résultat est une meilleure affinité, une meilleure compatibilité entre la matrice polymère et les charges qui peut mener à une meilleure dispersion de ces dernières. Un exemple est l'acide stéarique, un acide gras avec des propriétés amphiphiles lui permettant d'interagir à la fois avec des composés hydrophiles et hydrophobes, des caractéristiques opposées que l'on retrouve souvent avec la matrice polymère et les charges [41–43]. Par exemple, le PP est hydrophobe et les charges métalliques hydrophiles en raison de la couche surfacique d'oxyde métallique.

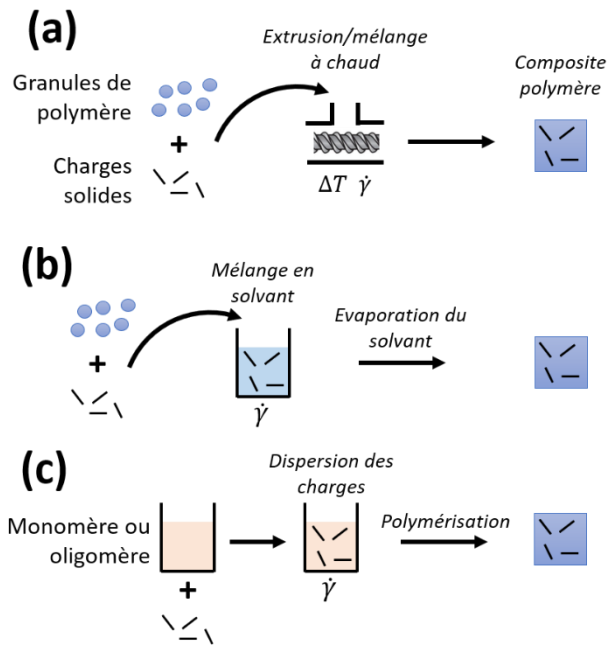


Figure I - 15 : Représentation schématique des trois principales méthodes de fabrication d'un composite polymère. (a) Mélange à l'état fondu, (b) Mélange en solvant et (c) polymérisation in-situ.

b. Propriétés électromagnétiques des matériaux composites polymères

i. Conductivité électrique des matériaux composites

Comme affirmé dans la partie modélisation théorique, une des principales caractéristiques d'un matériau requises pour qu'il présente des propriétés de blindage EM est son caractère conducteur électrique. Malheureusement, il ne suffit pas de mettre des charges conductrices dans une matrice polymère pour obtenir un composite conducteur. Il faut que ces charges percolent sur l'ensemble du composite, c'est-à-dire pour un échantillon mesuré entre deux points qu'il existe au moins un chemin continu constitué de charges conductrices permettant le passage du courant. Le seuil de percolation est la concentration de charge, pour un composite et une méthode de fabrication donnés, pour laquelle le premier chemin se forme. L'idéal pour obtenir un matériau composite homogène présentant une bonne conductivité électrique est de se situer bien au-dessus de ce seuil de percolation en termes de concentration de charges conductrices. Une représentation schématique de la percolation est présentée en Figure 16.

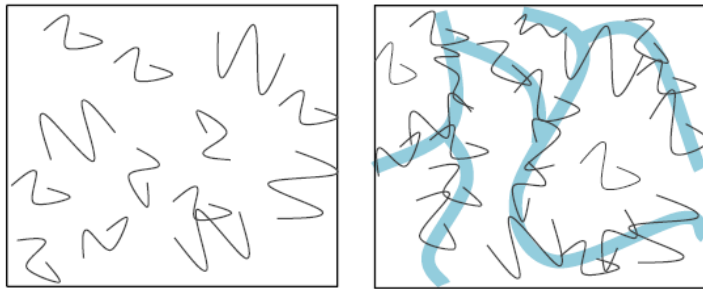


Figure I - 16 : Représentation schématique de la percolation électrique de charge linéique dans une matrice polymère. Gauche : sous le seuil de percolation, aucun chemin continu n'est formé, le matériau est isolant. Droite : au-dessus du seuil de percolation, un ou plusieurs chemins de conduction peuvent être formés, le matériau devient conducteur.

Un seuil de percolation bas signifie qu'il est nécessaire d'introduire moins de charges conductrices pour obtenir un matériau conducteur, ce qui peut réduire les impacts négatifs des charges sur la densité du composite, sa mise en œuvre ou ses propriétés mécaniques. Les paramètres influant sur le seuil de percolation sont multiples mais on peut en distinguer deux principaux : le rapport d'aspect des charges et la dispersion/distribution des charges dans la matrice polymères. Le rapport d'aspect d'une charge est le rapport de ses dimensions caractéristiques. Le plus faible rapport d'aspect est celui d'une sphère égale à 1, mais il peut atteindre plusieurs centaines pour les CNT par exemple. Raviden et al. ont mesuré un seuil de percolation d'environ 10 %vol pour du noir de carbone (rapport d'aspect proche de 1) dispersé dans une matrice EMA [17] et Dravid et al. un seuil de percolation proche de 13 vol% pour des microsphères de Nickel (rapport d'aspect 1) dispersées dans une matrice PEK [27]. Avec des CNT mono parois de rapport d'aspect 1000, Huang et al. ont obtenu un seuil de percolation beaucoup plus faible égal à 0,06 vol% dans une matrice époxy [44]. Balberg et al. ont proposé une formule permettant d'estimer le seuil de percolation φ_c d'une dispersion aléatoire et isotrope de fibres rigides de longueur L et de rayon r dans une matrice donnée [45] :

$$\left(\frac{L}{r}\right) \varphi_c = 3 \quad (37)$$

Cette formule prédit un seuil de percolation de 0,1 vol% pour le composite époxy/CNT de Huang et al. [44], ce qui est proche de la valeur expérimentale. Un composite à base de charges conductrices est isolant pour une concentration de charges inférieure au seuil de percolation et voit sa conductivité augmenter rapidement au-dessus de ce même seuil. En s'appuyant sur la théorie des transitions de phase, Kirkpatrick a proposé une équation empirique décrivant l'évolution de la conductivité au-dessus du seuil de percolation [46] :

$$\sigma = \sigma_0 \cdot (\varphi - \varphi_c)^t \quad \text{pour } \varphi > \varphi_c \quad (38)$$

La conductivité du composite est σ , σ_0 est une constante de conductivité dont la valeur est liée à la conductivité intrinsèque des charges, φ est la fraction volumique de charge, φ_c le seuil de percolation et t un exposant critique relatif à la théorie des transitions de phase. Ce dernier exposant est égal à la dimension de la percolation moins un, soit égal à 1 pour une percolation en 2 dimensions (sur un plan) et à 2 pour une percolation en 3 dimensions (dans un volume). La conductivité électrique théorique d'un composite chargé fictif en fonction de la fraction volumique de charge selon l'Eq. 38 est représentée en Figure 17. Les paramètres sont fixés à $\varphi_c = 1 \text{ vol\%}$, $\sigma_0 = 10^6 \text{ S/m}$ et $t = 2$. En dessous de 1 vol% de charge, la conductivité est très faible, le matériau est isolant. Au-dessus du seuil de percolation, la conductivité augmente très rapidement et tend ensuite vers la valeur de σ_0 .

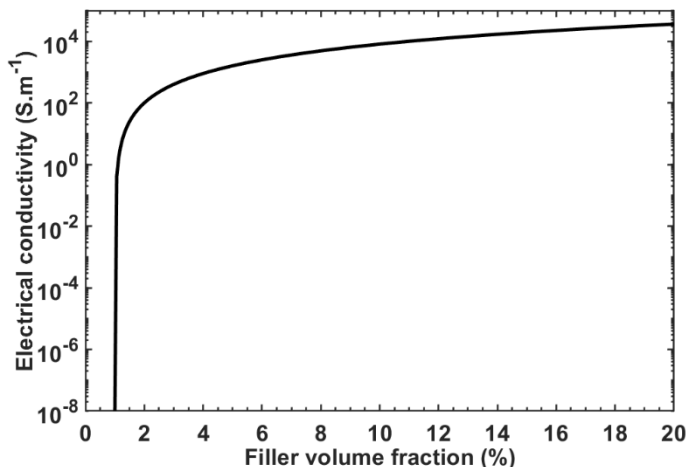


Figure I - 17 : Conductivité électrique théorique en fonction de la fraction volumique de charge avec seuil de percolation selon l'Eq. 38. $\varphi_c = 1 \text{ vol\%}$, $\sigma_0 = 1.10^6 \text{ S/m}$ et $t = 2$.

La dispersion/distribution des charges dans la matrice polymère est également un paramètre important influant sur le seuil de percolation. La dispersion représente la répartition globale des charges dans le composite (échelle macroscopique). Une bonne dispersion des charges dans la matrice est indispensable afin d'obtenir un composite homogène. La distribution désigne l'organisation des charges à l'échelle microscopique : celles-ci peuvent être réparties à égale distance les unes des autres ou alors sous forme d'agrégats. Il est possible d'avoir une bonne dispersion de charges distribuées en agrégats : on a alors des agrégats de tailles similaires répartis dans l'ensemble du composite. Ces définitions sont schématisées en figure 18.

En considérant les schémas de la figure 18, on peut se rendre compte que selon la façon dont on organise les charges dans l'espace, on peut faire percoler ou non un système. En les dispersant bien et distribuant bien (Fig. 18-a), il se peut que l'on ne percole pas si la concentration de fibres n'est pas

assez élevée. Par contre, si l'on disperse bien les charges et qu'on les rassemble dans des agrégats se touchant les uns les autres, laissant des zones de polymères vides de charge (Fig. 18-d), alors le système peut percoler et on obtient un matériau conducteur. Contrairement au rapport d'aspect qui dépend de la charge choisie, la dispersion/distribution de charge est un paramètre difficile à maîtriser et à optimiser. De nombreuses études portent sur ces paramètres afin d'abaisser les seuils de percolation des charges des matériaux composites.

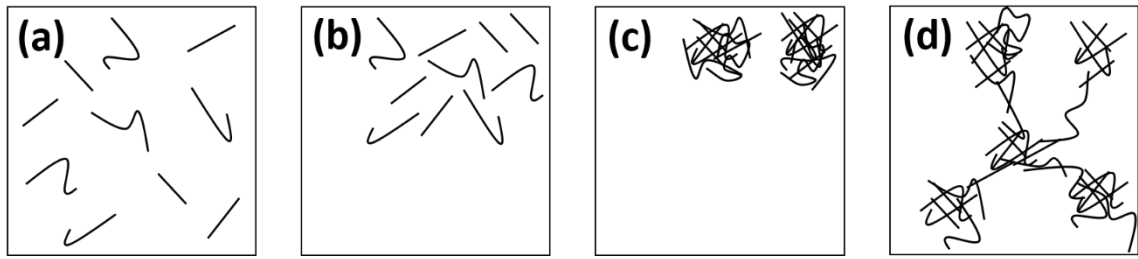


Figure I - 18 : Dispersion et distribution de charges linéiques. (a) Bien dispersées et distribuées. (b) Mal dispersées mais bien distribuées. (c) Mal dispersées et distribuées en agrégats. (d) Bien dispersées et distribuées en agrégats.

Les charges peuvent être par exemple ségrégées, c'est-à-dire concentrées dans une partie du composite avec les autres zones pauvres en charge. Ceci permet d'abaisser grandement le seuil de percolation et d'obtenir des composites de meilleures conductivités pour des taux de charge plus faibles. Un premier exemple pour parvenir à la ségrégation est l'introduction de charges dans la matrice polymère à l'état « semi-solide ». Les charges telles quelles, ou présentes dans un mélange très concentré avec un polymère, sont mélangées avec des granules de résine polymérique en-dessous de la température de fusion du polymère. L'ensemble est ensuite pressé à chaud, ce qui permet d'obtenir des grains de polymère pur enrobés de charges conductrices et collés les uns avec les autres. Le volume accessible aux charges pour percoler est plus faible car elles n'ont pas accès au cœur des grains de polymère, ce qui leur permet de percoler pour des concentrations de charges plus faibles [33,47–50]. La fabrication d'un tel composite hétérogène peut avoir des conséquences indésirables sur les propriétés mécaniques du matériau qui peut être fragilisé voire friable si l'adhésion entre les grains n'est suffisamment bonne. En fait, cette voie est plus une curiosité de laboratoire qu'une réalité industrielle. Une deuxième méthode est l'utilisation d'un mélange de polymères immiscibles. Ces matériaux sont conçus de telle façon à ce que les charges conductrices se concentrent dans une des phases ou à l'interphase [51] entre les deux polymères. A nouveau, le volume accessible aux charges est diminué et celles-ci peuvent percoler à des concentrations plus basses. Si les charges sont

préférentiellement regroupées dans une phase plutôt que l'autre, cette phase doit elle-même percoler dans le matériau pour donner un matériau conducteur. C'est pour cette raison que cette méthode est souvent appelée la « double percolation » [17,52,53]. Une représentation schématique des structures obtenues par ces deux méthodes est présentée en Figure 19.

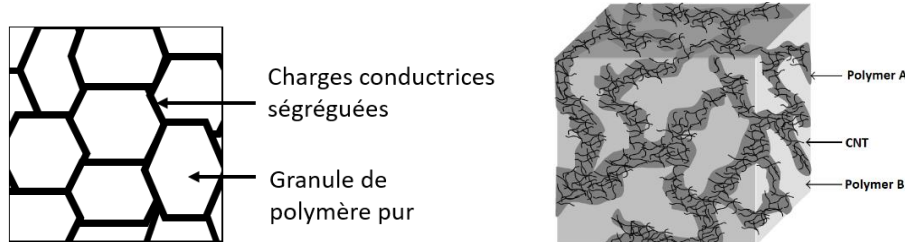


Figure I - 19 : Composites polymères avec charges ségrégées. Gauche : ségrégation des charges par mélange à basse température avec granules de polymère pur et compression. Droite : Mélange de deux polymères immiscibles avec ségrégation des charges (CNT) dans une des phases. Extrait de Pisitsak et al. [53]

Dans le Tableau 2 sont listées quelques valeurs de seuil de percolation et de conductivité pour des matériaux composites polymères avec différentes charges conductrices dont le rapport d'aspect est précisé. On peut rapidement remarquer que les charges de faible rapport d'aspect (sphériques ou peu allongées) mènent à des seuils de percolation élevés, de 8 à 15 % volumique, tandis que celles de grands rapports d'aspect (fibres et tubes) permettent d'obtenir des seuils très faibles proches ou inférieurs au pourcent volumique. Avec des nanofils de cuivre, Al-Saleh et al. rapportent le plus faible seuil de percolation à 0,24 %vol. Ainsi, leurs composites peuvent présenter une conductivité métallique avec une très faible concentration de charges métalliques. On peut également remarquer que des conductivités adaptées pour le blindage EM, soit supérieures à 1 S/m, sont atteintes pour des taux de charge très importants pour les charges sphériques (> 18 vol%) mais pas pour les charges de haut rapport d'aspect, soulignant l'importance de maximiser ce dernier paramètre. Enfin, parmi ce dernier type de charge, on peut remarquer que la valeur de conductivité la plus haute rapportée est atteinte par une charge métallique. Les CNT, charges carbonées de haut rapport d'aspect, atteignent tout de même des conductivités de l'ordre de $10^2 - 10^3$ S/m, amplement suffisant pour le blindage EM, pour des taux de charge raisonnable de 7,5 – 10 %vol.

Dans le Tableau 3 sont comparés les seuils de percolation et les conductivités de matériaux composites avec une distribution de charges homogène ou ségrégée. On remarque rapidement que les structures ségrégées atteignent les seuils de percolation les plus faibles, avec une valeur telle que

0,013 %vol pour des CNT ségrégues par compression entre des granules de PE [50]. Pour des concentrations en charges égales, les composites avec structure ségrégée présentent des conductivités plus importantes d'un facteur de 10 à 100. En termes de blindage EM, un tel changement de valeur de la conductivité peut faire passer un matériau de transparent aux ondes EM à un matériau présentant un blindage EM non négligeable.

Tableau I - 2 : Seuils de percolation et conductivités électriques maximales de composites conducteurs rapportés dans la littérature. La conductivité maximale est associée au taux de charge adjacent.

Matrice polymère	Charge conductrice	Rapport d'aspect	Seuil de percolation	Taux de charge	Conductivité (S/m)	Réf.
EVA ^a	Noir de Carbone	1	8 vol%	19 vol%	1	[54]
EVA	Fibre de carbone	800	5 vol%	8 vol%	50	[54]
HDPE	Graphite	1 - 3	15 vol%	20 vol%	3,2	[55]
Epoxy	CNT	240	3,1 vol%	7,5 vol%	20	[44]
PS	CNT	1000	0,5 vol%	10 vol%	100	[56]
PEK ^b	Nanoparticule de Nickel	1	13 vol%	18 vol%	1,6	[27]
PP	Fibre d'acier inox	600	1 %vol	1,5 %vol	0,5	[28]
PS	Nanofil de cuivre	80	0,24 %vol	2,1 %vol	1000	[29]

^aEthylène-acétate de vinyl , ^bPolyéthercétone

Tableau I - 3 : Seuils de percolation et conductivités électriques pour des répartitions de charges homogènes ou ségrégées rapporté dans la littérature.

Matrice polymère	Charge conductrice	Répartition des charges	Seuil de percolation	Taux de charge	Conductivité (S/m)	Réf.
PE	CNT	Homogène	0,31 %vol	2,5 vol%	6	[50]
PE	CNT	Ségrégée	0,013 %vol	2,5 vol%	50	[50]
EMA	Noir de carbone	Homogène	10 vol%	15 vol%	0,01	[17]
EMA/EOC ^a	Noir de carbone	Ségrégée ^b	5 vol%	15 vol%	1	[17]
UHMWPE	Nickel	Ségrégée	1,015 %vol	2,58 %vol	2000	[33]

^a Polyéthylène acrylate de méthyle / Copolymère polyéthylène-octane, ^bdans la phase EMA.

Une première conclusion de la littérature concernant les propriétés de conduction électrique des matériaux composites polymères est que le choix de la charge conductrice est primordial. Une charge de haut rapport d'aspect mènera à des seuils de percolation plus faibles permettant d'introduire moins de charges dans la matrice pour atteindre de bonnes propriétés électriques. Les charges métalliques permettent en général d'atteindre les conductivités les plus élevées mais leur concentration doit être limitée pour ne pas alourdir le matériau composite final. Les stratégies de ségrégation de charges sont également très intéressantes puisqu'elles permettent d'abaisser le seuil de percolation et d'augmenter la conductivité du composite.

ii. Les techniques de mesure du blindage électromagnétique

Avant de présenter les efficacités de blindage rapportées dans la littérature, il est important de savoir comment ces valeurs ont été mesurées. Une simple mesure d'impédance (liée à la conductivité) peut être suffisante pour le blindage électrique à basses fréquence ; on peut alors se limiter à la maximisation de la conductivité comme évoqué précédemment. Pour des fréquences d'onde EM plus élevées, des méthodes de mesures du blindage EM plus élaborées sont nécessaires.

Il existe de nombreuses méthodes de mesure de l'efficacité de blindage d'un matériau. On se propose ici de présenter les plus utilisées : la mesure d'impédance en basse fréquence, la mesure en cellule coaxiale, la mesure en cellule guide d'onde, la mesure par antenne en chambre anéchoïque et la chambre de réverbération. La génération de l'onde incidente et la mesure des ondes transmises et réfléchies se font en général à l'aide d'un analyseur vectoriel de réseau (VNA). Cet appareil a l'avantage de pouvoir générer et mesurer avec beaucoup de sensibilité et de résolution temporelle des amplitudes d'onde sur de très larges gammes de fréquences (DC – GHz).

Pour les études de blindage EM en basses fréquences, soient les fréquences où il n'a pas ou peu de phénomènes capacitifs, inductifs et d'absorption d'onde (Hz – kHz), la mesure du blindage EM se fait par une simple mesure d'impédance de l'échantillon [9]. Un échantillon de faible impédance présentera un bon blindage dans les basses fréquences (Fig. 9 et Eq. 32).

Pour la mesure en **cellule coaxiale**, la géométrie des câbles coaxiaux amenant l'onde EM du VNA à l'échantillon est conservée par la cellule de mesure. L'échantillon en forme de disque est placé transversalement dans la cellule, entre le conducteur central et la gaine extérieure. Un grand avantage de ce type de cellule de mesure est la très large gamme de fréquence dans laquelle cette cellule peut

mesurer les propriétés de blindage [57]. Certaines cellules peuvent ainsi mesurer des fréquences des Hz jusqu'aux GHz. Leur taille et géométrie sont adaptées aux gammes de fréquence de mesure. Au-delà de cette gamme de fréquence, des phénomènes de réflexion, d'absorption et de résonance dans la cellule peuvent perturber la mesure. Un contact électrique de qualité (faible résistance de contact) est souvent requis entre l'échantillon et la cellule pour une bonne mesure du blindage. Les ondes EM dans une cellule coaxiale sont des ondes progressives se propageant dans la direction du câble coaxial. Le champ électrique est radial à la gaine centrale et le champ magnétique couplé est transversal. Une représentation schématique des champs en géométrie coaxiale est représentée en Figure 20.

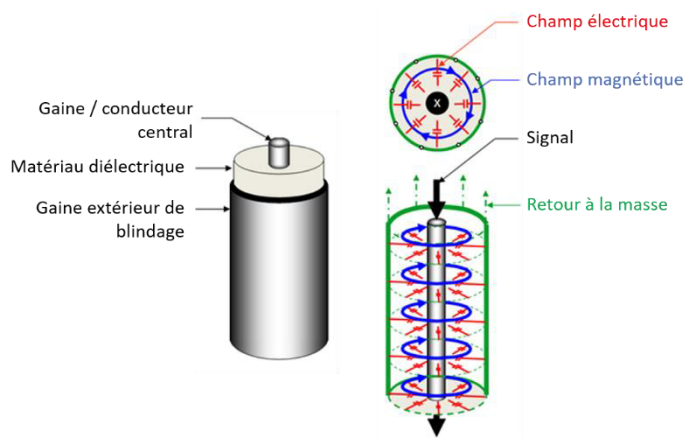
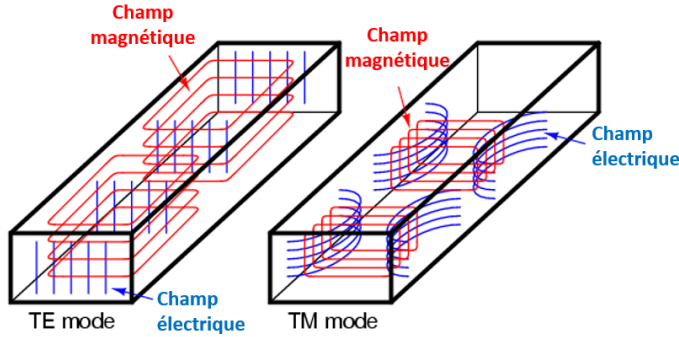


Figure I - 20 : Représentation schématique des champs électriques et magnétiques en cellule coaxiale. Gauche : composition matérielle générale d'un câble coaxial. Droite : coupe transversale (haut) et vue longitudinale (bas).

Les **guides d'onde** sont des cellules de mesure constituées d'une cavité métallique creuse avec des adaptateurs coaxiaux à ses extrémités. L'échantillon mesuré sépare la cavité en deux parties de façon à ce que l'onde EM passe au travers, d'un adaptateur coaxial à l'autre. L'avantage de ces cellules est leur facilité d'utilisation avec un échantillon rectangulaire simplement introduit dans la cellule sans considération de contacts électriques parfaits avec la cellule. Son désavantage peut être la gamme de fréquence de mesure plus réduite comparée à la cellule coaxiale. La taille de la cavité du guide est un paramètre déterminant permettant la propagation de certaines fréquences seulement [58]. Des guides d'onde souvent utilisés sont ceux de la bande X (8,2 – 12,4 GHz) et de la bande K_u (12,4 – 18 GHz) par exemple. A l'intérieur d'un guide d'onde, une onde EM progressive s'y propageant se réfléchie sur les parois de la cavité. La superposition des ondes incidentes et réfléchies entraîne la formation d'une onde stationnaire dont la longueur d'onde dépend des modes de propagation

autorisés dans le guide d'onde (eux-mêmes dépendant de la taille de la cellule). A la différence de la cellule coaxiale, les ondes EM à l'intérieur d'un guide d'onde sont donc des ondes stationnaires. Des exemples de modes de propagation transverse électrique (TE) et transverse magnétique (TM) en guide d'onde sont représentés schématiquement en Figure 21. Les cellules de mesure coaxiale et guides d'onde seront présentées plus en détail dans la partie Méthodologie (Chapitre II).



*Figure I - 21 : Représentation schématique des champs électrique et magnétique en guide d'onde.
Exemple d'un mode transverse électrique TE (gauche) et transverse magnétique TM (droite).*

Dans la **mesure en chambre anéchoïque**, l'échantillon sous forme de plaque peut être introduit dans la paroi de la chambre avec une antenne émettrice d'onde à l'extérieur de la chambre et une à l'intérieur. Il peut également être placé entre les deux antennes à l'intérieur de la chambre. Un avantage de cette méthode de mesure est la très grande gamme de fréquence accessible (avec plusieurs types d'antennes) en onde EM progressive avec des conditions de champ libre sans perturbation grâce au caractère blindé de la chambre et la présence de matériaux absorbants sur les parois de la chambre, empêchant la mesure des ondes réfléchies sur ces parois par exemple [59]. Le défaut de ce dispositif est son coût et son envergure, ne le rendant pas accessible facilement à tous les laboratoires. Les mesures de furtivité EM (surpression totale du champ incident) sont souvent réalisées en chambre anéchoïque [60].

Enfin, la **chambre de réverbération électromagnétique** est constituée d'une cavité réfléchissante (en général d'assez grande taille, soit de la taille d'un four, soit d'une pièce entière), d'une antenne émettrice et une réceptrice, souvent orientées différemment, et d'un brasseur d'onde EM. Ce dernier est en général formé de différentes plaques métalliques toutes orientées différemment et est souvent mis en rotation lors de la mesure. La réflexion des ondes EM sur ce brasseur crée un environnement dans lequel les ondes se propagent dans toutes les directions, contrairement aux méthodes précédentes unidirectionnelles, imitant la pollution EM isotropique de l'environnement

extérieur. Cette méthode de mesure est souvent utilisée pour évaluer les capacités de dépollution électromagnétique d'un matériau absorbant. Pour cela, ce dernier est simplement posé dans la chambre fermée et son influence sur le niveau d'ondes EM reçues après réverbérations multiples est mesurée [61]. Une représentation schématique de la mesure en chambre anéchoïque et en chambre de réverbération est présentée en Figure 22.

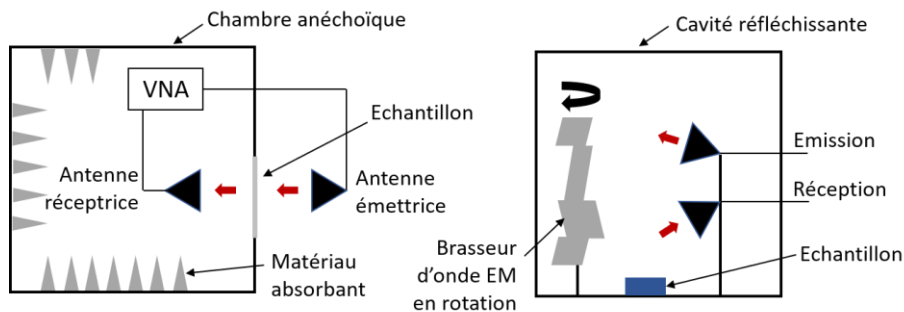


Figure I - 22 : Représentation schématique de la mesure de blindage ou absorption EM en chambre anéchoïque (gauche) et en chambre de réverbération (droite).

iii. Valeurs de blindage électromagnétique de matériaux composites polymères rapportées dans la littérature

La littérature scientifique contient un nombre très important de travaux portant sur le blindage EM des matériaux composites dû à la multiplicité des matrices polymères et charges utilisables. Ainsi, on compte près de 180 articles scientifiques sur le blindage EM des matériaux composites publiés en 2017, 200 en 2018, 250 en 2019 et plus de 300 en 2020. L'intérêt pour ce domaine de recherche est donc croissant. De très nombreuses revues rassemblent et résument régulièrement une grande partie de ces travaux [62–64]. On présente ici une partie des travaux les plus pertinents rapportés sur le blindage EM des matériaux composites polymère.

1- Le choix de la charge conductrice

De par leur nature conductrice et leur faible densité, les charges carbonées sont des candidates intéressantes pour constituer des composites légers aux propriétés de blindage EM. Le noir de carbone est le plus classique et en général le moins onéreux de cette catégorie de charge. Cependant, son faible

rapport d'aspect souvent proche de 1 requiert l'introduction de grandes quantités de charges pouvant modifier fortement les propriétés mécaniques de la matrice polymère d'accueil.

Les nanotubes de carbone et le graphène (Figure 14) sont des charges très utilisées pour la fabrication de matériaux composites avec des propriétés de blindage électromagnétique grâce à leur haut rapport d'aspect dépassant souvent 100. Ceci permet d'introduire très peu de charges dans la matrice polymère pour obtenir des propriétés de blindage, comme expliqué dans la partie précédente traitant de la conductivité. Le graphite, introduit dans un composite, présente en général des valeurs de blindage moins importantes que le graphène auquel il est analogue. La structure empilée de ses feuillets lui permet en effet d'atteindre des rapports d'aspect moins importants. George et al. [20] ont étudié des composites PP – CNT qu'ils ont observés au microscope électronique à balayage comme présenté en Figure 23. On y distingue d'une part les CNT seuls de diamètre 10 – 20 nm et de longueur 1 – 10 µm, ce qui signifie des rapports d'aspect compris entre 50 et 1000. On peut aussi voir ces mêmes CNT dispersés dans une matrice PP où ils apparaissent bien dispersés. Concernant les propriétés de blindage EM, les auteurs rapportent une efficacité de blindage (Eq. 17) de 48 dB pour 20 %m de CNT à une fréquence de 8 GHz et une épaisseur d'échantillon de 2 mm. C'est ainsi plus de 99,99 % de la puissance d'une onde EM incidente de cette fréquence qui est bloquée par ce matériau qui rentre donc dans les exigences commerciales classiques en termes de blindage EM.

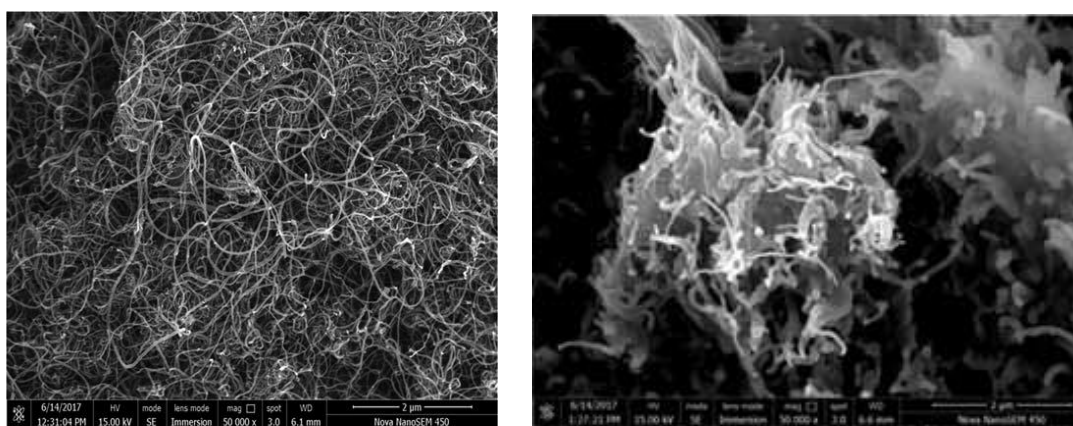


Figure I - 23 : Images obtenues par microscopie électronique à balayage (FE-SEM) au grossissement x 50 000. Gauche : Des nanotubes de carbone multi-parois. Droite : CNT dans une matrice PP à une concentration de 20 %m. Extrait de George et al. [20]

Les charges métalliques sont également très utilisées dans les matériaux composites pour obtenir des propriétés de blindage EM. La conductivité intrinsèque de ces charges, une fois percolées dans la matrice polymère, permet d'obtenir des efficacités de blindage très importantes pour de faibles taux de charge. La forte densité intrinsèque des métaux incite souvent à utiliser des charges

conductrices hybrides dont la conductivité reste métallique mais dont la densité est réduite. L'utilisation de MXenes, ou de particules et de fibres constituées d'un matériau de faible densité recouvertes d'une fine couche de métal permet par exemple d'avoir des charges de conductivité métallique mais de densité acceptable.

Les propriétés de blindage EM de quelques matériaux composites avec différentes charges conductrices rapportés dans la littérature sont listées dans le Tableau 4 pour une fréquence d'onde incidente de 8,2 GHz, la fréquence la plus souvent étudiée dans ce type de travaux (la bande X, 8,2 – 12 GHz, est la bande de fréquence la plus souvent mesurée). L'épaisseur de l'échantillon mesuré est également un paramètre important influant sur l'efficacité de blindage.

En général, les auteurs rapportent une augmentation des propriétés de blindage de leur composite lorsqu'ils augmentent la concentration en charge (liée à l'augmentation de la conductivité) et l'épaisseur de leur échantillon. Lorsque la gamme de fréquence mesurée est suffisamment grande, ils constatent aussi une augmentation du blindage avec la fréquence, liée à l'apparition du phénomène d'absorption d'onde [8,19,69,70]. Ces éléments concordent donc avec le modèle théorique simple du blindage développé précédemment.

Le Tableau 4 a été divisé en plusieurs catégories. En haut du tableau sont présentés des composites à base de noir de carbone et de fibres de carbone. Ces composites montrent des propriétés de blindage correctes mais au prix d'un taux de charge et d'une épaisseur d'échantillon élevés. Ensuite viennent les composites à base des charges carbonées à haut rapport d'aspect, les CNT et le graphène. Avec ces charges, les matériaux composites possèdent de meilleures propriétés de blindage (deux composites CNT sont au-dessus de 40 dB) avec des épaisseurs d'échantillon et taux de charge plus faibles qu'avec les autres charges carbonées. Le composite à base de graphène présente un blindage non négligeable avec un taux de charge de seulement 0,5 %vol. L'efficacité de blindage de 40 dB devrait être facilement atteinte en augmentant légèrement la concentration en graphène.

Pour les charges métalliques, les composites basés sur les charges de faible rapport d'aspect (nanoparticules de nickel et nanocristaux de fer) présentent de bonnes propriétés de blindage mais pour des taux de charge importants ayant un fort impact sur la densité finale du matériau composite. Au contraire, les charges de haut rapport d'aspect (fibres et nanofils) atteignent les exigences commerciales de blindage pour de faibles concentrations en charge. L'efficacité de 35 dB est atteinte pour une épaisseur minimale de 0,21 mm pour les composites à base de nanofils de cuivre : une épaisseur d'échantillon plus importante permettrait aisément de dépasser les 40 dB. Enfin, une dernière catégorie de charges assimilées métalliques est présentée en bas de tableau. Il s'agit de

charges hybrides : des fibres d'un matériau léger recouvertes d'argent (le plus conducteur des métaux [71]). Ces charges allient donc haut rapport d'aspect, conductivité métallique et faible densité. Ces propriétés impactent positivement les valeurs d'efficacité de blindage atteintes par les composites basés sur ces charges, 50 dB, pour une épaisseur faible, 1,5mm, et des taux de charge raisonnables. Du fait du caractère hybride de ces charges, la concentration réelle en métal du composite est inférieure à la concentration en charge, réduisant d'autant plus l'impact de ces charges sur la densité du composite.

Tableau I - 4 : Efficacité de blindage EM à la fréquence de 8,2 GHz de matériaux composites avec différentes charges rapportés dans la littérature

Matrice polymère	Charge conductrice	Taux de charge	Conductivité (S/m)	Epaisseur (mm)	Blindage EM (dB)	Réf.
PDMS	Noir de carbone	40 %m	1	2	27	[65]
EVA	Fibre de carbone	22 %m	50	3,5	30	[54]
PS	CNT	20 %m	100	2	30	[56]
PVP^a	CNT	10 %m	200	1	42	[8]
PP	CNT	20 %m	70	2	44	[20]
PVA^b	Graphène	0,5 %vol	50	1	20	[66]
PEK	Nanoparticule de Nickel	60 %m	1,6	1,6	27	[27]
PVDF	Nanocristaux de fer	35 %vol	50	2	39	[67]
PP	Fibre d'acier inox	1,5 %vol	0,5	3,2	40	[28]
PS	Nanofil de cuivre	2,1 %vol	1000	0,21	35	[29]
Epoxy	Fibre de verre argentées	19 %vol	-	1,58	51	[32]
PLA^c	Fibre de PLA argentées	34,4 %m	254	1,5	50	[68]

^a Polyvinylpyrrolidone, ^b alcool polyvinyle, ^c acide polylactique

Un premier enseignement que l'on peut tirer de la littérature scientifique est le choix de la charge conductrice à inclure dans une matrice polymère pour obtenir de bonnes propriétés de blindage EM. L'avantage va aux CNT, au graphène et aux charges métalliques hybrides de haut rapport

d'aspect et densité modérée. Les charges métalliques simples peuvent également être intéressantes à la condition de limiter leur concentration pour ne pas alourdir le matériau final.

2- Effets de synergie entre les charges conductrices

Beaucoup d'auteurs rapportent un effet de synergie lorsqu'ils combinent des charges différentes au sein d'un même matériau composite [70,72–74]. Ainsi, l'efficacité de blindage de la combinaison de charge est plus importante que celle qui correspond aux charges seules pour la même concentration. Ces effets de synergie sont présentés dans le Tableau 5.

Dans les composites présentés dans le tableau ci-dessous, on peut constater l'effet de synergie entre charges conductrices qui améliore l'efficacité de blindage. Pour le composite à base de SEBS, CNT et graphène, le blindage EM des composites chargés à 10 %m soit de graphène, soit de CNT est inférieur à celui du mélange CNT-8%m + Graphène-2%m. Dans les autres exemples, l'introduction d'une charge conductrice supplémentaire dans des composites à base de CNT mène à une augmentation du blindage pour une concentration de charge totale identique, mettant en évidence l'effet de synergie de charges. Les gains en blindage rapportés sont compris en général entre 5 et 15 dB, des valeurs non négligeables pour des épaisseurs d'écran relativement fines (1-2mm). On peut voir que les CNT sont à la base de beaucoup de matériaux composites présentant des effets synergétiques, soulignant à nouveau l'intérêt de cette charge carbonée.

Tableau I - 5 : Effets de synergie entre charges conductrices sur le blindage EM rapportés dans la littérature. Blindage mesuré à 8,2 GHz.

Matrice polymère	Charges	Epaisseur (mm)	Concentration totale	Blindage charge 1 (dB)	Blindage charge 2 (dB)	Blindage mélange (dB)	Réf.
SEBS ^a	CNT / Graphène	2	10 %m	20	7	24	[72]
SEBS	CNT / Graphène	2	15 %m	30	9	37	[72]
PS	CNT / SiO ₂ @rGO ^b	1,3	3 %m	14	-	30	[73]
PC / SAN ^c	CNT / rGO-Co ^d	5,5	3 %m	22	-	26	[70]

^a Polystyrene-poly(éthylène-butylène), ^b particules de SiO₂ recouverte d'oxyde de graphène réduit,

^c copolymère styrène-acrylonitrile, ^d oxyde de graphène réduit décoré de particules de Cobalt

L'efficacité de la synergie entre charges conductrices pour le blindage doit cependant être nuancée. Zhang et al. n'ont relevé aucun effet synergétique en mélangeant des CNT et des nano-plaquettes de graphène, avec le composite CNT seuls présentant toujours une efficacité de blindage plus importante que le mélange [75]. Les auteurs lient cette absence de synergie à une forte différence de conductivité intrinsèque entre les charges (facteur 1000) combinée à une grande résistance de contact entre les deux types de charge.

3- Effet de la structuration et de la morphologie d'un matériau composite sur ses propriétés de blindage EM

Comme présenté dans la partie portant sur la conductivité des composites, la distribution des charges dans un matériau composite peut avoir un impact sur le seuil de percolation des charges conductrices, la conductivité du matériau et a fortiori ses propriétés de blindage EM [76]. Comme évoqué précédemment, les deux techniques de ségrégation principales sont par mélange de polymères immiscibles [17,51,77,78] ou par compression à chaud d'un mélange de granules de polymère pur solides avec des charges [33,47–50]. Cette dernière technique est également utilisée en voie solvant [30,79].

Par compression de granules de PE recouverts de charges conductrice, Jia et al. et Duan et al. ont obtenu des structures ségréguées avec des zones fortement chargées et percolantes dans le matériau et des zones dépourvues de charges (initialement les granules de PE), respectivement avec des charges carbonées et métalliques. Des clichés optiques de ces structures sont présentées en Figure 24 [33,50]. Les propriétés en blindage EM des composites à distribution de charges ségréguées de quelques matériaux composites issus de la littérature sont listées et comparées à des matériaux à distribution homogène dans le Tableau 6.

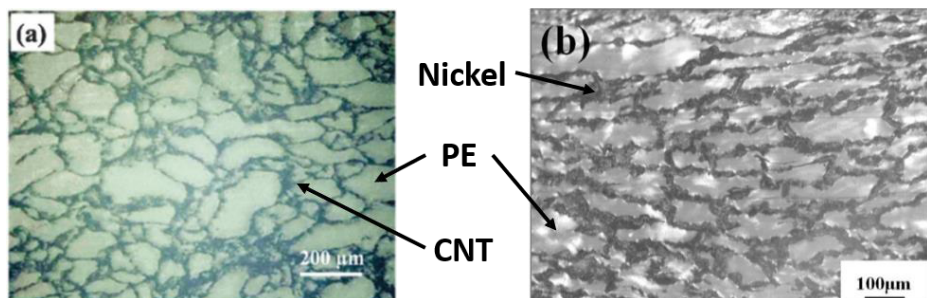


Figure I - 24 : Clichés optiques de structures de composites ségréguées. (a) PE-CNT, extrait de Jia et al. [50]. (b) PE-Nickel, extrait de Duan et al. [33].

Tableau I - 6 : Efficacité de blindage à 8,2 GHz de matériaux composites polymères à distribution de charges ségrégée et homogène rapportées dans la littérature.

Matrice polymère	Charge conductrice	Répartition des charges	Taux de charge	Conductivité (S/m)	Epaisseur (mm)	Blindage EM (dB)	Réf.
EMA	Noir de carbone	Homogène	30 %m	0,01	2	1	[17]
EMA/EOC	Noir de carbone	Ségréguée ^a	30 %m	1	2	31	[17]
EVA	CNT	Homogène	2 %m	0,02	2,1	2	[77]
PE/EVA	CNT	Ségréguée ^b	2 %m	13,5	2,1	33	[77]
PE	CNT	Homogène	5 %m	6	2,1	32	[50]
PE	CNT	Ségréguée	5 %m	50	2,1	45	[50]
PVDF	Nanocristaux de fer	Homogène	35 %vol	50	2	39	[67]
UHMWPE	Nickel	Ségréguée	2,58%vol	2000	2	52	[33]

^a dans la phase, ^b dans la phase EVA

Les deux techniques de ségrégation de charge (par mélange de polymères immiscibles ou mécaniquement par compression à chaud) permettent d'atteindre en général des efficacités de blindage plus importantes que la distribution homogène des charges. Dans le tableau ci-dessus, la ségrégation de charges induisant un seuil de percolation abaissé se traduit par une augmentation de la conductivité de composite d'un facteur 10 à 100 pour une concentration de charges conductrices donnée. Les effets sur le blindage EM sont également impressionnantes, avec des composites à base de noir de carbone ou de CNT passant de matériaux quasi-transparents aux ondes EM (1-2 dB) à un matériau aux très bonnes propriétés de blindage EM (> 30 dB). Par ségrégation des charges, en général, un matériau possédant déjà des propriétés de blindage EM les verra augmenter. Le bas du tableau présente deux matériaux composites à base de charges métalliques de faible rapport d'aspect. La ségrégation des charges métalliques semble avoir un double effet : la quantité nécessaire de charge pour obtenir des propriétés de blindage est réduite et le blindage lui-même est augmenté. Cette technique de ségrégation des charges est donc d'autant plus intéressante pour les matériaux composites à base de charges métalliques. Le seuil de percolation réduit permet d'atteindre des composites à conductivité métallique, et donc potentiellement un blindage très important, pour une

concentration en charge métallique réduite, limitant ainsi l'impact négatif de ces charges sur la densité du matériau composite final.

Au-delà de l'augmentation du blindage due à l'augmentation de la conductivité du composite, beaucoup d'études prétendent que la structure ségrégée des matériaux composites peut également augmenter le blindage [76]. L'aspect hétérogène du matériau entraîne des réflexions internes de l'onde supplémentaires, celle-ci pouvant être réfléchie à chaque nouvelle interface entre une zone concentrée en charges et une zone appauvrie. Ces nouvelles réflexions allongent le trajet moyen de l'onde EM au sein du matériau qui peut alors subir d'avantages de phénomènes d'absorption, ce qui augmente l'efficacité de blindage du composite.

Comme évoqué précédemment, malgré la forte amélioration des propriétés de blindage des matériaux composites aux charges ségrégées, cette ségrégation peut avoir un impact négatif important sur les propriétés mécaniques du matériaux polymères, telles que son module d'Young ou son allongement à la rupture [80–82]. Ainsi, Zhai et al. ont mesuré une allongement à la rupture passant de 300% en l'absence de charge à 50% avec 3 %vol de CNT dans un mélange ségrégué PP / PE / CNT [81]. Cette dégradation est encore plus importante quand les échantillons sont mis en forme par moulage à chaud sous pression que par injection sous presse. Pour un composite avec CNT ou nano-feuilles de graphène ségrégés mécaniquement à chaud entre des granules de PE, Ren et al. ont constaté une légère augmentation du modèle d'Young sous 0,5 %m de charge puis une diminution rapide du même paramètre au-dessus de cette concentration [82]. Les auteurs attribuent ce phénomène aux microfissures présents dans le matériau ségrégué au niveau des zones fortement chargées à l'interface entre les granules de polymère pur. Lorsque la concentration en charge augmente, ces zones finissent par se rejoindre et les microfissures peuvent alors s'agrandir en macrofissures, dégradant fortement la résistance en traction du matériau.

Une autre technique analogue à la ségrégation des charges est le moussage des matériaux composites. Comme la ségrégation des charges, le moussage permet en général d'abaisser le seuil de percolation des charges à l'échelle de la mousse en réduisant le volume accessible aux charges. Cette technique permet ainsi d'obtenir des matériaux composites moussés présentant de bonnes propriétés de blindage EM avec une densité de composite largement réduite [19,28,75,83–86]. Cette catégorie de matériaux est cependant différente des matériaux solides, avec des propriétés mécaniques différentes les empêchant par exemple de constituer seuls un élément de structure.

4. Conclusion de cette revue de littérature

a. Résumé des études antérieures de la littérature

De la littérature scientifique très fournie sur les matériaux composites polymères appliqués au blindage EM, il est possible de tirer quelques conclusions générales. Tout d'abord, la modélisation théorique du blindage EM permet d'identifier les paramètres importants régissant l'efficacité de blindage d'un écran. Dans un modèle théorique avec hypothèses d'un matériau linéaire (grandeur comme la conductivité indépendantes de la fréquence), homogène et isotrope, les principaux paramètres sont la conductivité électrique du matériau, l'épaisseur de l'écran et la fréquence de l'onde EM incidente. De nombreuses simplifications de ce modèle existent pour des gammes de fréquences et des types d'échantillon donnés, ainsi que de nombreux modèles théoriques plus élaborés visant à prédire le blindage EM d'un matériau sans mesure de conductivité préalable et à partir des propriétés physiques intrinsèques des constituants du composite.

Le choix d'une charge conductrice de grand facteur de forme permet d'obtenir les meilleures valeurs de conductivité électrique et d'efficacité de blindage EM pour des taux de charges très limités, moins de 10 %m. Les CNT entrent dans cette catégorie et les études menées à leur sujet rapportent de très bonnes propriétés des matériaux composites basés sur ces nanocharges. La faible densité de ce type de charge carbonée permet également d'obtenir des matériaux composites de densité à peine plus élevée que celle du polymère. Les composites à base de graphène montrent des propriétés similaires mais les CNT ont l'avantage d'être plus « démocratisés » et produits de façon quasi-industrielles de nos jours [87].

Les charges métalliques ou hybrides métalliques permettent également d'obtenir des composites aux propriétés de blindage très importantes grâce à leur conductivité métallique élevée. La concentration en métal, de densité élevée, doit cependant être minimisée pour limiter la densité du matériau composite. L'utilisation de charges métalliques hybrides s'avère alors salutaire concernant ce dernier paramètre, comme par exemple des fibres de verre ou de polymère recouvertes de métal alliant densité modérée et conductivité métallique. Ainsi, des valeurs de blindage élevées ont été rapportées pour des composites à base de CNT (42 dB, 1 mm) et de fibres de verre argentées (50 dB, 1,5 mm).

La distribution des charges dans le composite est un paramètre important. La distribution de charges dites ségrégée permet d'abaisser le seuil de percolation des charges de façon notable. Par

mélange de polymères immiscibles ou par compression directe à chaud d'un mélange solide de granules de polymère et charges conductrices, les propriétés de blindage EM de ces structures sont grandement améliorées en comparaison aux distributions homogènes de charges. L'impact négatif sur les propriétés mécaniques du matériau est cependant important, en particulier pour les composites à charges ségrégues par compression.

b. Problématiques et orientations du projet de thèse

L'objectif de ce projet de recherche est le développement d'un matériau composite thermoplastique aux propriétés de blindage électromagnétique. L'objectif au niveau de l'efficacité de blindage est fixé à 40 dB (99,99 % de la puissance de l'onde incidente bloquée, valeur commerciale) pour une épaisseur de 1 mm et dans la gamme de fréquence 100 MHz – 10 GHz couvrant les ondes EM présentent dans les domaines automobile et aéronautique telles que les ondes radio, le téléphone, la 4-5G, le Bluetooth, le Wi-Fi, les ondes radar civil, etc. Cette valeur est atteinte dans plusieurs études mais pour des épaisseurs plus importantes ou des gammes de fréquence plus réduites que notre cahier des charges. Le challenge de ce projet est donc de dépasser la valeur des 40 dB en respectant ce cahier des charges.

La densité du composite doit être minimale afin de s'inscrire dans l'allègement des véhicules à viser de réduire leurs émissions de gaz à effet de serre. Elle devra ainsi être comprise entre celle de la matrice polymère pure (environ $0,9 - 1 \text{ g.cm}^{-3}$) et la valeur de $1,5 \text{ g.cm}^{-3}$. Concernant les propriétés mécaniques (en traction par exemple) du matériau composite, elles devront être les plus proches possibles de la matrice polymère pure utilisée pour fabriquer le composite. Le matériau composite devra également être facilement mis en œuvre et mis en forme afin de pouvoir être produit à l'échelle industrielle par les méthodes classiques de l'industrie plastique (extrusion, injection, etc). Un dernier paramètre non négligeable est le prix du composite : la ou les matrices polymères utilisées ainsi que la ou les charges conductrices utilisées devront être disponibles en quantités industrielles et à un prix raisonnable.

Ainsi, les problématiques du projet de thèse sont :

- Quelles charges conductrices introduites dans une matrice polymère permettent d'obtenir la meilleure efficacité de blindage tout en minimisant la densité du composite (soit un taux de charge minimale) et l'impact sur les propriétés mécaniques du matériau par rapport à la matrice polymère pure ?

- Pour un taux de charges conductrices constant, quelles sont les moyens d'augmenter les propriétés de blindage du matériau (morphologie du matériau, ségrégation des charges) ?
- Comment modéliser les propriétés de blindage EM d'un matériau composite en fonction des propriétés intrinsèques des charges et de leur distribution dans la matrice polymère ?

Le choix de la matrice polymère se porte ainsi sur le PP, un matériau thermoplastique très utilisé dans les applications de structures et de pièces automobiles, bon marché et dont l'utilisation comme matrice de matériau composite pour blindage EM a été de nombreuses fois rapportée dans la littérature.

Considérant les éléments relevés de la littérature scientifique, les premières études expérimentales du projet se porteront sur l'étude de matériaux composites à base de CNT. Une attention particulière sera portée sur la modélisation théorique des propriétés de blindage de ces composites avec une dispersion homogène des charges. L'impact de l'introduction des CNT dans la matrice PP sur la densité, la mise en œuvre et les propriétés mécaniques du matériau sera également investiguée.

En prenant comme référence les composites PP – CNT, des charges métalliques seront également étudiées en raison de la conductivité intrinsèque plus importante de ces charges. A cause de la densité élevée de ce type de charge, un intérêt particulier sera porté sur la minimisation du seuil de percolation afin d'obtenir un composite de densité limitée, de conductivité métallique et donc avec une grande efficacité de blindage EM. La simplicité de fabrication du matériau composite sera privilégiée avec une liste réduite de composants facilement accessibles et une mise en forme robuste. Comme avec les composites PP – CNT, les propriétés de blindage de ces composites seront modélisées théoriquement en considérant la nature métallique des charges et leur distribution dans la matrice polymère.

Références

- [1] Moureaux, P. "Exposition aux champs électromagnétiques - Evaluer le risque en entreprise sans mesure. www.inrs.fr," (2017).
- [2] Sadiku, M. N. O. "Elements of electromagnetics" (Oxford University Press, 2015). doi:0199321388.
- [3] Rothwell, E. J. and M. J. Cloud. "Electromagnetics" (CRC Press, 2018).
- [4] Demaret et al. and Groupe RNI Carsat - Cram. "Champs Electromagnétiques, ED 4200-4220, INRS," (2014).
- [5] MarketsandMarkets. "EMI Shielding Market by Material (EMI Shielding Tapes & Laminates, Conductive Coatings & Paints, Metal Shielding, Conductive Polymers, EMI Filters), Method (Radiation, Conduction), Industry, and Region - Global Forecast to 2025" 146 (2020).
- [6] Schultz, R. B., V. C. Plantz and D. R. Brush. "Shielding theory and practice," *IEEE Trans. Electromagn. Compat.* **30**, 187–201 (1988).
- [7] Sun, J., W. Wang and Q. Yue. "Review on Microwave-Matter Interaction Fundamentals and Efficient Microwave-Associated Heating Strategies," *Materials* **9**, 231 (2016).
- [8] Nasouri, K., A. M. Shoushtari and M. R. M. Mojtabaei. "Theoretical and experimental studies on EMI shielding mechanisms of multi-walled carbon nanotubes reinforced high performance composite nanofibers," *J. Polym. Res.* **23**, 71 (2016).
- [9] Haddad, F., B. Bayard and B. Sauviac. "Low-Frequency Relation Between Transfer Impedance and Shielding Effectiveness of Braided Cables and Grid Shields," *IEEE Trans. Electromagn. Compat.* 1–8 (2020) doi:10.1109/TEMC.2019.2960163.
- [10] Kittel, C. "Theory of the Dispersion of Magnetic Permeability in Ferromagnetic Materials at Microwave Frequencies," *Phys. Rev.* **70**, 281–290 (1946).
- [11] Steinberg, K., M. Scheffler and M. Dressel. "Microwave inductance of thin metal strips," *J. Appl. Phys.* **108**, 096102 (2010).
- [12] Michii, T., M. Seto, M. Yamabe, Y. Kubota, G. Aoki and H. Ohtsuka. "Study on Warpage Behavior and Filler Orientation during Injection Molding," *Int. Polym. Process.* **23**, 419–429 (2008).
- [13] Hoang, N. N., M. Jean-Louis and W. Jean-Luc. "Modeling of Electromagnetic Shielding Effectiveness of Multilayer Conducting Composites in the Microwave Band," in *2006 First International Conference on Communications and Electronics* 482–485 (IEEE, 2006). doi:10.1109/CCE.2006.350874.
- [14] Peng, Z., J. Peng, Y. Peng and J. Wang. "Complex conductivity and permittivity of single wall carbon nanotubes/polymer composite at microwave frequencies: A theoretical estimation," *Sci. Bull.* **53**, 3497–3504 (2008).
- [15] Xia, X., A. D. Mazzeo, Z. Zhong and G. J. Weng. "An X-band theory of electromagnetic interference shielding for graphene-polymer nanocomposites," *J. Appl. Phys.* **122**, 025104 (2017).
- [16] Xia, X., Y. Wang, Z. Zhong and G. J. Weng. "A theory of electrical conductivity, dielectric constant, and electromagnetic interference shielding for lightweight graphene composite foams," *J. Appl. Phys.* **120**, 085102 (2016).
- [17] Ravindren, R., S. Mondal, P. Bhawal, Shek. M. N. Ali and N. C. Das. "Superior electromagnetic interference shielding effectiveness and low percolation threshold through the preferential distribution of carbon black in the highly flexible polymer blend composites," *Polym. Compos.* **40**, 1404–1418 (2019).
- [18] Huang, X., X. Qi, F. Boey and H. Zhang. "Graphene-based composites," *Chem Soc Rev* **41**, 666–686 (2012).
- [19] Zhao, B., C. Zhao, M. Hamidinejad, C. Wang, R. Li, S. Wang, K. Yasamin and C. B. Park. "Incorporating a microcellular structure into PVDF/graphene–nanoplatelet composites to tune their electrical conductivity and electromagnetic interference shielding properties," *J. Mater. Chem. C* **6**, 10292–10300 (2018).

- [20] George, G. *et al.* "Morphological, dielectric, tunable electromagnetic interference shielding and thermal characteristics of multiwalled carbon nanotube incorporated polymer nanocomposites: A facile, environmentally benign and cost effective approach realized via polymer lat," *Polym. Compos.* **39**, E1169–E1183 (2018).
- [21] Kum, C. K., Y.-T. Sung, M. S. Han, W. N. Kim, H. S. Lee, S.-J. Lee and J. Joo. "Effects of morphology on the electrical and mechanical properties of the polycarbonate/multi-walled carbon nanotube composites," *Macromol. Res.* **14**, 456–460 (2006).
- [22] Li, S. "Highly filled biochar/ultra-high molecular weight polyethylene/linear low density polyethylene composites for high-performance electromagnetic interference shielding," *Compos. Part B* **153**, 277-284 (2018).
- [23] Dang, Z.-M., K. Shehzad, J.-W. Zha, T. Hussain, N. Jun and J. Bai. "On Refining the Relationship between Aspect Ratio and Percolation Threshold of Practical Carbon Nanotubes/Polymer Nanocomposites," *Jpn. J. Appl. Phys.* **50**, 080214 (2011).
- [24] Mehrali, M., E. Sadeghinezhad, S. Latibari, S. Kazi, M. Mehrali, M. N. B. M. Zubir and H. S. Metselaar. "Investigation of thermal conductivity and rheological properties of nanofluids containing graphene nanoplatelets," *Nanoscale Res. Lett.* **9**, 15 (2014).
- [25] Stempien, Z., T. Rybicki, E. Rybicki, M. Kozanecki and M. I. Szynkowska. "In-situ deposition of polyaniline and polypyrrole electroconductive layers on textile surfaces by the reactive ink-jet printing technique," *Synth. Met.* **202**, 49–62 (2015).
- [26] Bora, P. J., N. Shahidsha, G. Madras, Kishore and P. C. Ramamurthy. "Novel poly (vinyl butyral) (PVB)/polyaniline-cenosphere composite film for EMI shielding," in *AIP Conference Proceedings* **1728**, 020646 (2016). doi:10.1063/1.4946697.
- [27] Dravid, S. V., S. D. Bhosale, S. Datar and R. K. Goyal. "Nickel Nanoparticle-Filled High-Performance Polymeric Nanocomposites for EMI Shielding Applications," *J. Electron. Mater.* **49**, 1630–1637 (2020).
- [28] Ameli, A., M. Nofar, S. Wang and C. B. Park. "Lightweight Polypropylene/Stainless-Steel Fiber Composite Foams with Low Percolation for Efficient Electromagnetic Interference Shielding," *ACS Appl. Mater. Interfaces* **6**, 11091–11100 (2014).
- [29] Al-Saleh, M. H., G. A. Gelvès and U. Sundararaj. "Copper nanowire/polystyrene nanocomposites: Lower percolation threshold and higher EMI shielding," *Compos. Part Appl. Sci. Manuf.* **42**, 92–97 (2011).
- [30] Gelvès, G. A., M. H. Al-Saleh and U. Sundararaj. "Highly electrically conductive and high performance EMI shielding nanowire/polymer nanocomposites by miscible mixing and precipitation," *J Mater Chem* **21**, 829–836 (2011).
- [31] Tan, Y.-J., J. Li, Y. Gao, J. Li, S. Guo and M. Wang. "A facile approach to fabricating silver-coated cotton fiber non-woven fabrics for ultrahigh electromagnetic interference shielding," *Appl. Surf. Sci.* **458**, 236–244 (2018).
- [32] Olivero, D. A. and D. W. Radford. "A multiple percolation approach to EMI shielding composites incorporating conductive filaments," *J. Reinf. Plast. Compos.* **17**, 674–690 (1998).
- [33] Duan, H., Y. Xu, D.-X. Yan, Y. Yang, G. Zhao and Y. Liu. "Ultrahigh molecular weight polyethylene composites with segregated nickel conductive network for highly efficient electromagnetic interference shielding," *Mater. Lett.* **209**, 353–356 (2017).
- [34] Nasouri, K. and A. M. Shoushtari. "Fabrication of magnetite nanoparticles/polyvinylpyrrolidone composite nanofibers and their application as electromagnetic interference shielding material," *J. Thermoplast. Compos. Mater.* **31**, 431–446 (2018).
- [35] Jiles, D. *"Introduction to Magnetism and Magnetic Materials"* (CRC Press, 2015).
- [36] Li, X., X. Yin, S. Liang, M. Li, L. Cheng and L. Zhang. "2D carbide MXene Ti₂CTX as a novel high-performance electromagnetic interference shielding material," *Carbon* **146**, 210–217 (2019).

- [37] Wang, L., L. Chen, P. Song, C. Liang, Y. Lu, H. Qiu, Y. Zhang, J. Kong and J. Gu. "Fabrication on the annealed Ti₃C₂Tx MXene/Epoxy nanocomposites for electromagnetic interference shielding application," *Compos. Part B Eng.* **171**, 111–118 (2019).
- [38] Shahzad, F., M. Alhabeb, C. B. Hatter, B. Anasori, S. Man Hong, C. M. Koo and Y. Gogotsi. "Electromagnetic interference shielding with 2D transition metal carbides (MXenes)," *Science* **353**, 1137–1140 (2016).
- [39] Pearson, J. R. "*Mechanics of Polymer Processing*" (Springer Science & Business Media, 1985).
- [40] Tadmor, Z. and C. G. Gogos. "*Principles of Polymer Processing*" (John Wiley & Sons, 2013).
- [41] Auscher, M. C., R. Fulchiron, N. Fougerouse, T. Périé and P. Cassagnau. "Zirconia based feedstocks: Influence of particle surface modification on the rheological properties," *Ceram. Int.* **43**, 16950–16956 (2017).
- [42] Papirer, E., J. Schultz and C. Turchi. "Surface properties of a calcium carbonate filler treated with stearic acid," *Eur. Polym. J.* **20**, 1155–1158 (1984).
- [43] Lin, C., B. Wang, Y. Cheng and C. Wang. "Influence of stearic acid on the structure and rheological behavior of injection-molded ZTA suspensions," *Mater. Sci.-Pol.* **31**, 36–42 (2013).
- [44] Huang, Y., N. Li, Y. Ma, F. Du, F. Li, X. He, X. Lin, H. Gao and Y. Chen. "The influence of single-walled carbon nanotube structure on the electromagnetic interference shielding efficiency of its epoxy composites," *Carbon* **45**, 1614–1621 (2007).
- [45] Balberg, I., C. H. Anderson, S. Alexander and N. Wagner. "Excluded volume and its relation to the onset of percolation," *Phys. Rev. B* **30**, 3933–3943 (1984).
- [46] Kirkpatrick, S. "Percolation and Conduction," *Rev. Mod. Phys.* **45**, 574–588 (1973).
- [47] Cui, C.-H., D.-X. Yan, H. Pang, X. Xu, L.-C. Jia and Z.-M. Li. "Formation of a Segregated Electrically Conductive Network Structure in a Low-Melt-Viscosity Polymer for Highly Efficient Electromagnetic Interference Shielding," *ACS Sustain. Chem. Eng.* **4**, 4137–4145 (2016).
- [48] Wu, H.-Y., L.-C. Jia, D.-X. Yan, J. Gao, X.-P. Zhang, P.-G. Ren and Z.-M. Li. "Simultaneously improved electromagnetic interference shielding and mechanical performance of segregated carbon nanotube/polypropylene composite via solid phase molding," *Compos. Sci. Technol.* **156**, 87–94 (2018).
- [49] Yu, W.-C., J.-Z. Xu, Z.-G. Wang, Y.-F. Huang, H.-M. Yin, L. Xu, Y.-W. Chen, D.-X. Yan and Z.-M. Li. "Constructing highly oriented segregated structure towards high-strength carbon nanotube/ultrahigh-molecular-weight polyethylene composites for electromagnetic interference shielding," *Compos. Part Appl. Sci. Manuf.* **110**, 237–245 (2018).
- [50] Jia, L.-C., D. X. Yan, C. H. Cui, X. Jiang, X. Ji and Z. M. Li. "Electrically conductive and electromagnetic interference shielding of polyethylene composites with devisable carbon nanotube networks," *J. Mater. Chem. C* **3**, 9369–9378 (2015).
- [51] Chen, J., Y. Shi, J. Yang, N. Zhang, T. Huang, C. Chen, Y. Wang and Z. Zhou. "A simple strategy to achieve very low percolation threshold via the selective distribution of carbon nanotubes at the interface of polymer blends," *J. Mater. Chem.* **22**, 22398 (2012).
- [52] Ajitha, A. R., P. Mohammed Arif, M. K. Aswathi, P. M. Lovely, V. G. Geethamma, K. Nandakumar, T. Sabu and T. Volova. "An effective EMI shielding material based on poly(trimethylene terephthalate) blend nanocomposites with multiwalled carbon nanotubes," *New J. Chem.* **42**, 13915–13926 (2018).
- [53] Pisitsak, P., R. Magaraphan and S. C. Jana. "Electrically Conductive Compounds of Polycarbonate, Liquid Crystalline Polymer, and Multiwalled Carbon Nanotubes," *J. Nanomater.* **2012**, 1–10 (2012).
- [54] Das, N. C., D. Khastgir, T. K. Chaki and A. Chakraborty. "Electromagnetic interference shielding effectiveness of carbon black and carbon fibre filled EVA and NR based composites," *Compos. Part Appl. Sci. Manuf.* **31**, 1069–1081 (2000).

- [55] Song, J., W. Yang, F. Fu and Y. Zhang. "The Effect of Graphite on the Water Uptake, Mechanical Properties, Morphology, and EMI Shielding Effectiveness of HDPE/Bamboo flour composites," *BioResources* **9**, 3955–3967 (2014).
- [56] Arjmand, M., T. Apperley, M. Okoniewski and U. Sundararaj. "Comparative study of electromagnetic interference shielding properties of injection molded versus compression molded multi-walled carbon nanotube/polystyrene composites," *Carbon* **50**, 5126–5134 (2012).
- [57] Hong, Y. K., C. Y. Lee, C. K. Jeong, D. E. Lee, K. Kim and J. Joo. "Method and apparatus to measure electromagnetic interference shielding efficiency and its shielding characteristics in broadband frequency ranges," *Rev. Sci. Instrum.* **74**, 1098–1102 (2003).
- [58] Marcuvitz, N. and M. I. of T. R. Laboratory. "Waveguide Handbook" (IET, 1951).
- [59] Ortlek, H. G., T. Alpyildiz and G. Kilic. "Determination of electromagnetic shielding performance of hybrid yarn knitted fabrics with anechoic chamber method," *Text. Res. J.* **83**, 90–99 (2013).
- [60] Chen, H., W. Ma, Z. Huang, Y. Zhang, Y. Huang and Y. Chen. "Graphene-Based Materials toward Microwave and Terahertz Absorbing Stealth Technologies," *Adv. Opt. Mater.* **7**, 1801318 (2019).
- [61] Pastore, R., A. Delfini, D. Micheli, A. Vricella, M. Marchetti, F. Santoni and F. Piergentili. "Carbon foam electromagnetic mm-wave absorption in reverberation chamber," *Carbon* **144**, 63–71 (2019).
- [62] Thomassin, J.-M., C. Jérôme, T. Pardoen, C. Bailly, I. Huynen and C. Detrembleur. "Polymer/carbon based composites as electromagnetic interference (EMI) shielding materials," *Mater. Sci. Eng. R Rep.* **74**, 211–232 (2013).
- [63] Wanasinghe, D. and F. Aslani. "A review on recent advancement of electromagnetic interference shielding novel metallic materials and processes," *Compos. Part B Eng.* **176**, 107207 (2019).
- [64] Wanasinghe, D., F. Aslani, G. Ma and D. Habibi. "Review of Polymer Composites with Diverse Nanofillers for Electromagnetic Interference Shielding," *Nanomaterials* **10**, 541 (2020).
- [65] Al-Saleh, M. H. and U. Sundararaj. "X-band EMI shielding mechanisms and shielding effectiveness of high structure carbon black/polypropylene composites," *J. Phys. Appl. Phys.* **46**, 035304 (2013).
- [66] Marka, S. K., B. Sindam, K. C. James Raju and V. V. S. S. Srikanth. "Flexible few-layered graphene/poly vinyl alcohol composite sheets: synthesis, characterization and EMI shielding in X-band through the absorption mechanism," *RSC Adv.* **5**, 36498–36506 (2015).
- [67] Gargama, H., A. K. Thakur and S. K. Chaturvedi. "Polyvinylidene fluoride/nanocrystalline iron composite materials for EMI shielding and absorption applications," *J. Alloys Compd.* **654**, 209–215 (2016).
- [68] Zhang, K., H.-O. Yu, K.-X. Yu, Y. Gao, M. Wang, J. Li and S. Guo. "A facile approach to constructing efficiently segregated conductive networks in poly(lactic acid)/silver nanocomposites via silver plating on microfibers for electromagnetic interference shielding," *Compos. Sci. Technol.* **156**, 136–143 (2018).
- [69] Jana, P. B., A. K. Mallick and S. K. De. "Electromagnetic interference shielding effectiveness of short carbon fibre-filled polychloroprene vulcanized by barium ferrite," *J. Mater. Sci.* **28**, 2097–2104 (1993).
- [70] Pawar, S. P. and S. Bose. "Extraordinary Synergy in Attenuating Microwave Radiation with Cobalt-Decorated Graphene Oxide and Carbon Nanotubes in Polycarbonate/Poly(styrene- co -acrylonitrile) Blends," *ChemNanoMat* **1**, 603–614 (2015).
- [71] Buch, A. "Pure metals properties: A scientific and technical handbook" (1999).
- [72] Kuester, S., N. R. Demarquette, J. C. Ferreira, B. G. Soares and G. M. O. Barra. "Hybrid nanocomposites of thermoplastic elastomer and carbon nanoadditives for electromagnetic shielding," *Eur. Polym. J.* **88**, 328–339 (2017).
- [73] Wu, K., L. Wu, W. Yang, S. Chai, F. Chen and Q. Fu. "Largely enhanced electrical properties of polymer composites via the combined effect of volume exclusion and synergy," *RSC Adv.* **6**, 51900–51907 (2016).

- [74] Wu, J., Z. Ye, H. Ge, J. Chen, W. Liu and Z. Liu. "Modified carbon fiber/magnetic graphene/epoxy composites with synergistic effect for electromagnetic interference shielding over broad frequency band," *J. Colloid Interface Sci.* **506**, 217–226 (2017).
- [75] Zhang, H., G. Zhang, M. Tang, L. Zhou, J. Li, X. Fan, X. Shi and J. Qin. "Synergistic effect of carbon nanotube and graphene nanoplates on the mechanical, electrical and electromagnetic interference shielding properties of polymer composites and polymer composite foams," *Chem. Eng. J.* **353**, 381–393 (2018).
- [76] Pang, H., L. Xu, D.-X. Yan and Z.-M. Li. "Conductive polymer composites with segregated structures," *Prog. Polym. Sci.* **39**, 1908–1933 (2014).
- [77] Jia, L.-C., D.-X. Yan, C.-H. Cui, X. Ji and Z.-M. Li. "A Unique Double Percolated Polymer Composite for Highly Efficient Electromagnetic Interference Shielding," *Macromol. Mater. Eng.* **301**, 1232–1241 (2016).
- [78] Sultana, S. M. N., S. P. Pawar, M. Kamkar and U. Sundararaj. "Tailoring MWCNT Dispersion, Blend Morphology and EMI Shielding Properties by Sequential Mixing Strategy in Immiscible PS/PVDF Blends," *J. Electron. Mater.* **49**, 1588–1600 (2020).
- [79] Maiti, S., S. Suin, N. K. Shrivastava and B. B. Khatua. "A strategy to achieve high electromagnetic interference shielding and ultra low percolation in multiwall carbon nanotube–polycarbonate composites through selective localization of carbon nanotubes," *RSC Adv.* **4**, 7979 (2014).
- [80] Ren, F., Z. Li, L. Xu, Z. Sun, P. Ren, D. Yan and Z. Li. "Large-scale preparation of segregated PLA/carbon nanotube composite with high efficient electromagnetic interference shielding and favourable mechanical properties," *Compos. Part B Eng.* **155**, 405–413 (2018).
- [81] Zhai, W., S. Zhao, Y. Wang, G. Zheng, K. Dai, C. Liu and C. Shen. "Segregated conductive polymer composite with synergistically electrical and mechanical properties," *Compos. Part Appl. Sci. Manuf.* **105**, 68–77 (2018).
- [82] Ren, P.-G., Y.-Y. Di, Q. Zhang, L. Li, H. Pang and Z.-M. Li. "Composites of Ultrahigh-Molecular-Weight Polyethylene with Graphene Sheets and/or MWCNTs with Segregated Network Structure: Preparation and Properties," *Macromol. Mater. Eng.* **297**, 437–443 (2012).
- [83] Hwang, S. "Tensile, electrical conductivity and EMI shielding properties of solid and foamed PBT/carbon fiber composites," *Compos. Part B Eng.* **98**, 1–8 (2016).
- [84] Ju, J., T. Kuang, X. Ke, M. Zeng, Z. Chen, S. Zhang and X. Peng. "Lightweight multifunctional polypropylene/carbon nanotubes/carbon black nanocomposite foams with segregated structure, ultralow percolation threshold and enhanced electromagnetic interference shielding performance," *Compos. Sci. Technol.* **193**, 108116 (2020).
- [85] Xu, Z. and H. Hao. "Electromagnetic interference shielding effectiveness of aluminum foams with different porosity," *J. Alloys Compd.* **617**, 207–213 (2014).
- [86] Xu, L., L. C. Jia, D. X. Yan, P. G. Ren, J. Z. Xu and Z. M. Li. "Efficient electromagnetic interference shielding of lightweight carbon nanotube/polyethylene composites via compression molding plus salt-leaching," *RSC Adv.* **8**, 8849–8855 (2018).
- [87] MarketsandMarkets. "Carbon Nanotubes (CNT) Market by Type, Method, Application - Global Forecast to 2023" 158 (2018).

Chapter II. Materials and Methods

Chapter II. Materials and methods: processing and properties measurement of polymer composite materials

1. Introduction

In this chapter are presented the raw materials used in the fabrication of studied composite materials, processing and sample fabrication methods, and measurement methods of obtained composites physical properties. A brief “Materials and methods” is reported in each experimental chapter and sums up experimental methods (processing, sample fabrication, properties measurements) in the same chapter. In this chapter, materials and experimental methods used in this doctoral research are described in detail. Attention is particularly focused on experimental measurements of electromagnetic interference shielding effectiveness and start-of-the-project developments and improvements.

2. Raw materials and composite materials fabrication methods

a. Polymer matrices and conductive fillers

The main polymer matrix used is a thermoplastic polyolefin resin: grade PPH 7060 polypropylene (H is for homopolymer since polymerized from one sole monomer). The polymer is supplied by Total, France. This grade is one intermediate viscosity, with existing grades of higher and lower viscosity. Those grades are identical in chemical properties and only differ by the average length of their polymer chains. Occasionally, a more viscous grade of PP as well as polystyrene (PS) and low density polyethylene (LDPE) will be used. Some relevant physical properties of these polymer matrices are listed in Table 1.

Table II - 1: Some physical properties of the polymer matrices used in this research project

Matrix	Grade	Melt temperature T_m (°C)	Melt Flow Index MFI (g/10 mins)	Density (relative to water)	Young modulus (MPa)
Polypropylene	PPH 7060	165	12 ^a	0.905	1550
	PPH 3060	165	1.8 ^a	0.905	1400
Low density polyethylene	LD 0304	111	4 ^b	0.924	250
Polystyrene	PS 1160	$T_g = 95$	2.4 ^c	1.05	3200

^a Measured at 230°C under 2,16 kg weight, ^b 190°C – 2,16 kg, ^c 200°C – 5 kg

Those polymers can be processed in the temperature range 180 – 200°C considering their melt temperatures. Polystyrene does not display a melt temperature because of its amorphous nature. Its glass transition temperature is indicated, and it will be processed at 200°C as well. Polymer matrices display various viscosities represented through their melt flow index (MFI). The two PP matrices viscosities can be compared – PP 3060 is more viscous than PP 7060 – but comparison with the other polymer matrices is less obvious due to different MFI measurement methods. PP 7060 seems to be the most fluid of all matrices though. Concerning their densities, they are low (close to unity) and close to one another. Material stiffness is shown through its Young modulus (supplier data). At room temperature, the PS matrix is the hardest and the LDPE the softest, PP matrices being situated in between.

The three used conductive fillers are CNT, tin microparticles and silver-coated glass microfibers. Dimensions, aspect ratios, intrinsic electrical conductivity and density of those filler are listed in Table 2. More precisely, CNT are multi-walls carbon nanotubes (MWCNT) in comparison to single-wall carbon nanotubes (SWCNT). It grossly consists in many SWCNT imbricated in one another. MWCNT are in general simpler to produce than SWCNT and therefore cheaper, with similar electrical properties [1]. Studied CNT are NC 7000 grade supplied by Nanocyl, Belgium in the form of a high concentration PP masterbatch. CNT weight concentration of the masterbatch is 20 ± 1 wt% which corresponds to a CNT volume concentration of 10 ± 0.5 vol%. It was decided to only deal with volume concentration of filler in the rest of the project. The error of CNT content indicated by the supplier is then very low. PP matrix used in the masterbatch is the same grade as PP 7060.

Volume to weight relative concentration transition equations are as follow:

$$C_w = \frac{C_{vol} \cdot d_{filler}}{C_{vol} \cdot d_{filler} + (1 - C_{vol}) \cdot d_{polymer}} \quad (1)$$

$$C_{vol} = \frac{c_w/d_{filler}}{c_w/d_{filler} + 1 - c_w/d_{polymer}} \quad (2)$$

Tin microparticles were provided by GoodFellow, France. Those spherical particles have diameters ranging from 10 to 80 μm with an average diameter of 45 μm . Purity of tin is 99%.

Silver-coated glass microfibers provided by Hart Materials, UK. They are composed of glass fibers whose surface is coated with a thin layer of silver. Silver content of the filler is 20 wt% which correspond to a silver surface layer thickness of about 0.1 μm (with a fiber diameter of 15 μm).

Aspect ratios of the studied conductive fillers are vastly different by one to two orders of magnitude. As indicated in the previous chapter, a filler high aspect ratio can lead to a low percolation threshold and a lowered amount of fillers needed to get a conductive composite. In our case, we can predict for similar fillers distribution in a polymer matrix that $\varphi_{c,TinPart} > \varphi_{c,AgGlassFib} > \varphi_{c,CNT}$. Filler intrinsic conductivities are also different from one filler to another with higher values for the metal filler (or hybrid metal) of one to two order of magnitude compared to CNT. For a similar percolated filler concentration, better composite conductivity and EMI shielding properties are then expected with the metal fillers. As for filler densities, CNT and Ag-coated glass fibers have the advantage of a lower density compared to tin particles. That can lead to the non-negligible advantage of a light composite material.

Table II - 2: Size and physical properties of conductive fillers used in the project

Conductive filler	Diameter (μm)	Length (μm)	Aspect ratio	Intrinsic conductivity (S.m^{-1})	Density (kg.m^{-3})
CNT	$9,5 \times 10^{-3}$	1,5	160	10^6 [2]	2100
Tin Microparticle	45	-	1	$9,17 \times 10^6$	7290
Ag-coated glass Microfiber	15	180	12	$6,3 \times 10^7$	2800

Each filler has its advantages and drawbacks, but the silver-coated microfibers seem to be the best compromise with a high aspect ratio and a metal conductivity. Its only disadvantage would be its price as it depends on silver market price and its production has not been industrialized yet.

b. Composite materials processing and samples fabrication

The melt mixing process is used to make composite materials from pure polymer and conductive fillers (see previous chapter for the other mixing methods and the advantages of the melt mixing method). Equipment used for composites processing were an internal batch mixer (small scale) and a twin-screw extruder (large scale).

i. Internal batch mixer

The internal mixer used was a Thermoscientific Polylab OS Rheodrive 7 Haake internal mixer. It is composed of a 69 cm³ tank with two contra-rotating mixing roller rotors. This equipment is pictured in Figure 1. The internal mixer has the advantage of being of quick and easy use. Multiple mixes of various compositions can be made in a short time span. Its disadvantage would be to produce only about 50 g of composite for each run. This amount is enough to make several samples destined to electrical and EMI shielding measurement but is not enough to fabricate injected under press samples. This mixing method was used with composites based on tin particles or Ag-coated glass fibers as multiple different composite compositions were tested: PP, PS or LDPE as polymer matrix, different concentrations of filler, addition or not of CNT, addition or not of stearic acid, and different mixing speed.

Mixer temperature is chosen according to used polymer matrix and filler. For instance, a mixing temperature of 200°C is used with PP and PS matrices, and 180°C with LDPE matrix. Mixing temperature is lowered to 190°C with tin particles in order to avoid possible partial melting during mixing due to self-heating ($T_{m,tin} = 231^\circ\text{C}$). The rotor speed is initially set to 20 rpm (low speed) for raw materials introduction. Polymer matrix pellets are first introduced. Once they are molten (mixer temperature sensor indicates a mix temperature above the polymer melt temperature) the fillers are introduced. Mixing speed is then set to higher values of efficient mixing. The used rotor speeds and mixing times (in general around 10 mins) are indicated in the methods part of each experimental chapter. A low rotor speed of 30 rpm is used with tin particles to limit self-heating for instance, but a higher speed of 100 rpm is used with silver-coated glass fibers as it was observed that it led to better composite EMI shielding properties.

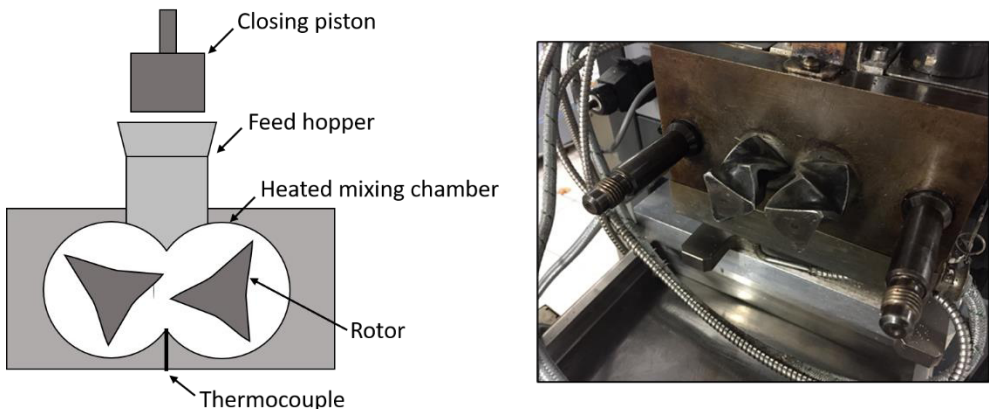


Figure II - 1: Internal haake mixer. Left: scheme. Right: open tank with the two visible contra-rotating mixing roller rotors.

Torque applied on the rotor by the mix can be monitored through all the mixing experiment and can give us an idea of the mixing shear force in the mix. An example of internal mixer measured torque in function of time is displayed in Figure 2. Pure PP 7060 or the same PP with 15 vol% of tin particles with delayed introduction of stearic acid are compared. One can see the increase of torque with the introduction of the tin particles that led to an increased mix viscosity. Torque then decreases as particles are dispersed in the polymer melt. On the contrary, introduction of stearic acid leads to a brutal drop of torque and is linked to the lubricating effects of the fatty acid. Again, torque then increased back as stearic acid gets partially dispersed in the polymer melt. These phenomena will be discussed in detail in Chapter V.

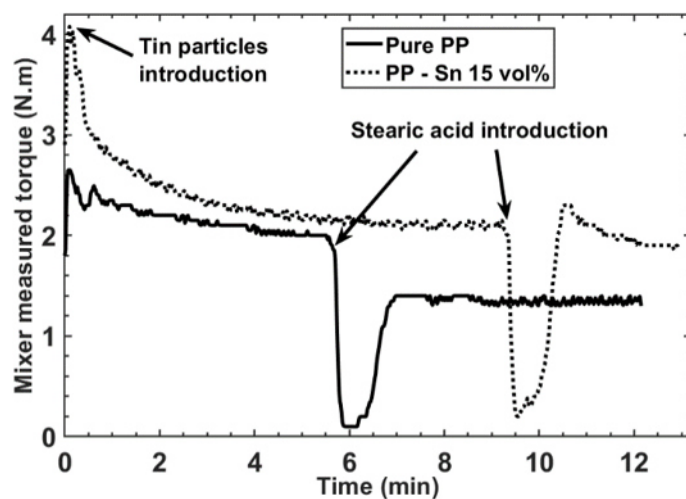


Figure II - 2: Example of internal mixer measured torque versus time. Pure PP 7060 or same PP with 15 vol% of tin particles with delayed introduction of 10 vol% stearic acid.

Once mixing is over, the chamber is opened, mixed material is carefully extracted and cooled first in open air and then in liquid nitrogen. The cooled mix is then pelletized in a Pulverisette 19 grinder to get millimeter sized pellets. Liquid nitrogen cooling is used to get under polymer glass transition temperature. Thus, the material is brittle, easily pelletized without sticking to the grinder blades.

ii. Twin-screw extruder

The twin-screw extruder used was a Leistritz ZSE18. Length to diameter ratio is 60 and the screw speed was set to 300 rpm. The advantage of this equipment is its ability to mix great amounts of materials in a limited period of time (3 kg/hour) compared to the internal mixer. The mix composition is limited to concentration variations over one mixing session though as equipment purge is needed before and afterward. This mixing method was chosen for PP/CNT masterbatch dilution with pure PP 7060 in order to get lower CNT concentration composite materials. The required amount of masterbatch and pure polymer matrix for each diluted composite are weighted and the two pellet types are mixed together in a bag. For instance, to obtain a 15 wt% CNT composite, masterbatch (20 wt% CNT concentration) input must be 2.25 kg/h and PP 7060 input must be 0.75 kg/h, that is a 75/25 weight ratio. The solid pellets are then fed to the extruder. At each concentration change (dilution change), the mix is collected after a waiting period of 5 mins required for concentration stabilization at the die exit of the extruder. The extruded stand is cooled down with blown air on a rolling mill and cut in pellets with a grinder, all done continuously. The used extruder is depicted in Figure 3-a.

iii. Samples hot compression molding

To make samples suitable for electrical conductivity and EMI shielding measurements, the obtained composite material pellets are hot pressed in specially designed mold in a Servitec Polystat 200 T press. The press temperature is set to 200°C and the pressure is progressively increased from 10 bar to 250 bar over a 10 mins time period. The mold is then removed from the press and cooled down under pressure thanks to weights. Samples are extracted from the mold once it has cooled down. For electrical conductivity measurements, plaques of dimension 50mm x 75mm x 1mm are made. Similar plaques with additional thicknesses are made for EMI shielding Waveguide measurements. For EMI shielding measurement in coaxial cell, disks of 23mm diameter and thickness from 0.5 to 3mm are

made. This diameter is specially design for the sample to fit in the cell. The hot press is depicted in Figure 3-b.

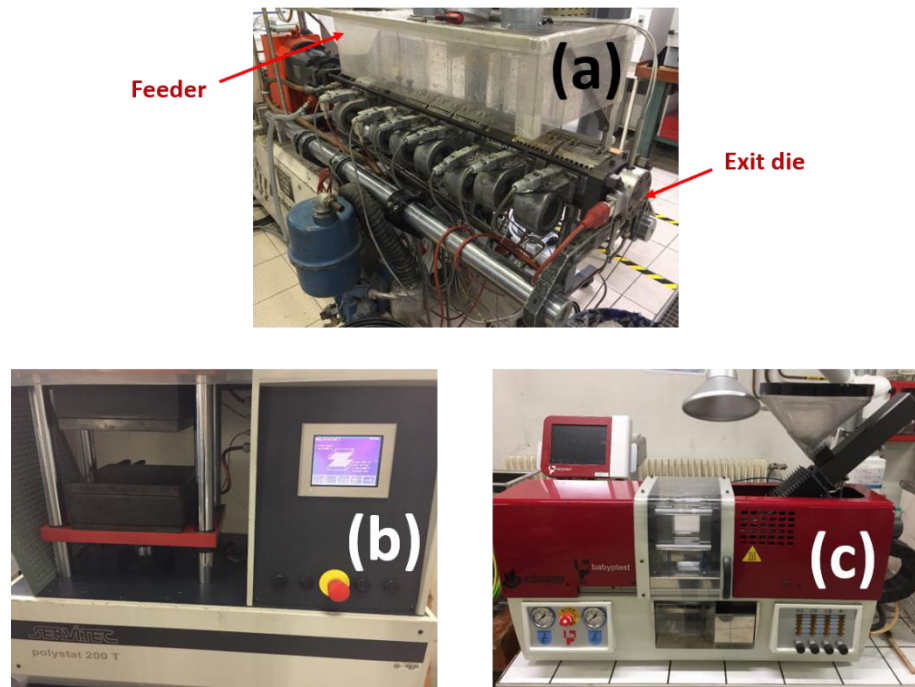


Figure II - 3: Composite materials used processing equipment. (a) Twin-screw extruder, (b) Hot compression press and (c) Injection press.

iv. Samples injection molding

Some samples were also molded by injection under pressure in a Babyplast 6/12 Standard injection press. Dogbone samples for mechanical traction tests were made with this equipment as it entails way less imperfections in the samples that can affect measured mechanical properties than hot compression molded samples. A standard mold is used for these samples. The thinner part of the dogbone is 2mm thick, 4mm wide and 50mm long (Figure 4). Plaques of dimension 100mm x 20mm x 2mm are also obtained by injection molding and are destined to electrical conductivity and EMI shielding measurement of injected samples. Actual injected plaque thickness was measured to be 1.8 mm due to material retraction. The used equipment is depicted in Figure 3-c.

Injection conditions were set to 210°C temperature and 80 bars pressure for PP – CNT and PP – Ag-coated glass fibers composites. However, the PP – CNT 10 vol% composite (masterbatch)

proved difficult to be injected and required more drastic injections conditions: 250°C temperature and 130 bars pressure (maximal pressure available with the used equipment). Industrial production on this latter composite would thus be more challenging than the other studied composite materials.

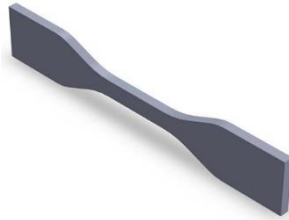


Figure II - 4: Dogbone sample used for mechanical traction tests and obtained by injection molding. The center part is 2mm-thick, 4mm-wide and 50mm-long.

3. Properties characterization of studied composite materials

a. Electrical contacts metallization and conductivity measurements

Measurement of electrical conductivity is done through the measurement of a sample resistance knowing its geometry and dimensions. However, only the resistance of the sample must be measured to get the correct conductivity value, and all other resistance contributions in the experimental setup have to be negligible. Cables resistance can be neglected as well as the contact resistance between the metal cables and the measuring device or the metal electrodes. However, the imperfect solid-solid contacts between the electrodes and the sample can lead to a non-negligible contact resistance. The surface of both the sample and the electrode is not perfectly plane, hence the electrode/sample contact is not a plane-plane contact but a multiple punctual contact as schematized on Figure 5. It entails the appearance of a high contact resistance between the metal electrode and the sample and then an error on the determination of sample conductivity. Two methods exist to get rid of this contact resistance. A first method is to use a four-points setup where contact resistance can be measured and subtracted from the measured sample resistance. The second method, used in this project, is sample surface metallization. It consists in transforming the sample surface into a metal electrode by coating it with metal that fits in all surface rugosities. It can be done coating the surface with a metal solution (metal particles dispersed in a solvent) or by metal sputtering. This last technique

was used with a Cressington Sputter coater 108auto using pure gold – a stainless metal of great conductivity – as sputtered metal.

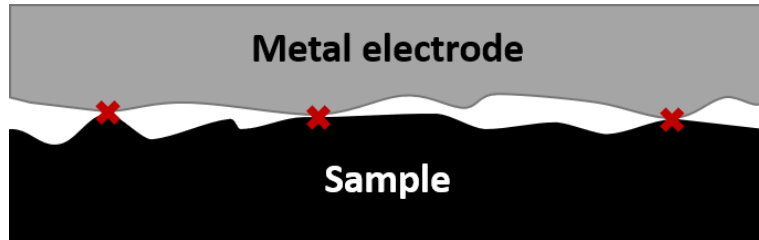


Figure II - 5: Punctual electrical contacts between non perfectly plane surfaces of metal electrode and sample.

Samples were placed at a distance of 5 cm from the metallizer gold target and metallized under a 0.1 mbar vacuum for 600s with a current of 40 mA. Not the whole sample was gold metallized, masks were used to prevent metallization of some parts of the surface sample. A metallized plaque of PP/CNT composite material is showed in Figure 6-a. Sample resistance R is then measured using a Fluke 289 multimeter and a Novocontrol Alpha broadband dielectric/impedance spectrometer for double checking. Conductivity σ is then determined thanks to the distance L between the electrodes, sample width w and thickness d ($\sigma = \frac{L}{R.S} = \frac{L}{R.w.d}$). The variation of sputtered gold layer thickness (measured with a quartz probe) and measured sample resistance in function of metallization time is displayed in Figure 6-b for a PP – CNT 10 vol% composite. Sputtered gold layer thickness increases linearly with metallization time. Sample resistance without metallization ($t=0s$) is high equal to 3.85Ω compared to metallized ones and is due to contact resistance. It then rapidly drops as gold is coated on sample surface and is stable past 500-600s, hence the chosen metallization time, at about 1.35Ω . Thus, metallization more than halves measured sample resistance. As there are two electrode/sample contacts, contact resistance in this case can be estimated to about 1Ω . A wrong value of conductivity of 205 S/m would have been measured without metallization although the composite material conductivity is actually equal to 580 S/m . Contact resistance being virtually constant from one sample to another, its importance is lesser for less conductive samples (higher resistance) but becomes a real problem for more conductive samples (lower sample resistance sometimes orders of magnitude lower than contact resistance) where their conductivity can be totally “hidden” by contact resistance. Metallizing electrical contacts thus shows indispensable for correct electrical conductivity measurements.

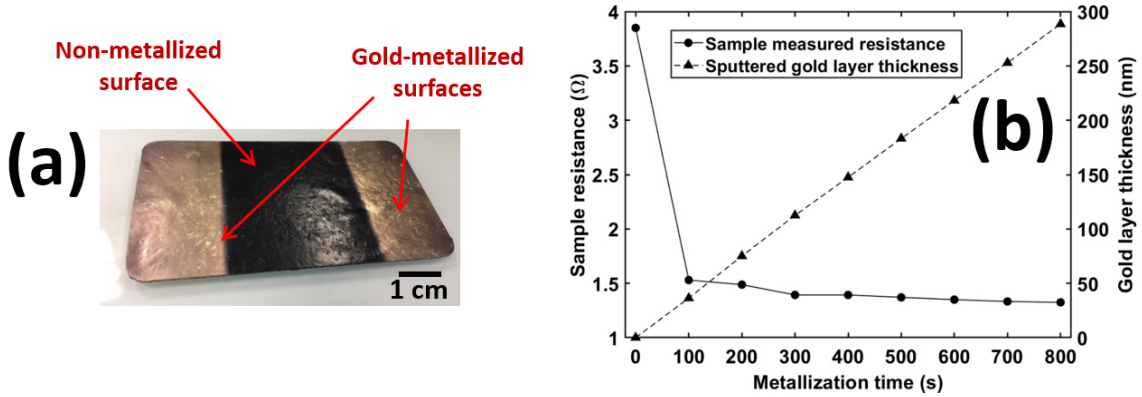


Figure II - 6: Gold surface metallization of studied conductive composite materials. (a) PP-CNT composite plate samples gold metallized for an electrical conductivity measurement. (b) Measured sample resistance and corresponding sputtered gold layer thickness in function of the duration of metallization. PP – 10 vol% CNT composite, length 42mm, width 44.4mm and thickness 1.2mm.

b. Composite materials EMI shielding effectiveness measurements

Two types of measurements cells are used to measure samples EMI shielding effectiveness: a coaxial cell and waveguide cells. The characteristics, advantages and drawbacks of these two types of cells were presented in the previous review of literature chapter I.

Both cells are connected to the same Vectorial Network Analyser (VNA), an Anritsu Shockline 2 ports VNA MS 45522B. This device can measure EMI shielding from 50 kHz to 20 GHz EM wave frequency. The measured frequency range is set depending on the measurement cell used. VNA power is set to 0 dBm which correspond to a low wave power of 1 mW (for instance a wave power of 1 W can be dangerous to humans). The Intermediate Frequency Band Width (IFBW) is set to 100 Hz. It reflects the VNA set resolution: a lower IFBW will lead to lower signal to noise ratio but longer measurement time (a longer measurement time is needed to get a thinner frequency resolution). This value was chosen as to get a good frequency resolution with a reasonable measurement time. For each frequency point, the VNA measures the scattering parameters from one port through the sample to the other port, S_{11} (reflection back to port 1), S_{12} (transmission from port 1 to port 2), S_{22} (reflection back to port 2), S_{21} (transmission from port 2 to port 1). Those parameters are complex numbers. For a linear and passive sample (our case and in general the case of conductive composite materials), we have $|S_{11}| = |S_{22}|$ and $|S_{12}| = |S_{21}|$. The total shielding SE_T , reflection shielding SE_R and absorption shielding SE_A can be calculated from the scattering parameters:

$$R = |S_{11}^2| \quad (3)$$

$$T = |S_{21}^2| \quad (4)$$

$$SE_T = -\log_{10}(T) \quad (5)$$

$$SE_R = -\log_{10}(1 - R) \quad (6)$$

$$SE_A = -\log_{10}\left(\frac{T}{1-R}\right) \quad (7)$$

$$SE_T = SE_R + SE_A \quad (8)$$

Contrary to the theoretical model presented in the previous chapter, simple reflection and multiple internal reflections cannot be separated in the experimental measurement and are both included in the measured SE_R . However, as indicated previously as well, those multiple internal reflections can be neglected if $SE_A > 10$ dB. Shielding effectiveness is expressed in Decibels, the reductions of wave amplitude and power with different EMISE are listed in Table 3. Relations between shielding effectiveness, wave amplitude and power are showed in Equation I-17, page 23.

Table II - 3: Transmitted wave amplitude and power at different shielding effectiveness

EMISE (dB)	Transmitted wave amplitude (%)	Transmitted wave power (%)
0	100	100
10	32	10
20	10	1
30	3.2	0.1
40	1	0.01
60	0.1	10^{-4}
80	0.01	10^{-6}
100	10^{-4}	10^{-8}

VNA sensibility (maximum shielding effectiveness measurable) is about 90-110 dB depending on the measurement cell used. Before measurement, the VNA has to be calibrated. Calibration is done manually thanks to a TOSLKF50A-20 type K(f) (DC to 20 GHz, 50 Ω) calibration kit. Four standards are measured: for each port separately a 50 Ω load, a short circuit and an open circuit. A loss free thru standard with the two ports connected is then measured.

For each composite composition, three or four samples are measured to insure statistical significance of the results. For each sample, each frequency point is the average of three measurements.

i. Coaxial cell measurements

The coaxial cell used in this research project is EpsiMu Multiwave PE 13mm which enables EMI shielding measurement from 50 kHz to 8 GHz. This frequency range covers applications such as radio waves, RFID, phone (GSM), 4G, wi-fi and Bluetooth. A 3mm diameter hole is drilled in the center of previously hot-pressed composite material samples to order for it to be inserted in the cell sample holder. Electrical contacts with the cell sample holder are gold metallized using a circular mask (6 mm inner diameter, 13 mm outer diameter which corresponds to sample holder). Coaxial measurement cell (picture and schematic representation) and a metallized sample are shown in Figure 7. Once metallized, the sample is inserted in the sample holder, the cell is assembled and EMI shielding effectiveness is measured. Maximal shielding sensitivity of this VNA – coaxial cell combination was observed to be 100 dB. Samples that would display a higher shielding effectiveness could not be correctly measured (underestimated value of EMI shielding).

Again, sample metallization revealed to be essential. In Figure 8 is displayed the EMI shielding effectiveness in function of incident wave frequency of a PP – 10 vol% CNT composite materials of 1mm thickness. Shielding of the as is sample and the same gold-metallized sample are compared. A clear difference can be spotted between the two curves. A shielding difference as high as 10 dB can be spotted in the low frequencies around 1 MHz with lower shielding measured on the non-metallized sample. This difference is far from being negligible. The gap between the curves diminishes when frequency increases, still equal to non-negligible values of 8.5 and 3.6 dB at 100 MHz and 1 GHz respectively. Above 5 GHz frequency, the two curves meet and measured shielding values are identical for the metallized and non-metallized sample. Thus, with the coaxial measurement cell, a very wide part of the measured frequency range is affected by contact resistance negative effect.

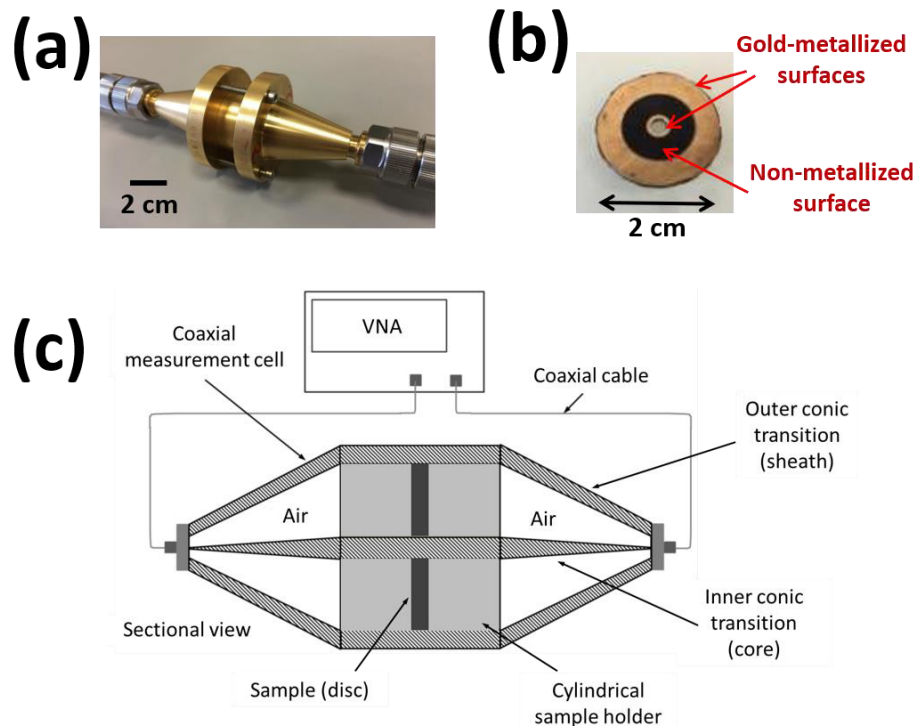


Figure II - 7: EMI shielding measurement in coaxial cell. (a) Picture of the used coaxial cell. (b) Metallized sample. (c) Scheme of the coaxial cell.

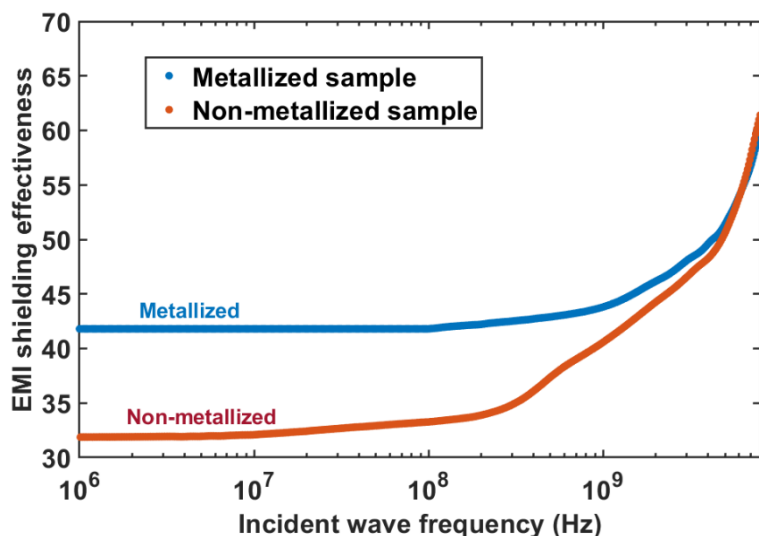


Figure II - 8: EMI shielding effectiveness measured in coaxial cell in function of incident wave frequency of the same sample as is or gold-metallized. The sample are PP-CNT composite materials with 20 wt% CNT and 1mm thickness.

Electrical contact resistance is then far from being negligible in particular to measure low frequency EMI shielding. We can estimate the impact of this undesirable resistance using the low frequency theoretical model equation presented in Eq. I-32, page 28. This model predicts for the metallized sample a resistance of 0.4Ω considering the constant low frequency shielding effectiveness (42 dB). If we add the contact resistance of 1Ω (1.4Ω total) estimated previously, theoretically predicted EMI shielding drops to 31 dB which is coherent with experimental observations. The error committed because of contact resistance is even larger for higher shielding values. For instance, for a sample that would exhibit 80 dB, the presence of a 1Ω contact resistance leads to the measurement of a shielding effectiveness of 34 dB (estimated with the same theoretical model), that is a huge error of 46 dB.

ii. Waveguide cell measurement

The waveguide cells used are the Pasternack PE-W90S00A-6 and Pasternack PE-W62S001-6 that can measure the respective frequency range 8.2 – 12.4 GHz (X-band) and 12.4 – 18 GHz (Ku-band). In these frequency bands can be found applications such as 5G and civilian road radar. The two waveguide cells are depicted in Figure 9. Hot pressed composite material plaques are cut to fit in the waveguide cavity, are then inserted in the waveguide, the latter in closed and EMI shielding effectiveness is measured.

No sample metallization is needed with the waveguide cells as metallization of the contacts between the sample and the cell cavity showed no shielding value change. An example of measured shielding effectiveness in function of frequency in the X-band waveguide is displayed in Figure 10 for two 2mm-thickness samples of PP – CNT composites with 5 or 10 vol% CNT. One can see small oscillations of the shielding effectiveness with frequency. Those oscillations are entirely due to the measurement cell and the wave frequency. As explained in previous Chapter I, the wave inside a waveguide is stationary with wave amplitude minima and maxima regularly spaced inside the cell. Those extrema shift as the frequency of the wave – and its wavelength – are changed. Oscillation maxima correspond to when amplitude maxima are situated on the coaxial-waveguide adapters and inversely oscillation minima correspond to when amplitude minima are situated on the adapters.

EMI shielding effectiveness of the 10 vol% CNT sample look irregular. Actually, this sample reached the maximum shielding sensibility of this VNA – waveguide association situated around 90 dB.

For a same sample, EMI shielding effectiveness is continuous at 12.4 GHz when switching from one waveguide to the other.

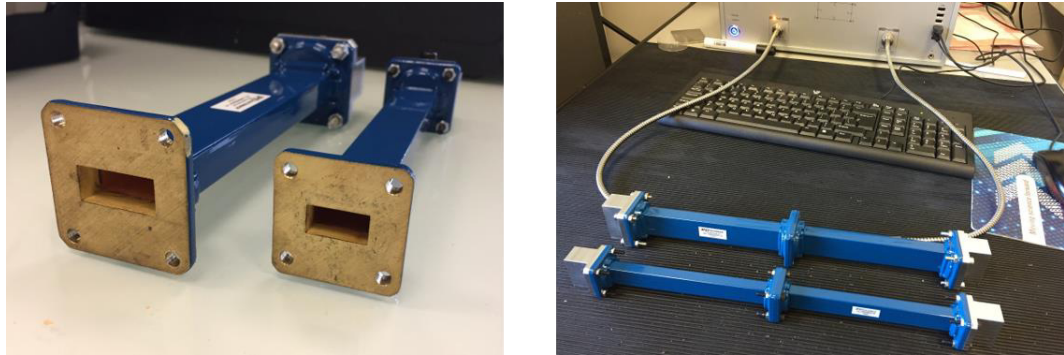


Figure II - 9: Waveguide cells used in this research project. Left: Open X-band (larger one) and K_u-band (smaller one) waveguides. Right: Closed waveguide with the VNA.

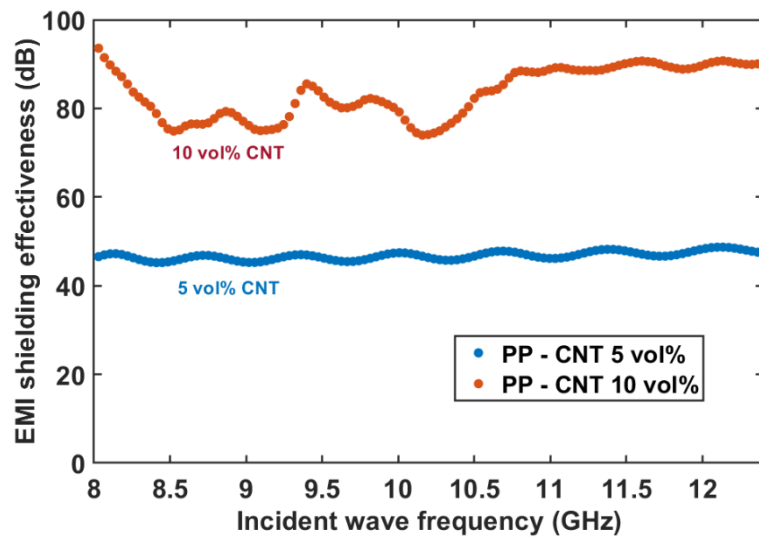


Figure II - 10: EMI shielding effectiveness measured in the X-band waveguide in function of incident wave frequency. Shown samples are PP/CNT composites of 5 and 10 vol% CNT, and both 2mm thickness.

iii. Electromagnetic properties of injected samples

Injected 1.8mm-thick plates of PP – CNT composite electrical and EMI shielding properties were measured and showed different from the hot compressed samples. In PP – CNT composites for instance, for samples of identical thickness and filler concentration, the injection molded samples exhibit lower electrical conductivity and EMI shielding effectiveness measured in both cell types compared to hot compressed samples. This phenomenon is displayed in Figure 11. Composite electrical conductivity (average over several samples) is observed to be inferior for injection molded samples compared to hot compression molded ones by a factor 1.5 to 2 depending on CNT concentration (Fig. 11-a). Both samples were gold-metallized for conductivity measurements as well as EMI shielding measurement in coaxial cell (Fig. 11-b). The latter shows a lowered shielding effectiveness of 10 dB for the injected sample compared to the hot compressed one. A similar drop is observed at the other CNT concentrations as well as in waveguide measurements (Fig. 11-c) at different CNT concentrations.

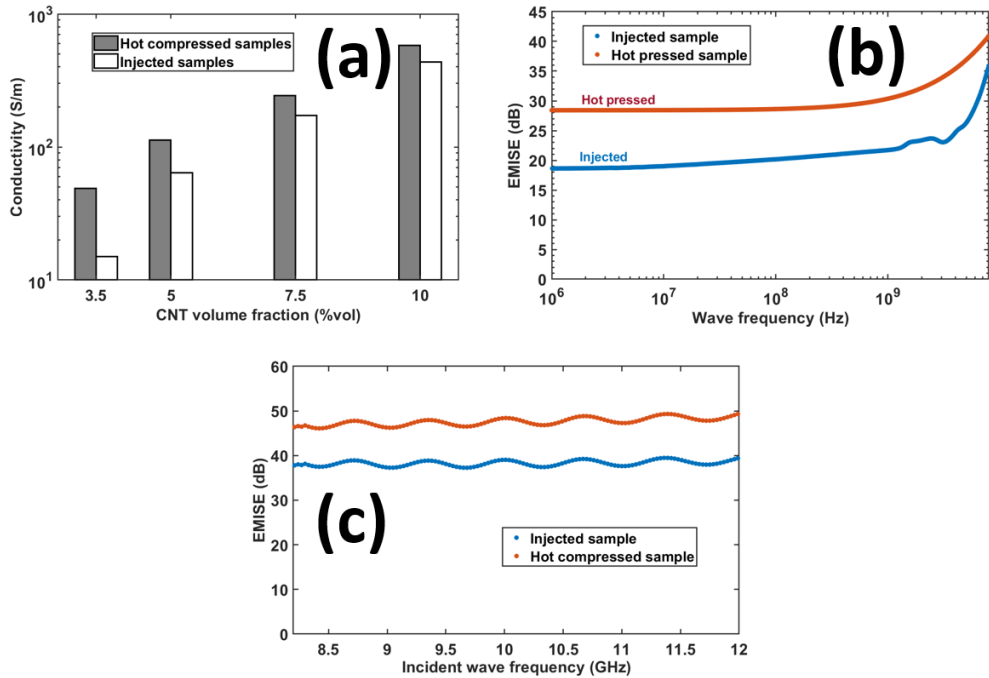


Figure II - 11: Electromagnetic properties of PP – CNT composites injection or hot compression molded. (a) Electrical conductivity for different CNT concentrations. (b) EMI shielding measured in coaxial cell in function of frequency. 3.5 vol% CNT and 1.8mm thickness. (c) Same as before in X-band waveguide cell. 5 vol% CNT and 1.8mm thickness.

These properties drops are comparable to the existence of a contact resistance as observed previously. A proposed hypothesis is then that injection molding leads to the formation of a surface layer of reduced conductivity on injected samples. High shear rates are involved during injection molding, in particular for the matter in contact with the mold walls. Those high shear rates can lead to a lower filler concentration as well as a depercolated filler network in those regions, making our hypothesis plausible. Arjmand et al. observed similar drops of electromagnetic properties of injected samples compared to hot compressed ones [3]. They attributed this phenomenon to an orientation of the fillers (CNT) due to injection high shear. Oriented CNT have then a reduced probability of touching one another, leading to a global drop of composite electrical conductivity and a fortiori EMI shielding properties. Other studies observed such a filler orientation [4], [5]. Scanning electron microscopy observations of our injected samples showed no particular CNT orientation (Fig. 12-a). However, observation of the sample surface (sectional view) revealed the presence of a thin surface layer with less CNT than in the sample volume (Fig. 12-b). The use of the 2^{ary} electrons sensor showed an electrons accumulation on the surface layer of the sample (whitened zone on Fig. 12-c), revealing a less conductive surface layer. This less conductive surface layer thickness layer is estimated to be about 5 μm from the pictures.

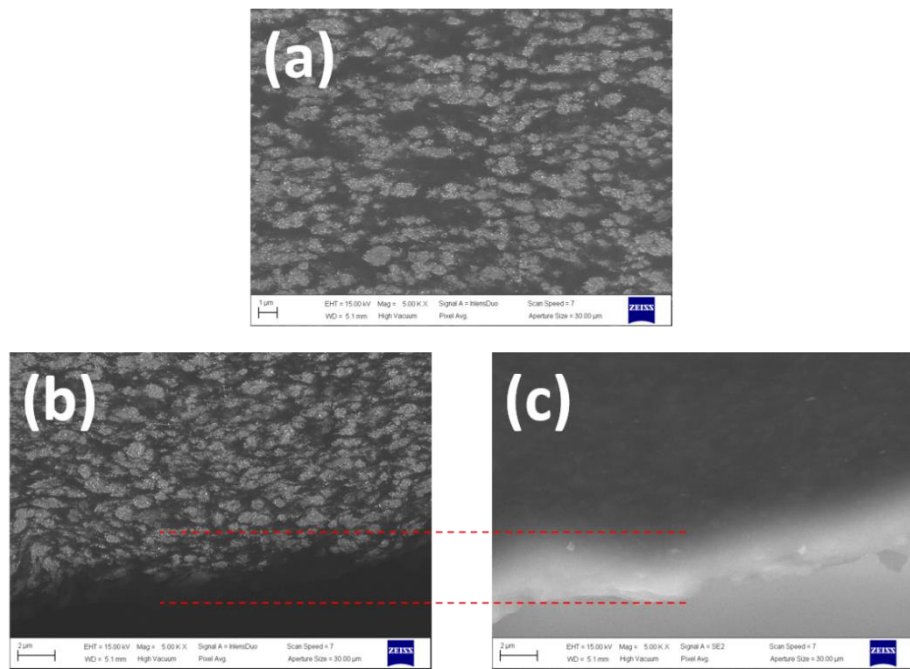


Figure II - 12: SEM images of an injected PP – CNT 5 vol% sample (sectional view). (a) Sample core, InlensDuo sensor. (b) Sample surface, InlensDuo sensor. (c) Same sample zone as before, 2^{ary} electrons sensor.

Conductivity decrease can be deeper though with a core conductivity value retrieved at a higher depth than 5 μm . The conductivity variation with depth is not thought to brutally drop with a given thickness surface layer of reduced conductivity and just below it a constant core conductivity. It is rather expected that conductivity progressively increases from the surface to a certain depth where it gets equal to sample core conductivity. This certain depth is unknown but at least larger than 5 μm .

To back the hypothesis of a reduced surface conductivity of injected samples, two experiments were carried on. On the one hand, the surface layer of injected samples was sanded down with sandpapers and compared to a compressed sample of equal thickness. On the other hand, a compressed sample was sandwiched between two pure PP layers and its shielding effectiveness was measured. Results are displayed in Figure 13.

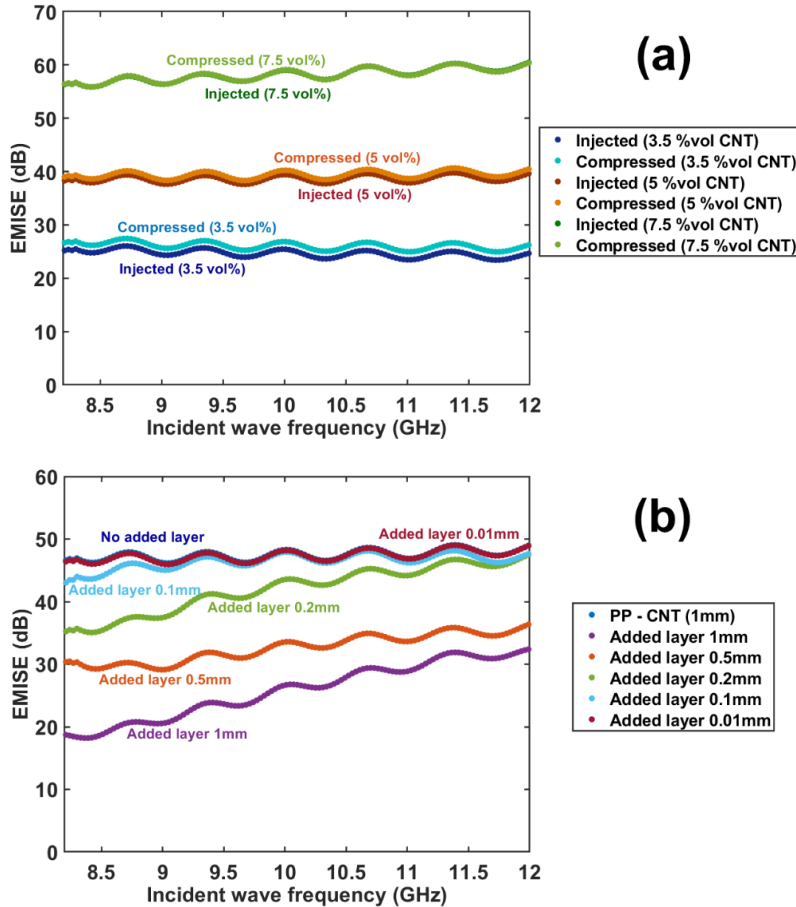


Figure II - 13: Effect of less conductive surface layer on measured EMI shielding measured in X band waveguide. (a) Sanded down to 1.5mm injection molded samples of PP – CNT composites compared with the same thickness and CNT concentration hot compressed samples. Injected and compressed curves of the 7.5 %vol CNT sample are superposed. (b) 1mm-thick PP – 7.5 vol% CNT sandwiched between two isolative pure PP layers of different thickness. PP CNT layer alone and added layer 0.01mm curves are superposed.

Sanding down injected samples 0.15mm on each side (0.3mm total) led to a sample exhibiting equal shielding effectiveness as hot compressed samples (Fig. 13-a). Sanding down 0.05mm on each side (0.1mm total) led to the same observations. Thinner sanding could not be done with precision. Conclusion is that the lowered conductivity surface layer thickness is less than 50 µm. Similar observations were made with coaxial cell measurements.

Sandwiching a 1mm-thick PP – CNT composite (7.5 vol% CNT) between two isolative pure PP layers of given thicknesses led to a reduced value of measured EMI shielding in waveguide cell (Fig. 13-b). Sandwiching the PP – CNT composite between two isolative layers of 1mm thickness (3mm-thick sample total) led to a decrease of measured EMI shielding effectiveness of more than 20 dB. This drop diminishes as the thickness of the added pure PP layers is reduced. Shielding is only very slightly reduced when adding 2 x 0.1mm isolative layers and is not changed when adding 2 x 0.01mm. In coaxial cell, the measured shielding was zero for all samples with added isolative layers since electrical contact between the conductive sample and the cell was cut. It might be risky to link this second experiment to what happens exactly with injected samples, but it shows that it can be challenging to measure conductivity and EMI shielding properties of a heterogeneous composite materials in particular when its surface properties are quite different from its core properties.

These two experiments added to SEM observations tend to back up our hypothesis of a reduced conductivity surface layer in injection molded samples. The injected sample reduced conductivity compared to hot compressed ones could also be a combination of this phenomenon with filler orientation as suggested in the literature. Conclusion is that great caution must be applied when measuring electrical conductivity and EMI shielding properties of a heterogeneous composite material with for instance different core and surface properties.

c. Optical and scanning electron microscopy observations of studied composite materials

i. *Samples preparation*

For transmission optical microscopy observations, samples had to be cut in thin layers of 20 to 100 µm thickness so light can go through. For SEM observations, samples had to be surfaced carefully to reduce rugosity to a minimum (around 10 nm roughness). All these preparations were done using a Leica RM2265 microtome and a Leica UC7 ultramicrotome. Equipment is depicted in Figure 14-a.

Micrometer thick layers destined to optical microscopy observations could be cut at room temperature (Figure 14-b). However, sample surfacing for SEM observations requires the cutting (the removal) of nanometer thick layers of composite materials and had to be done at -70°C (under polymer glass transition temperature).

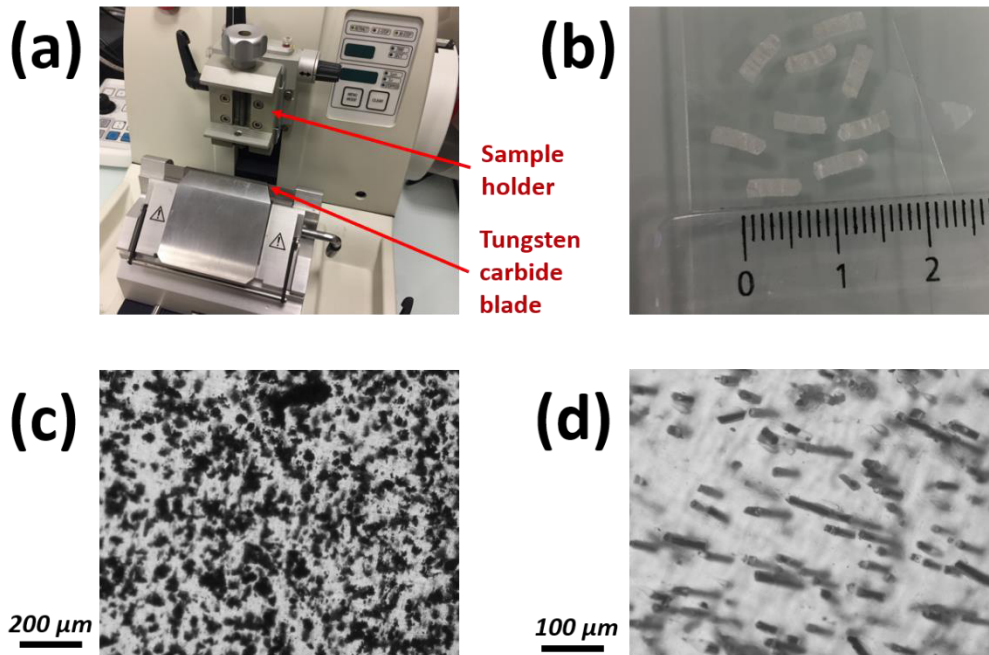


Figure II - 14: Composite materials optical observations. (a) Microtome cutter used to make thin layers of composite for observation showed in (b). (c) PP – 15 vol% tin particles composite. 20μm layer and x10 magnification. (d) PP – 10 vol% Ag-coated glass fibers composite. 20μm layer and x20 magnification.

ii. Observations

For optical microscopy observations, an Olympus BX 41 microscope coupled with an Olympus DP 26 camera. Lens of magnification x4, x10 and x20 were used. Images analysis were done with CellSensEntry software. The thinly cut layer of composite were sandwiched between two glass slides and observed with the microscope at different magnification. Examples of taken pictures are showed in Figure 14-c and 14-d.

For SEM observations, a Zeiss Merlin Compact scanning electron microscope was used. Surfaced samples were introduced in the device chamber under an advanced vacuum. A scheme of

SEM observation is displayed in Figure 15. The working distance (between the final condenser lens and the sample) was set to 5 mm and the optimized electron acceleration voltage was set between 10 and 20 kV depending on sample and magnification to get the best image resolution. The acceleration voltage and working distance (WD) must be adjusted and directly depends on the sample surface conductivity. A high voltage on an isolative surface will lead to electrons accumulations and whitening of the image. A low voltage on a conductive surface will entail few detected electrons as they are evacuated through the conductive sample and will lead a dark image. SEM images of PP – CNT composites were showed in Figure 12. Two sensors are used for these measurements. A first used detector measures 2^{ary} electrons, electrons emitted when the sample atoms are excited by the incident accelerated electrons. The second detector combines 2^{ary} electrons detection to backscattered electrons detections (InLensDuo). The latter are primary accelerated electrons whose course has been deviated by sample atoms and electronic clouds. This detection in general probes the sample more deeply and is less sensitive to charges accumulation.

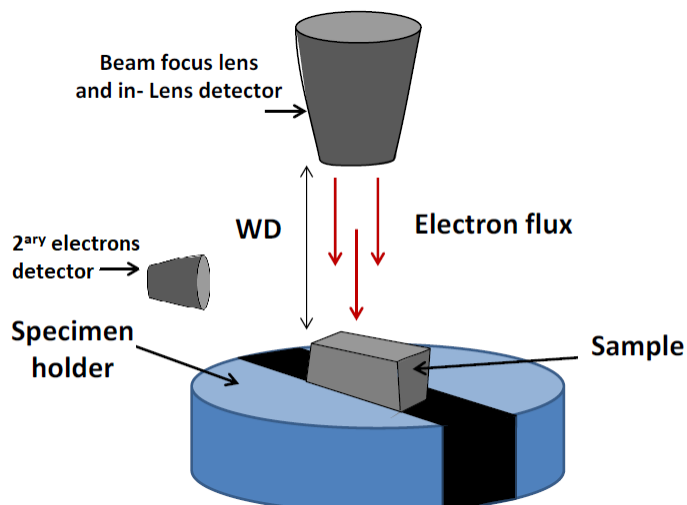


Figure II - 15: Scheme of scanning electron microscopy observations of surfaced composite materials.

d. Molten polymers, composite materials and liquid metals rheological measurements

Rheological measurements were done in an ARES G-2 rheometer from TA Instruments. For molten pure polymer matrices and composite materials, measurements were done with a 25mm diameter parallel-plate geometry. Prior to measurement, the materials were hot compression molded

into discs of 1mm thickness and 25mm diameter. A Couette geometry is used to measure liquid metal properties. This specific measurement is detailed in Chapter IV. Measuring temperature is set on the empty geometry and the zero-gap as well as measured torque and normal force are calibrated. Material disc is introduced between the parallel plates and when sample temperature reaches measuring temperature, the gap is set to 1mm. The excess matter that outstrips from the geometry is removed. A first strain sweep experiment at constant 1 rad/s frequency is carried on to identify the material linear domain (constant measured G' and G''). A frequency sweep experiment is then carried on from 100 rad/s to 0.01 rad/s while setting experimental strain to a linear domain value. Strain is progressively increased during experiment to conserve a good measurement resolution while making sure linear conditions are met (no brutal G' and G'' change). Strain sweep and frequency sweep curves are displayed in Figure 16.

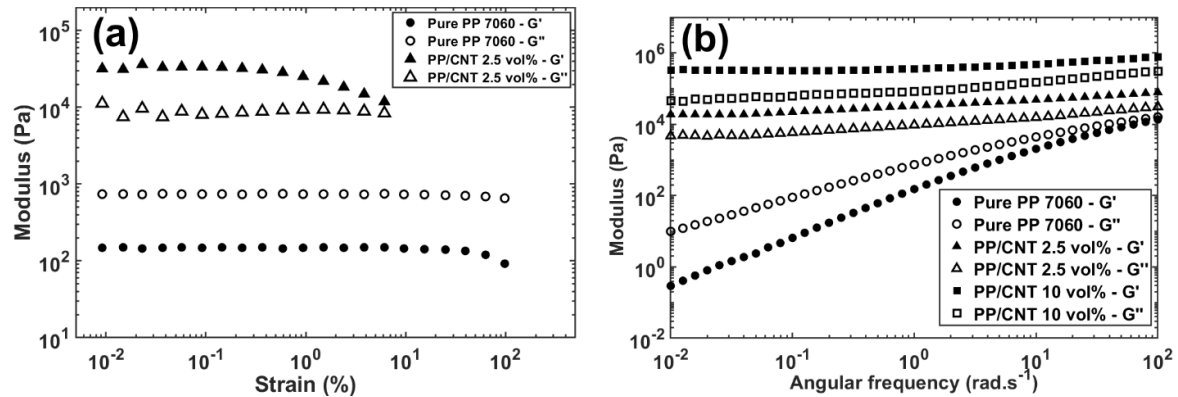


Figure II - 16: Rheological properties of molten pure PP 7060 and PP – CNT composites measured at 200°C. (a) Moduli in function of measurement strain at constant angular frequency 1 rad/s. (b) Frequency sweep with adapted measurement strain.

Linear domain is wider with pure PP 7060 than with the same polymer loaded with 2.5 vol% CNT, which is often observed and well known as the Payne effect with loaded polymer matrices (Fig. 16-a). Thus, at 1 Hz angular frequency, linear domain ranges from 0.01 to 40 % strain and from 0.01 to 0.2% strain for pure PP and PP – CNT 2.5 vol% respectively. Linear domain range generally depends on oscillation frequency. A higher frequency (higher oscillation speed) tends to reduce linear domain range (from the high to the low strains). That is why in frequency sweeps, strain can be increased in the lower frequencies while remaining in linear conditions. In Fig. 16-b is shown the frequency variations (frequency sweep) of the storage modulus G' – which describes the elastic component of the material – and the loss modulus G'' – which describes the viscous dissipation

component of the material. Whereas G'' is superior to G' for pure PP 7060 with a low frequency decrease (flowing behavior), the ratio is inverted for loaded matrices with a low frequency plateau revealing the percolated nature of the filler network (with higher moduli in general). As expected, moduli increase with filler concentration.

e. Measurement of tensile mechanical properties of composite materials

Mechanical characterizations of our composites are done by tensile-strength tests. This test gives a good idea of the mechanical properties of the solid materials such as its stiffness (through the Young modulus) and its resistance to elongation (yield and break). A Shimadzu Autograph AG – X Plus traction tester with a 10 kN load cell was used for traction tests. Dog bones samples are injection molded as said previously, compression molded samples leading to reduced traction mechanical properties because of the important defects induced by this molding method. The traction tester measures force and frame course which are translated into stress and strain with sample geometry. Measurement speed is set to 10 points per second. Traction speed is set to 1mm/min between 0 and 2 % strain to measure Young modulus. This parameter is measured taking the slope of the load curve at strain = 0 (an average of the derivative of stress in function of strain is taken on the first 10 points). Traction speed is then set to 10 mm/min from 2% strain until break. At first, stress increases linearly with strain (slope equal to Young Modulus), this is the elastic regime. When variation stops to be linear, the sample enters the plastic regime. In this regime, strain variation can be large with quite small variation of stress, in particular for thermoplastic materials. The maximum value of stress reached in this regime is called yield stress associated with a yield strain. Breaking of the sample – visible on the sample directly – is associated with a brutal drop of measured stress. In Figure 17 is shown the used traction tester and an example of a traction load curve of a PP – CNT 2.5 vol% composite sample. The different mechanical properties of the material are determined as indicated on the graph. For this sample, the measured Young Modulus is 2180 MPa, yield stress is 35.4 MPa, yield strain is 5.7%, stress and strain at break are respectively 25 MPa and 76%. It can happen for certain samples that they break before displaying a plastic behavior (fragile behavior versus ductile behavior). In this case, no yield properties can be measured.

At least 7 samples are tested for each composite composition to insure statistical significance of the results.

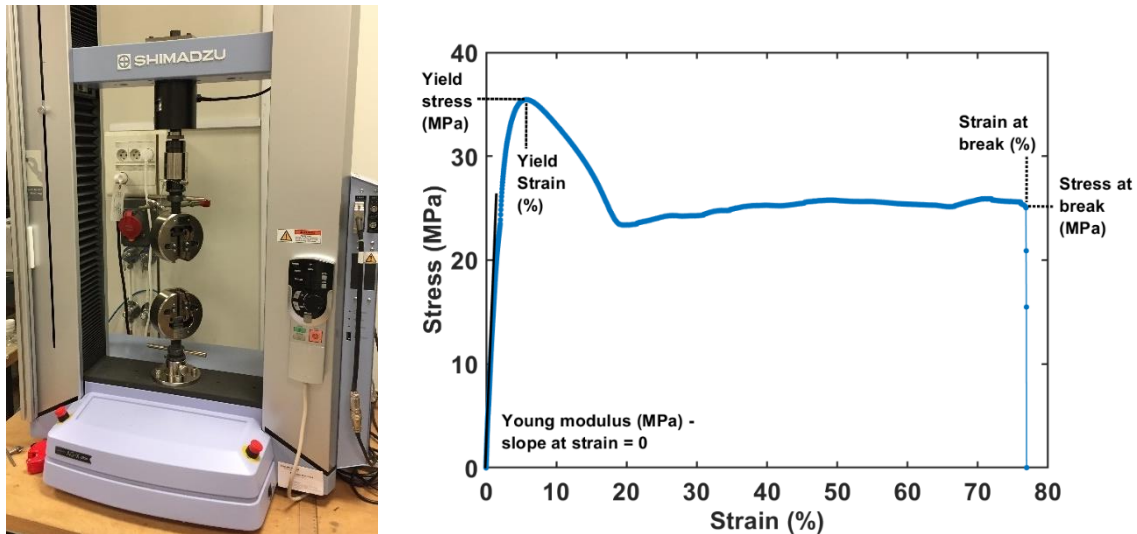


Figure II - 17: Mechanical traction tests on injected composite material dog bones. Left: Tensile test equipment. Right: Load curve of PP – 2.5 vol% sample with experimentally measured mechanical properties.

f. Surface property measurement: water drop contact angle

The water contact angle measurement method was chosen as surface characterization of filler properties. This method is quick and of easy use to differentiate hydrophilic from hydrophobic surfaces. This method is used to evaluate the surface properties of stearic acid (hydrophobic), metal filler (hydrophilic) and their mixes. A Kruss Easydrop experimental setup coupled with a Hamilton 500 μ L syringe and an Allied Vision Technology Stingray camera is used to measure water contact angle (Figure 18). The latter is linked to surface energies between the solid surface S, the liquid L and the air G by the Young equation:

$$\gamma_{SG} = \gamma_{SL} + \gamma_{LG} \cdot \cos(\theta) \quad (9)$$

The full determination of surface energy requires the use of water, a polar and dispersive liquid, and a fully dispersive liquid, generally diiodomethane. Contact angle with water alone can testify of the hydrophobic/hydrophilic nature of the surface. If $\theta < 90^\circ$, the surface is considered hydrophilic and if $\theta > 90^\circ$ the surface is considered hydrophobic.

A 1 μ L deionized water droplet is dropped on the analyzed surface. Once the drop is stabilized, contact angle is measured thanks to the Drop Shape Analysis software as shown on Figure 18. The

shown example of a 50/50 %vol mix of stearic acid and tin microparticles displays a hydrophobic nature with a contact angle superior to 90°.

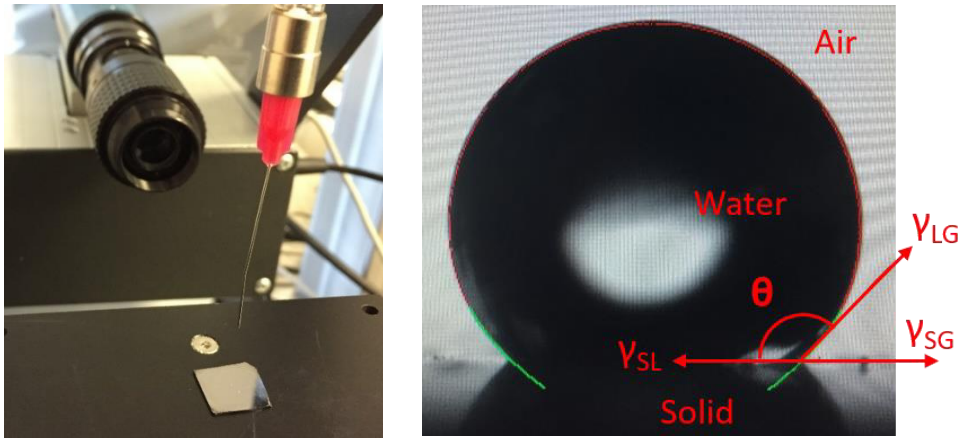


Figure II - 18: Water contact angle measurement on sample surface. Left: Experimental setup with drop off needle and camera. Right: Water droplet on a 50/50 %vol stearic acid – tin particles mix surface. Drop shape is identified and contact angles are measured by the treatment software (red and green lines).

g. Chemical analysis of fillers and composite materials

Chemical analysis of as is or stearic acid treated filler, and of composite materials is done thanks to infrared (IR) spectroscopy. This method relies of the characteristic vibrations of chemical groups, and can identify and quantify the chemical groups present in a measured sample. For chemical characterization of as is or stearic acid treated metal filler, those are grinded and pressed in a KBr disc (200mg KBr with 1.25 wt% sample). KBr is a transparent-to-IR matrix. Transmission IR spectroscopy is performed on those discs in dry and CO₂ free chamber in a ThermoScientific iS-10 spectrometer between 1000 and 4000 cm⁻¹ light wavenumber. A background spectrum in empty chamber is acquired prior sample measurement. A liquid nitrogen cooled detector is used and set to high spectral resolution and 256 scans.

For the PP – metal filler composite materials, thin layers (20μm-thick) are cut from the bulk material using microtome as evoked earlier. Samples are laid down a pure KBr disc and analyzed using a ThermoScientific Nicolet iN 10 MX IR microscope. This device enabled us to focus IR measurements on a particular region of the composite (20x20 μm² probed area). IR measurements is done in light

wavenumber ranging from 1000 to 3500 cm^{-1} with a liquid nitrogen cooled detector set on high spectral resolution and 256 scans.

For both measurement methods, at least 3 samples per mix or composite composition are measured to insure statistical significance of the results. IR absorbance is measured and the final result curve of absorbance in function of wavenumber is the average of the 3 measured samples. An example of the IR spectrum of pure stearic acid (in KBr disc) is displayed in Figure 19. General absorbance reaches correct measurable values between 0 and 1. Values higher than 2 are too high for a correct quantification of chemical groups concentration and could need a reduced sample concentration in the KBr disc. In the stearic acid spectrum, several absorption bands and peaks linked to chemical groups can be identified [6]. The two peaks at 2916 and 2850 cm^{-1} are related to C-H single bonds. The wide medium intensity band between 2700 and 3400 cm^{-1} can be attributed to the acid O-H bond. The high intensity peak at 1702 cm^{-1} is related to carboxyl C=O double bond. The peaks at 1470 cm^{-1} as well as the smaller peaks in its surroundings are associated to the bending and rocking modes of the CH_2 and CH_3 groups. The peak at 1300 cm^{-1} is associated to carboxyl C-O single bond.

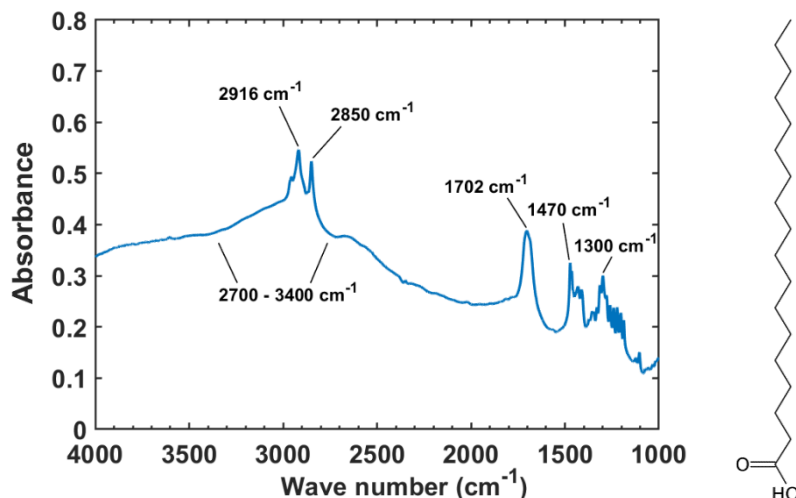


Figure II - 19: IR spectrum of pure stearic acid in KBr disc (1.25 wt%) and chemical structure of the molecule.

References

- [1] W. Andreoni, Ed., *The Physics of Fullerene-Based and Fullerene-Related Materials*, **vol. 23**. Dordrecht: Springer Netherlands, 2000.
- [2] T. W. Ebbesen, H. J. Lezect, H. Hiura, H. F. Ghaemi, and T. Thio, "Electrical conductivity of individual carbon nanotubes," *Nature* **382**, 54–56, 1996.
- [3] M. Arjmand, T. Apperley, M. Okoniewski, and U. Sundararaj, "Comparative study of electromagnetic interference shielding properties of injection molded versus compression molded multi-walled carbon nanotube/polystyrene composites," *Carbon* **50**, 5126–5134 (2012)
- [4] F. Yu *et al.*, "Anisotropic multilayer conductive networks in carbon nanotubes filled polyethylene/polypropylene blends obtained through high speed thin wall injection molding," *Polymer* **54**, 6425–6436 (2013)
- [5] W.-C. Yu *et al.*, "Constructing highly oriented segregated structure towards high-strength carbon nanotube/ultrahigh-molecular-weight polyethylene composites for electromagnetic interference shielding," *Compos. Part Appl. Sci. Manuf.* **110**, 237–245 (2018)
- [6] G. Socrates, *Infrared and Raman Characteristic Group Frequencies: Tables and Charts*. John Wiley & Sons, (2004).

Chapter III. Experimental and theoretical study of EMI shielding properties of Carbon Nanotubes- based composite materials

Chapter III. Experimental and theoretical study of EMI shielding properties of Carbon Nanotubes-based composite materials

Abstract

The electrical and electromagnetic shielding interference properties of composite materials made of polypropylene (PP) and carbon nanotubes (CNT) have been investigated in a broad frequency range, both experimentally and theoretically. A remarkably low percolation threshold of only 0.4 vol% and an exceptional shielding performance reaching effectiveness values as high as 90 dB are reported. The shielding effectiveness has been measured between 50 MHz and 18 GHz using two experimental methods (coaxial cell and wave guide cell) and the results were systematically correlated with the conductivity values of our composite materials. Furthermore, an EMI shielding theoretical model was developed and employed to predict the shielding properties of our PP/CNT composite materials as well as of numerous other composite materials reported in the literature and made by employing different polymer matrices and different types of fillers (carbon black, carbon fibers, bamboo charcoal, mesoporous carbon, copper nanowires, reduced graphene oxide). An excellent agreement is found between our theoretical calculations and the experimental data upon systematically varying the frequency of the incident wave, the fillers content and the sample thickness. Our model is allowing one thus to predictively design materials required to exhibit a specific value of EMI shielding effectiveness and operating in a specific frequency range. This can be of significant importance in numerous applications where shielding electromagnetic interference phenomena plays an important role.

Keywords: nanocomposites, EMI shielding, electrical conductivity, theoretical modelling

Reformatted version of the paper originally published in:

Composite Part B: engineering, 2020, Volume 189, page 107866

Polypropylene/Carbon nanotubes composite materials with enhanced electromagnetic interference shielding performance: properties and modeling

Hubert Lecocq¹, Nicolas Garois², Olivier Lhost³, Philippe-Franck Girard⁴,

Philippe Cassagnau¹, A. Serghei¹

¹*Institut des Matériaux Polymères, Université de Lyon, 69622 Villeurbanne, France*

²*HUTCHINSON SA CRI, 45120 Chalette Sur Loing, France*

³*TOTAL Research and Technology Feluy, C 7181, Feluy, Belgium*

⁴*TOTAL – Saclay, 91120 Palaiseau, France*

1. Introduction

With the rapid development of electronics and remote communications in the recent decades, our environment is increasingly polluted with electromagnetic waves. In the proximity of working electronic devices, these waves can create electromagnetic interference phenomena (EMI) which can be detrimental to their normal operation. Limiting the possibility of stacking emitters, receptors and sensitive circuits in confined spaces such as in in-vehicle systems, their main consequences are loss of data and even total dysfunction of certain devices. To counteract this phenomenon, sensitive devices and devices emitting undesirable and potentially harmful EM radiation must be shielded to avoid EMI. Electronic conductive materials can serve as shield to minimize or even eliminate these interference phenomena through reflection and absorption of EM waves. However, a high electrical conductivity is needed in order to obtain a substantial shielding performance. As it is commonly agreed, materials with a conductivity below 10^{-10} S/m are considered insulating, between 10^{-10} and 10^{-7} S/m they can be used for antistatic applications, between 10^{-7} and 1 S/m they are suitable for electrostatic charge dissipation (ESD), and they show EMI shielding properties above 1 S/m. Metals are therefore the materials of choice for EMI shielding due to their high electronic conductivity [1] but their high density, cost and processing temperature incite industrial companies to consider alternative approaches, such as for instance lighter conductive polymer composite (CPC) materials.

By introducing conductive fillers inside a polymer matrix, one can get a light conductive material that can display EMI shielding properties. Composite materials for EMI shielding is a subject of major interest considering the large number of papers reported in this field and summarized in several recent reviews [2,3]. Polymer matrices commonly used for EMI shielding materials are both

thermoplastics like PC [4,5], PP [6,7], PE [8,9], PS [10,11], PLA [12,13], PMMA [14,15], ABS [16,17] or PVDF [18,19] and thermosets like epoxy resins [20,21], PDMS [22,23] or PU [24,25]. Several types of conductive fillers can be dispersed in polymer matrices in order to get CPC such as metal fillers like steel fibers [26], copper [27,28], silver [29] nanowires, or metal oxide fillers like magnetite ferrite Fe_3O_4 [30,31]. Due to their lightweight and high conductivity, carbon-based fillers are most frequently used. Carbon black [6,32,33], graphite [34,35], carbon fibers [8,36], graphene [19,37], carbon nanotubes (CNT) [4,7,38–40] or graphene nanoplatelets [41,42] are examples of carbon conductive fillers. Combinations of different fillers in the same CPC is also common and often lead to synergy effects between the fillers: the EMI shielding of a CPC material using combined fillers can be higher than the sum of shielding effectiveness values of the same composite material but using only one type of filler [15,30,43–45]. Fillers segregation is also often used to enhanced electrical and EMI shielding properties of composite materials: in an immiscible polymer blend, carbon or metal conductive fillers can be segregated into one of the two polymer phases [28,33]. In order to disperse conductive fillers in polymer matrices and get good electrical conductivity and EMI shielding properties, three main processing methods exist: (i) in-situ polymerization [46] where the fillers are dispersed in the liquid monomer before polymerization; (ii) solution blending [7,13–15,20,23–25] where the polymer matrix is first dissolved in an appropriate solvent, then the fillers are dispersed into the polymer solution and finally the solvent is subsequently evaporated by vacuum and/or temperature treatment and (iii) melt blending [8,12,16–18,38–42] where the fillers are directly dispersed in the molten state of the polymer matrix. In general, in-situ polymerization and solution casting give the best results in terms of conductivity and EMI shielding properties, but melt blending has the advantage of being quicker and not requiring the use of dangerous organic solvents or reactants, which makes it best adapted for processing on an industrial scale.

In parallel with the increasing number of experimental studies on the EMI shielding properties of composite materials, the interest in theoretical models has grown over the recent years [1,47–53]. The importance of the incident wave frequency, shield thickness, composite conductivity, complex dielectric permittivity, magnetic permeability, fillers dispersion and distribution in the polymer matrix has been investigated in different theoretical approaches [1,47–53]. However, until now, each of the theoretical models has been applied to a rather limited amount of specific experimental results and no theoretical approach has been developed to validate a large collection of experimental data gathered from the multitude of different experimental studies reported so far in the scientific literature. This challenge represents the main goal and the main achievement of the present study. As a second achievement, we report PP/CNT composite materials with exceptional EMI shielding performance reaching effectiveness values as high as 90 dB, among the highest reported values in the

scientific literature so far. By analyzing the wave propagation phenomena and the fundamental mechanisms governing the wave/matter interactions in combination with the theory of percolation that describes the conductivity of composite materials, we developed a theoretical approach that provides an excellent agreement not only to the experimental results obtained for our PP/CNT composite materials but also to numerous other composite materials reported in the literature and made with different polymer matrices and with fillers of different nature (carbon black, carbon fibers, bamboo charcoal, mesoporous carbon, copper nanowires, polyether sulfone, reduced graphene oxide). Our model is allowing one thus to predictively design materials with a specific value of EMI shielding effectiveness and operating in specific frequency range, which can be of significant importance in numerous applications where electromagnetic interference phenomena play an important role.

2. EMI shielding theoretical model

The EMI shielding effectiveness of a given shield is generally defined as:

$$SE = -10 \log_{10} \left(\frac{P_t}{P_i} \right) = -20 \log_{10} \left(\frac{E_t}{E_i} \right) = -20 \log_{10} \left(\frac{H_t}{H_i} \right) \quad (1)$$

P_i , E_i and B_i are the incident power, electric field amplitude and magnetic field amplitude of the EM wave, respectively, and P_t , E_t and B_t the power and amplitudes of the transmitted wave through the shield. The shielding effectiveness is expressed in dB: while at 10 dB 68% of the wave power is blocked by the shield, at 40 dB it is 99.99% of the wave power that is shielded. In general, a shielding value of 30 to 40 dB is required for commercial applications, but higher shielding values are usually required for aeronautical or military applications.

When an incident electromagnetic wave hits an EMI shield, several phenomena take place, as illustrated in Figure 1. First, a part of the EM wave gets reflected at the first air-material interface and does not penetrate the material at all. This shielding mechanism is called simple reflection. The other part of the wave gets into the shield, goes through its thickness and undergoes electromagnetic absorption (the second main shielding mechanism) all along the way. The wave power gets dissipated and transformed into thermal energy through induced current dissipation, dielectric polarization, interfacial polarization, eddy current dissipation, hysteresis loss and magnetic resonance loss [54]. When the EM wave gets to the second material-air interface, a part of the wave goes through the interface and it is transmitted to the receptor. The other part of the wave gets reflected at this second interface and goes back to the first interface. On the way, it undergoes again electromagnetic

absorption and gives rise to a secondary reflection at the first interface and a secondary transmitted wave as it gets back to the second interface, etc. This phenomenon is called multiple internal reflections. As a shielding material gets more and more sophisticated in its composition and structure, other mechanisms can intervene in the total shielding. The presence of particular conductive fillers and multiple interfaces in heterogeneous materials can give rise to many internal reflections as the wave can reflect on each of these elements, increasing the EMI shielding effectiveness of the material [3,19,26,51]. The simple reflection is due to a discontinuity of the incident EM wave impedance. The wave impedance Z (or η) characterizes the propagation of an EM wave in a given field and depends on the properties of the field. It is commonly defined as [1,47]:

$$Z = \frac{E}{H} = \sqrt{\frac{\mu^*}{\epsilon^*}} = \sqrt{\frac{j\omega\mu'}{\sigma+j\omega\epsilon'}} \quad (2)$$

where E is the electric field and H the magnetic field of the EM wave in the material. μ^* and ϵ^* are the complex magnetic permeability and dielectric permittivity of the material. Hence, the wave impedance is a complex number. ω is the angular frequency of the wave ($\omega = 2\pi f$, f the wave frequency), μ' and ϵ' are the real part of the permeability and permittivity, respectively, σ is the electronic conductivity of the material and j the imaginary number $\sqrt{-1}$. The wave impedance of vacuum (and air) is a constant equal to $Z_0 = \sqrt{\mu_0/\epsilon_0} \approx 377 \Omega$. The bigger the difference is between the air impedance Z_0 and the wave impedance Z , the more important will be the phenomenon of single reflection.

In order to describe the phenomenon of electromagnetic absorption of an EM wave of frequency f inside a material of conductivity σ and magnetic permeability μ , a characteristic length called skin depth is defined as [1,55]:

$$\delta = \sqrt{\frac{2}{\mu\omega\sigma}} = \sqrt{\frac{1}{\mu\pi f\sigma}} \quad (3)$$

Inside the material, the amplitude of the EM wave decreases exponentially with the propagation length. After propagating through a length equal to δ , the wave losses $1 - 1/e \approx 63\%$ of its original amplitude. As the electrical conductivity of a material increases, its skin depth decreases leading to an increase of the absorption loss. Skin depth also decreases with increasing frequency, giving rise to a substantial increase of absorption when it becomes thinner than the shield thickness (Fig. S1 and S2, page 120, in the Supplementary Information Part).

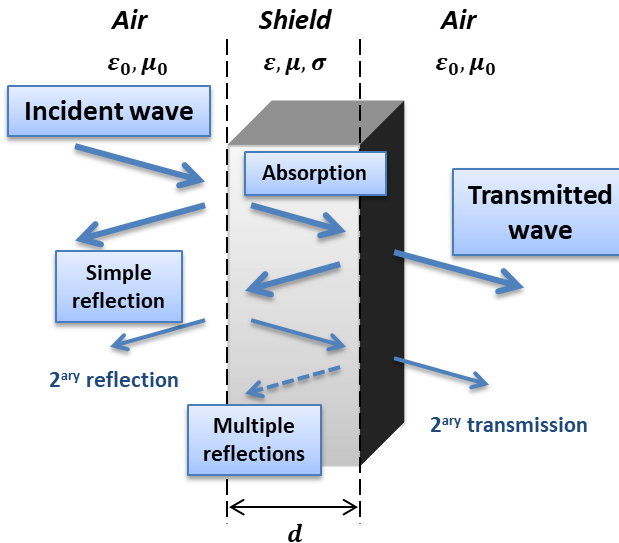


Figure III - 1: Schematic representation of EMI shielding mechanisms

To establish our EMI shielding theoretical model, we take a shield of thickness d , electrical conductivity σ , real part of the permeability and permittivity μ' and ε' . A plane progressive EM wave of frequency f is sent onto the surface of the shield under normal incidence and the amplitude of the transmitted wave is calculated. Our material is supposed homogeneous, meaning the wavelength λ of the incident EM wave is larger than the heterogeneities of the material (distance between fillers, small spatial variations of fillers concentration, etc.), and isotropic (no fillers orientation or favored direction for the wave propagation). Taking the good conductor approximation $\sigma/\omega\varepsilon' \gg 0$, a condition met by all our samples, the following expressions of EMI shielding effectiveness can be then obtained [1,48,51,56]:

$$SE_T = SE_A + SE_R + SE_M \quad (4)$$

$$SE_A = 20 \cdot \frac{d}{\delta} \cdot \log_{10}(e) \quad (5)$$

$$SE_R = -20 \cdot \log_{10} \left(\left| \frac{4Z_0Z}{(Z+Z_0)^2} \right| \right) \quad (6)$$

$$SE_M = 20 \cdot \log_{10} \left(\left| 1 - \left(\frac{Z-Z_0}{Z+Z_0} e^{-d/\delta} \right)^2 \right| \right) \quad (7)$$

where $|.|$ denotes absolute value of a complex number.

As displayed in Equations 4-7, the theoretical EMI shielding effectiveness has the advantage of being composed of three terms, each of them having a physical meaning that describes a main shielding mechanism: absorption, simple reflection and multiple internal reflections. To analyze the influence of each of the mechanisms, we plotted in Figure 2-a the total shielding effectiveness calculated as a function of the incident wave frequency from 1 MHz to 100 GHz for a material with a

relative real permittivity $\varepsilon_r = 1$, relative permeability $\mu_r = 1$, DC electrical conductivity $\sigma = 1000 \text{ S/m}$ and a thickness of 1 mm. In the lower frequencies, from 1 MHz to 100 MHz, the SE is constant and originates mainly from reflection since absorption is null [57]. Above 100 MHz, SE increases rapidly and is now due to both reflection and absorption as the skin depth of the material decreases rapidly with increasing frequency. The characteristic frequency marking the transition between the simple reflection and the reflection and absorption regime obviously depends on the shield characteristics (conductivity, thickness, permeability).

On Fig. 2-b, each of the terms of Eq. 4 is plotted separately. Absorption is null at low frequencies and increases rapidly above a certain frequency, giving rise at high frequencies to a dominating SE contribution. At this critical frequency f_c , the skin depth of the material is equal to the thickness of the shield. It is defined as:

$$f_c = \frac{1}{\pi \mu \sigma d^2} \quad (8)$$

In the example illustrated in Fig. 2-b the critical frequency $f_c \approx 250 \text{ MHz}$ and one can indeed see the absorption shielding rapidly increasing above this frequency. Simple reflection decreases as the incident wave frequency increases. This is due to a decreasing impedance gap between the air and the material with increasing frequency (Eq. 2 and Fig. S3, page 121, from Supplementary Information Part). The simple reflection tends to zero as the wave impedance in the material Z tends to the air impedance Z_0 (when Z and Z_0 are equal, the logarithm in Eq. 6 becomes equal to 0). The influence of the multiple internal reflections is zero in the high frequency range, above the absorption critical frequency f_c . For frequencies higher than f_c , the contribution of the wave absorption becoming considerably strong, the EM wave gets largely absorbed as it goes back and forth between the two surfaces of the sample, strongly diminishing thus the contribution of the multiple internal reflections. This has been reported multiple times in the past where the multiple internal reflections are considered negligible when the absorption is higher than 10 dB [1,24,58,59]. Below this critical frequency, the value of multiple internal reflections SE is negative: the wave has multiple occasions to be transmitted and the total SE decreases. This value increases to zero as the absorption starts progressively to play an important role. Thus, multiple internal reflections between the two air-material interfaces is detrimental to the EMI shielding properties of the material [6]. However, the multiple internal reflections within the material due to fillers and heterogeneous interfaces can participate positively in the total SE [3,19,26,51]. Below the absorption critical frequency, the decrease in the simple reflection and the increase in the multiple internal reflections compensate each other giving rise to a constant value which corresponds to a reflection plateau observed in the total SE curve. In conclusion, shielding effectiveness is governed by simple and multiple internal reflections that give

a constant shielding value below the absorption critical frequency and becomes dominated by absorption above this critical frequency where the SE rapidly increases with frequency. The total SE separated into the three different shielding contributions of a material with a conductivity of 10 S/m and 100 S/m are plotted in the Figure S4, page 121, of the Supplementary Information Part.

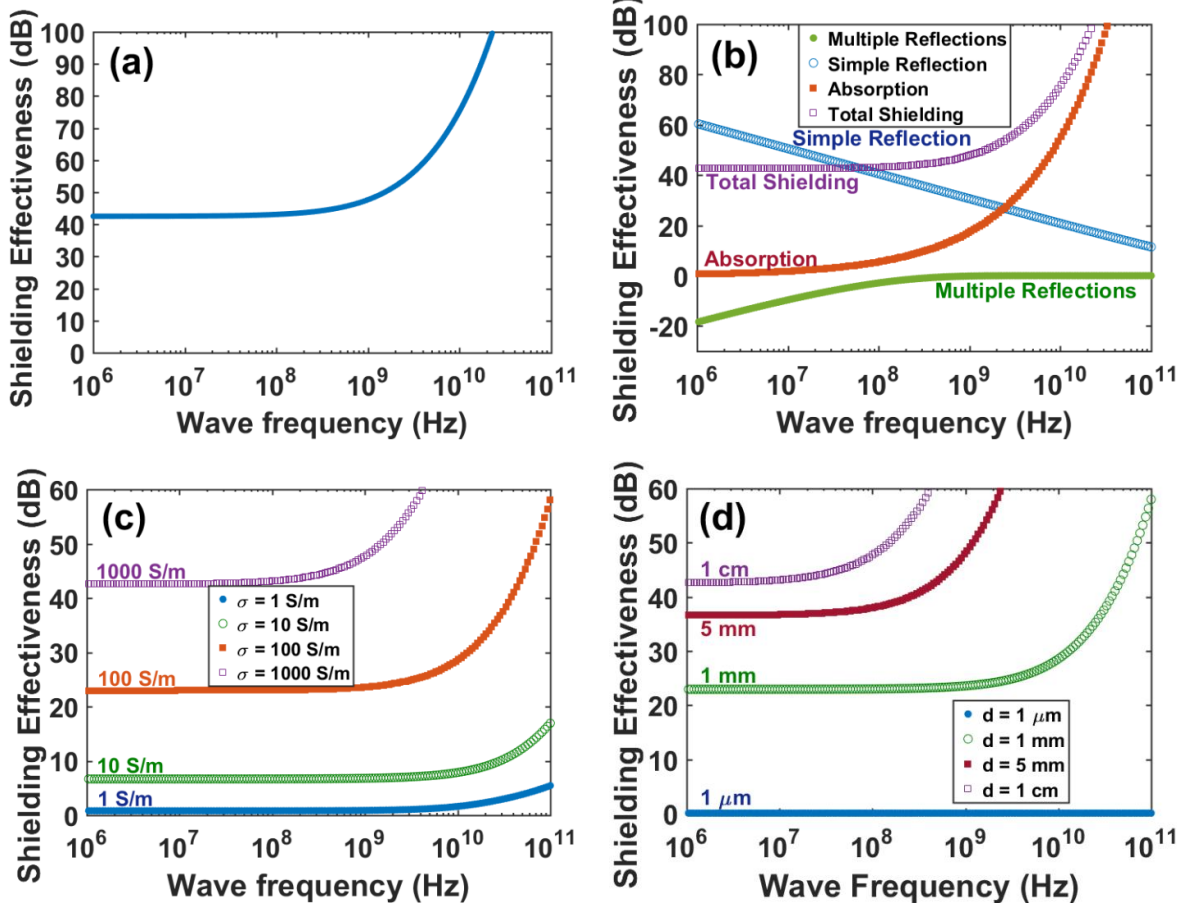


Figure III - 2: EMI Shielding curves as a function of frequency obtained from the theoretical model. (a) Shield composed of 1mm-thick material with $\epsilon = 1$, $\mu = 1$, $\sigma = 1000 \text{ S.m}^{-1}$. (b) Theoretical contributions of each of the shielding mechanisms to total EMI shielding for the same shield. (c) Theoretical EMISE curves for a 1mm-thick material with $\epsilon = 1$, $\mu = 1$, and four different conductivities, as indicated. (d) Theoretical EMISE curves for a material with $\epsilon = 1$, $\mu = 1$, $\sigma = 100 \text{ S.m}^{-1}$ and four different thicknesses, as indicated.

The critical frequency f_c depends on the properties of the shield, in particular on its conductivity and thickness. As one or the other increases, the critical frequency decreases, shifting the onset of the absorption mechanism to lower frequencies. The consequences are multiples: SE at high frequencies increases because of a higher absorption (Eq. 3 & 5), but, more surprisingly, shielding at low frequencies (below f_c) is also increased. This is because the enhanced absorption lowers the

contribution of multiple internal reflections (Eq. 7). Increasing material conductivity has another important consequence: it widens the impedance gap, increasing shielding by simple reflection at low frequencies (Eq. 2 & 6).

The influence of material conductivity and thickness are discussed in Figs. 2-c & 2-d. As shown in Fig. S5, page 122, of the Supplementary Information Part, the real magnetic permeability μ' also has an influence of the total shielding: when μ' increases, the critical frequency f_c is shifted to lower frequencies, increasing shielding at high frequencies but with no increase in SE below f_c (the decrease in the multiple internal reflections is counterbalanced by the decrease of the contribution of simple reflection). With the good conductor approximation $\sigma/\omega\epsilon' \gg 0$, the real part of the permittivity has very low influence on the total shielding [48] (Eq. 2 and Fig. S6, page 122, from Supplementary Information Part). As a consequence, the parameters that have a significant influence on the total shielding are the incident wave frequency f , the sample thickness d , the sample DC conductivity σ and the sample magnetic permeability μ' .

The previous Equations 5-7 are often simplified using the good conductor approximation to get the following approximations [24,50,53]:

$$SE_A = 8.7 \frac{d}{\delta} = 8.7 d \sqrt{\pi f \mu \sigma} \quad (9)$$

$$SE_R = 39.5 + 10 \log_{10} \frac{\sigma}{2\pi f \mu} \quad (10)$$

$$SE_M \approx 20 \log_{10} |1 - e^{-SE_A}| = 0 \text{ if } SE_A > 10 \text{ dB} \quad (11)$$

3. Materials and methods

a. Materials

Polypropylene PP 7060 ($d=0.905$, MFI=12 g/10min, $T_f=165^\circ\text{C}$) supplied by Total SA was used as polymer matrix in this study. The CNT/PP were prepared using a masterbatch Plasticyl PP2001 purchased from Nanocyl (Belgium) with a CNT concentration of $20 \text{ w\%} \pm 1 \text{ w\%}$ ($10 \text{ vol\%} \pm 0.5 \text{ vol\%}$). The NC7000 CNT, produced by catalytic chemical vapor deposition (CCVD), are multi-walled carbon nanotubes (MWCNT) of average diameter 9.5 nm and length 1.5 μm . They are characterized by a surface area of 250-300 m^2/g and a volume conductivity of 10^6 S/m .

b. Fabrication of PP — CNT polymer composites

PP/CNT polymer composites were fabricated using the melt blending method. PP 7060 and the CNT masterbatch Plasticyl PP2001 were dried overnight at 70°C and mixed together in a twin screw extruder Leistritz ZSE18 (L/D=60, 300 rpm, 200°C, 3 kg/h), varying the ratio between PP and CNT masterbatch in order to get composites with CNT concentrations ranging from 0.5 to 15%*m* (0.25 to 7.5 vol%). The obtained composite pellets were then hot pressed at 200°C in a Servitec polystat 200T press to get plates of various thicknesses.

c. Scanning Electron Microscopy

Before observation, the surface of PP/CNT composites was prepared using cryo-ultramicrotomy (Leica UC7). A flat surface having a roughness smaller than 10 nm was thus obtained. Observations were then carried out in a Zeiss Merlin Compact scanning electron microscope in an advanced vacuum. The working distance (distance between the final condenser lens and the sample) was around 5 mm and for each sample, an optimized electron acceleration voltage between 10 and 20 kV was determined in order to get the best resolution. Images are taken using a InLensDuo detector which detects secondary and backscattered electrons. Exact measurement conditions are indicated on each SEM images (EHT = Electron High Tension, Mag = Magnification, WD = Working Distance).

d. Electrical characterization of PP — CNT polymer composites

In order to measure the electrical conductivity of PP – CNT composites, plaques of dimension $50 \times 75 \times 1 \text{ mm}^3$ were measured along their length to get the surface conductivity (the thickness being all the time much smaller than the length and width of the plaques). The electrical contacts were gold metallized to eliminate the influence of the contact resistance. The electrical conductivity was measured with a Novocontrol Alpha Broadband Dielectric / Impedance Spectrometer and a Fluke 289 multimeter for double checking the measured values.

e. EMI shielding measurements of PP — CNT polymer composites

EMI shielding of PP/CNT composites was measured using an Anritsu Shockline 2 ports VNA (MS 46522B) and two types of measurement cells (Fig. 3). From 50 kHz to 8 GHz, a coaxial cell (EpsiMu

Multiwave PE 13 mm) has been used to measure the EMI shielding effectiveness EMISE (Fig. 3-a). Ring-shaped samples of various thicknesses were used with this cell and electrical contacts between the cell and the sample were gold metallized. Between 8.2 and 12.4 GHz (X band) and between 12.4 and 18 GHz (K_u band), two waveguide cells have been used (Pasternack PE-W90S001-6 1701 and PE-W62S001-6 1650) (Fig. 3-b). For these waveguide cells, the samples were in the form of small plates of various thicknesses. Before each set of measurements, the VNA is calibrated and the empty cells are measured to validate that no shielding occurs in the measured frequency band. The power was set to 0 dBm, which corresponds to 1 mW, and each point was the average of 5 measurements. The total shielding effectiveness SE_T , the reflection shielding SE_R and the absorption shielding SE_A were calculated from the measured S-parameters S_{11} and S_{21} [2,3,45]:

$$R = |S_{11}|^2 \quad (12)$$

$$T = |S_{21}|^2 \quad (13)$$

$$SE_T = -\log_{10}(T) \quad (14)$$

$$SE_R = -\log_{10}(1 - R) \quad (15)$$

$$SE_A = -\log_{10}\left(\frac{T}{1-R}\right) \quad (16)$$

$$SE_T = SE_R + SE_A \quad (17)$$

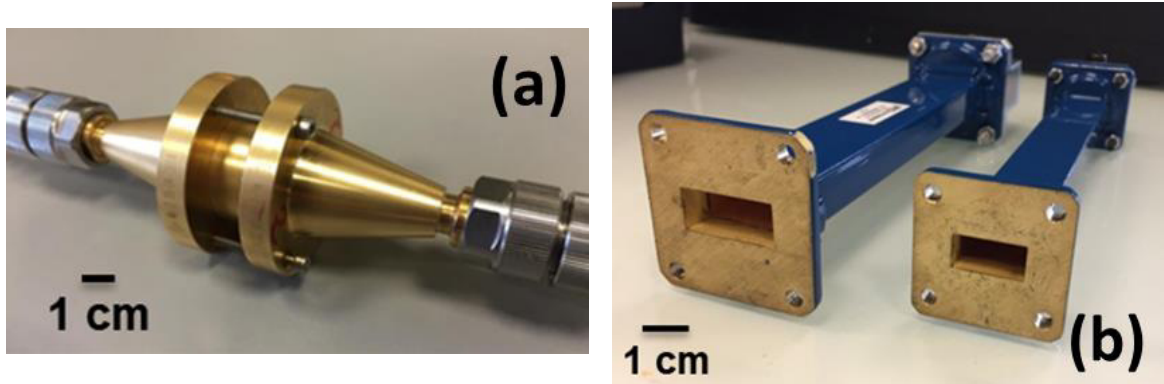


Figure III - 3: Measurement cells employed in our study. (a) Coaxial measurement cell to measure EMI shielding from 50 kHz to 8 GHz. (b) waveguides measuring EMI shielding from 8.2 to 12.4 GHz (left) and from 12.4 to 18 GHz (right).

4. Results and discussions

a. Electrical conductivity of PP—CNT composites

The electrical conductivity values of PP/CNT composites are listed in Table 1 and displayed in Figure 4. Below 0.5 vol% (1 w%) of CNT, the composite is insulating. Above this concentration, close to the percolation threshold, the conductivity increases rapidly and reaches the maximum value of 580 S/m at 10% volume (20% weight) CNT. Xu et al. [40] and Jia et al. [58] got similar results, reporting a percolation threshold of 0.84 vol% CNT and a maximum conductivity of about 200 S/m at 16 vol% CNT, and a percolation threshold of 0.31 vol% CNT, both randomly dispersed in polyethylene. The percolation threshold depends on the aspect ratio of the conductive fillers dispersed in the composite, which is the ratio between the largest and the smallest spatial dimension of the fillers. A high aspect ratio will result in a low percolation threshold, which is a good mean to get electrical conductivity and EMI shielding properties for low filler contents. The aspect ratio of our CNT fillers, with an average diameter of 9.5 nm and a length of 1.5 μm , is thus about 160.

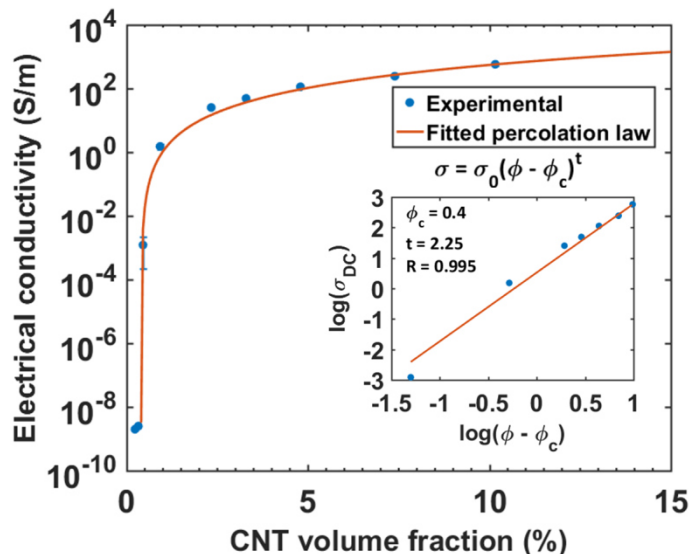


Figure III - 4: DC electrical conductivity (σ) as a function of CNT volume fraction in PP /CNT composites (blue dots). The percolation law obtained from fitting the experimental data is plotted in red.

Table III - 1: CNT volume fraction and the measured DC conductivity of all the conductive polymer composites investigated in this study.

CNT vol%	σ (S/m)
0.25	2.0×10^{-9}
0.35	2.5×10^{-9}
0.5	1.2×10^{-3}
1	1.5
2.5	25
3.5	49
5	110
7.5	240
10	580

A linear decrease in the percolation threshold is expected for conducting “sticks” or elongated inclusions [2,60,61]. Balberg et al. [62] proposed the following relationship for a random isotropic configuration of long sticks with length L and radius r :

$$\left(\frac{L}{r}\right) \varphi_c = 3 \quad (18)$$

Following this equation, a theoretical percolation threshold of 0.95 vol% is predicted for our PP/CNT composites. It is in reasonable agreement with our experimental observations, though a little higher. This could be explained by the fact that CNT are not rigid sticks but may exhibit a non-negligible curvature when dispersed in the polymer matrix [63]. Our experimental results show that the melt blending dispersion of the CNT in our PP matrix is very satisfactory since it gives us a very low percolation threshold, competing with the ones corresponding to solution blending dispersions [53]. It is also important to keep in mind that the samples were shaped by compression moulding, a method that induces a possible filler orientation and enables thereby to reach very low percolation thresholds. However, the most frequently used method for shaping in the plastic industry is the injection moulding, because it has the advantage of being cheap and quick. However, because of the high shear during the process, this method can induce large fillers orientation effects in loaded polymer matrices. These orientation effects can have a negative impact on the percolation threshold that tends to increase and on the composites conductivity that tends to decrease when compared to the composite materials moulded by compression [38,64]. Experimental DC conductivity data are often fitted by an empirical percolation law [53,58] defined as [65]:

$$\sigma = \sigma_0 (\varphi - \varphi_c)^t \text{ with } \varphi > \varphi_c \quad (19)$$

where φ_c is the percolation threshold, σ_0 is a constant related to the intrinsic conductivity of the filler and t a critical exponent dependent on the dimensionality of the conductive network (for 3D network like in our composite materials, it is expected to be equal to 2).

Fitting our experimental data with this percolation law, the following fitting parameters are obtained $\varphi_c = 0.004$, $\sigma_0 = 1.08 \times 10^5$ S/m and $t = 2.25$. The percolation threshold of our PP/CNT composite is 0.4 vol% according to the fitting, in agreement with our experimental observations. The value of σ_0 is quite reasonable, given the intrinsic conductivity of our CNT fillers of 10^6 S/m. The lower value of σ_0 could be attributed to the imperfect electrical contacts between the CNT fillers in the volume of the composite materials [51,52]. The value of t close to 2 is in accordance with the 3-D dimensional nature of our CNT network in the PP matrix. The fitting curve is plotted with the experimental data in Fig. 4.

b. EMI shielding effectiveness of PP—CNT composites in coaxial cell

The EMI shielding effectiveness of PP-CNT composites was measured first in a coaxial cell from 50 MHz to 8 GHz. FM radio, Wi-Fi, Bluetooth, cellphone and GPS waves are examples of applications operating in this wide frequency range [3]. With this type of cell, the sample is exposed to the incidence of a progressive plane EM wave in the far field regime. Examples of SE versus frequency for 5 vol% and 10 vol% CNT composites (1mm thickness) are displayed in Figure 5-a.

As predicted by the theoretical model, the shielding is constant at low frequencies (determined by the reflection regime) and increases above a certain critical frequency (where both reflection and absorption contribution play a role). This behaviour is especially visible for the 10 vol% CNT composite. The shielding effectiveness of this composite is constant (42 dB) at low frequencies (from 50 MHz to 1 GHz) and increases rapidly in the high frequency range, reaching 60 dB at 8 GHz. At this frequency of 8 GHz, the skin depth of this composite material (10 vol% CNT) is equal to 0.23 mm, thus thinner than the sample which has a thickness of 1 mm. This explains the high EMI shielding performance that has been obtained. The theoretical absorption critical frequency f_c (Eq. 8) of this composite is equal to 440 MHz, which is in agreement with the onset of absorption in the experimental curve.

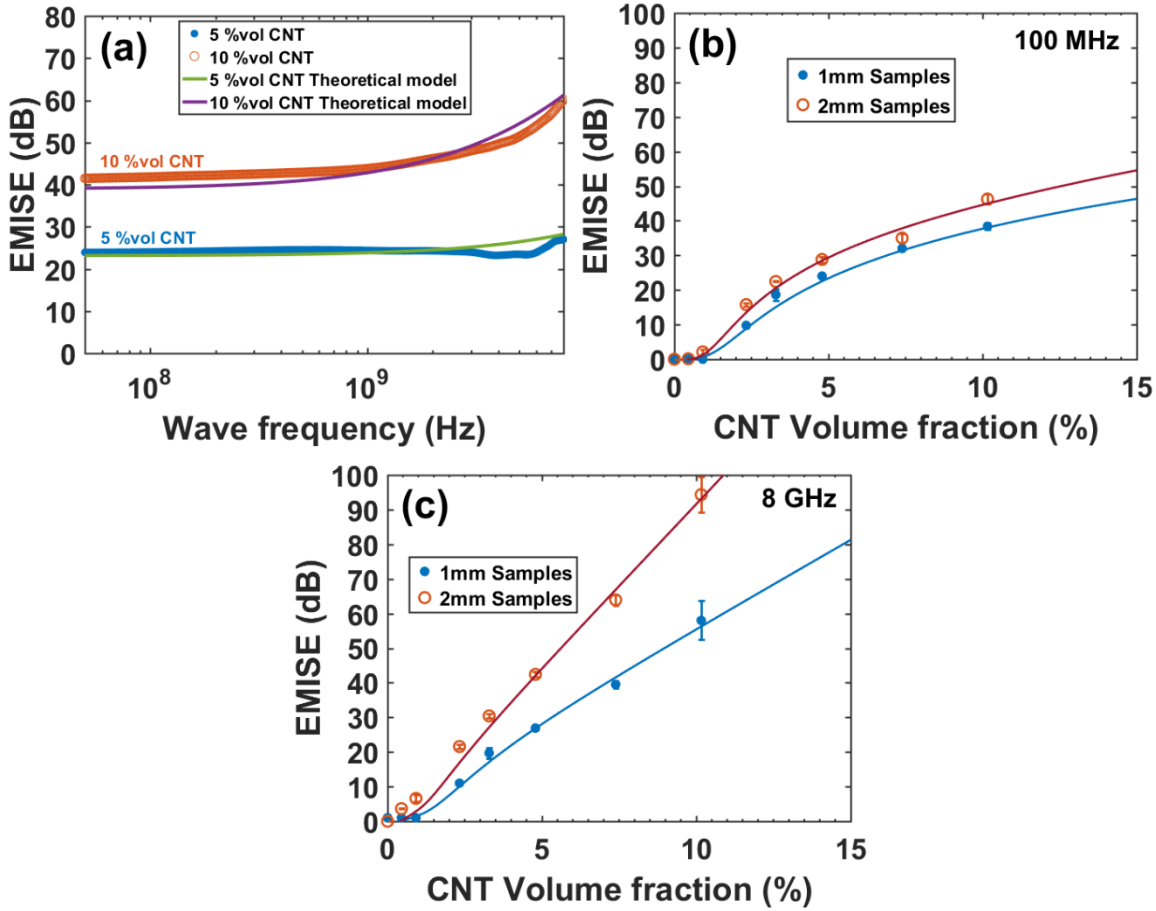


Figure III - 5: EMI Shielding effectiveness of PP/CNT composites measured in the coaxial cell from 50 kHz to 8 GHz. (a) Experimental shielding of 5 and 10% vol. CNT composites as a function of incident wave frequency (thick lines). The experimentally measured conductivity of these composites is used in the theoretical model to get the theoretical shielding curves (thin lines). (b) Experimental shielding of composites as a function of CNT volume fraction (dots) at 100 MHz incident wave frequency. By taking into account the experimental percolation law into the shielding theoretical model gives the theoretical shielding curves plotted as thin lines. (c) Same as before but at 8 GHz incident wave frequency.

The experimental results for 5 vol% CNT show a constant SE on almost the entire frequency range, showing only a reflection regime. For this composite, f_c is equal to 2.2 GHz, which is too high to observe significant absorption before 8 GHz. Taking the experimentally measured conductivities of these two composites, their thickness 1 mm, the relative permittivity of PP $\epsilon_r = 2.2$ and the relative real permeability $\mu_r = 1$, we can plot a theoretical curve of SE in dependence on the wave frequency using Eq. 4-7. The resulting theoretical curves are plotted together with the experimental curves in Fig. 5-a. Within an error of only 2 dB, an excellent agreement is found. The theoretical skin depth of these two composite samples versus in dependence on the incident wave frequency is presented in Fig. S7, page 123, of the Supplementary Information Part. The theoretical skin depth of these two composites decreases with frequency (Eq. 3), indicating that the absorption phenomenon becomes

more important. For a given shield conductivity and thickness, absorption becomes significant when the incident wave frequency is higher than the critical frequency f_c (Eq. 8), or, equivalently, when the skin depth is smaller than the sample thickness. In Figs. 5-b and 5-c, the shielding effectiveness of our PP/CNT composites in dependence on the CNT volume concentration at 100 MHz and 8 GHz for two sample thicknesses (1 and 2 mm) is presented.

At both frequencies, SE increases with the CNT content, as expected since the composite conductivity increases with increasing the CNT content. Similar observations were made in other studies [4,7,24,39]. While being very weak (less than 10 dB) for concentrations close to the percolation threshold, shielding effectiveness for the 10 vol% CNT composite material reaches impressive values of 94 dB at 8 GHz for a sample thickness of 2 mm. This exceptionally high shielding value is due to the excellent electrical conductivity of this composite. As also predicted by the theoretical model, for a given CNT content, the SE is higher at 2 mm thickness than at 1 mm and is higher at 8 GHz than at 100 MHz.

Taking into account the experimental percolation law (Eq. 19) into the theoretical model (Eq. 4-7) with PP $\epsilon_r = 2.2$, $\mu_r = 1$, and using a thickness of 1 or 2 mm enables us to determine the EMI shielding effectiveness in dependence on the CNT volume content at any incident wave frequency. The theoretical curves are plotted with the experimental data in Figs. 5-b and 5-c. The first thing one can notice is that the theoretical model is in good agreement with the experimental data, for both thicknesses and for both frequencies. At 100 MHz the SE increases slowly with the CNT concentration (and so with the electrical conductivity), showing a logarithmic-like behaviour. On contrary, at 8 GHz the SE increases rapidly with CNT concentration, following a rather linear dependence. The difference between two shapes can be explained by considering the mechanisms involved in shielding: at 100 MHz only the simple reflection contributes to shielding whereas both reflection and absorption contributions give rise to shielding at 8 GHz, with absorption being more effective than reflection.

The evolution of the EMI shielding of PP/CNT composites with the sample thickness for three distinct CNT concentrations at 100 MHz and 8 GHz is presented in Figures 6-a and 6-b. As theoretically predicted, a larger thickness gives a higher shielding effectiveness: SE at 100 MHz is lower than at 8 GHz because of the appearance of absorption at high frequencies. A remarkable shielding performance of more than 80 dB is reached by the 7.5 vol% CNT at 8 GHz incident wave frequency. In a similar way to the conductivity variations, the shape of the curves at 100 MHz (Fig. 6-a) and at 8 GHz (Fig. 6-b) are different: slow logarithmic-like increase of SE at 100 MHz due to the shielding mechanism by reflection and a rapid linear increase of SE at 8 GHz due to the highly efficient absorption. The positive influence of the sample thickness on the EMI shielding has been reported in previous studies as well [12,66,67]. Taking the experimental conductivities of the three composites, PP $\epsilon_r = 2.2$ and

$\mu_r = 1$, the theoretical curves according to (Eq. 4-7) are plotted in Figures 6-b and 6-c in dependence on the sample thickness at 100 MHz and 8 GHz. A good agreement is observed with the experimental data measured at different CNT concentrations and at different thicknesses.

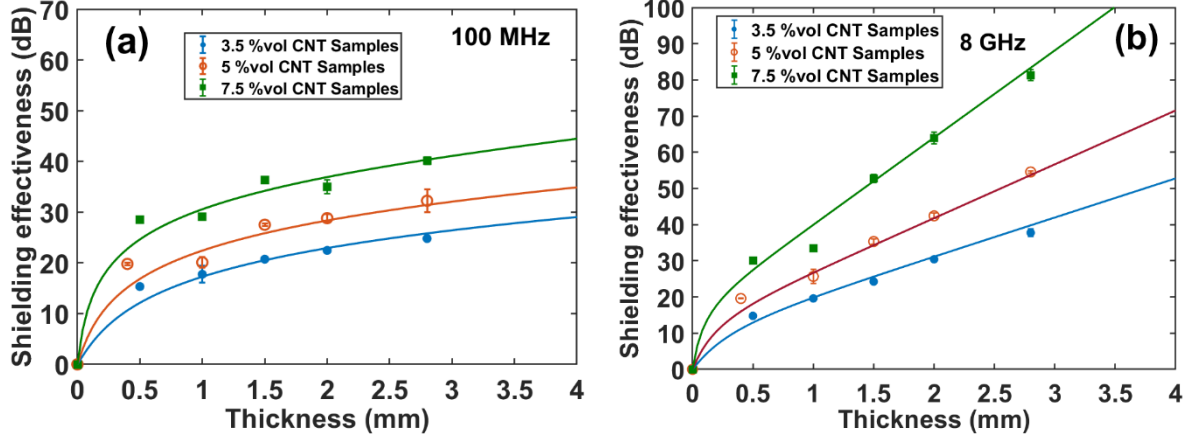


Figure III - 6: EMI Shielding effectiveness of PP/CNT composites as a function of sample thickness, measured in the coaxial cell from 50 KHz to 8 GHz. (a) Measured at 100 MHz wave frequency for three CNT volume fractions (dots). Experimental conductivities of these composites are used in the theoretical model to get the theoretical shielding curves (thin lines). (b) Same as before, but at 8 GHz incident wave frequency.

c. EMI shielding effectiveness of PP—CNT composites in waveguide cells

The EMI shielding effectiveness of PP/CNT composites was also measured in two waveguide cells, for measuring the shielding from 8.2 to 12.4 GHz (X band) and from 12.4 to 18 GHz (K_u band). Satellite communication, weather monitoring, position and speed radars waves can be found in these two frequency bands [3]. In waveguide cells, the sample is put under the incidence of stationary EM waves in the transverse electric regime [68]. The data of the two waveguides are displayed on the same graph, in Fig. 7, in the frequency range between 8.2 – 18 GHz. In Figure 7-a, shielding effectiveness of PP – CNT composite versus incident wave frequency is presented for different CNT concentrations at a constant 1 mm sample thickness. In spite of this moderate thickness, a SE value of 90 dB is reached at 18 GHz for the 10 vol% CNT composite. In the same way as with the coaxial cell, one can note that the shielding effectiveness increases with the incident wave frequency and with the CNT concentration because of wave absorption and the increase of the conductivity. The increase with the frequency is larger for the most concentrated samples in CNT: this is explained by the fact that the higher the conductivity is the more important the absorption is. A similar behaviour was found in previous studies [7,24,39].

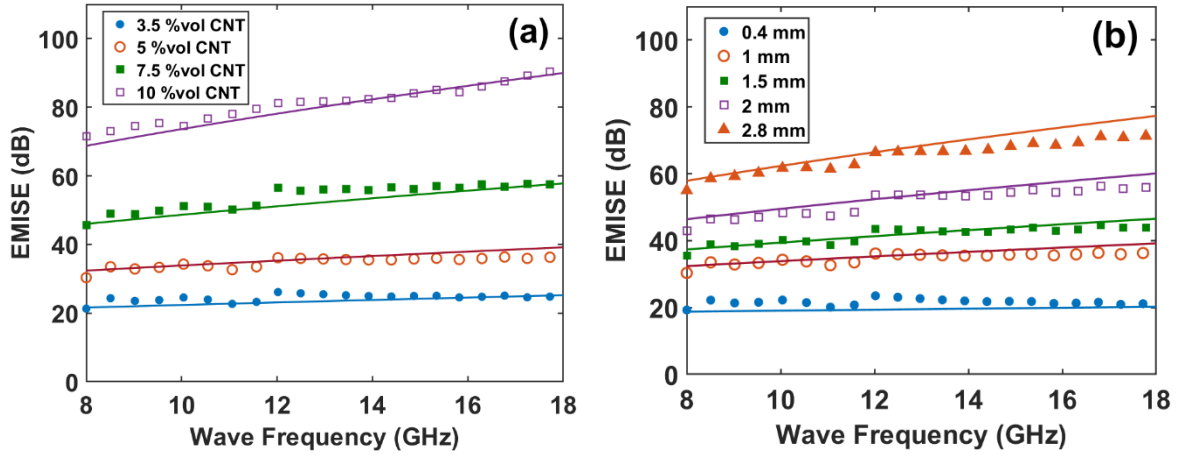


Figure III - 7: EMI Shielding Effectiveness of PP/CNT composites as a function of incident wave frequency measured in the waveguide cells. (a) Concentration dependence: experimental shielding of 1mm-thick samples of four different CNT volume fractions (dots). The experimentally measured conductivity of these composites is used in the theoretical model to get the theoretical shielding curves (thin lines). (b) Thickness dependence: experimental shielding of 5% CNT volume fraction composite at five different sample thicknesses. The experimentally measured conductivity of these composites and the sample thicknesses are used in the theoretical model to get the theoretical shielding curves (thin lines).

In Fig. 7-b, SE of PP – CNT composites versus frequency is shown for different sample thicknesses at a constant CNT concentration of 5 vol%. Even for this rather low CNT content, a non-negligible shielding of 20 dB is found for a film of 0.4 mm thickness while shielding of more than 70 dB is reached at 18 GHz for a sample thickness of 2.8 mm. These results are similar to those obtained by the coaxial cell, and they agree as well with the theoretical predictions. For a given CNT content, EMI shielding increases with sample thickness and incident wave frequency. The higher the thickness is, the more pronounced the increase of shielding with the frequency becomes, due to the more important influence of absorption (Eq. 3, 5 & 8). These phenomena were also reported in other studies [12,66,67]. The theoretical curves of Figs. 7-a and 7-b were plotted versus frequency using the theoretical model (Eq. 4-7) with PP $\epsilon_r = 2.2$, $\mu_r = 1$, and the corresponding values for the sample thickness and conductivity. One more time the theoretical model provides a good fit to the experimental data for all thicknesses and CNT concentrations. Many theoretical calculations were rather successfully in previous studies using a similar theoretical approach [47,48,50,52,53]. At 8 GHz, the SE values measured with the coaxial cell and with the waveguide cell are very close, differing by only a few dB. Thus, those two methods of measuring shielding are compatible and complementary, and can be combined to get a wider frequency range for characterising EMI shielding. Since the wave guide method is most frequently used in the scientific literature, our study enables one to compare our results to those obtained in previous studies [2,3].

The enhanced value of shielding obtained with our PP/CNT composites can be explained by the high intrinsic conductivity of the CNT fillers. In the same time, the interactions between the fillers and the polymer matrix also play an important role. Polypropylene, a hydrophobic and non-polar material, has weak interactions with the CNT fillers which are more hydrophilic and polar due to the partial oxidation of their surface [69,70]. CNT-CNT interactions are thus favourable, leading to good electrical contacts between the fillers and, thus, to an enhanced electrical conductivity and shielding performance.

d. SEM of PP/CNT composites

In order to check the distribution of fillers within the volume of the composite material, SEM investigations have been carried-out for the highest filler concentration used in the present study (10%vol). The SEM images, presented in the Supplementary Information Part (Fig. S8, page 123) clearly indicate a good distribution of fillers, with a negligible presence of aggregates and agglomerates.

e. Advantages and limits of our theoretical model

The experimental data previously presented showed that the theoretical approach developed in current study (Eq. 4-7) is able to describe and predict accurately the shielding behaviour of our PP/CNT composite materials. Furthermore, it is compatible with both the coaxial and waveguide experimental measurements, and allows us thus to compare the experimental and theoretically predicted contributions of the different shielding mechanisms to the total SE. Using Equation 15 and 16, we can determine the experimental reflection SE_{R-exp} and absorption SE_{A-exp} contributions from the scattering S-parameters. The reflection contribution includes both the simple reflection and the multiple internal reflections (they cannot be separated in the measurement). The theoretical reflection SE_{R-th} (the sum of SE_R and SE_M) and absorption SE_{A-th} contributions are calculated from Equation 5-7. The contributions for three different CNT concentrations, three different incident wave frequencies and a constant 2 mm sample thickness are shown in Figure 8.

It is observed that, for a given frequency, both the reflection and absorption contributions increase with the CNT concentration in the same way as the composite conductivity. This is in agreement with the theoretical prediction that conductivity increases both the reflection and the absorption contribution to the shielding effectiveness. Secondly, for a given CNT concentration, the reflection contribution decreases and the absorption contribution increases with increasing frequency,

for both experimental and theoretical curves. This is as well in agreement with our theoretical predictions as indicated in Figure 2-b: the simple reflection contribution decreases with frequency whereas the absorption increases (multiple internal reflections contribution can be neglected considering the fact that the absorption is higher than 10 dB). At 8 GHz (Fig. 8-b) and 18 GHz (Fig. 8-c) the theoretical prediction of reflection and absorption contributions are very close to their experimental counterparts. On contrary, there are important gaps between theoretical and experimental values of contributions at 1 GHz (Fig. 8-a). The model tends to over-evaluate the reflection and under-evaluate the absorption contribution. Although the experimental and theoretical total shielding values at this frequency are in good agreement, slight difficulties in evaluating different shielding contributions become apparent. Nevertheless, the experimental results of shielding contribution measurements are in accordance with previous studies [24,71–73].

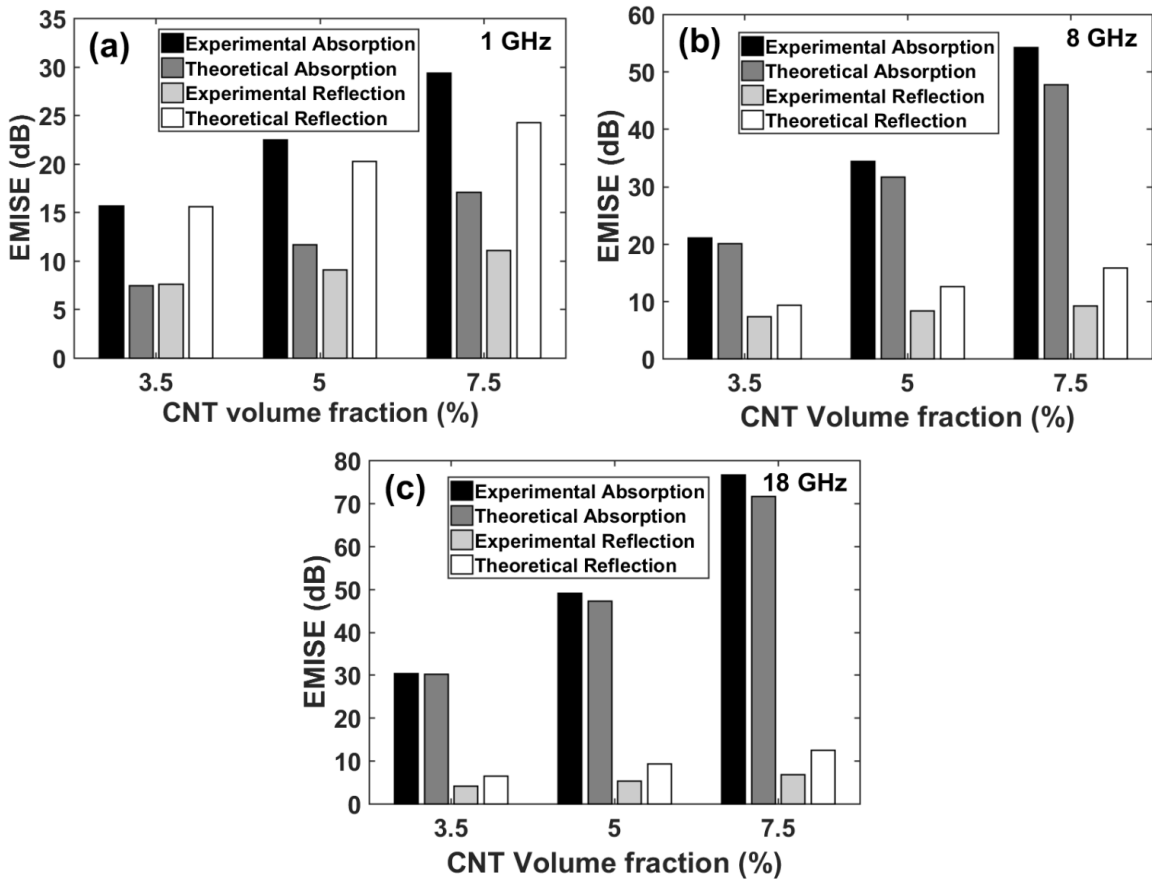


Figure III - 8: EMI shielding mechanism contributions in PP/CNT composites at 2 mm thickness. Experimentally measured and theoretically calculated values of reflection shielding and absorption shielding are compared in composites at three different CNT concentrations. (a) Experimental (coaxial measurement cell) and theoretical shielding contributions at 1 GHz. (b) Experimental (waveguide measurement cell) and theoretical shielding contributions at 8 GHz. (c) As before, at 18 GHz.

In order to generalize our theoretical approach, the shielding effectiveness of a multitude of other composite materials reported in the literature has been predicted according to eqs. 1-4 and compared the experimental results. The composite measured DC conductivity, polymer dielectric permittivity, sample thickness, incident wave frequency and the magnetic permeability were used to calculate the theoretical shielding. To maximize the amount of available data, we chose the 8 GHz incident wave frequency and the 1 and 2 mm sample thicknesses, in order to have identical parameters to our study. Figure 9 shows the theoretical master curves of shielding effectiveness versus composite conductivity for the 1 and 2 mm thicknesses, as well as the experimental data retrieved from the literature.

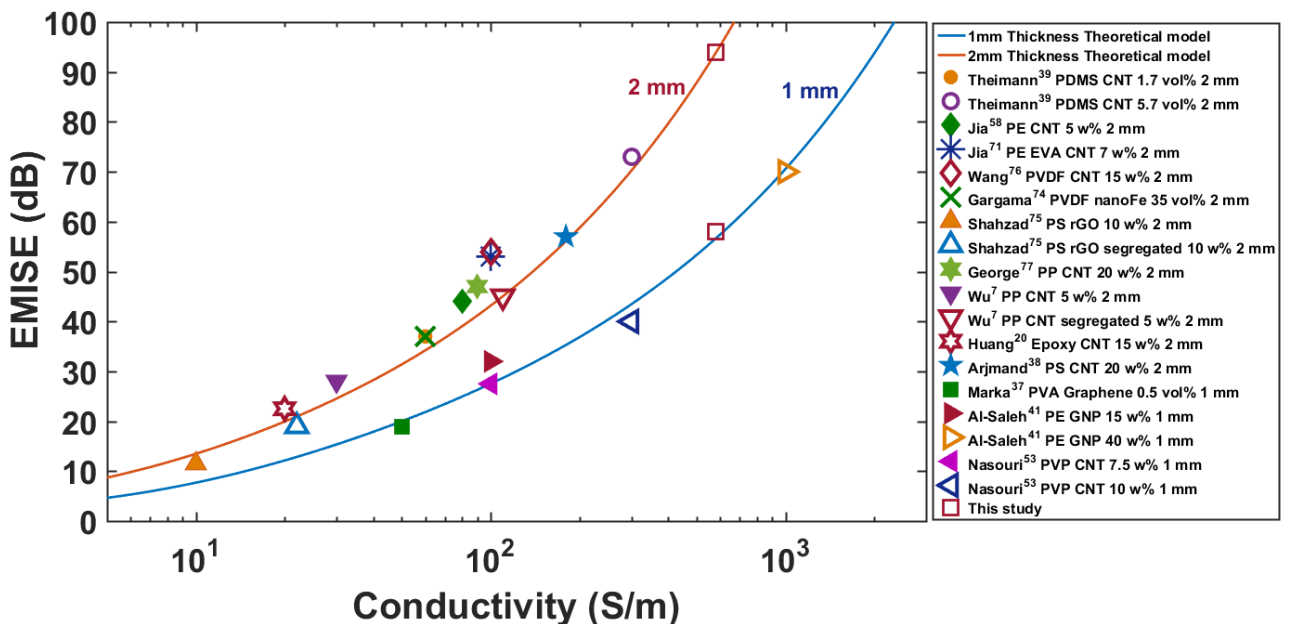


Figure III - 9: Comparison between our theoretical model and EMI shielding data found in the literature at incident wave frequency 8 GHz. The shielding effectiveness is plotted as a function of conductivity. Relative permittivity is set to 2.2, relative permeability to 1 and sample thickness either to 1 or 2 mm in the theoretical curves. The composites matrices, filler concentrations and sample thicknesses of literature data are specified in the legend.

As one can see, the majority of the experimental data found in the literature are close to the theoretical curves, for both thicknesses of 1 and 2 mm. Not only the shielding performance of CNT as conductive fillers but also of nanocrystalline iron [74], reduced graphene oxide [75] (rGO), graphene [37] and graphene nanoplatelets [41] appear to be in agreement with our theoretical calculations. The error is in general less than 5 dB. As one can notice, the composite conductivity is an essential parameter for obtaining EMI shielding properties. SE goes from around 10 dB for both thicknesses at the low conductivity of 10 S/m to very high values of 70 dB for 1 mm and more than 100 dB for 2 mm

sample thickness at 1000 S/m. Yet, some literature data points in Figure 9 are deviating from the theoretical model. It is for instance the case of Wang et al. [76] (PVDF CNT 15 w% 2mm) and Jia et al. [58,71] (PE CNT 5 w% 2 mm and PE EVA CNT 7 w% 2mm). However, their composite materials were heterogeneous: they are segregated structures where the fillers are not homogeneously distributed in the composite and so the electrical and dielectric properties are not uniform in the volume of the investigated samples. Although it could potentially bring enhanced EMI shielding properties to the material, it is not compatible with our theoretical model where homogeneous and isotropic materials are taken into account. This could explain the deviations from the theoretical model observed in these two studies. Not represented on Figure 9, our theoretical model predicts with success the results of countless other studies. Among others, Zhou et al. [14] got a conductivity of 100 S/m and an EMISE of 18 dB at 8 GHz and 0.4 mm thickness with a PMMA loaded with 40 w% mesoporous carbon, and the model predicts 17.5 dB. Kum et al. [4] measured a DC conductivity of 30 S/m and a shielding effectiveness of around 13 dB at 1.5 GHz and 1 mm thickness with a PC loaded with 7 w% CNT, and our model predicts 14 dB. Al-Saleh et al. [27] mixed PS with 2.1 vol% of copper nanowires to get a conductivity of 1000 S/m and EMISE of 34 dB at 12.4 GHz and 0.21 mm thickness and the model predicts 32 dB. Other composites found in the literature and not displayed in figure 9 are listed in Table 2. The experimentally measured SE values and the values theoretically predicted by our theoretical approach are very close, with gaps no larger than 2 dB.

Thus, our theoretical approach is compatible with many other composite materials reported in the literature. This opens the perspective of performing reverse engineering. From specifications of a given EMI shielding application like the required level of shielding effectiveness, the shielding material thickness and the targeted frequency band, one is able to predict the material conductivity that is needed and, in our case, also the amount of CNT needed in the PP matrix. For instance, for a required EMI shielding of 40 dB (99.99% of wave power shielded) at 1 mm thickness in the frequency range between 100 MHz – 18 GHz, the theoretical model predicts a minimum conductivity of 720 S/m. Using the experimental electrical percolation law expressed by (Eq. 19), this value of conductivity would correspond to a CNT concentration of 11.2 vol% (22.4 wt%) in PP matrix. Our experimental results showed that the 10 vol% CNT composite already meets this shielding requirement, leading to a model prediction that is in agreement with our experimental observations. If the same shielding of 40 dB is required in the same frequency range but with a thickness of 2 mm, this would correspond to a composite conductivity of 400 S/m and a CNT concentration of 8.75 vol% (17.5 wt%).

Table III - 2: Characteristics and EMI shielding properties of composites found in the literature and not displayed in Figure 9. Experimental shielding values are compared with values calculated with our theoretical model.

Polymer Matrix	Filler	Filler content	σ (S/m)	EMIS meas. frequency	Sample thickness (mm)	Experimental SE (dB)	Theoretical prediction (dB)	Ref.
PC	CNT	7 w%	30	1.5 GHz	1	13	14	[4]
PP	CB ^a	10 vol %	45	10 GHz	2.8	42	41	[6]
PE	CF ^b	10 vol%	130	1.5 GHz	2	36	35	[8]
PE	Biochar ^c	70 w%	25	1.5 GHz	3	25	23	[9]
PLA	Ag	5.8 vol%	254	8.2 GHz	1.5	49	53	[13]
PMMA	MesC ^d	40 w%	100	8.2 GHz	0.4	18	17.5	[14]
ABS	CNT	5 w%	30	12.4 GHz	2.8	40	36	[17]
PU	CNT	1 w%	10	8.2 GHz	2.5	19	18	[24]
PS	CuNW ^e	2.1 vol%	1000	8 GHz	0.21	34	32	[27]
PE	CNT	16.2 vol%	90	8.2 GHz	2.5	45	48	[40]
PC	CNT	4 w%	6	8.5 GHz	3.5	14.5	16	[66]
PC ABS	CNT	3 w%	10	1.5 GHz	2	8.5	10.5	[78]
PES ^f	CNT	20 w%	500	8.2 GHz	0.5	36	36	[79]
PE	CF	9.4 w%	1250	1.5 GHz	0.8	45	47	[80]
PS	rGO ^g	3.47 vol%	60	8.2 GHz	2.5	41	40	[81]

^aCarbon black, ^bCarbon fiber, ^cBamboo charcoal, ^dMesoporous carbon, ^eCopper nanowires, ^fPolyether sulfone, ^gReduced graphene oxide

5. Conclusion

Light, easily processable, cheap PP/CNT conductive polymer composite materials have been prepared by melt mixing and their EMI shielding properties have been investigated between 1 MHz and 18 GHz by using two different experimental methods (co-axial measurement cell and wave-guide cells). Both measurement methods led to comparable results. A low percolation threshold of only 0.4% and an exceptional EMI shielding performance reaching effectiveness values SE as high as 90 dB at 18 GHz incident wave frequency are reported. The shielding performance of our materials is among the highest effectiveness values reported in the scientific literature so far for materials prepared by melt mixing.

The wave propagation phenomenon is analysed by taking into consideration three different mechanisms of wave/matter interaction (simple reflection, absorption and multiple reflections) in systematic correlation to the electrical properties of our composite materials and the thickness of the investigated samples. This analysis, combined with a model of electrical percolation that describes the conductivity of composite materials, leads to a theoretical approach that shows an excellent agreement to the experimental results obtained for our composite samples but as well for a multitude of other studies reported in the literature, where other polymer matrices and other types of fillers, of different nature, have been investigated.

The deviations between the theory and experiments observed in a few cases were related to a heterogeneous distribution of properties. The theoretical investment necessary to treat heterogeneous properties is very elaborate and is out-of-the scope of the present contribution but remains an important goal of our future studies. The systematic correlation between the shielding effectiveness, the conductivity and sample thickness revealed and validated in our study, both experimentally and theoretically, allows one thus to predictively design materials required to exhibit a specific EMI effectiveness value and operating in a specific frequency range. This can be of significant importance in a multitude of applications where materials having the ability of shielding electromagnetic interference phenomena are demanded.

The 10 vol% CNT composite material reaches the 40 dB (1 mm thickness) project objective. However, shaping of this composite was found to be difficult (injection molding, see Chapter II) and its tensile mechanical properties showed great changes compared to pure PP matrix (see Figure S V – 3, page 191). CNT-based composites are actually limited by the intrinsic conductivity of the fillers, which pushed us toward the study of more conductive fillers: metal materials.

References

- [1] Schulz, R. B., V. C. Plantz and D. R. Brush. "Shielding theory and practice," *IEEE Trans. Electromagn. Compat.* **30**, 187–201 (1988).
- [2] Thomassin, J.-M., C. Jérôme, T. Pardoën, C. Bailly, I. Huynen and C. Detrembleur. "Polymer/carbon based composites as electromagnetic interference (EMI) shielding materials," *Mater. Sci. Eng. R Rep.* **74**, 211–232 (2013).
- [3] Sankaran, S., K. Deshmukh, M. B. Ahamed and S. K. Khadheer Pasha. "Recent advances in electromagnetic interference shielding properties of metal and carbon filler reinforced flexible polymer composites: A review," *Compos. Part Appl. Sci. Manuf.* **114**, 49–71 (2018).
- [4] Kum, C. K., Y.-T. Sung, M. S. Han, W. N. Kim, H. S. Lee, S.-J. Lee and J. Joo. "Effects of morphology on the electrical and mechanical properties of the polycarbonate/multi-walled carbon nanotube composites," *Macromol. Res.* **14**, 456–460 (2006).
- [5] Xing, D., L. Lu, K. S. Teh, Z. Wan, Y. Xie and Y. Tang. "Highly flexible and ultra-thin Ni-plated carbon-fabric/polycarbonate film for enhanced electromagnetic interference shielding," *Carbon* **132**, 32–41 (2018).
- [6] Al-Saleh, M. H. and U. Sundararaj. "X-band EMI shielding mechanisms and shielding effectiveness of high structure carbon black/polypropylene composites," *J. Phys. Appl. Phys.* **46**, 035304 (2013).
- [7] Wu, H.-Y., L.-C. Jia, D.-X. Yan, J. Gao, X.-P. Zhang, P.-G. Ren and Z.-M. Li. "Simultaneously improved electromagnetic interference shielding and mechanical performance of segregated carbon nanotube/polypropylene composite via solid phase molding," *Compos. Sci. Technol.* **156**, 87–94 (2018).
- [8] Al-Saleh, M. H., G. A. Gelves and U. Sundararaj. "Carbon nanofiber/polyethylene nanocomposite: Processing behavior, microstructure and electrical properties," *Mater. Des. 1980-2015* **52**, 128–133 (2013).
- [9] Li, S., A. Huang, Y.-J. Chen, D. Li and L.-S. Turng. "Highly filled biochar/ultra-high molecular weight polyethylene/linear low density polyethylene composites for high-performance electromagnetic interference shielding," *Compos. Part B Eng.* **153**, 277–284 (2018).
- [10] Maiti, S., N. K. Shrivastava, S. Suin and B. B. Khatua. "Polystyrene/MWCNT/Graphite Nanoplate Nanocomposites: Efficient Electromagnetic Interference Shielding Material through Graphite Nanoplate–MWCNT–Graphite Nanoplate Networking," *ACS Appl. Mater. Interfaces* **5**, 4712–4724 (2013).
- [11] Wu, K., L. Wu, W. Yang, S. Chai, F. Chen and Q. Fu. "Largely enhanced electrical properties of polymer composites via the combined effect of volume exclusion and synergy," *RSC Adv.* **6**, 51900–51907 (2016).
- [12] Cui, C.-H., D.-X. Yan, H. Pang, X. Xu, L.-C. Jia and Z.-M. Li. "Formation of a Segregated Electrically Conductive Network Structure in a Low-Melt-Viscosity Polymer for Highly Efficient Electromagnetic Interference Shielding," *ACS Sustain. Chem. Eng.* **4**, 4137–4145 (2016).
- [13] Zhang, K., H.-O. Yu, K.-X. Yu, Y. Gao, M. Wang, J. Li and S. Guo. "A facile approach to constructing efficiently segregated conductive networks in poly(lactic acid)/silver nanocomposites via silver plating on microfibers for electromagnetic interference shielding," *Compos. Sci. Technol.* **156**, 136–143 (2018).
- [14] Zhou, H., J. Wang, J. Zhuang and Q. Liu. "Synthesis and electromagnetic interference shielding effectiveness of ordered mesoporous carbon filled poly(methyl methacrylate) composite films," *RSC Adv.* **3**, 23715 (2013).
- [15] Zhang, H., G. Zhang, M. Tang, L. Zhou, J. Li, X. Fan, X. Shi and J. Qin. "Synergistic effect of carbon nanotube and graphene nanoplates on the mechanical, electrical and electromagnetic interference shielding properties of polymer composites and polymer composite foams," *Chem. Eng. J.* **353**, 381–393 (2018).

- [16] Jyoti, J., S. Basu, B. P. Singh and S. R. Dhakate. "Superior mechanical and electrical properties of multiwall carbon nanotube reinforced acrylonitrile butadiene styrene high performance composites," *Compos. Part B Eng.* **83**, 58–65 (2015).
- [17] Sachdev, V. K., S. K. Sharma, M. Tomar, V. Gupta and R. P. Tandon. "EMI shielding of MWCNT/ABS nanocomposites in contrast to graphite/ABS composites and MWCNT/PS nanocomposites," *RSC Adv.* **6**, 45049–45058 (2016).
- [18] Kumar, G. S., D. Vishnupriya, A. Joshi, S. Datar and T. U. Patro. "Electromagnetic interference shielding in 1–18 GHz frequency and electrical property correlations in poly(vinylidene fluoride)–multi-walled carbon nanotube composites," *Phys. Chem. Chem. Phys.* **17**, 20347–20360 (2015).
- [19] Ma, X., B. Shen, L. Zhang, Y. Liu, W. Zhai and W. Zheng. "Porous superhydrophobic polymer/carbon composites for lightweight and self-cleaning EMI shielding application," *Compos. Sci. Technol.* **158**, 86–93 (2018).
- [20] Huang, Y., N. Li, Y. Ma, D. Feng, F. Li, X. He, X. Lin, H. Gao and Y. Chen. "The influence of single-walled carbon nanotube structure on the electromagnetic interference shielding efficiency of its epoxy composites," *Carbon* **45**, 1614–1621 (2007).
- [21] Wang, L. *et al.* "Electromagnetic interference shielding MWCNT-Fe₃O₄@Ag/epoxy nanocomposites with satisfactory thermal conductivity and high thermal stability," *Carbon* **141**, 506–514 (2019).
- [22] Park, S.-H., E.-H. Cho, J. Sohn, P. Theilmann, K. Chu, S. Lee, Y. Sohn, D. Kim and B. Kim. "Design of multi-functional dual hole patterned carbon nanotube composites with superhydrophobicity and durability," *Nano Res.* **6**, 389–398 (2013).
- [23] Bera, R. *et al.* "An approach to widen the electromagnetic shielding efficiency in PDMS/ferrous ferric oxide decorated RGO–SWCNH composite through pressure induced tunability," *Chem. Eng. J.* **335**, 501–509 (2018).
- [24] Gupta, T. K., B. P. Singh, S. Teotia, V. Katyal, S. R. Dhakate and R. B. Mathur. "Designing of multiwalled carbon nanotubes reinforced polyurethane composites as electromagnetic interference shielding materials," *J. Polym. Res.* **20**, 169 (2013).
- [25] Ghosh, S., S. Ganguly, S. Remanan, S. Mondal, S. Jana, P. K. Maji, N. Singha and N. Ch. Das. "Ultra-light weight, water durable and flexible highly electrical conductive polyurethane foam for superior electromagnetic interference shielding materials," *J. Mater. Sci. Mater. Electron.* **29**, 10177–10189 (2018).
- [26] Ameli, A., M. Nofar, S. Wang and C. B. Park. "Lightweight Polypropylene/Stainless-Steel Fiber Composite Foams with Low Percolation for Efficient Electromagnetic Interference Shielding," *ACS Appl. Mater. Interfaces* **6**, 11091–11100 (2014).
- [27] Al-Saleh, M. H., G. A. Gelves and U. Sundararaj. "Copper nanowire/polystyrene nanocomposites: Lower percolation threshold and higher EMI shielding," *Compos. Part Appl. Sci. Manuf.* **42**, 92–97 (2011).
- [28] Ravindren, R., S. Mondal, K. Nath and N. C. Das. "Prediction of electrical conductivity, double percolation limit and electromagnetic interference shielding effectiveness of copper nanowire filled flexible polymer blend nanocomposites," *Compos. Part B Eng.* **164**, 559–569 (2019).
- [29] Ma, J., K. Wang and M. Zhan. "A comparative study of structure and electromagnetic interference shielding performance for silver nanostructure hybrid polyimide foams," *RSC Adv.* **5**, 65283–65296 (2015).
- [30] Pawar, S. P., D. A. Marathe, K. Pattabhi and S. Bose. "Electromagnetic interference shielding through MWNT grafted Fe₃O₄ nanoparticles in PC/SAN blends," *J. Mater. Chem. A* **3**, 656–669 (2015).
- [31] Nasouri, K. and A. M. Shoushtari. "Fabrication of magnetite nanoparticles/polyvinylpyrrolidone composite nanofibers and their application as electromagnetic interference shielding material," *J. Thermoplast. Compos. Mater.* **31**, 431–446 (2018).

- [32] Das, N. C., D. Khastgir, T. K. Chaki and A. Chakraborty. "Electromagnetic interference shielding effectiveness of carbon black and carbon fibre filled EVA and NR based composites," *Compos. Part Appl. Sci. Manuf.* **31**, 1069–1081 (2000).
- [33] Ravindren, R., S. Mondal, P. Bhawal, Shek. M. N. Ali and N. C. Das. "Superior electromagnetic interference shielding effectiveness and low percolation threshold through the preferential distribution of carbon black in the highly flexible polymer blend composites," *Polym. Compos.* **40**, 1404–1418 (2019).
- [34] Jiang, X., D.-X. Yan, Y. Bao, H. Pang, X. Ji and Z.-M. Li. "Facile, green and affordable strategy for structuring natural graphite/polymer composite with efficient electromagnetic interference shielding," *RSC Adv.* **5**, 22587–22592 (2015).
- [35] Zhou, H., H. Deng, L. Zhang, Z. Wu, S. Deng, W. Yang, Q. Zhang, F. Chen and Q. Fu. "Toward multi-functional polymer composites through selectively distributing functional fillers," *Compos. Part Appl. Sci. Manuf.* **82**, 20–33 (2016).
- [36] Chauhan, S. S., M. Abraham and V. Choudhary. "Superior EMI shielding performance of thermally stable carbon nanofiber/poly(ether-ketone) composites in 26.5–40 GHz frequency range," *J. Mater. Sci.* **51**, 9705–9715 (2016).
- [37] Marka, S. K., B. Sindam, K. C. James Raju and V. V. S. S. Srikanth. "Flexible few-layered graphene/poly vinyl alcohol composite sheets: synthesis, characterization and EMI shielding in X-band through the absorption mechanism," *RSC Adv.* **5**, 36498–36506 (2015).
- [38] Arjmand, M., T. Apperley, M. Okniewski and U. Sundararaj. "Comparative study of electromagnetic interference shielding properties of injection molded versus compression molded multi-walled carbon nanotube/polystyrene composites," *Carbon* **50**, 5126–5134 (2012).
- [39] Theilmann, P., D.-J. Yun, P. Asbeck and S.-H. Park. "Superior electromagnetic interference shielding and dielectric properties of carbon nanotube composites through the use of high aspect ratio CNTs and three-roll milling," *Org. Electron.* **14**, 1531–1537 (2013).
- [40] Xu, L., L.-C. Jia, D.-X. Yan, P.-G. Ren, J.-Z. Xu and Z.-M. Li. "Efficient electromagnetic interference shielding of lightweight carbon nanotube/polyethylene composites via compression molding plus salt-leaching," *RSC Adv.* **8**, 8849–8855 (2018).
- [41] Al-Saleh, M. H. "Electrical and electromagnetic interference shielding characteristics of GNP/UHMWPE composites," *J. Phys. Appl. Phys.* **49**, 195302 (2016).
- [42] Hamidinejad, M., B. Zhao, A. Zandieh, N. Moghimian, T. Filleter and C. B. Park. "Enhanced Electrical and Electromagnetic Interference Shielding Properties of Polymer–Graphene Nanoplatelet Composites Fabricated via Supercritical-Fluid Treatment and Physical Foaming," *ACS Appl. Mater. Interfaces* **10**, 30752–30761 (2018).
- [43] Kuester, S., N. R. Demarquette, J. C. Ferreira, B. G. Soares and G. M. O. Barra. "Hybrid nanocomposites of thermoplastic elastomer and carbon nanoadditives for electromagnetic shielding," *Eur. Polym. J.* **88**, 328–339 (2017).
- [44] Sharma, M., D. Singh, A. Menon, G. Madras and S. Bose. "Suppressing Electromagnetic Radiation by Trapping Ferrite Nanoparticles and Carbon Nanotubes in Hierarchical Nanoporous Structures Designed by Crystallization-Induced Phase Separation," *ChemistrySelect* **3**, 1189–1201 (2018).
- [45] Zhao, B., S. Wang, C. Zhao, R. Li, S. M. Hamidinejad, Y. Kazemi and C. B. Park. "Synergism between carbon materials and Ni chains in flexible poly(vinylidene fluoride) composite films with high heat dissipation to improve electromagnetic shielding properties," *Carbon* **127**, 469–478 (2018).
- [46] Kim, S. et al. "Electromagnetic Interference (EMI) Transparent Shielding of Reduced Graphene Oxide (RGO) Interleaved Structure Fabricated by Electrophoretic Deposition," *ACS Appl. Mater. Interfaces* **6**, 17647–17653 (2014).
- [47] Nhan, H. N., M. Jean-Louis and W. Jean-Luc. "Modeling of Electromagnetic Shielding Effectiveness of Multilayer Conducting Composites in the Microwave Band," in *2006 First International Conference on Communications and Electronics* 482–485 (IEEE, 2006). doi:10.1109/CCE.2006.350874.

- [48] Liu, Z., G. Bai, Y. Huang, Y. Ma, F. Du, F. Li, T. Guo and Y. Chen. "Reflection and absorption contributions to the electromagnetic interference shielding of single-walled carbon nanotube/polyurethane composites," *Carbon* **45**, 821–827 (2007).
- [49] Peng, Z., J. Peng, Y. Peng and J. Wang. "Complex conductivity and permittivity of single wall carbon nanotubes/polymer composite at microwave frequencies: A theoretical estimation," *Sci. Bull.* **53**, 3497–3504 (2008).
- [50] Al-Saleh, M. H. and U. Sundararaj. "Electromagnetic interference shielding mechanisms of CNT/polymer composites," *Carbon* **47**, 1738–1746 (2009).
- [51] Xia, X., Y. Wang, Z. Zhong and G. J. Weng. "A theory of electrical conductivity, dielectric constant, and electromagnetic interference shielding for lightweight graphene composite foams," *J. Appl. Phys.* **120**, 085102 (2016).
- [52] Xia, X., A. D. Mazzeo, Z. Zhong and G. J. Weng. "An X-band theory of electromagnetic interference shielding for graphene-polymer nanocomposites," *J. Appl. Phys.* **122**, 025104 (2017).
- [53] Nasouri, K., A. M. Shoushtari and M. R. M. Mojtabaei. "Theoretical and experimental studies on EMI shielding mechanisms of multi-walled carbon nanotubes reinforced high performance composite nanofibers," *J. Polym. Res.* **23**, 71 (2016).
- [54] Sun, J., W. Wang and Q. Yue. "Review on Microwave-Matter Interaction Fundamentals and Efficient Microwave-Associated Heating Strategies," *Materials* **9**, 231 (2016).
- [55] Biswas, S., G. P. Kar and S. Bose. "Microwave absorbers designed from PVDF/SAN blends containing multiwall carbon nanotubes anchored cobalt ferrite via a pyrene derivative," *J. Mater. Chem. A* **3**, 12413–12426 (2015).
- [56] Joo, J. and A. J. Epstein. "Electromagnetic radiation shielding by intrinsically conducting polymers," *Appl. Phys. Lett.* **65**, 2278–2280 (1994).
- [57] Shacklette, L. W., N. F. Colaneri' and P. O. Box. "EMI SHIELDING MEASUREMENTS OF CONDUCTIVE POLYMER BLENDS," *IEEE Trans. Instrum. Meas.* **41**, 291–297 (1992).
- [58] Jia, L.-C., D.-X. Yan, C.-H. Cui, X. Jiang, X. Ji and Z.-M. Li. "Electrically conductive and electromagnetic interference shielding of polyethylene composites with devisable carbon nanotube networks," *J. Mater. Chem. C* **3**, 9369–9378 (2015).
- [59] Kaiser, K. L. "*Electromagnetic Shielding*" (CRC Press, 2005).
- [60] Lagarkov, A. N. and A. K. Sarychev. "Electromagnetic properties of composites containing elongated conducting inclusions," *Phys. Rev. B* **53**, 6318–6336 (1996).
- [61] Grimes, C. A., C. Mungle, D. Kouzoudis, S. Fang and P. C. Eklund. "The 500 MHz to 5.50 GHz complex permittivity spectra of single-wall carbon nanotube-loaded polymer composites," *Chem. Phys. Lett.* **319**, 460–464 (2000).
- [62] Balberg, I., C. H. Anderson, S. Alexander and N. Wagner. "Excluded volume and its relation to the onset of percolation," *Phys. Rev. B* **30**, 3933–3943 (1984).
- [63] Rodney, D., M. Fivel and R. Dendievel. "Discrete Modeling of the Mechanics of Entangled Materials," *Phys. Rev. Lett.* **95**, 108004 (2005).
- [64] Yu, F., H. Deng, Q. Zhang, K. Wang, C. Zhang, F. Chen and Q. Fu. "Anisotropic multilayer conductive networks in carbon nanotubes filled polyethylene/polypropylene blends obtained through high speed thin wall injection molding," *Polymer* **54**, 6425–6436 (2013).
- [65] Kirkpatrick, S. "Percolation and Conduction," *Rev. Mod. Phys.* **45**, 574–588 (1973).
- [66] Karimi, P., M. Ostoj Starzewski and I. Jasiuk. "Experimental and computational study of shielding effectiveness of polycarbonate carbon nanocomposites," *J. Appl. Phys.* **120**, 145103 (2016).

- [67] Pande, S., A. Chaudhary, D. Patel, B. P. Singh and R. B. Mathur. "Mechanical and electrical properties of multiwall carbon nanotube/polycarbonate composites for electrostatic discharge and electromagnetic interference shielding applications," *RSC Adv.* **4**, 13839 (2014).
- [68] Marcuvitz, N. and M. I. of T. R. Laboratory. "Waveguide Handbook" (IET, 1951).
- [69] Akbar, S., E. Beyou, P. Chaumont and F. Melis. "Effect of a Nitroxyle-Based Radical Scavenger on Nanotube Functionalisation with Pentadecane: A Model Compound Study for Polyethylene Grafting onto MWCNTs," *Macromol. Chem. Phys.* **211**, 2396–2406 (2010).
- [70] Farzi, G., S. Akbar, E. Beyou, P. Cassagnau and F. Melis. "Effect of radical grafting of tetramethylpentadecane and polypropylene on carbon nanotubes' dispersibility in various solvents and polypropylene matrix," *Polymer* **50**, 5901–5908 (2009).
- [71] Jia, L.-C., D.-X. Yan, C.-H. Cui, X. Ji and Z.-M. Li. "A Unique Double Percolated Polymer Composite for Highly Efficient Electromagnetic Interference Shielding," *Macromol. Mater. Eng.* **301**, 1232–1241 (2016).
- [72] Yu, W.-C., J.-Z. Xu, Z.-G. Wang, Y.-F. Huang, H.-M. Yin, L. Xu, Y.-W. Chen, D.-X. Yan and Z.-M. Li. "Constructing highly oriented segregated structure towards high-strength carbon nanotube/ultrahigh-molecular-weight polyethylene composites for electromagnetic interference shielding," *Compos. Part Appl. Sci. Manuf.* **110**, 237–245 (2018).
- [73] Sachdev, V. K., S. Bhattacharya, K. Patel, S. K. Sharma, N. C. Mehra and R. P. Tandon. "Electrical and EMI shielding characterization of multiwalled carbon nanotube/polystyrene composites," *J. Appl. Polym. Sci.* **131**, n/a-n/a (2014).
- [74] Gargama, H., A. K. Thakur and S. K. Chaturvedi. "Polyvinylidene fluoride/nanocrystalline iron composite materials for EMI shielding and absorption applications," *J. Alloys Compd.* **654**, 209–215 (2016).
- [75] Shahzad, F., S. H. Lee, S. M. Hong and C. M. Koo. "Segregated reduced graphene oxide polymer composite as a high performance electromagnetic interference shield," *Res. Chem. Intermed.* **44**, 4707–4719 (2018).
- [76] Wang, H., K. Zheng, X. Zhang, X. Ding, Z. Zhang, C. Bao, L. Guo, L. Chen and X. Tian. "3D network porous polymeric composites with outstanding electromagnetic interference shielding," *Compos. Sci. Technol.* **125**, 22–29 (2016).
- [77] George, G. et al. "Morphological, dielectric, tunable electromagnetic interference shielding and thermal characteristics of multiwalled carbon nanotube incorporated polymer nanocomposites: A facile, environmentally benign and cost effective approach realized via polymer lat," *Polym. Compos.* **39**, E1169–E1183 (2018).
- [78] Han, I.-S., Y. K. Lee, H. S. Lee, H. G. Yoon and W. N. Kim. "Effects of multi-walled carbon nanotube (MWCNT) dispersion and compatibilizer on the electrical and rheological properties of polycarbonate/poly(acrylonitrile–butadiene–styrene)/MWCNT composites," *J. Mater. Sci.* **49**, 4522–4529 (2014).
- [79] Abbas, N. and H. T. Kim. "Multi-walled carbon nanotube/polyethersulfone nanocomposites for enhanced electrical conductivity, dielectric properties and efficient electromagnetic interference shielding at low thickness," *Macromol. Res.* **24**, 1084–1090 (2016).
- [80] Cabrera, E. D., S. Ko, X. Ouyang, E. Straus, L. J. Lee and J. M. Castro. "Technical feasibility of a new approach to electromagnetic interference (EMI) shielding of injection molded parts using in-mold coated (IMC) nanopaper," *J. Polym. Eng.* **34**, 739–746 (2014).
- [81] Yan, D.-X., H. Pang, B. Li, R. Vajtai, L. Xu, P.-G. Ren, J.-H. Wang and Z.-M. Li. "Structured Reduced Graphene Oxide/Polymer Composites for Ultra-Efficient Electromagnetic Interference Shielding," *Adv. Funct. Mater.* **25**, 559–566 (2015).

Supplementary Information

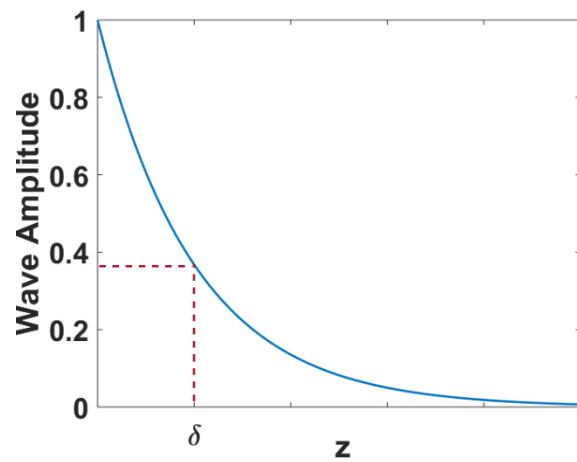


Figure S III - 1: EM wave relative amplitude versus distance of penetration z within a sample of skin depth δ .

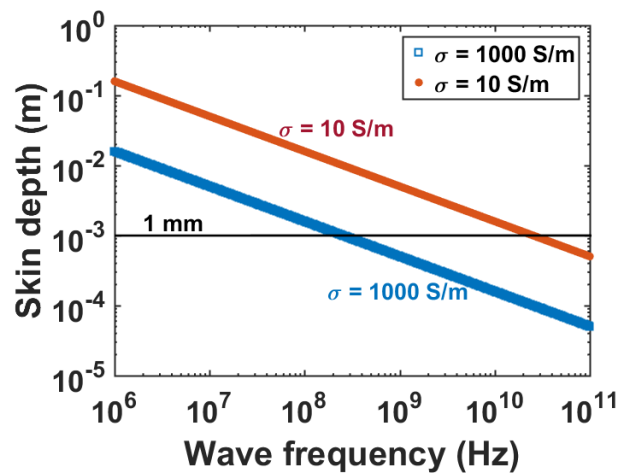


Figure S III - 2: Theoretical absorption characteristic length or skin depth versus the incident wave frequency for two materials of thickness 1 mm, dielectric permittivity $\epsilon = 1$, magnetic permeability $\mu = 1$ and different values of electrical conductivity ($\sigma = 1000 \text{ S/m}$ and $\sigma = 10 \text{ S/m}$, as indicated). The black line is a guide for the eyes to emphasize the critical frequency at which the material skin depth becomes equal to the material thickness.

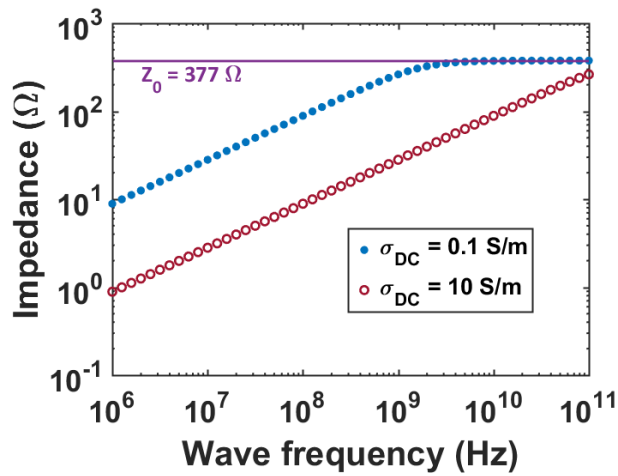


Figure S III - 3: Electromagnetic wave impedance versus wave frequency when the wave is propagating in materials with relative permittivity $\epsilon' = 1$, magnetic permeability $\mu' = 1$ and two different values of electrical conductivity ($\sigma = 0.1 \text{ S/m}$ and $\sigma = 10 \text{ S/m}$, as indicated). The purple line is a guide for the eyes corresponding the air impedance of 377Ω .

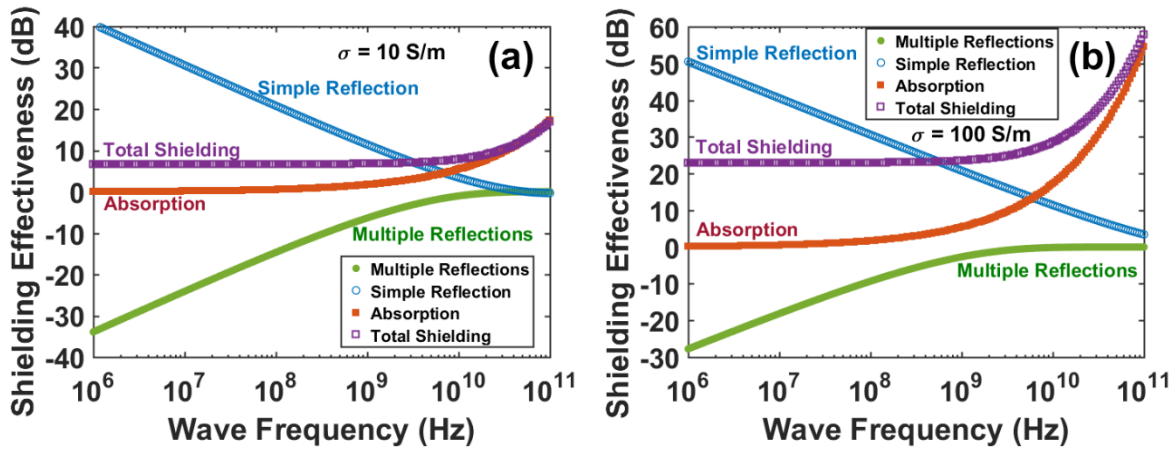


Figure S III - 4: Theoretical total shielding and contributions to total EMI shielding of each of the shielding mechanisms of materials with thickness $d = 1 \text{ mm}$, relative dielectric permittivity $\epsilon' = 1$, magnetic permeability $\mu' = 1$, and two different values of electrical conductivity: (a) $\sigma = 10 \text{ S/m}$ and (b) $\sigma = 100 \text{ S/m}$.

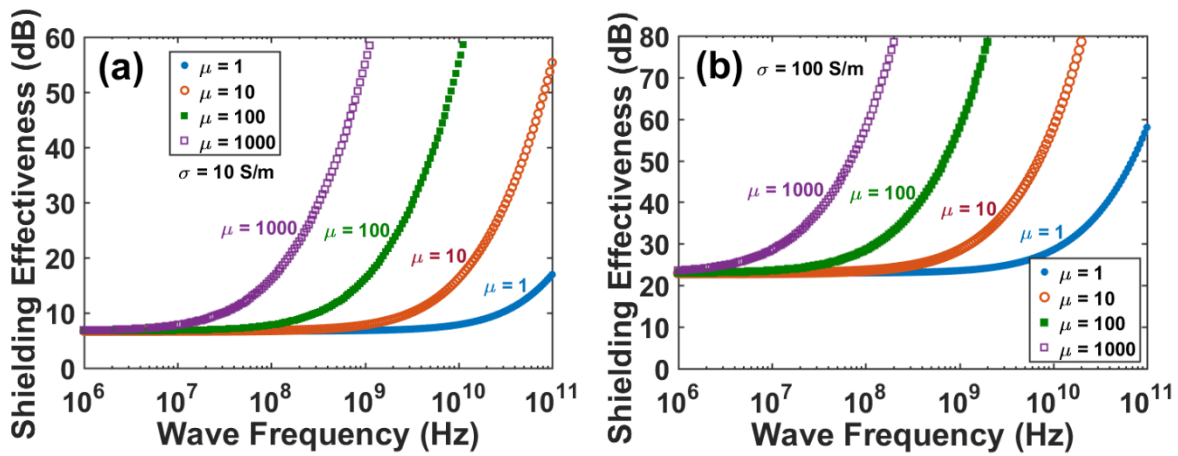


Figure S III - 5: (a) EMI Shielding effectiveness versus incident wave frequency for materials of thickness $d = 1 \text{ mm}$, relative dielectric permittivity $\epsilon' = 1$, electrical conductivity $\sigma = 10 \text{ S/m}$ and four different values of relative magnetic permeability $\mu' = 1, 10, 100$ or 1000 . (b) Same as before, but with an electrical conductivity of $\sigma = 100 \text{ S/m}$.

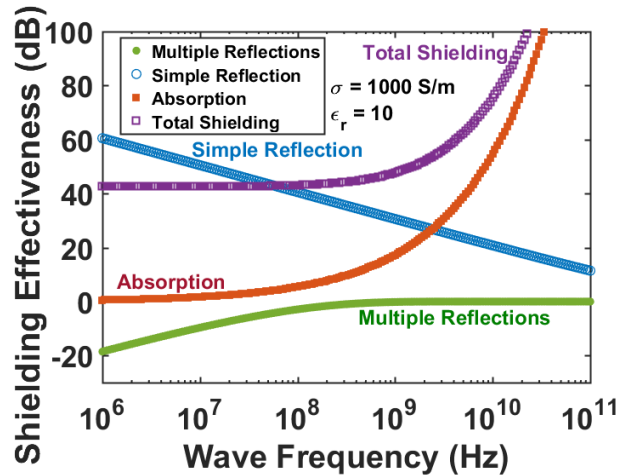


Figure S III - 6: Theoretical total shielding and contributions to total EMI shielding of each of the shielding mechanisms for the material as in Fig. 2b (thus $d = 1 \text{ mm}$, $\mu = 1$, $\sigma = 1000 \text{ S/m}$) but with an increased relative dielectric permittivity $\epsilon_r' = 10$. No changes are observed as compared to Figure 2-b.

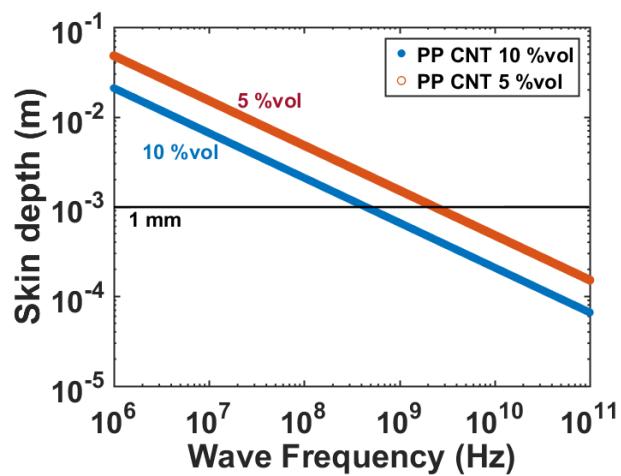


Figure S III - 7: Theoretical skin depth versus the incident wave frequency for the PP/CNT composites of concentration 5 and 10 %vol. These curves were calculated from the experimental conductivity 110 S/m for 5 %vol CNT and 580 S/m for 10% vol. The black line is a guide for the eyes to emphasize the critical frequency at which the material skin depth becomes equal to the material thickness.

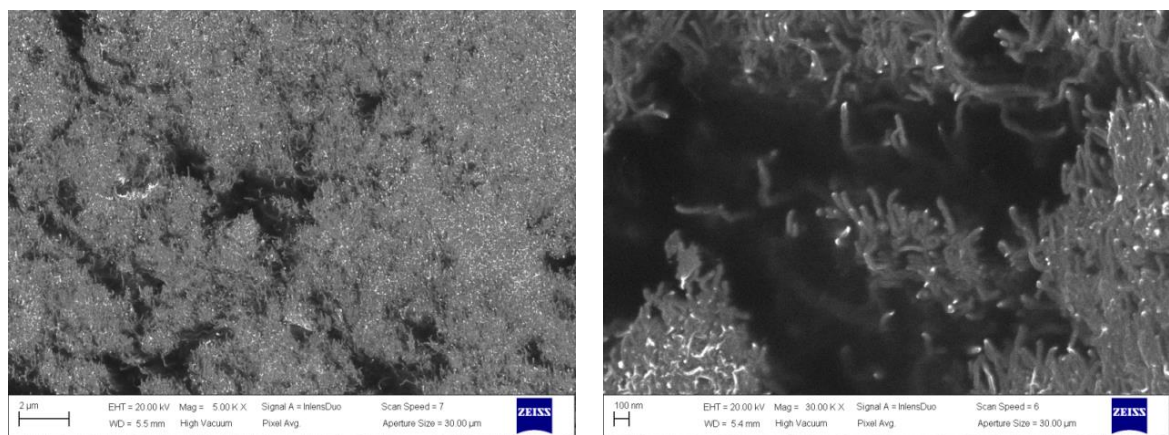


Figure S III - 8: SEM images of the PP/CNT composite at 10 %vol CNT at x5000 magnification (left) and x30,000 magnification (right).

Chapter IV. Study of liquid metal as a potential candidate for highly conductive composite filler

Chapter IV. Study of liquid metal as a potential candidate for highly conductive composite filler

Context

The previously developed EMI shielding theoretical model predicts a shielding effectiveness of 40 dB at 1 mm shield thickness and 100 MHz and higher wave frequency (project objective) for a composite material conductivity of 600 S.m^{-1} . This value was barely reached by the most concentrated PP – CNT composite (10 vol% CNT, masterbatch) which also suffers from processing difficulties (injection molding) and great changes of mechanical properties compared to the pure PP resin. This type of composite material is actually limited by the intrinsic conductivity of CNT. The use of a more conductive filler is then necessary to reach the project goals. Metal fillers are the ideal candidates as testifies the high shielding effectiveness values reported in the literature (Chapter I). The high density of this kind of filler requires minimal filler concentration in the composite and hence the use of strategies to lower the electrical percolation threshold. A notable difference between CNT and certain metals (tin, gallium) is the possibility to have the metal in liquid state over the typical polymer processing temperature range. In these works, we wanted to explore the possibility of processing molten PP with metals (tin and eutectic SnAgCu alloy) in their liquid state to get a high conductivity composite material. The two liquids turned out to be incompatible as they completely separated before the materials solidification. The use of a supplementary percolated solid phase of high surface tension (ferrite or magnesite), so to have favored interactions with the liquid metal, was unsuccessful as well. Our study then focuses on rheological measurements to assess the viscosity ratio and interfacial tension between these two highly incompatible materials.

Abstract

Using the retraction method of a deformed drop, the interfacial tension between polypropylene (PP) and two different molten metals (tin and eutectic SnAgCu alloy) has been measured at 250°C and 230°C, respectively. Systematic rheological investigations of the materials under study enabled us to measure the viscosity of the polymer matrix and that of the metal liquids. A viscosity of 1.9mPa.s and 2mPa.s in the melt is thus reported for tin and SnAgCu alloy, respectively. Based on these investigations, the interfacial tension between the molten metals and the polymer matrix is determined for the first time. The influence of the polymer matrix viscoelasticity and liquid metal surface oxidation was analyzed in order to determine the most accurate conditions for measuring the interfacial tension between the polymer and the liquid metal. Values as high as 350 mN.m⁻¹ (for PP/SnAgCu) and 140 mN.m⁻¹ (PP/ tin) are reported, indicating a poor affinity between the molten metal and the polymer matrix. By temperature quenching the dispersion of the liquid metal drops in the polypropylene under constant shear, the formation of solid metal ellipsoids is obtained, with a characteristic size that is limited by the critical deformation parameter defined by Taylor. Our study offers thus an experimental approach of measuring the interfacial tension between two highly incompatible liquids, opening in the same time a promising perspective for obtaining, by a rheological approach, metal particles with a non-negligible form factor.

Keywords: Interfacial tension, rheology, liquid metal, droplet relaxation

Reformatted version of the revised paper originally published in:

Journal of Rheology, 2021, Volume 65, Issue 3, pages 391-404

Droplet relaxation of molten metals in polypropylene matrix:

Measurement of the interfacial tension

Hubert Lecocq¹, Olivier Lhost², Anatoli Serghei¹, Philippe Cassagnau¹

¹*Institut des Matériaux Polymères, Université de Lyon, 69622 Villeurbanne, France*

²*TOTAL Research and Technology Feluy, C 7181, Feluy, Belgium*

1. Introduction

The main advantage of developing polymer composite materials is the immense variety of polymer matrices and fillers available that can be combined in order to achieve the optimized properties and performance required in a broad range of industrial applications. Among fillers, carbon black [1,2], carbon nanotubes [3], graphene [4], silica [5], titanium dioxide [6], and metal fillers [7] are the most commonly used to obtain functional properties such as reinforced mechanical properties, electrical or thermal conductivity, electromagnetic interference shielding, liquid or gas barrier or permeability properties, etc. In the last decades, much attention has been focused on liquid metal/polymer composite materials [8–13]. The ability of controlling the processing of such composites is expected to lead to new materials with enhanced rheological, mechanical and electrical properties [14,15], but as well to the development and fabrication of low-cost, flexible electronic components such as microscale wires, circuit elements, electrodes and electromagnets [16]. Flexible electronics [17–19] and 3D printing of hybrid polymer-metal materials [20–24] are fields of prime interest, as they will greatly influence the development of fabrication methods of the novel wearable electronics of tomorrow. Liquid state metals have an undeniable advantage in flexible polymer-based electronics and the use of molten polymers can be of great help in the challenging 3D printing of molten metals. Understanding the interactions between those two highly different materials and the rheological properties of a liquid metal / molten polymer blend is thus crucial in developing these novel technologies. Promising liquid metal materials with a low melting temperature T_m are for instance gallium ($T_m=29.8^\circ\text{C}$), indium ($T_m=156.6^\circ\text{C}$), and tin ($T_m=231^\circ\text{C}$), as well as eutectic alloys: eGaN ($T_m=15.7^\circ\text{C}$), eSnPb ($T_m=183^\circ\text{C}$), and eSnAgCu ($T_m=217^\circ\text{C}$ [25]). Such low melting temperatures enable one to work with liquid metal materials at room temperature or at temperatures commonly used for polymer processing ($180\text{--}250^\circ\text{C}$). For instance, by dispersing droplets of liquid GaIn in a polymer matrix

made of a blend of PMVS and PMHS, Wang et al. obtained a composite material with highly interesting properties of thermal conductivity [17]. One of the main challenges when dealing with liquid metal/polymer composites are the big difference in their rheological properties [25–28], polymers being usually more viscous than liquid metals. Another challenge is related to the large interfacial tension between these two types of materials [29–31], which leads to tremendous difficulties in controlling the particles dispersion and blend morphology. Measuring viscosity of liquid metals and alloys is generally more demanding than for usual thermoplastics (such as for instance melt polypropylene). Pure liquid metals and alloys display a Newtonian constant behavior at all shear rates, but under oxidative environments oxide layers can form on their surface. These oxide layers can lead to changes in the viscoelastic properties of the liquid metals and alloys, increasing the viscosity in the low frequency regime [32,33] and giving to these materials the behavior of a threshold fluid or Bingham fluid [34,35].

As for the measurement of the interfacial tension that characterizes the affinity between different liquids, the first experimental approaches started with the methods of plaque tensiometer [36], small capillary tube [37] and contact angle [38,39], issued from the pioneer work of Jurin and Laplace. As these methods apply to measuring interfacial tension between two distinct and separated liquids (or a liquid and a solid) with often limiting constraints of temperature, new developments allowing one to carry out this kind of measurements directly in a blend of two immiscible liquids have been proposed by Taylor and Grace [40,41]. Many experimental methods were developed from these major studies to measure the interfacial tension between two liquids, one of them being related, for instance, to the dispersion of a minor phase into a major phase representing the matrix. These methods can be divided into three categories [42]. The first category relies on equilibrium methods where the surface tension is calculated from a final state of a system, such as for instance the pendant drop method [43], the Sessile drop method [44] and the spinning drop method [45]. The second category concerns dynamic rheological measurements using Palierne's [46] or Bousmina's [47] models to determine interfacial tension values. The last category of measurements are dynamic methods, such as the breaking thread method (BTM [48]), the imbedded fiber retraction method (IFRM [49]), the imbedded disk retraction [50], and the retraction of deformed drop method (RDDM). The latter, developed by Luciani et al. [51], involves dispersing small liquid droplets of micrometric size into a liquid matrix. The drops of spherical shape are then deformed by shear or elongation for a limited period of time; the deformation is then stopped and the retraction of the drop back to a sphere is monitored. For Newtonian fluids, the characteristic time of retraction is governed by the materials' viscosity, the drop size and the interfacial tension. Compared with other approaches, this

method has the considerable advantage of being easy and quick to implement while enabling one in the same time to measure a large number of droplets, which directly leads to a statistically significant value of the interfacial tension [42]. This method has been extensively used so far to determine the interfacial tension between molten polymers [51–60].

In this work, we aim to determine the interfacial tension between molten tin (at 250°C) or molten tin eutectic alloy SnAgCu (95.6% Sn, 3.5% Ag, 0.9% Cu; at 230°C) with two polypropylene matrices (PP) of different viscosities using the RDDM method [51]. Considering the fact that this method requires to know the viscosity of the two liquids used in the blend, the rheological properties of Sn, SnAgCu and the two PP polymers were measured under nitrogen atmosphere to determine their viscosity. Interfacial tension was then measured using the RDDM approach, in a device especially developed for this purpose. A large interfacial tension is obtained, indicating a poor affinity between the two liquids. The influence of polymer matrix viscoelasticity on the measured relaxation times and consequently on the measurement of the interfacial tension will be discussed, by taking into consideration previously reported studies. Additionally, we show that solid metal ellipsoids can be easily obtained by our approach, which can be of potential interest for a subsequent development of polymer/metal composite materials with a lower percolation threshold and high conductivity value.

2. Retraction of deformed drop theoretical models

From the pioneer work of Grace and Taylor [40,41], the drop deformation, its aspect ratio and retraction are controlled by two dimensionless parameters, the viscosity ratio of two liquid phases [51], defined as:

$$p = \eta_d / \eta_m \quad (1)$$

and the capillary number, given by:

$$C_a = \frac{\sigma R}{\gamma_{12}} \quad (2)$$

The latter represents the ratio between forces that tend to deform the drop, shear or elongation, and the surface forces that aims to bring the drop back to a sphere. η_d and η_m are respectively the zero-shear viscosity of the dispersed phase and of the matrix (the liquid metal and the

polymer matrix in our study). σ is the stress imposed to the drop (elongation or shear), R the radius of the drop and γ_{12} the interfacial tension between the two phases.

According to Taylor, after the cessation of the drop deformation under flow, the drop goes back to a sphere shape and the drop deformation parameter D follows the equation:

$$D = D_0 \exp\left(-\frac{\gamma_{12} \cdot t}{R_0 \cdot \eta_{eq}}\right) = D_0 \exp\left(-t/\tau_d\right) \quad (3)$$

$$D = \frac{L-B}{L+B} \quad (4)$$

with L and B being respectively the long and short axis lengths of the ellipsoid shape drop during and just after flow and D_0 is the deformation parameter at $t = 0$ when the flow stops. $D = 0$ when the drop gets back its spherical shape. η_{eq} is the equivalent viscosity of the blend and τ_d the characteristic retraction time of the drop defined as:

$$\eta_{eq} = \eta_m \frac{(2p+3)(19p+16)}{40(p+1)} \quad (5)$$

$$\tau_d = \frac{\eta_{eq} \cdot R_0}{\gamma_{12}} \quad (6)$$

When there is an extremely low viscosity ratio between the dispersed phase and the matrix, the expression of η_{eq} can be simplified. Indeed, if $\eta_m \gg \eta_d$, then $p \ll 1$. τ_d and η_{eq} can then be expressed as:

$$\eta_{eq} = \frac{48}{40} \eta_m \quad (7)$$

$$\tau_d = \frac{48 \cdot \eta_m \cdot R_0}{40 \cdot \gamma_{12}} \quad (8)$$

Thus, the characteristic retraction time of a droplet is independent of the dispersed phase viscosity. In this precise case, one does not need a highly precise determination of the viscosity of the dispersed phase to measure the interfacial tension between the two phases.

By monitoring the time evolution of the droplet retraction, one can follow the variation of D versus time and deduce τ_d . Knowing the viscosity of the dispersed phase and the matrix, the interfacial tension between the two phases can be calculated from Eq. 5 and 6 (or 7 and 8 if $\eta_m \gg \eta_d$).

The viscoelasticity of the polymer matrix can have an influence on the droplet retraction time. The studied polymer matrices can actually be assimilated to Boger fluids [61]. These fluids flow with a constant Newtonian viscosity but can exhibit viscoelasticity at certain shear rates. For immiscible

dispersions of liquid droplets in a molten polymer matrix, Greco develop a 2nd-order theory based on the 1st-order theory of Taylor to take into account viscoelastic effects as 2nd-order perturbations [62]. Non-Newtonian effects are accounted for by considering 2nd-order fluids, which show a constant viscosity and a first normal stress difference proportional to the square of the shear rate. Several theories such as Maffettone-Minale, Jackson-Tucker and Yu-Bousmina [63–65] were developed relying on Greco's work to model the deformation and relaxation of dispersed immiscible droplets in a matrix, considering the viscoelastic properties of the dispersed phase and that of the matrix.

To assess the influence of viscoelasticity in our systems, the Deborah number comparing viscoelastic effects to interfacial tension importance are calculated:

$$\mathcal{D}_e = \frac{\tau_{\text{elasticity}}}{\tau_{\text{interfacial}}} = \frac{\Psi_1 \cdot \gamma_{12}}{2 \cdot R_0 \cdot \eta_m^2} = \frac{\tau_w \cdot \gamma_{12}}{R_0 \cdot \eta_m} \quad (9)$$

where Ψ_1 is the first normal stress coefficient related to the first normal stress difference N_1 ($\Psi_1 = N_1 / \dot{\gamma}^2 = 2 \cdot \eta_m \cdot \tau_w$) and τ_w is the polymer matrix weight relaxation time. The weight matrix relaxation time ($\tau_w = \eta_m \cdot J_e^0$) was chosen over the number relaxation time ($\tau_n = \eta_m / G_N^0$) since it better traduces the viscoelastic nature of the polymer. J_e^0 is the zero-shear compliance ($J_e^0 = 1 / \eta_0^2 \lim_{\omega \rightarrow 0} G'(\omega) / \omega^2$) and G_N^0 the first plateau modulus [66]. A Deborah number higher than 1 indicates a non negligible influence of polymer matrix viscoelasticity on the droplet relaxation.

Cardinaels and Moldenaers synthetized the effects of viscoelasticity and confinement on the deformation and relaxation of dispersed drops in a polymer matrix with experimental data and the previously cited theoretical models [67]. In the case corresponding to our system, they predicted and observed a retardation of drop relaxation. This leads to an underestimated characteristic relaxation time and thus an overestimated interfacial tension value as observed in this work. This retardation is even higher for long measurement times and can lead to a larger underestimation of relaxation time. In the case of a viscoelastic droplet in a Newtonian polymer matrix, the models predict an acceleration of droplet retraction and an overestimation of interfacial tension. Trettheway and Leal also observed a significantly slowed down relaxation process of a Newtonian drop in a boger fluid attributed to viscoelastic effects and that prevents the calculation of the interfacial tension directly from the relaxation characteristic time [68].

For each system, the Deborah number will be calculated to assess the importance of matrix viscoelasticity and whether it can have an impact on the measurement of interfacial tension.

3. Materials and methods

a. Materials

Homopolymer polypropylene PP 7060 ($T_f = 165^\circ\text{C}$, MFI = 12 g/10 min, medium viscosity matrix) and PP 3060 ($T_f = 165^\circ\text{C}$, MFI = 1.8 g/10 min, high viscosity matrix) were provided by Total SA France. Pure tin powder and eutectic SnAgCu alloy (coil) were purchased from Goodfellow France. The eutectic SnAgCu alloy is composed of 95.6% Sn, 3.5% Ag and 0.9% Cu and has a melting temperature of 217°C.

b. Rheological measurements

An ARES G-2 rheometer from TA Instruments was used to characterize the rheological properties of the polymer materials and of the molten metals. A 25mm-diameter parallel-plate measurement geometry was used to study the two polymer matrices and a Couette geometry was used to study the liquid metal and alloy.

For the polypropylene matrix, discs of 25mm-diameter and 1mm-thickness were hot pressed at 200°C and 250 bars in a Servitec polystat 200 T press. The two PP were then characterized at 230 and 250°C (4 discs per temperature per polymer) under nitrogen atmosphere to avoid polymer degradation. The linear domain was analyzed by a strain sweep measurement between 0.01 and 100% strain at a constant frequency of 10 rad.s⁻¹. The samples were then investigated under a frequency sweep between 500 and 0.01 rad.s⁻¹ at constant strain (the highest possible while staying in linear regime). The strain was increased for the lowest frequency decade to conserve good measurement resolution. The rheological properties of both polymer matrices as a function of the angular frequency at 230°C are displayed in Figure 1. Zero-shear viscosity values are obtained from the low frequency plateaus. Zero-shear compliances, weight and number relaxation times were also determined from the experimental rheological curves. These values and their corresponding temperatures are listed in Table 1, for both investigated matrices. The error bars are the standard deviation over four measured samples.

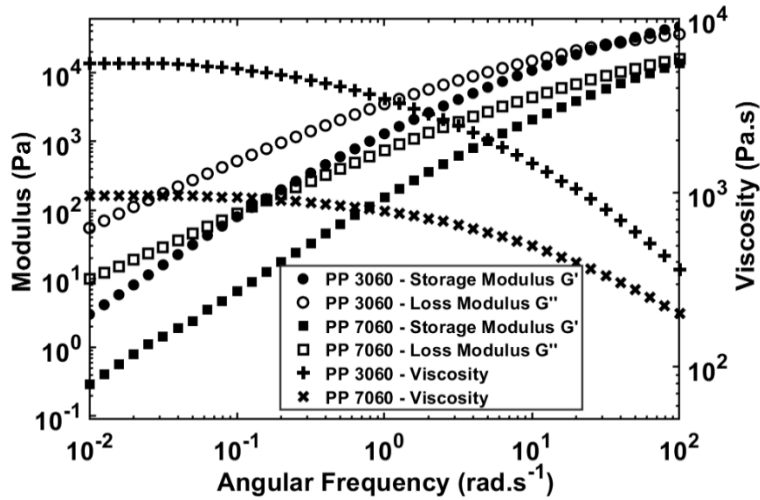


Figure IV - 1: Rheological properties of PP 3060 and PP 7060 versus angular frequency at 230°C under nitrogen atmosphere. Storage and loss moduli scale is the left y-axis, and viscosity scale is the right y-axis.

Table IV - 1: Measured zero-shear viscosity values of studied polypropylene matrices and determined zero-shear compliance, and weight and number relaxation times.

Polypropylene	Temperature (°C)	Zero-shear viscosity (Pa.s)	J_e^0 (Pa ⁻¹)	τ_w (s)	τ_n (s)*
PP 7060	230	990 ± 50	0.00025	0.25	0.0006
PP 7060	250	950 ± 30	0.00025	0.24	0.0005
PP 3060	230	5400 ± 330	0.00043	2.3	0.003
PP 3060	250	4500 ± 250	0.00043	2.0	0.0025

*First plateau modulus $G_N^0 = 200\,000\text{ Pa}$ [66]

For the metal materials, the SnAgCu coil was cut in small pieces and immersed in a 1 M HCl solution to remove the surface oxide. Tin powder underwent the same treatment. Dried metal or alloy was then melted in the Couette cup (230°C for SnAgCu and 250°C for tin) under nitrogen atmosphere and the Couette bob was completely immersed into the melt. The metal quantity was determined for the bob being totally immersed in the liquid metal. Small amounts of liquid metal flux to avoid the presence of any surface oxide layer were used directly in the Couette geometry before measurement [33]. The method is depicted in Figure 2. After a 100 s⁻¹ pre shear for 10s, the sample underwent a constant steady shear under nitrogen atmosphere for about one minute while the torque was measured, for values of shear rate between 0.02 and 1000 s⁻¹. The value of flow viscosity was measured once the torque reached an equilibrium value and the measurement was repeated three times for each shear rate to insure statistical significance.

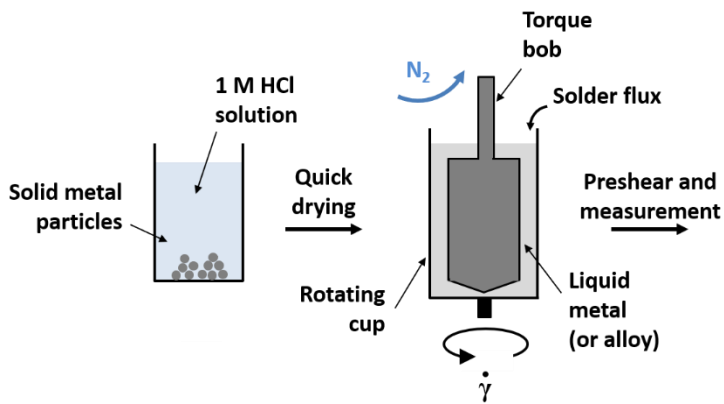


Figure IV - 2: Liquid tin and eutectic SnAgCu alloy viscosity measurement method in air or nitrogen atmosphere.

c. Determination of interfacial tension by RDDM

The retraction drop measurement was performed on a Linkam CSS-450 high temperature stage coupled with a Leitz Orthoplan microscope (transmission mode) with 20X lens (Fig. 3-a). Two small plaques of polymer (either PP 7060 or 3060) were hot pressed to 0.5mm-thickness, and eutectic SnAgCu alloy pieces or tin powder, previously treated with HCl solution, were sandwiched between the plaques. The whole setup was inserted in the stage and the latter was set to measurement temperature (230°C for eutectic SnAgCu alloy and 250°C for tin). Stage gap was set to 1mm. When the target temperature was reached, a shear rate of 2 s^{-1} was imposed to the melt for 30s to disperse the liquid metal into microscopic drops of radius spanning from some micrometers to several hundred micrometers. The RDDM was then implemented on drops of radius between 20 and 200 μm : a shear rate between 0.2 and 1 s^{-1} was imposed to the drop for 5 s and the drop retraction was monitored (6 images/s) once the shear was stopped as schematized in Fig. 3-b. The shear entails the deformation of the liquid spherical drop into an elliptical shape whose axis lengths are monitored though time during the retraction. For each liquid metal droplet, the interfacial tension is determined through the measurement of the characteristic retraction time according to Eq. 3 & 8.

In Fig. 3-c the tridimensional deformation of the drop under shear between two glass plates is schematized. The drop does not deform in a direction parallel to the plates but under a tilt angle θ . The top view is seen through the microscope and if the angle θ is too high, the error made on the measurement of the length $2L$ of the ellipse major axis can be important. Nevertheless, no major error

is made in the measurement of the minor axis length $2w$. Taylor demonstrated the dependence of this orientation angle on the applied deformation [69] according to:

$$\theta = \frac{1}{2} \operatorname{Arctan} \left(\frac{2}{\lambda} \right) \quad (10)$$

The applied deformation is λ . The maximal orientation is obtained for smallest deformations. For greater deformations, the droplet orients itself in the direction of flow.

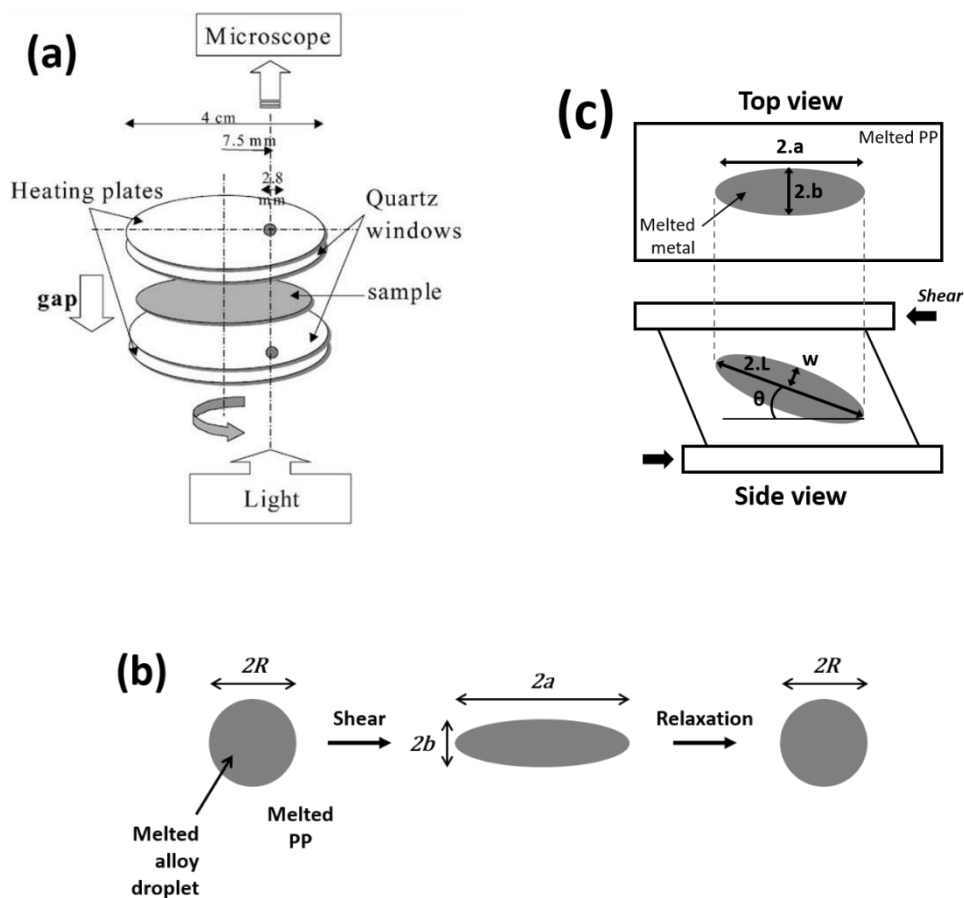


Figure IV - 3: Retraction of deformed drop measurement. (a) Scheme of the shear temperature stage coupled with transmission optical microscope. The sample and plates are confined in a thermally regulated enclosure. The bottom quartz window can rotate at a given speed to impose shear to the sample. (b) Principle of the retraction of deformed drop method. A stabilized and perfectly spherical drop of melted metal in the polymer matrix undergoes a constant shear for a limited period of time to adopt an elliptic shape. Once the shear is interrupted, the relaxation of the drop back to a sphere is recorded. (c) Three-dimensional orientation of the droplet under shear between two glass plates.

One can significantly reduce the error of the determination of the major axis length by making the hypothesis that the ellipsoid resulted from the droplet deformation is symmetrical. The major axis length L can then be calculated from the value of the minor axis length b :

$$L = \frac{8R_0^3}{b^2} \quad (11)$$

with R_0 being the initial spherical droplet radius. In this study, the directly measured value of the major axis a was compared to the calculated value L by using Eq. 11. No significant difference was noted and both values led to the determination of the same interfacial tension. Thus, the deformation of the droplet was high enough to be oriented in the direction of the flow and the length of the major axis could be measured through the measurement of the length a (Fig. 3-c, top view).

Confinement can have an impact on droplet relaxation times [70]. Cardinaels and Moldenaers concluded that these effects are minor when the confinement ratio is $2R/H = 0.4$ [67]. With a stage gap set to 1 mm and the maximum radius of studied liquid metal droplet of 200 μm , the maximum confinement ratio of our systems is indeed 0.4. The influence of confinement on the droplet relaxation time can, thus, be ignored.

4. Results and discussion

a. Rheology of liquid tin and eutectic SnAgCu alloy

Measurement results for the eutectic SnAgCu alloy at 230°C are displayed in Figure 4. The surface oxide that can form before and during the measurement can be neglected because of the pre-treatment of the solid metal materials in a 1 M HCl solution, the introduction of flux in the Couette geometry and the measurement under inert nitrogen atmosphere [33]. A pre-shear was additionally applied before measurement by prevention, in order to remove any surface oxide crust that could eventually have formed [71]. The viscosity versus shear rate of eutectic SnAgCu alloy at 230°C either under air atmosphere or under inert nitrogen atmosphere and with flux to avoid any oxidation is displayed in Fig. 4-a. Viscosity measurement is carried-out well above the melting temperature of the alloy ($T_m=217^\circ\text{C}$) to insure a fully liquid state of the molten metal [71]. Under inert nitrogen atmosphere, the viscosity is constant, showing values between 0.001 and 0.01 Pa.s. On contrary, under an oxidative air atmosphere, the metal displays a decreasing viscosity with increasing shear (similar to

a shear thinning behavior). Under these conditions, an oxide crust forms at the surface of the liquid metal. If the oxide crust is continuous from the bob shaft to the wall, it can lead to an increase in the apparent viscosity. However, at higher shear rates, the flow prevents the formation of a continuous crust and the measured viscosity gets closer to the viscosity of the liquid metal. The influence of this oxide crust is especially significant in the low shear rates when the oxide layer has more time to form and its integrity is less affected by the low shear rates. The viscosity values measured under inert and oxidative conditions seem to converge in the high shear region where the high shear prevents the formation of any surface oxide crust. A similar phenomenon is observed for pure tin at 250°C in Fig. 4-b. Oxidation layers on solid metals in open air can reach some tens of nm thickness on time scales from seconds to hours [72,73]. Considering the high temperature and the liquid state of the metal facilitating diffusion of atoms and molecules, the oxide surface layer in an oxygen rich atmosphere would be thicker. Its thickness can thus be estimated to be several tens of nm to one hundred nm approximately [74–76]. For both metals, there is a slight increase in the viscosity values and in the error bars in the low shear rate region under inert atmosphere. This can be attributed to the formation of surface oxide crust in spite of all precautions taken. A slight increase in viscosity can also be spotted in the high shear rate region of the graph, between 10^2 and 10^3 s $^{-1}$, for both the liquid metals, under air and under nitrogen. This can be attributed to minor nonlinear shear effects present at those very high shear rates.

To experimentally determine the metal viscosity, an average is taken between 0.2 and 2 s $^{-1}$ shear rate since our approach requires a close to zero shear viscosity without the negative influence of surface oxide. The experimental values are listed in Table 2 and compared with viscosities values found in the scientific literature. Similar to our work, Elton et al. measured the viscosity of tin at 250°C and got 0.1 Pa.s at 0.2 s $^{-1}$ under inert argon atmosphere and 3 mPa.s using flux, implying that an inert atmosphere is not enough to completely eliminate the influence of oxide surface layer [33]. Brooks et al. reported a tin viscosity of 1.85 mPa.s at its melting temperature of 231°C [77] and Gancarz et al. a tin viscosity of 1.8 mPa.s at 250°C [31]. The later also measured the viscosity of a tin silver alloy (Sn 96.4 %, Ag 3.6 %) at 250°C and reported 1.9 mPa.s. The viscosity of liquid metals and alloys follows an Arrhenius law in dependence on temperature. Gancarz et al. also reported the Arrhenius parameters of the tin silver alloy which enables us to determine its viscosity at 230°C. A value of 2 mPa.s is obtained which is coherent with our experimental value. The proximity of tin and SnAg alloy viscosities and Arrhenius parameters is not unexpected, considering the low content of silver in the alloy. The influence of the liquid flux used to remove surface oxide is observed to be negligible as

only a small amount was used and was only in contact with the bob shaft (Fig. 2). This is confirmed by the agreement of our results with the ones found in the literature.

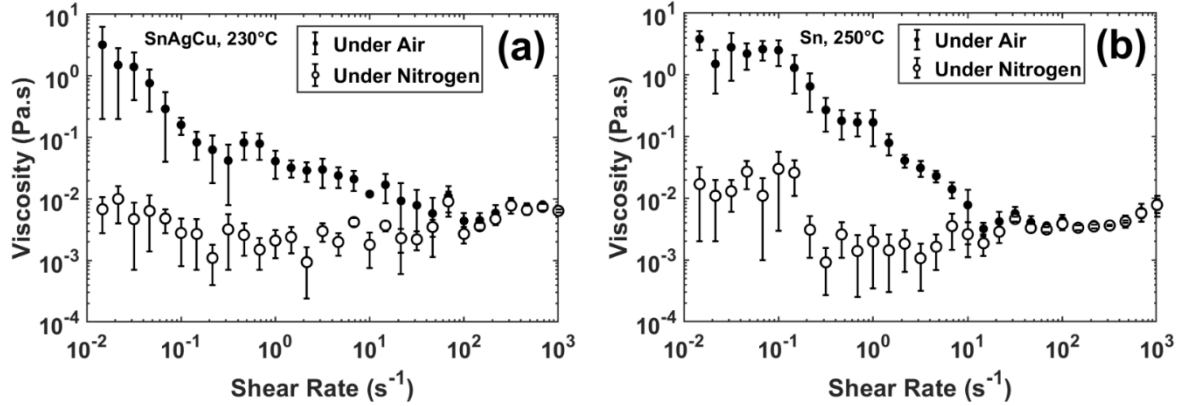


Figure IV - 4: Shear viscosity curves of liquid metals under air (no flux) or nitrogen atmosphere (with flux). (a) Eutectic SnAgCu alloy at $T=230^{\circ}\text{C}$. (b) Tin at $T=250^{\circ}\text{C}$.

Table IV - 2: Viscosity values of liquid metals, measured in this work and reported in the literature.

Material	Zero shear viscosity (Pa.s)	Temperature (°C)	Method of measurement	Reference
SnAgCu alloy	$(2 \pm 1) \times 10^{-3}$	230	Couette	This work
SnAg3.6	1.9×10^{-3}	250	Capillary	[31]
Tin	$(1.9 \pm 1) \times 10^{-3}$	250	Couette	This work
Tin	1.87×10^{-3}	250	Capillary	[31]
Tin	$2 - 3 \times 10^{-3}$	250	Couette	[33]

b. Interfacial tension measurement by RDDM

In the previous part, it has been shown that there is a large viscosity gap between the polymer matrices and the liquid metals ($\eta_d/\eta_m < 10^{-6}$). Thus, we have $p \ll 1$, consequently, the Eqs. 5 & 6 can be simplified in Eq. 7 & 8.

An example of the retraction of a drop of 90 μm radius of liquid eutectic SnAgCu alloy in the PP 3060 (high viscosity) matrix at 230°C is showed in Figure 5. This system was chosen to be analyzed in detail, as the high viscosity matrix leads to long relaxation times and well observable droplet

relaxations. At $t=0$ s, just after shear interruption, the drop is well deformed: the D parameter (Eq. 4) reaches a value of 0.51. The drop then retracts quickly, the elliptic shape is still noticeable at 1.2s and 2s with values of D of 0.19 and 0.09 respectively. After 3s, the elliptic shape is not readily discernable anymore: at 2.8s, $D = 0.05$ and at 4s, $D = 0.02$. After 15s, the drop got its spherical shape back and $D = 0$. The evolution of the ellipse axis lengths and the D parameter versus time are displayed in Figure 6-a and 6-b respectively. As mentioned before, the decrease of the axis lengths back to R_0 and D back to 0 takes place quickly, following an exponential kinetics. 90% of the retraction is completed in less than 3s and the ellipse axis lengths are almost equal after 4s. In the caption of Fig. 6-b, the logarithm of D versus time is represented and fitted with an exponential law, as predicted by Eq. 3. The fit is good with $R^2 = 0.9985$ and enables us to determine a characteristic retraction time of $\tau_d = 1.24$ s. Using this characteristic time and the radius of the drop $R_0 = 90 \mu\text{m}$, we can calculate the interfacial tension between liquid SnAgCu and PP 3060 at 230°C according to Eq. 8. Using the same system, other liquid metal droplets were measured using the RDDM method.

The liquid metal droplet displayed in Fig. 5 shows a little asymmetry, especially in the early retraction stages. The origin of this asymmetry can be multiple: Taylor evoked, for extremely small viscosity ratios ($p \ll 1$), a thinning of the tips of an elongated drop that eventually leads to tip streaming. Greco pointed out deviations from ellipsoid shapes because of 2nd order viscoelastic and confinement effects [62].

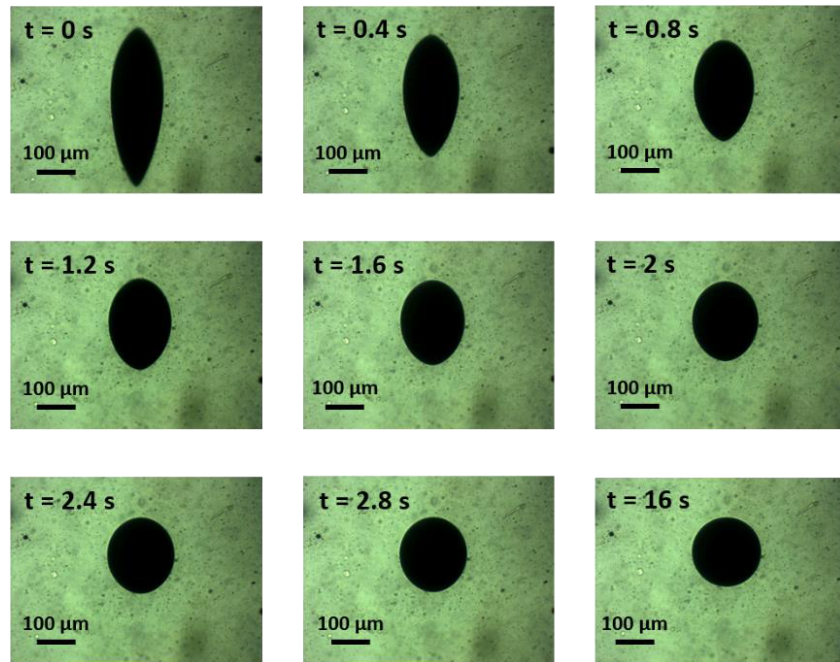


Figure IV - 5: Relaxation of a melted SnAgCu alloy drop (diameter = 90 μm) in PP 3060 matrix after a shear period at rate 0.8 s^{-1} , at a constant temperature of 230°C. The shear rate and matrix viscosity are sufficient to considerably deform the metal drop. At 16s, the droplet is back to a spherical shape.

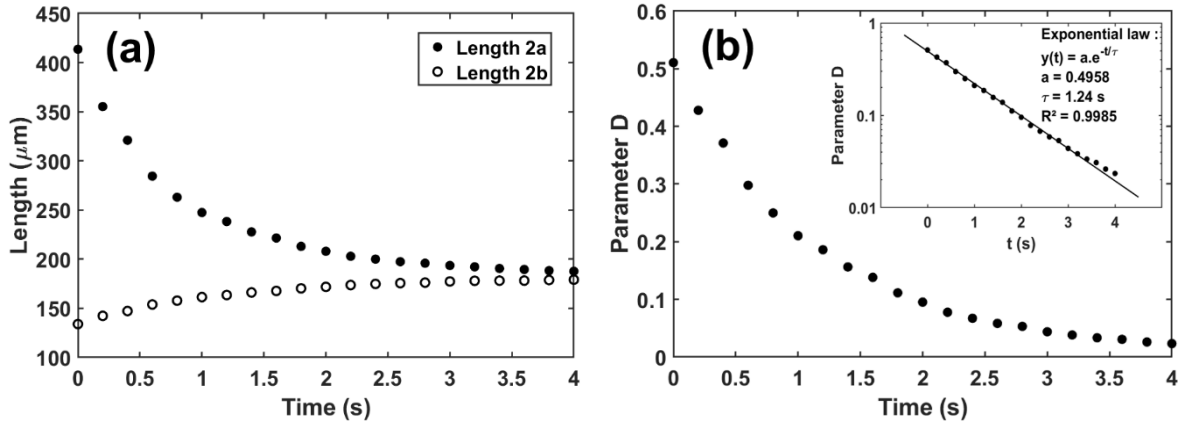


Figure IV - 6: Relaxation dynamics of the droplet depicted in Figure 4. (a) Length of the ellipse major 2a and minor 2b axes versus time during drop retraction. (b) Same for deformation parameter D. In caption: the logarithm of D versus time and the best exponential fit to the experimental points.

Three other systems were studied: SnAgCu alloy with PP 7060 at 230°C (medium viscosity), and pure tin with PP 3060 or PP 7060 at 250°C. The characteristic relaxation time versus droplet radius is displayed in Figure 7. As predicted by Eq. 8, a linear relation was expected between the characteristic relaxation time and the droplet radius. This is indeed the case since the experimental points can be easily fitted using a linear dependence of slope $48\eta_m/40\gamma_{12}$.

For each system, the influence of the matrix viscoelasticity was assessed by calculating the corresponding Deborah number (Eq. 9). This led to values between 3 and 7.4 with an average of 5 for PP 3060, and between 0.4 and 0.64 with an average of 0.5 for PP 7060. This order of magnitude analysis leads to the conclusion that viscoelastic effects are not negligible with the PP 3060 polymer matrix but they can be ignored for PP 7060. The use of Taylor's equations to determine interfacial tension values is then valid solely for PP 7060. However, there seems to be a linear dependency between relaxation time and droplet radius for PP 3060 also, but which cannot be directly linked to an interfacial tension value because of the matrix viscoelasticity. A rapid calculation of the Weissenberg numbers, ratio of elastic forces over viscous forces ($\mathcal{W}_i = \tau_w \cdot \dot{\gamma}$) during droplet preshear ($0.2 - 1 \text{ s}^{-1}$) at 230°C yields the values of 0.5 – 2.3 for PP 3060 and 0.05 – 0.25 for PP 7060. These low numbers can again be linked to a weak influence of PP matrix viscoelasticity during droplet retraction in PP 7060 but not in PP 3060 [68]. The relaxation of the studied liquid metals was additionally tested in a PP matrix of even lower viscosity (three times lower than PP 7060), but the droplet relaxations were too fast to be correctly measured. Thus, the PP 7060 matrix appears to be the best compromise for measurable relaxation times and minimal polymer matrix viscoelasticity effects.

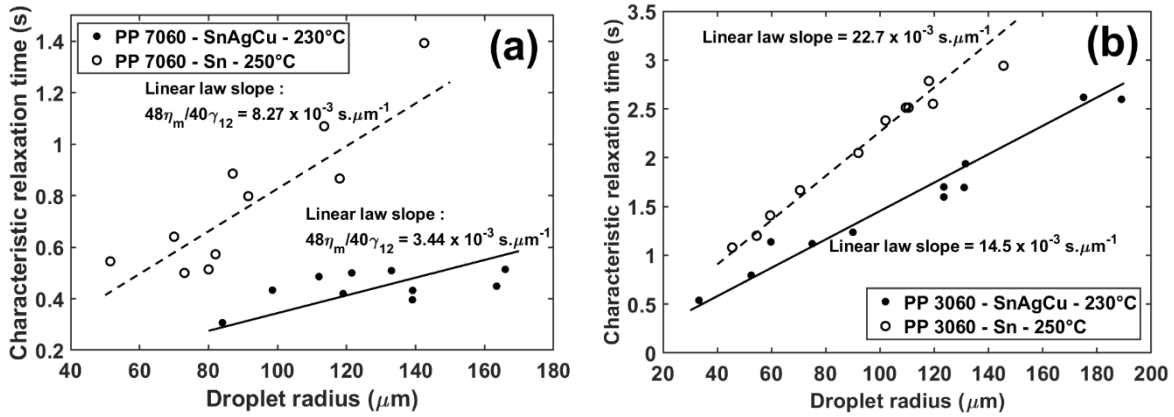


Figure IV - 7: Relaxation characteristic time versus droplet radius for SnAgCu metal alloy at 230°C and pure Sn at 250°C in the two different melted polypropylene matrices. (a) Medium viscosity PP 7060. (b) High viscosity PP 3060. Experimental points are fitted with linear laws. The slopes of the laws are indicated.

The interfacial tension values are listed in Table 3. The error gaps are determined from the standard deviations between all the interfacial tensions calculated for one system. The relative errors are globally inferior to 10%, in agreement with the error ranges reported already for the retraction of a deformed drop method [42]. One can also note that the measured interfacial tension is higher for the eutectic SnAgCu alloy than for the pure tin. Both metals display an interfacial tension with the two polymers much higher than the interfacial tension between two polymers.

No investigations on the interfacial tension value between liquid metals and polymers are reported so far, making this work to be the first of its kind. When comparing our measured polymer/molten metal interfacial tension to values reported for polymer/polymer melts, a difference that can go up to one or even two decades can be observed: polymer/polymer interfacial tensions range typically from 1 to 15 mN/m [51,52,79,80] while liquid metal/polymer interfacial tension is found between 100 and 500 mN/m.

Table IV - 3: Values of interfacial tension measured in this study compared to calculated theoretical values.

Materials	Temperature (°C)	Experimental (mN.m ⁻¹)	Estimated theoretical value ^a	Estimated theoretical value ^b
PP7060 / SnAgCu	230	350 ± 40	386	366
PP7060 / tin*	250	140 ± 20	408	-

^aLiquid metal surface tension value from [31], ^bfrom [78], *tin surface is oxidized

We can compare our experimental values to theoretical predictions according to the Owens, Wendt and Wu equations [30,81]:

$$\gamma_{12} = \gamma_1 + \gamma_2 - \frac{4\gamma_1^d \cdot \gamma_2^d}{\gamma_1^d + \gamma_2^d} - \frac{4\gamma_1^p \cdot \gamma_2^p}{\gamma_1^p + \gamma_2^p} \quad (12)$$

$$\gamma_{12} = \gamma_1 + \gamma_2 - 2 \cdot \sqrt{\gamma_1^d \cdot \gamma_2^d} - \frac{4\gamma_1^p \cdot \gamma_2^p}{\gamma_1^p + \gamma_2^p} \quad (13)$$

Eq. 12 is the harmonic-mean equation fitted for interfaces between organic liquids and organic polymers, and Eq. 13 is the geometric-harmonic-mean equation fitted for the interface between high- and low-energy phases such as metal and organic polymers [30]. The second equation seems thus to be more suitable to our setup. Values of surface energy of PP, tin and eutectic SnAgCu can be found in the scientific literature: Elias et al. reported the surface tension of PP 7060 and its temperature dependence using the Guggenheim relation [5,82] as follows:

$$\gamma = \gamma(0) \cdot \left(1 - \frac{T}{T_{cr}}\right)^{11/9} \quad (14)$$

With for PP 7060, $\gamma(0) = 47.2 \text{ mN/m}$ and $T_{cr} = 914 \text{ K}$, one gets a surface tension value of 17.8 mN/m at 230°C and 16.7 mN/m at 250°C . The same values will be taken for PP 3060 as there is no chemical difference between the two polymers. Elias et al. also reported a value of 0 for the polar component of PP 7060. Thus, in Eq. 13 the polar adhesion work (last term) will be zero. For eutectic SnAgCu alloy, Gancarz et al. [31] and Moser et al. [78] report surface tension values for Sn-Ag3.6% alloy and Sn-Ag3.2%-Cu0.6% alloy respectively. They both use a linear law to describe the temperature evolution of the surface energy according to the works of Keene [83]:

$$\gamma = a + b \cdot T \quad (15)$$

For Sn-Ag3.6 alloy, Gancarz et al. reported values of $a = 625 \text{ mN/m}$ and $b = -0.110 \text{ mN/(m.K)}$, and Moser et al. reported values of $a = 586 \pm 8 \text{ mN/m}$ and $b = -0.082 \pm 0.0095 \text{ mN/(m.K)}$ for Sn-Ag3.2%-Cu0.6% alloy. These reported values enable us to calculate the surface tension for our eutectic Sn-Ag3.5%-Cu0.9% alloy at 230°C : 570.2 mN/m and 545 mN/m respectively for Sn-Ag3.6 alloy and Sn-Ag3.2%-Cu0.6% alloy. Gancarz et al. [31] also reported a value of surface tension for pure tin of 589 mN/m at 250°C , and values of $a = 624 \text{ mN/m}$ and $b = -0.117 \text{ mN/(m.K)}$ for Eq. 15.

Using Eq. 13, we can calculate the theoretical value of the interfacial tension between tin or eutectic SnAgCu alloy, and PP 7060 or 3060. The calculated values are listed in Table 3 and compared with the experimentally measured values for each system. For eutectic SnAgCu alloy, the experimental

and theoretical values are remarkably close. For the PP 7060 / SnAgCu system, the two theoretical predictions are even in the error gap.

With pure tin, the experimental values are quite far from theoretical ones, suggesting a reduced tin surface tension due to surface oxidation. Despite all precautions taken to reduce the impact of surface oxide layers, a non-negligible effect can be supposed, leading to a reduction of the measured interfacial tension. Numerous studies report the large decrease of the surface tension of liquid metals, including tin and SnAgCu alloys, in the presence of surface oxide [84–87]. Fiori et al. reported a liquid tin surface tension at a temperature of 840 K going from 520 mN/m under 10^{-9} Pa oxygen partial pressure to less than 460 mN/m at 1 Pa oxygen partial pressure [85]. The rich oxygen atmosphere was only maintained for 8 mins before going to 2.10^5 Pa so that equilibrium value of surface tension in rich oxygen atmosphere was not reached. In the same way, Ricci et al. reported a decreasing value of liquid tin surface tension at 818 K temperature from 533 mN/m at 10^{-7} Pa oxygen partial pressure to 498 mN/m at 10^{-1} Pa oxygen partial pressure [84]. Khan et al. reported a surface tension value for liquid eutectic GaIn alloy at room temperature going from 509 mN/m in the absence of oxide to a value tending toward zero under oxidative conditions [87].

Thus, the presence of surface oxide greatly diminishes the surface tension measured for liquid metals. This could explain the lower values of the interfacial tension determined between pure tin and the polymer matrices in our experiment. To support this conjecture, after more than 2h on the high temperature stage, we noticed the appearance of a surface roughness of the droplets and a stiffening of the drops for the PP/pure tin samples, most likely due to the accumulation of tin oxide. For eutectic SnAgCu alloy, the excellent agreement to the theoretical values has to be related the fact that this commercial alloy made for solder contains solder flux micro-inclusions, preventing thereby the formation of surface oxide layers.

In the case of a viscoelastic droplet in a Newtonian polymer matrix, the theoretical models cited before [63,67] predict an acceleration of the droplet relaxation leading to an overestimation of the interfacial tension. Any viscoelastic effect due to the presence of an oxide layer on the surface of the liquid metal would be overrun by the lowered surface tension implied by the presence of the oxide, leading to a reduced value of the measured interfacial tension.

Eq. 14 and 15 describe a decreasing surface tension of both liquid metal and polymer with temperature. Theoretically predicted values of interfacial tension between PP and eSnAgCu at 230, 250 and 300°C are respectively 366, 369 and 379 mN.m⁻¹ [78]. Interfacial tension between liquid metal

and PP is thus expected to vary little with temperature in the typical temperature range of polymer processing.

c. Dynamic morphology freezing by temperature quenching

These high values of interfacial tension have multiple consequences. In the mixing process of liquid metal-polymer composites, for instance, it can lead to a rapid demixing of the two phases if the polymer phase is not viscous enough. The only morphology accessible in this kind of composites is dispersed spherical drops of liquid metal in the polymer matrix. Furthermore, percolation of drops is impossible since it would lead to coalescence and demixing. Quenching the samples under shear appears thus to be an effective way of obtaining solid non-spherical metal particles with an elliptic shape. The behavior of liquid metal/polymer composites is in this respect different from immiscible polymers composites. With the latter, a multitude of morphologies can be obtained by varying the temperature, the viscosity ratio and the polymers content ratio [52,88,89], while quenching can be employed to get more complex co-continuous morphologies [90,91].

Liquid droplets of SnAgCu alloy dispersed in PP 3060 matrix (higher viscosity) at 230°C was deformed under constant shear (0.5 or 1 s⁻¹), subsequently followed by a quenching with a rate of -30°C/min to the temperature of 170°C (thus, below the metal melting temperature of 217°C but above the polymer melting temperature of 165°C). As a result, a dispersion of solid ellipsoid drops in the molten PP matrix is observed (Figure 8). The pictures were taken once the constant shear rate was stopped at 170°C. The drops distribution seems to be limited in size with ellipsoids long axis no bigger than 100 µm for a shear rate of 1 s⁻¹ (Fig. 8-a) and no bigger than 170 µm for 0.5 s⁻¹ (Fig. 8-b). Small spherical drops could be spotted for both shear rates, indicating that the shear rate was not strong enough to significantly deform the small drops as well. In Fig. 8-a, for a shear rate of 1 s⁻¹, all the ellipsoid drops seem similar in size. The ellipse long axes are comprised between 40 and 100 µm and the corresponding deformation parameter D ranges from 0.27 to 0.46. For the 0.5 s⁻¹ shear rate (Fig. 8-b) the distributions are broader, with long axis lengths comprised between 50 and 170 µm and D parameters comprised between 0.15 and 0.45. One can also notice that significantly more undeformed spherical droplets of greater size are observed for 0.5 s⁻¹ shear rate than for 1 s⁻¹. This is explained by the fact that, during the constant shearing, the viscous forces get higher for higher shear rates, leading to more drop breakups and generating consequently smaller drops.

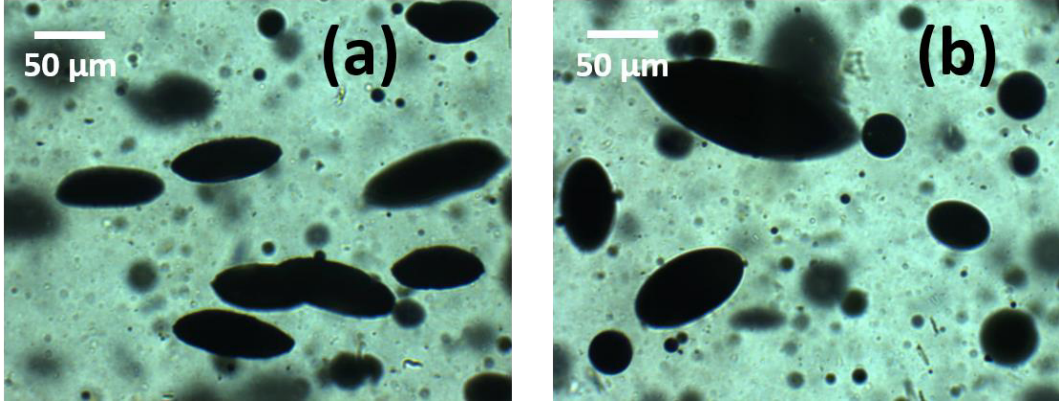


Figure IV - 8: Quenched PP 3060 – SnAgCu alloy system under shearing. Liquid metal drops are frozen in ellipsoid shapes. Quenching under shear rate of 1 s⁻¹ (a) and 0.5 s⁻¹ (b).

This quenching experiment has been done multiple times in the past for immiscible polymer/polymer blends in order to control the formation of ellipsoid droplets similar to our case [92] or of polymer fibers [53,93]. Taylor has worked on the morphology of an immiscible liquid phase dispersed in a liquid matrix under constant shear [69]. Depending on the phase viscosity ratio, interfacial tension and shear intensity, the dispersed drops can deform continuously in long filaments that can break up in multiple drops due to Rayleigh – Plateau instabilities. The important parameters to be considered are the viscosity ratio p and the Taylor capillary number C_a (Eqs. 1 & 2). Taylor showed that when interfacial tension cannot balance the viscous forces, instabilities appear and break ups happen, generally when $D > D_{crit} = 0.5$. According to Taylor, if the interfacial forces are dominant ($p \ll 1$), the deformation in the steady state under constant shear flow is given by:

$$D = C_a \frac{19p+16}{16p+16} \approx C_a \quad (16)$$

Then the capillary number is the significant parameter of droplet deformation and break up with a critical value (critical capillary number) at $C_{a,crit}$. If $C_a < C_{a,crit}$ droplets deform but do not break and if $C_a > C_{a,crit}$ droplets can break. The determination of this critical capillary number has been the subject of many studies and compiled on a single master curve by Grace (often known as the Grace curve [41,94,95]). Based on these works, De Bruijn confirmed the Grace curve and proposed an equation with five parameters to determine the critical capillary number with the viscosity ratio for $p < 3.8$ [96]:

$$\log(C_{a,crit}) = -0.506 - 0.0994 \log p + 0.124(\log p)^2 - \frac{0.115}{\log p - 0.611} \quad (17)$$

The calculation of $C_{a,crit}$ with our system gives a value of 2×10^5 . Given that, before shear, we have a dispersion of spherical droplets of radius comprised between 10 and 500 μm , the capillary numbers associated to drop sizes are comprised between 0.06 and 3 for 0.5 s^{-1} shear rate and between 0.12 and 6 for 1 s^{-1} shear rate. Thus, we are in the case where $C_a < C_{a,crit}$ and according to Taylor's theory, the drops deform without breaking.

In a drop dispersion under simple shear, Rumscheidt and Mason [97] classified the drops deformation and break-up in four patterns according to the viscosity ratio p . For $p > 4$, the drops deform but cannot break. For $p \approx 1$, the drops deform into ellipsoidal shape, pinch and break into two smaller drops. For $p < 1$, the drops elongate into long fibers that can break into two smaller drops of same size with smaller satellite drops between them. For $p \ll 1$, an extraction of small drops from the ends of elongated elliptical drops (called tip streaming) can be observed. This last mechanism seems to correspond to our case where a decreased drops size is observed alongside smaller spherical drops that does not deform, probably as a result of the tip streaming and visible in Fig. 8-a and 8-b. Grace also suggested that in a drops dispersion, all the drops might not experience the same levels of stress, some of them undergoing important shear and others barely any, resulting in a final size distribution that can be rather broad [41].

In conclusion, for our system composed of a fluid liquid metal alloy in a high viscosity polymer matrix under constant shear, the favored breakup mechanism seems to be the tip streaming. This results when quenching to a dispersion of solid ellipsoid drops of reduced size compared to the initial state before shear and smaller solid spherical drops that did not deform significantly with shear. The maximum size of the ellipsoid drops seems to be driven by the relation between the deformation parameter D and the capillary number C_a (Eq. 16): under constant shear the drops deform and D tends to the capillary number which is of the order of 1 or higher for drops of radius 100 μm or higher. The drops then break up (most probably by tip streaming) when their deformation D reaches the critical value $D_{crit} = 0.5$ determined by Taylor. C_a decreases as the drop size decreases and when it gets smaller than 0.5, the drop does not break up anymore and gets stable. The maximal size of the ellipsoid drop is then driven by $D_{max} = D_{crit} = 0.5$ as observed in Fig. 8-a and 8-b. Most dispersions of liquid metal drops in a polymer matrix contain spherical drops [17,19]. A dispersion of ellipsoids can lead for instance to lower percolation thresholds in a conductive composite material, reducing thereby the metal amount needed in the polymer matrix, with density and cost reductions as benefits.

5. Conclusion

In the present paper, we measured the interfacial tension between polypropylene and two molten metals (liquid eutectic SnAgCu alloy and liquid tin) using the method of shape relaxation of a deformed drop (RDDM). This study is the first of its kind, since there have been no reports so far of investigations on the interfacial tension between a liquid metal and a molten polymer matrix in the scientific literature. Systematic rheological measurements of the investigated materials were carried-out to measure the zero shear viscosities required in the RDDM approach. Since the viscosity of metal liquids is extremely sensitive to the presence of metal oxides, all experiments were performed under an oxygen-free environment. For the polypropylene matrices, zero shear viscosity values in the order of thousands Pa.s were measured, while for the liquid metals the zero shear viscosity was around 2 mPa.s. Our composite materials were thus characterized by an extremely low viscosity ratio $\eta_d/\eta_m (< 10^{-6})$. Using a Linkam high temperature stage coupled with a transmission microscope, spherical drops of liquid metal in PP matrix were deformed into elliptic shape drops and their retraction to spheres was video monitored. From the characteristic relaxation times of numerous drops of diverse radius, we calculated the interfacial tension values between PP and liquid tin or eutectic SnAgCu alloy. High values of interfacial tensions were measured, highlighting the poor affinities between PP and liquid metals, which makes impossible the percolation of liquid droplets in a polymer composite without coalescence and demixing, unlike in common polymer-polymer blends.

Using the Owens, Wendt and Wu equations, we compared our measured interfacial tension values to theoretical estimations using data from the scientific literature. A good agreement between theoretical and experimental values was noted with the eutectic SnAgCu alloy, but not with tin because of oxidation effects.

An interfacial tension value of 350 mN.m⁻¹ at 230°C between PP 7060 and eutectic SnAgCu alloy was measured. This system was chosen as it limited matrix viscoelasticity ($D_e < 1$) and metal oxide influences on interfacial tension measurement, while leading to measurable droplet relaxation times. We, thus, proved the possibility of using RDDM to measure interfacial tension between liquid metals and polymer matrices.

A quenching experiment under shear led to the creation of solid ellipsoid drops. The values of viscosity ratios, actual and critical capillary numbers suggest a tip streaming drop break-up mechanism. The final size of the drops is driven by the relation between the deformation parameter and the

capillary number, and the maximal size of the ellipsoid drops is reached when the deformation parameter reaches the value of 0.5, as observed by Taylor.

References

- [1] Sumita, M., K. Sakata, S. Asai, K. Miyasaka and H. Nakagawa. "Dispersion of fillers and the electrical conductivity of polymer blends filled with carbon black," *Polym. Bull.* **25**, 265–271 (1991).
- [2] Medalia, A. I. "Effect of carbon black on dynamic properties of rubber vulcanizates," *Rubber Chem Tech* **51**, 437–523 (1978).
- [3] Lecocq, H., N. Garois, O. Lhost, P.-F. Girard, P. Cassagnau and A. Serghei. "Polypropylene/carbon nanotubes composite materials with enhanced electromagnetic interference shielding performance: Properties and modeling," *Compos. Part B Eng.* **189**, 107866 (2020).
- [4] Huang, X., X. Qi, F. Boey and H. Zhang. "Graphene-based composites," *Chem Soc Rev* **41**, 666–686 (2012).
- [5] Elias, L., F. Fenouillot, J. C. Majeste and Ph. Cassagnau. "Morphology and rheology of immiscible polymer blends filled with silica nanoparticles," *Polymer* **48**, 6029–6040 (2007).
- [6] Wu, G., S. Gan, L. Cui and Y. Xu. "Preparation and characterization of PES/TiO₂ composite membranes," *Appl. Surf. Sci.* **254**, 7080–7086 (2008).
- [7] Ameli, A., M. Nofar, S. Wang and C. B. Park. "Lightweight Polypropylene/Stainless-Steel Fiber Composite Foams with Low Percolation for Efficient Electromagnetic Interference Shielding," *ACS Appl. Mater. Interfaces* **6**, 11091–11100 (2014).
- [8] Zheng, Q., X.-W. Zhang, Y. Pan and X.-S. Yi. "Polystyrene/Sn-Pb alloy blends. I. Dynamic rheological behavior," *J. Appl. Polym. Sci.* **86**, 3166–3172 (2002).
- [9] Zhang, X.-W., Y. Pan, Q. Zheng and X.-S. Yi. "Polystyrene/Sn-Pb alloy blends. II. Effect of alloy particle surface treatment on dynamic rheological behavior," *J. Appl. Polym. Sci.* **86**, 3173–3179 (2002).
- [10] Dickey, M. D., R. C. Chiechi, R. J. Larsen, E. A. Weiss, D. A. Weitz and G. M. Whitesides. "Eutectic Gallium-Indium (EGaIn): A Liquid Metal Alloy for the Formation of Stable Structures in Microchannels at Room Temperature," *Adv. Funct. Mater.* **18**, 1097–1104 (2008).
- [11] Wu, D., L. Wu, J. He, M. Zhang and C. Yan. "Poly(phenylene sulfide)/low-melting-point metal composites. I. Transient viscoelastic properties and crystallization kinetics," *J. Polym. Sci. Part B Polym. Phys.* **46**, 677–690 (2008).
- [12] Nesaei, S., D. J. Cavanagh and A. Gozen. "Rheology of liquid metal particle-based polymer composites: A comparative study," *J. Rheol.* **63**, 559–568 (2019).
- [13] Wang, Z., J. Ren, R. Liu, X. Sun, D. Huang, W. Xu, J. Jiang, K. Ma and Y. Liu. "Three dimensional core-shell structured liquid metal/elastomer composite via coaxial direct ink writing for electromagnetic interference shielding," *Compos. Part Appl. Sci. Manuf.* **136**, 105957 (2020).
- [14] Bo, G., L. Ren, X. Xu, Y. Du and S. Dou. "Recent progress on liquid metals and their applications," *Adv. Phys. X* **3**, 1446359 (2018).
- [15] Lashkari, O. and R. Ghomashchi. "The implication of rheology in semi-solid metal processes: An overview," *J. Mater. Process. Technol.* **182**, 229–240 (2007).

- [16] Siegel, A. C., S. S. Shevkoplyas, D. B. Weibel, D. A. Bruzewicz, A. W. Martinez and G. M. Whitesides. "Cofabrication of Electromagnets and Microfluidic Systems in Poly(dimethylsiloxane)," *Angew. Chem. Int. Ed.* **45**, 6877–6882 (2006).
- [17] Wang, H. *et al.* "A Highly Stretchable Liquid Metal Polymer as Reversible Transitional Insulator and Conductor," *Adv. Mater.* **31**, 1901337 (2019).
- [18] Zhang, W., J. Chen, X. Li and Y. Lu. "Liquid Metal-Polymer Microlattice Metamaterials with High Fracture Toughness and Damage Recoverability," *Small* **16**, 2004190 (2020).
- [19] Fassler, A. and C. Majidi. "Liquid-Phase Metal Inclusions for a Conductive Polymer Composite," *Adv. Mater.* **27**, 1928–1932 (2015).
- [20] Fafenrot, S., N. Grimmelmann, M. Wortmann and A. Ehrmann. "Three-Dimensional (3D) Printing of Polymer-Metal Hybrid Materials by Fused Deposition Modeling," *Materials* **10**, 1199 (2017).
- [21] Andersen, K., Y. Dong and W. S. Kim. "Highly Conductive Three-Dimensional Printing With Low-Melting Metal Alloy Filament," *Adv. Eng. Mater.* **19**, 1700301 (2017).
- [22] Wang, T., T.-H. Kwok and C. Zhou. "In-situ Droplet Inspection and Control System for Liquid Metal Jet 3D Printing Process," *Procedia Manuf.* **10**, 968–981 (2017).
- [23] Ma, M. and H. Zhang. "An experimental study of pneumatic extruding direct writing deposition-based additive manufacturing," *Int. J. Adv. Manuf. Technol.* **97**, 1005–1010 (2018).
- [24] Kesler, M. S. *et al.* "Liquid direct reactive interface printing of structural aluminum alloys," *Appl. Mater. Today* **13**, 339–343 (2018).
- [25] Battezzati, L. and A. L. Greer. "The viscosity of liquid metals and alloys," *Acta Metall.* **37**, 1791–1802 (1989).
- [26] Chapman, T. W. "The viscosity of liquid metals," *AIChE J.* **12**, 395–400 (1966).
- [27] Chanda, M. "Plastics Technology Handbook" (CRC Press, 2017).
- [28] Utracki, L. A. "Melt flow of polymer blends," *Polym. Eng. Sci.* **23**, 602–609 (1983).
- [29] Taguet, A., P. Cassagnau and J.-M. Lopez-Cuesta. "Structuration, selective dispersion and compatibilizing effect of (nano)fillers in polymer blends," *Prog. Polym. Sci.* **39**, 1526–1563 (2014).
- [30] Wu, S. "Interfacial and Surface Tensions of Polymers," *J. Macromol. Sci. Part C Polym. Rev.* **10**, 1–73 (1974).
- [31] Gancarz, T., Z. Moser, W. Gąsior, J. Pstruś and H. Henein. "A Comparison of Surface Tension, Viscosity, and Density of Sn and Sn–Ag Alloys Using Different Measurement Techniques," *Int. J. Thermophys.* **32**, 1210–1233 (2011).
- [32] Doudrick, K., S. Liu, E. M. Mutunga, K. L. Klein, V. Damle, K. K. Varanasi and K. Rykaczewski. "Different Shades of Oxide: From Nanoscale Wetting Mechanisms to Contact Printing of Gallium-Based Liquid Metals," *Langmuir* **30**, 6867–6877 (2014).
- [33] Elton, E. S., T. C. Reeve, L. E. Thornley, I. D. Joshipura, P. H. Paul, A. J. Pascall and J. R. Jeffries. "Dramatic effect of oxide on measured liquid metal rheology," *J. Rheol.* **64**, 119–128 (2020).
- [34] Larsen, R. J., M. D. Dickey, G. M. Whitesides and D. A. Weitz. "Viscoelastic properties of oxide-coated liquid metals," *J. Rheol.* **53**, 1305–1326 (2009).
- [35] Xu, Q., N. Oudalov, Q. Guo, H. M. Jaeger and E. Brown. "Effect of oxidation on the mechanical properties of liquid gallium and eutectic gallium-indium," *Phys. Fluids* **24**, 063101 (2012).
- [36] Wilhelmy, L. "Ueber die Abhängigkeit der Capillaritäts-Constanten des Alkohols von Substanz und Gestalt des benetzten festen Körpers," *Ann. Phys. Chem.* **195**, 177–217 (1863).
- [37] Hogness, T. R. "The surface tensions and densities of liquid Mercury, Cadmium, Zinc, Lead, Tin and Bismuth," *J. Am. Chem. Soc.* **43**, 1621–1628 (1921).
- [38] Wenzel, R. N. "Resistance of solid surfaces to wetting by water," *Ind. Eng. Chem.* **28**, 988–994 (1936).

- [39] de Gennes, P. G. "Wetting: statics and dynamics," *Rev. Mod. Phys.* **57**, 827–863 (1985).
- [40] Taylor, G. I. "The viscosity of a fluid containing small drops of another fluid," *Proc. R. Soc. Lond. Ser. Contain. Pap. Math. Phys. Character* **138**, 41–48 (1932).
- [41] Grace†, H. P. "Dispersion phenomena in high viscosity immiscible fluid systems and application of static mixers as dispersion devices in such systems," *Chem. Eng. Commun.* **14**, 225–277 (1982).
- [42] Xing, P., M. Bousmina, D. Rodrigue and M. R. Kamal. "Critical Experimental Comparison between Five Techniques for the Determination of Interfacial Tension in Polymer Blends: Model System of Polystyrene/Polyamide-6," *Macromolecules* **33**, 8020–8034 (2000).
- [43] Anastasiadis, S. H. "The Determination of Interfacial Tension by Video Image Processing of Pendant Fluid Drops," *J. Colloid Interface Sci.* **119**, 55–66 (1986).
- [44] Coucoulas, L. M. and R. A. Dawe. "The calculation of interfacial tension from sessile drops," *J. Colloid Interface Sci.* **103**, 230–236 (1985).
- [45] Patterson, H. T., K. H. Hu and T. H. Grindstaff. "Measurement of interfacial and surface tensions in polymer systems," *J. Polym. Sci. Part C Polym. Symp.* **34**, 31–43 (1947).
- [46] Palierne, J. F. "Linear rheology of viscoelastic emulsions with interfacial tension," *Rheol. Acta* **29**, 204–214 (1990).
- [47] Bousmina, M. "Effect of interfacial tension on linear viscoelastic behavior of immiscible polymer blends," *Rheol. Acta* **38**, 251–254 (1999).
- [48] Elmendorp, J. J. "A study on polymer blending microrheology," *Polym. Eng. Sci.* **26**, 418–426 (1986).
- [49] Carriere, C. J., A. Cohen and C. B. Arends. "Estimation of Interfacial Tension Using Shape Evolution of Short Fibers," *J. Rheol.* **33**, 681–689 (1989).
- [50] Rundqvist, T., A. Cohen and C. Klason. "The imbedded disk retraction method for measurement of interfacial tension between polymer melts," *Rheol. Acta* **35**, 458–469 (1996).
- [51] Luciani, A., M. F. Champagne and L. A. Utracki. "Interfacial tension coefficient from the retraction of ellipsoidal drops," *J. Polym. Sci. Part B Polym. Phys.* **35**, 1393–1403 (1997).
- [52] Deyrail, Y., R. Fulchiron and P. Cassagnau. "Morphology development in immiscible polymer blends during crystallization of the dispersed phase under shear flow," *Polymer* **43**, 3311–3321 (2002).
- [53] Deyrail, Y., A. Michel and P. Cassagnau. "Morphology in Immiscible Polymer Blends During Solidification of an Amorphous Dispersed Phase under Shearing," *Can. J. Chem. Eng.* **80**, 1017–1027 (2002).
- [54] He, Y., Y. Huang, Q. Li, Y. Mei, M. Kong and Q. Yang. "Morphological hysteresis in immiscible PIB/PDMS blends filled with fumed silica nanoparticles," *Colloid Polym. Sci.* **290**, 997–1004 (2012).
- [55] Siahcheshm, P., F. Goharpey and R. Foudazi. "Droplet retraction in the presence of nanoparticles with different surface modifications," *Rheol. Acta* **57**, 729–743 (2018).
- [56] Fortelný and Jůza. "Description of the Droplet Size Evolution in Flowing Immiscible Polymer Blends," *Polymers* **11**, 761 (2019).
- [57] Amani, A., N. Balcázar, J. Castro and A. Oliva. "Numerical study of droplet deformation in shear flow using a conservative level-set method," *Chem. Eng. Sci.* **207**, 153–171 (2019).
- [58] Hassan, M. R. "Magnetic field induced ferrofluid droplet breakup in a simple shear flow at a low Reynolds number," *Phys. Fluids* **31**, 127104 (2019).
- [59] Elhamnia, M., G. H. Motlagh and S. H. Jafari. "A multiple approach in determination of interfacial tension of biodegradable melt-mixed PBAT/EVOH blends: Correlation of morphology, rheology and mechanical properties," *Polym. Test.* **82**, 106301 (2020).
- [60] Amani, A., N. Balcázar, A. Naseri and J. Rigola. "A numerical approach for non-Newtonian two-phase flows using a conservative level-set method," *Chem. Eng. J.* **385**, 123896 (2020).
- [61] Boger, D. V. "A highly elastic constant-viscosity fluid," *J. Non-Newton. Fluid Mech.* **3**, 87–91 (1977).

- [62] Greco, F. "Drop deformation for non-Newtonian fluids in slow flows," *J. Non-Newton. Fluid Mech.* **107**, 111–131 (2002).
- [63] Minale, M. "Deformation of a non-Newtonian ellipsoidal drop in a non-Newtonian matrix: extension of Maffettone–Minale model," *J Non-Newton. Fluid Mech* **123**, 151–160 (2004).
- [64] Jackson, N. E. and C. L. Tucker. "A model for large deformation of an ellipsoidal droplet with interfacial tension," *J. Rheol.* **47**, 659–682 (2003).
- [65] Yu, W., C. Zhou and M. Bousmina. "Theory of morphology evolution in mixtures of viscoelastic immiscible components," *J. Rheol.* **49**, 215–236 (2005).
- [66] Fulchiron, R., A. Michel, V. Verney and J. C. Roustant. "Correlations between relaxation time spectrum and melt spinning behavior of polypropylene. 1: Calculation of the relaxation spectrum as a log-normal distribution and influence of the molecular parameters," *Polym. Eng. Sci.* **35**, 513–517 (1995).
- [67] Cardinaels, R. and P. Moldenaers. "Droplet relaxation in blends with one viscoelastic component: bulk and confined conditions," *Rheol Acta* **49**, 941–951 (2010).
- [68] Tretheway, D. C. and L. G. Leal. "Deformation and relaxation of Newtonian drops in planar extensional flows of a Boger fluid," *J. Non-Newton. Fluid Mech.* **99**, 81–108 (2001).
- [69] Taylor, G. I. "The formation of emulsions in definable fields of flow," *Proc. R. Soc. Lond. Ser. -Contain. Pap. Math. Phys. Charact* **146**, 0501–0523 (1934).
- [70] Minale, M., S. Caserta and S. Guido. "Microconfined Shear Deformation of a Droplet in an Equiviscous Non-Newtonian Immiscible Fluid: Experiments and Modeling," *Langmuir* **26**, 126–132 (2010).
- [71] Turng, L. S. and K. K. Wang. "Rheological behaviour and modelling of semi-solid Sn-15% Pb alloy," *J. Mater. Sci.* **26**, 2173–2183 (1991).
- [72] Salt, F. W. and J. G. N. Thomas. "Determination of the oxide film thickness on Tin," *Nature* **178**, 434–435 (1956).
- [73] Sosiati, H., N. Kuwano and S. Hata. "Electron Microscopy of the Tin-oxide Nanolayer Formed on the Surface of Sn-Ag-Cu Alloys," *IOP Conf. Ser. Mater. Sci. Eng.* **196**, 012006 (2017).
- [74] Tamai, T., Y. Nabeta, S. Sawada and Y. Hattori. "Property of Tin oxide film formed on Tin-plated connector contacts," in 1–8 (2010). doi:10.1109/HOLM.2010.5619529.
- [75] Shin, H.-C., J. Dong and M. Liu. "Porous Tin Oxides Prepared Using an Anodic Oxidation Process," *Adv Mater* **16**, 237–240 (2004).
- [76] Hunter, M. S. and P. Fowle. "Determination of Barrier Layer Thickness of Anodic Oxide Coatings," *J. Electrochem. Soc.* **101**, 481–485 (1954).
- [77] Brooks, R. F., A. T. Dinsdale and P. N. Quested. "The measurement of viscosity of alloys—a review of methods, data and models," *Meas. Sci. Technol.* **16**, 354–362 (2005).
- [78] Moser, Z., W. Gasior, J. Pstruś and S. Ksieżarek. "Surface-tension measurements of the eutectic alloy (Ag-Sn 96.2 at.%) with Cu additions," *J. Electron. Mater.* **31**, 1225–1229 (2002).
- [79] Souza, A. M. C. and N. R. Demarquette. "Influence of coalescence and interfacial tension on the morphology of PP/HDPE compatibilized blends," *Polymer* **43**, 3959–3967 (2002).
- [80] Lepers, J.-C., B. D. Favis and R. J. Tabar. "The relative role of coalescence and interfacial tension in controlling dispersed phase size reduction during the compatibilization of polyethylene terephthalate/polypropylene blends," *J. Polym. Sci. Part B Polym. Phys.* **35**, 2271–2280 (1997).
- [81] Owens, D. K. and R. C. Wendt. "Estimation of the surface free energy of polymers," *J. Appl. Polym. Sci.* **13**, 1741–1747 (1969).
- [82] Guggenheim, E. A. "The Principle of Corresponding States," *J. Chem. Phys.* **13**, 253–261 (1945).
- [83] Keene, B. J. "Review of data for the surface tension of pure metals," *Int. Mater. Rev.* **38**, 157–192 (1993).

- [84] Ricci, E., L. Nanni and A. Passerone. "Oxygen transport and dynamic surface tension of liquid metals," *Philos. Trans. R. Soc. Lond. Ser. Math. Phys. Eng. Sci.* **356**, 857–870 (1998).
- [85] Fiori, L., E. Ricci and E. Arato. "Dynamic surface tension measurements on molten metal-oxygen systems: model validation on molten tin," *Acta Mater.* **51**, 2873–2890 (2003).
- [86] Lee, J., T. Tanaka, M. Yamamoto and S. Hara. "Effect of Oxygen on Surface Tension of Liquid Ag-Sn Alloys," *Mater. Trans.* **45**, 625–629 (2004).
- [87] Khan, M. R., C. B. Eaker, E. F. Bowden and M. D. Dickey. "Giant and switchable surface activity of liquid metal via surface oxidation," *Proc. Natl. Acad. Sci.* **111**, 14047–14051 (2014).
- [88] Vananroye, A., P. V. Puyvelde and P. Moldenaers. "Effect of Confinement on Droplet Breakup in Sheared Emulsions," *Langmuir* **22**, 3972–3974 (2006).
- [89] Vinckier, I., P. Moldenaers and J. Mewis. "Relationship between rheology and morphology of model blends in steady shear flow," *J. Rheol.* **40**, 613–631 (1996).
- [90] Bates, F. S. "Polymer-polymer phase behavior," *Science* **251**, 898–905 (1991).
- [91] Anastasiadis, S. H. "Interfacial Tension in Binary Polymer Blends and the Effects of Copolymers as Emulsifying Agents," in *Polymer Thermodynamics* (eds. Wolf, B. A. & Enders, S.) vol. 238 179–269 (Springer Berlin Heidelberg, 2010).
- [92] Verilhac, K., M. Desse, C. Carrot and F. Fenouillot. "Mixing of polar and nonpolar molten olefinic copolymer with polar liquids in conditions of very low viscosity ratio: Shear dominated flows," *J. Rheol.* **60**, 1121–1135 (2016).
- [93] Deyrail, Y. and P. Cassagnau. "Phase deformation under shear in an immiscible polymer blend: Influence of strong permanent elastic properties," *J. Rheol.* **48**, 505–524 (2004).
- [94] Karam, H. J. and J. C. Bellinger. "Deformation and Breakup of Liquid Droplets in a Simple Shear Field," *Ind. Eng. Chem. Fundam.* **7**, 576–581 (1968).
- [95] Torza, S., R. G. Cox and S. G. Mason. "Particle Motions in Sheared Suspensions XXVII. Transient and steady deformation and burst of liquid drops," *J. Colloid Interface Sci.* **38**, 395–411 (1972).
- [96] de Bruijn, R. A. "Deformation and breakup of drops in simple shear flows," (Eindhoven University of Technology, 1989).
- [97] Rumscheidt, F. D. and S. G. Mason. "Particle motions in sheared suspensions XII. Deformation and burst of fluid drops in shear and hyperbolic flow," *J. Colloid Sci.* **16**, 238–261 (1961).

Chapter V. Effects of stearic acid addition on shielding properties of metal fillers-based composite materials

Chapter V. Effects of stearic acid addition on shielding properties of metal fillers-based composite materials

Abstract

The electromagnetic interference shielding properties of polypropylene-based composite materials filled with two different types of metal fillers are presented in the current study. We show that a substantial enhancement in the shielding effectiveness by up to 50 dB can be obtained by a co-segregation effect induced by the addition of stearic acid. Thus, PP-based composite materials with a shielding effectiveness as high as 90 dB at 2 mm thickness (using tin particles) and 91 dB at 1 mm thickness (using Ag-coated glass microfibers) are reported. The mechanism for this enhancement effect is unraveled through the analysis of the filler surface properties and investigations of the stearic acid distribution in the volume of the composite materials. Our finding could represent a powerful approach for increasing the shielding effectiveness of composite materials filled with metal fillers, while lowering the percolation threshold and preserving good mechanical properties and low density values.

Keyword: EMI shielding, electrical conductivity, fatty acid, filler segregation, metal filler, conductive composites.

Reformatted version of paper originally submitted to:

ACS Materials and Interfaces

Co-segregation driven enhancement in the electromagnetic interference shielding effectiveness of polypropylene/hybrid metal fillers composite materials

Hubert Lecocq¹, Olivier Lhost², Philippe Cassagnau¹, Guillaume Sudre¹, Pierre Alcouffe¹, Anatoli Serghei¹

¹*Institut des Matériaux Polymères, Université de Lyon, 69622 Villeurbanne, France*

²*TOTAL Research and Technology Feluy, C 7181, Feluy, Belgium*

1. Introduction

The recent decades have witnessed the rapid development of electronics and remote communications, the latter relying on the emission and reception of electromagnetic (EM) waves. One consequence is the dramatic increase of environmental EM pollution. Though a priori harmless to mankind, this pollution can have serious consequences on sensitive electronic devices (pacemaker, plane guidance systems, radars) such as system dysfunction and breakdown. This topic is even more crucial in in-vehicle systems where wave emitters and receptors are stacked in a confined space, making them likely to interfere one with each other. Metal plates, films or meshes are today the most used approaches to shield electronics or cables from environmental EM pollution or to isolate an EM emitting device from its neighbors. These materials, however, suffer from their high cost, corrosion sensitivity and high density, making them for instance not an optimal choice for light vehicles with reduced greenhouse gas emissions.

A promising alternative is the use of light conductive polymer composites with electromagnetic interference (EMI) shielding properties. This type of materials has drawn great interest for research and development, as testifies the great number of studies and literature reviews on the subject [1–3]. The choice of polymers is wide with the use of thermoplastic resins such as polypropylene (PP), PA, PC, PLA or PVDF, and thermoset resins such as epoxy resins, PDMS or PU. Composite electrical conductivity has been identified as one of the main parameter required to reach high EMI shielding effectiveness (EMISE) [3,4]. Materials with a conductivity value below 10^{-10} S/m are usually considered insulating, between 10^{-10} and 10^{-7} S/m the material is ideal for antistatic applications, between 10^{-7} and 1 S/m for

electrostatic discharge dissipation and above 1 S/m the material is suited for EMI shielding. To reach this high value of electrical conductivity and gain thereby EMI shielding properties, the previously evoked polymer matrices are mixed with micro and nanofillers in order to get conductive composites and nanocomposites.

Carbon-based fillers are an attractive choice as they display good electronic conductivity combined with a low density. Examples of popular such fillers for EMI shielding are conductive polymers [5], carbon black [6,7], carbon fibers [8], carbon nanotubes (CNT) [9–11] and graphene [12,13]. Metal fillers are also widely used due to their intrinsic conductivity that can lead to an enhanced shielding performance: steel fibers [14], nickel or silver nanoparticles [15,16], iron nanocrystals [17], copper nanowires [18,19] and even liquid metal [20] are examples of fillers of metallic nature. The use of heavy fillers can however lead to composite materials of high densities [15]. Lately, much attention has been drawn to composites exhibiting great EMI shielding properties based on MXenes, 2D inorganic fillers consisting of layers of transition metal carbides, nitrides or carbonitrides [21–23]. Ryu et al. recently measured an EMI shielding slightly below 40 dB at a frequency of 8 GHz with a sample thickness of 2 mm, using PC/ABS composite filled with 20 phr carbon fibers [8]. Similar shielding properties at 1 mm thickness and 8 GHz frequency using a PP matrix filled with 7.5 vol% (15 wt%) carbon nanotubes has been reported in one of our previous studies [10]. By trapping liquid eutectic GaIn in thermoset PDMS filaments arranged into a mesh, Wang et al. measured a shielding value of 50 dB at 3 mm thickness and 8 GHz frequency [20]. Due to their limited intrinsic conductivity compared to metal fillers, carbon filler-based composites often lead to lower shielding properties at a given shield thickness, unless carbon filler loading is increased which can have negative consequences on composite processing [10]. Several strategies exist to tackle this problem. A first one is combining different fillers in one polymer matrix to obtain a synergetic effect: the combination of different fillers can lead to a higher shielding effectiveness than for composite materials prepared using only one type of filler [24–27]. A second possible strategy relies on filler segregation and composite foaming: the conductive fillers can be segregated in one (percolated) phase of the composite material while the other phase does not contain any fillers [28–32], while foaming can lead to a guided percolation phenomenon [14,26,33]. While being able to increase the composite electrical conductivity and EMI shielding properties without increasing the fillers loading, the fillers segregation strategy can have dramatic effects on composite mechanical properties such as elongation at break and shock resistance [30,31].

To solve these multiple challenges, much interest has been drawn on hybrid fillers which exhibit large aspect ratios, leading to low percolation thresholds, high conductivities and low densities.

These hybrid filler-based composites show enhanced EMI shielding properties with a reduced amount of fillers, decreasing thereby the composite material density [34–36]. Silver-coated light particles and fibers are effective fillers due to the conductivity of silver, the highest of all metals [37], leading thus to composite materials with high EMI shielding properties [38–41]. Zeng et al. measured a shielding of more than 60 dB at 2 mm thickness and 8 GHz frequency dispersing 0.3 vol% of Ag-PVP nanowires in PDMS [38]. Coating cotton fibers with silver, Tan et al. obtained an impressive shielding value of 71 dB at 0.5 mm thickness and 8 GHz frequency for 1.61 vol% silver content in a non-woven fabric [39]. Hybrid silver-coated light fibers have therefore great potential as fillers for light composite materials with enhanced conductivity and EMI shielding properties.

One of the main challenges in developing conductive polymer composites for EMI shielding applications is obtaining enhanced conductive and shielding properties without increasing the filler loading, since increased filler loading usually leads to higher composite density and decreased mechanical properties. Here we report that, at a constant filler loading, the electromagnetic interference effectiveness of composite materials filled with metal fillers can be increased by as much as 50 dB by a co-segregation effect induced by the addition of stearic acid [42,43] that leads to a drastic change in the composite morphology. At the same time, a substantially lower percolation threshold is obtained, combined with good mechanical properties and low density values. The mechanism of this enhancement effect is unraveled in the current study by investigating the filler surface properties and the distribution of the stearic acid in the volume of the composite materials. Our finding could represent a powerful approach for increasing the shielding effectiveness of composite materials filled with metal fillers, while lowering the percolation threshold and preserving good mechanical properties and low density values.

2. Materials and methods

a. Materials

Polypropylene PP 7060 (density = 0.905 g.cm⁻³, MFI index = 12 g/10min, melting point T_m = 165°C) supplied by Total S.A. was used as a polymer matrix in this study. Tin microparticles (density = 7.29 g.cm⁻³, melting point T_m = 231°C) were purchased from GoodFellow. The particles average diameter is 45 µm. Silver-coated glass microfibers were purchased from Hart Materials UK (Grade

SG180 FB20). They are characterized by a silver content of 20 wt%, an average length of 180 µm, an average diameter of 15 µm and a density of 2.8 g.cm⁻³. Stearic acid flakes (melting point T_m = 67-72°C, reagent grade, 95% purity) was purchased from Sigma-Aldrich-Merck. Tables 1 summarizes some of the physical and chemical properties of stearic acid.

Table V - 1: Some physical and chemical properties of stearic acid [44]

Chemical formula	Melting point (°C)	Boiling point (°C)	Density at RT (kg.m ⁻³)	Solubility in water at RT (mg.L ⁻¹)	Solubility in PP at 200°C	Surface tension at 70°C (mN.m ⁻¹)	Electrical conductivity (S.m ⁻¹)
C ₁₈ H ₃₆ O ₂	69.6	282.4	837.4	3	Poorly soluble	28.2	10 ⁻⁹ (Insulating)

b. Fabrication of PP – tin microparticles and Ag-coated glass microfibers composites

PP composites based on tin microparticles and Ag-coated glass microfibers were fabricated using the melt blending method. PP 7060 was mixed with the fillers and the stearic acid using an internal mixer (Thermoscientific Polylab OS RheoDrive 7 Haake, 69 cm³ tank, roller rotors). Polymer pellets were first introduced in the mixer tank at low mixing speed (20 rpm), then fillers and stearic acid were added once the polymer resin was molten. For tin microparticles, mixer temperature was set to 190°C and the compounds were mixed at 30 rpm for 10 min and 50 rpm for 3 min. These temperature and speed conditions were chosen to prevent particles overheating and melting. For Ag-coated glass microfibers, the mixing was carried out at 200°C, 50 rpm for 6 min and 100 rpm for 4 min. Filler concentrations between 3 and 30 vol% for the tin particles and between 0 and 15 vol% for the stearic acid were employed. The torque applied on mixer rotors was recorded during the mixing processes. After mixing, the obtained composites were frozen with liquid nitrogen and pelletized using a Pulverisette 19 grinder. The obtained pellets were hot pressed at 200°C and 250 bar into plates and discs of 1 or 2 mm thickness, using a Servitec polystat 200 T press.

c. Electrical characterization of composites

In order to measure the electrical conductivity of the PP composites, plates of 50 mm x 75 mm x 1 mm were measured along the direction parallel to the sample surface (thus, in the same direction as the electric field of the electromagnetic wave passing through the samples). The electrical contacts were gold metallized to eliminate the influence of the contact resistance. The DC electrical conductivity was measured with a Novocontrol Alpha Broadband Dielectric/Impedance Spectrometer and a Fluke 289 multimeter. Four samples of each composition were measured to insure statistical significance of the experimental data.

d. Broadband EMI shielding measurements of composites

The electromagnetic interference shielding effectiveness (EMISE) of PP composites was measured using an Anritsu Shockline 2 ports Vector Network Analyzer (VNA, MS 46522B) and two types of measurement cells. From 50 kHz to 8 GHz, a coaxial cell (EpsiMu Multiwave PE 13 mm) was employed. With this cell, ring-shaped samples were used and electrical contacts between the cell and the sample were gold metallized. Between 8.2 and 12.4 GHz (X band) and between 12.4 and 18 GHz (K_u band), two waveguide cells were used (Pasternack PE-W90S001-6 1701 and PE-W62S001-6 1650). For these waveguide cells, the samples were in the form of small plates fitting in the waveguides. Experimental setups are illustrated in a previous work [10]. EMI shielding properties of Ag-coated glass microfibers-based composites were measured on 1mm-thick samples. The EMI shielding properties of tin particles-based composites were measured on 2mm-thick samples. Four samples of each composition were measured to insure statistical significance of the experimental data.

Before each set of measurements, the VNA was calibrated and the empty cells were measured to validate that no shielding occurred in the measured frequency band. The power was set to 0 dBm, which corresponds to 1 mW, and each point was the average of 5 measurements. The total shielding effectiveness SE_T, the reflection shielding SE_R and the absorption shielding SE_A were calculated from the measured S-parameters S₁₁ and S₂₁ [1,4], as follows:

$$R = |S_{11}^2| \quad (1)$$

$$T = |S_{21}^2| \quad (2)$$

$$SE_T = -\log_{10}(T) \quad (3)$$

$$SE_R = -\log_{10}(1 - R) \quad (4)$$

$$SE_T = -\log_{10} \left(\frac{T}{1-R} \right) \quad (5)$$

$$SE_T = SE_R + SE_A \quad (6)$$

The EMI shielding effectiveness (EMISE) of a given shield is defined as:

$$SE = -10 \log_{10} \left(\frac{P_t}{P_i} \right) = -20 \log_{10} \left(\frac{E_t}{E_i} \right) = -20 \log_{10} \left(\frac{H_t}{H_i} \right) \quad (7)$$

P_i , E_i and H_i are the incident power, electric field amplitude and magnetic field amplitude of the EM wave, respectively, and P_t , E_t and H_t the power and amplitudes of the transmitted wave through the shield. The shielding effectiveness is expressed in dB: while at 10 dB, 90% of the incident wave power is blocked by the shield, at 40 dB it is 99.99% of the wave power that is shielded. In general, a shielding value of 30–40 dB is necessary for commercial applications, but higher shielding values are usually required for aeronautical or military applications. Several shielding mechanisms take place when an EM wave strikes a shield. First, a part of the wave is directly reflected at the first air-material interface due to a discontinuity in the EM wave impedance [4,45]:

$$Z = \frac{E}{H} = \sqrt{\frac{\mu^*}{\epsilon^*}} = \sqrt{\frac{j\omega\mu'}{\sigma+j\omega\epsilon'}} \quad (8)$$

E is the electric field and H the magnetic field of the EM wave in the material. μ^* and ϵ^* are the complex magnetic permeability and dielectric permittivity of the material, respectively. ω is the angular frequency of the wave ($\omega = 2\pi f$, f the wave frequency), μ' and ϵ' are the real part of the permeability and permittivity, respectively, σ is the electronic conductivity of the material and j the imaginary number ($j^2 = -1$). The wave impedance of vacuum (and air) is a constant equal to $Z_0 = \sqrt{\mu_0/\epsilon_0} \approx 377\Omega$. The bigger the difference is between the air impedance Z_0 and the wave impedance Z , the more important will be the phenomenon of single reflection. Then, a part of the wave penetrates the shield and undergoes electromagnetic absorption through the thickness of the shield due to induced current dissipation, dielectric polarization, interfacial polarization, eddy current dissipation, hysteresis loss and

magnetic resonance loss [46]. These phenomena are described by a characteristic absorption length, also called skin depth [4,46]:

$$\delta = \sqrt{\frac{2}{\mu' \omega \sigma}} = \sqrt{\frac{1}{\mu' \pi f \sigma}} \quad (9)$$

When going through a length of δ , the EM wave loses 63% of its amplitude due to absorption. Thus, absorption is more important at higher frequencies and for higher conductivity values or when magnetic materials are employed. A third shielding mechanism at play is the multiple internal reflections. As the EM wave reaches the second rear material-air interface, a part of the wave goes through but the other part is reflected back to the first interface. On the way back it undergoes absorption again, gets transmitted and reflected at the first air-material interface and goes back to the second rear interface. Thus, the wave goes through an infinite number of goings and comings between the two air-materials interfaces, while its amplitude decreases at each passage. These three shielding mechanisms and their impact on total EMI shielding of a material were treated in detail in a previous study and led to the general EMISE formula for a homogeneous and isotropic material [10]:

$$SE_T = SE_A + SE_R + SE_M \quad (10)$$

$$SE_A = 20 \cdot \frac{d}{\delta} \log_{10}(e) \quad (11)$$

$$SE_R = -20 \cdot \log_{10} \left(\left| \frac{4Z_0 Z}{(Z+Z_0)^2} \right| \right) \quad (12)$$

$$SE_M = 20 \cdot \log_{10} \left(\left| 1 - \left(\frac{Z-Z_0}{Z+Z_0} e^{-d/\delta} \right)^2 \right| \right) \quad (13)$$

$$f_c = \frac{1}{\pi \mu' \sigma d^2} \quad (14)$$

where d is the shield thickness. The general conclusions that can be drawn are that at low frequencies (lower than the absorption characteristic frequency f_c [4]), EMI shielding is constant and depends solely on composite conductivity and thickness. Above f_c , shielding increases rapidly with frequency because of wave absorption. Thus, for homogeneous and isotropic materials (non-magnetic) the main parameters having a meaningful impact on EMI shielding are the material electrical conductivity, its thickness and the incident wave frequency. An increase of one of these three parameters results in an increase in the shielding effectiveness (in particular above the absorption characteristic frequency f_c).

e. Optical microscopy

Before observation, PP composites were cut in thin layers of 20 and 50 µm thickness using a Leica RM2265 microtome. Microscopy observations were made using an Olympus BX 41 microscope coupled with an Olympus DP 26 camera. Lens of magnification x4, x10 and x20 were used. Image analysis was done using the CellSensEntry software.

f. Transmission Infrared spectroscopy on filler – stearic acid mixes

Different ratios of tin particles and stearic acid, and Ag-coated glass fibers and stearic acid were put in a beaker, heated 10 min at 100°C in an oven and mixed vigorously with a spatula for 5 min. 2.5 mg of each of these blends (cooled down to room temperature) were grinded with 197.5 mg of KBr powder, introduced in a hydraulic press and pressed into thin disks between two mirror-smooth plates. Transmission infrared spectroscopy measurements were carried out using a Thermoscientific iS-10 spectroscope. The sample discs were introduced in the spectroscope dry chamber and measured at wavelengths ranging from 1000 to 4000 cm⁻¹ with an MCT/A detector (256 scans, high spectral resolution). A background spectrum with an empty chamber was measured prior samples measurements. For each compound ratio, three different samples were measured and the final curve was the average of the three experimentally measured curves.

g. Contact angle measurement on filler – stearic acid mixes

Several grams of the tin particles and Ag-coated glass fibers previously blended with the stearic acid at 100°C were introduced in a hydraulic press and pressed between two mirror-smooth surfaces. Small discs with a smooth surface were obtained. Contact angle measurements were made using a Kruss Easydrop experimental setup coupled with a Hamilton 500 µL syringe and an Allied Vision Technology Stinray camera. A 1 µL deionized water droplet was placed on the surface of the disks. Once the drop was stabilized, a picture of it was taken and analyzed with the Drop Shape Analysis software that automatically measures contact angles. For each compound ratio, ten water drops

distributed over three different samples were measured to insure statistical significance of the experimental data.

h. Transmission infrared microscopy on PP – filler composites

Transmission infrared microscopy was used to investigate the distribution of the stearic acid in the PP – tin particles composites. Microtome cut layers of 20 μm thickness were measured to insure good beam transmission through the sample. A Thermoscientific Nicolet iN 10 MX infrared microscope was used in transmission mode to carry-out these measurements. Samples were placed on a pressed disk of pure KBr of approximately 1 mm thickness and inserted in the dry microscope chamber. A window of $20 \times 20 \mu\text{m}^2$ was probed in order to differentiate particles concentrated domains (called particles domain) and domains with a deficit of particles (called polymer domain). The different domains were measured at wavelengths ranging from 1000 to 3500 cm^{-1} with a MCT/A detector (256 scans, high spectral resolution). A background spectrum was measured through the KBr disk alone prior samples measurements. For each composite, three polymer domains and three particles domains were measured on three different samples (nine spectra for each domain type) to insure statistical significance of the experimental data. Around the stearic acid peak at 1710 cm^{-1} , the spectral area under the curve was measured between 1680 and 1740 cm^{-1} with a relevant baseline correction relying on free of stearic acid composites spectra.

3. Results and discussion

a. Electrical conductivity of PP composites

Experimentally measured values of electrical conductivity of PP composites are displayed in Figure 1. Fig. 1-a shows the electrical properties of the composites prepared with tin particles. In dependence on the particles volume fraction, the composite conductivity goes from 10^{-8} S/m to more than 10^4 S/m (corresponding to metal conductivity). For composites prepared without the addition of stearic acid (filled dots), the material is insulating up to 15 vol% of particles and reaches a conductivity of 870 S/m at 30 vol% of particles. The critical concentration for which the composite materials go from insulating to conductive properties, called the percolation threshold, is an important parameter in the study of conductive materials [47]. A reduced percolation threshold means the possibility of

having a conductive composite with a lower conductive filler content, which can be of great advantage to conserve good mechanical properties and a low density.

The addition of stearic acid into the PP – tin composites (1 vol% of stearic acid per 5 vol% of particles) has a two-fold positive effect. The first positive effect is a percolation threshold that is considerably lowered, from 15 vol% to 7 vol%. Several composites which were insulating in the absence of stearic acid become thus conductive when the stearic acid is added during the melt blending process. The other positive effect brought by the addition of the stearic acid is the increased conductivity on the saturation plateau of the percolation curve. Thus, for 20 vol% and 30 vol% particles concentrations, the conductivity increased from 140 to 1000 S/m and from 870 to 20,000 S/m, respectively, by adding the stearic acid. It is worth mentioning that the stearic acid has a negligible conductivity value [44], consequently, the increased conductivity obtained with the addition of the stearic acid cannot be attributed to an increment of the composites conductive content.

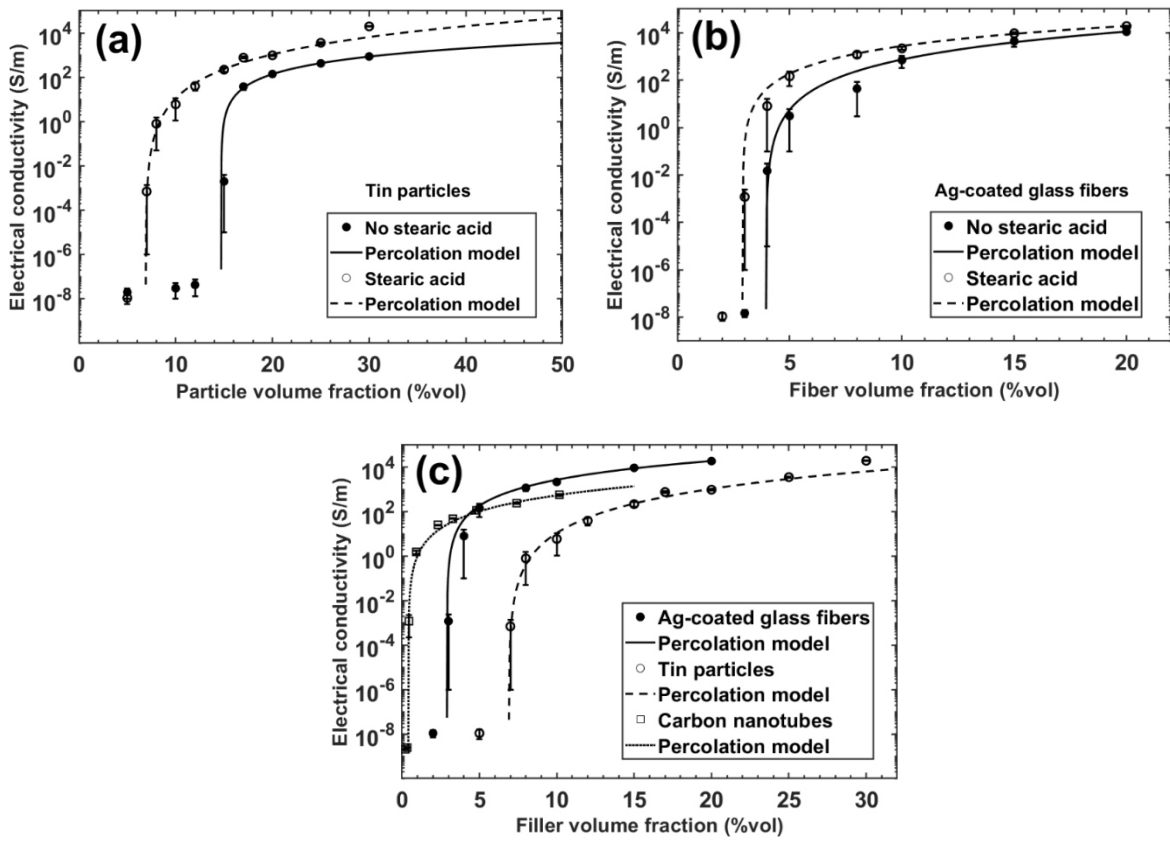


Figure V - 1: Electrical conductivity of PP/tin particles and PP/Ag-coated glass fibers composites. (a) Conductivity of PP - tin particles with and without stearic acid as a function of particle volume fraction (1 vol% of stearic acid per 5 vol% particles). Continuous lines are fitted percolation law. (b) Same as before with Ag-coated glass fibers. (c) Comparison of previous composites with stearic acid is made with PP – CNT composite from a previous work [10] (Chapter III).

Stearic acid is a saturated fatty acid with amphiphilic properties due to its carboxyl chemical head and long carbon tail. It can be fabricated artificially but is mainly obtained by splitting natural fats and oils. Sunflower oil, beef tallow and cocoa butter are great sources of stearic acid [44]. Thanks to their properties, fatty acids are often used in the processing and cosmetic industries. Their ability to interact and react with inorganic and metal surfaces can improve filler dispersion and stabilization in a polymer matrix as well as composite processability due to their lubricating effects [42,43,48–50]. Addition of stearic acid in composites containing conductive fillers was often linked with the improvement of mechanical, dielectric and conductive properties as well as EMI shielding properties [51–55]. Xiong et al. observed a decrease of composite resistivity from $10^{10} \Omega\text{.cm}$ to less than $10^6 \Omega\text{.cm}$ when adding 11.5 vol% of stearic acid to a PU/6.5 vol% carbon black composite [56]. Vanga-Bouanga et al. noticed the same phenomena in a HDPE/ polyaniline composite where the electrical conductivity at 10 wt% PANI increased from $3.3 \times 10^{-17} \text{ S/cm}$ to $7.3 \times 10^{-10} \text{ S/cm}$ when adding 1 wt% stearic acid [57]. These results are thus in agreement with the results presented in our study.

The experimental points can be fitted with the empirical percolation law proposed by Kirkpatrick [47]:

$$\sigma = \sigma_0(\varphi - \varphi_c)^t \quad \text{with } \varphi > \varphi_c \quad (15)$$

The composite conductivity is σ , σ_0 is a constant related to the intrinsic conductivity of the fillers and t a critical exponent dependent on the dimensionality of the conductive network. Fitting parameters are listed in Table 2.

Table V - 2: Percolation law fitting parameters according to Eq. 15 for PP composites with and without stearic acid. R is the determination coefficient.

Filler	Stearic acid (vol%)	φ_c	$\sigma_0 (\text{S/m})$	t	R^2
Tin particles	0	0.147	2.16×10^4	1.72	0.9961
	1 per 5 vol% particles	0.069	6.83×10^5	3.17	0.9413
Ag-coated glass fibers	0	0.0395	1.81×10^6	2.7	0.9953
	1 per 5 vol% fibers	0.029	9.44×10^5	2.2	0.9986

Conductivity constants obtained for PP/tin composites are lower than the tin intrinsic conductivity reported at $9.17 \times 10^6 \text{ S.m}^{-1}$ [37]. This can be attributed to the contact resistance between the tin particles that reduces the global composite conductivity. The constant is higher in the presence of stearic acid though, suggesting that the electrical contacts between the particles are better or more

numerous for a given amount of fillers. The critical exponent parameter t is close to 2 in the absence of stearic acid, suggesting a 3D homogeneous percolation. With the addition of stearic acid, this parameter is higher (= 3.17), suggesting a non-homogeneous 3D percolation. Exponent parameters higher than 2 are often found in segregated structures [18,58,59], implying filler segregating effects taking place in the presence of the stearic acid.

Similarly to tin particles, the composite materials prepared with silver-coated glass microfibers are insulating at low filler loading and the conductivity increases rapidly when the percolation threshold is reached. The experimental points can be fitted by the percolation law expressed by Eq. 15. The estimated percolation thresholds are thus 3.95 vol% without stearic acid and 2.9 vol% with the stearic acid. Though lowering the percolation threshold and increasing global composite conductivity, the effect of stearic acid is less pronounced with the Ag-coated microfibers than with the tin particles. The intrinsic electrical conductivity of silver is 6.3×10^7 S.m⁻¹ [37], higher than the conductivity constants obtained for our composite materials, implying a non-negligible contact resistance between the microfibers. Values close to 2 are obtained for the critical exponent t , suggesting a homogeneous 3D percolation [47].

In Fig. 1-c, the electrical properties of PP/tin particles and PP/Ag-coated fibers composites with stearic acid (1 vol% of stearic acid per 5 vol% of filler) are compared to the conductivity of CNT-based composites from a previous study [10] (same polymer matrix). The lowest percolation threshold are obtained with the CNT composites (0.4 vol%), but the highest conductivities are reached using metal fillers. The composites prepared with the silver-coated glass microfibers constitute thus a good compromise between a low percolation threshold/medium conductivity obtained with the CNT-based composites and high percolation threshold/high conductivity observed with tin particles-based composites. Consequently, fibers-based composites provide opportunities for high conductivity and high EMI shielding composite materials with low filler contents.

The conductivity of the PP composites prepared with the two types of fillers is shown in Fig. 2, as a function of the volume fraction of the stearic acid. At 15 vol% tin particles (Fig. 2-a), conductivity increases considerably even with the addition of 0.2 vol% of stearic acid. The large increase from 0.002 S/m for composites prepared without the addition of stearic acid to 2600 S/m with the addition of 10 vol% stearic acid can be explained by the fact that the 15 vol% particles concentration is very close to the percolation threshold. The increase is comparatively less important at 20 vol% particle since the composite material is already well percolated.

It can be noted that, for 15 vol% tin particles, conductivity decreases at 15 vol% stearic acid as compared to 10 vol% stearic acid. An excess of stearic acid seems thus to be deleterious to composite electrical properties. This matter will be discussed later. Similarly, for fiber-based composites (Fig. 2-b) at a given fiber content, the composite conductivity increases with the increase in the fatty acid volume fraction. At 8 and 10 vol% of Ag-coated glass fibers, conductivity goes from 44 S/m without stearic acid to 1200 S/m with 2 vol% of stearic acid and from 700 to 2200 S/m, respectively. A maximal value of 1.4×10^4 S/m was reached for 20 vol% fibers with 1.5 vol% stearic acid. Conductivity seems to decrease at higher fractions of fatty acid, as also observed for the tin particles.

Similar high conductivities were measured in some other studies. Duan et al. measured a conductivity value of 2648 S/m for 2.58 vol% of nickel particles dispersed in a UHMWPE polymer matrix [16]. Coating cotton fibers with 2.6 μm -thick layer of silver nanoparticles, Gao et al. measured a conductivity value of 9.8×10^5 S/m on non-woven fabric [19]. This study highlights the benefit of using Ag-coated fibers to reach high conductivity values.

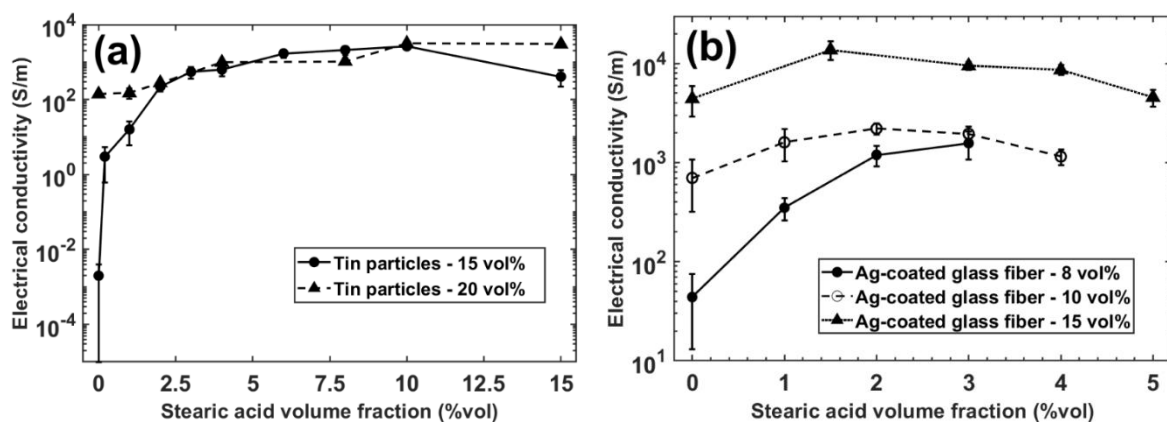


Figure V-2: Composites conductivity in function of stearic acid volume fraction. (a) PP – tin particles composites at 15 and 20 vol% particles. (b) PP – Ag-coated glass fibers composites at 8, 10 and 15 vol% fibers.

b. EMI shielding properties of PP composites measured in coaxial cell

The high electrical conductivities measured on our PP composites give them a great EMI shielding potential. Indeed, according to the shielding theoretical model presented in Eqs. 10–13, a high composite conductivity is expected to enhance the shielding properties. The EMI shielding properties measured in coaxial cell from 100 kHz to 8 GHz for PP/tin microparticles and PP/silver-coated glass microfibers composites prepared without the addition of stearic acid are shown in Figure 3-a and 3-b, respectively. The shielding effectiveness of PP/tin particles composites is 0 dB at 15 vol% particles but reaches 31 dB and 48 dB (at low frequencies) at 20 and 30 vol% particles, respectively.

A drop of shielding effectiveness can be observed at high frequencies, attributed to an inductive impedance contribution that is known to lower the effective conductivity of metal materials. This drop in EMI shielding with increasing frequency is also reported in numerous other studies dealing with metal filler-based materials and composites [60–67]. Lee et al. measured a drop of EMI shielding from 80 dB at 300 kHz to 60 dB at 12 GHz for a PS matrix filled with copper coated polymer beads [60]. For a bamboo fabric coated with silver and nickel, Lu et al. observed a decreasing shielding value from 54.5 dB at 30 MHz to 49 dB at 1 GHz [65].

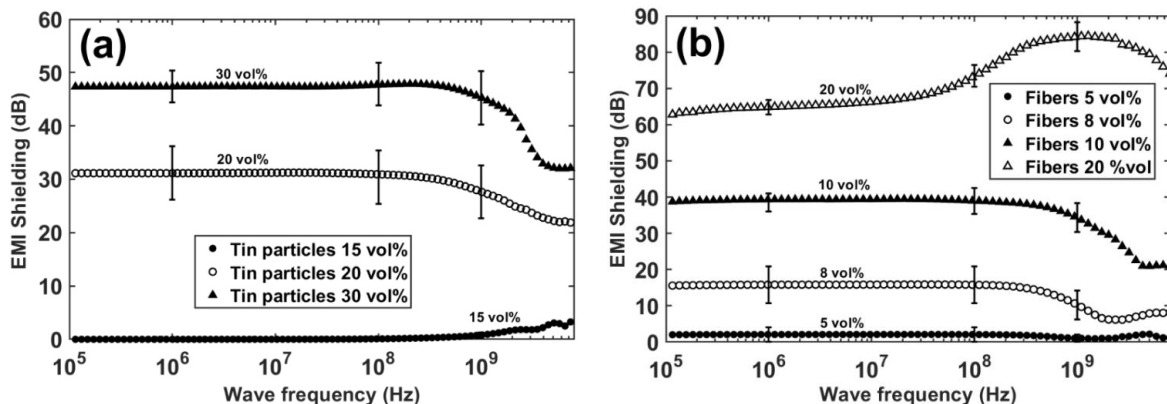


Figure V - 3: Shielding in function of frequency measured in coaxial cell of PP – tin particles and PP – Ag-coated glass fibers for different filler volume fraction. (a) PP – Tin particles composites, sample thickness is 2 mm. (b) PP – Ag-coated glass fibers composites, sample thickness is 1 mm.

Similar observations can be made for the PP/Ag-coated microfibers composites (Fig. 3-b): an increase in the global shielding effectiveness with increasing the fibers volume fraction and a drop of the shielding effectiveness at high frequencies are observed. Shielding values of 40 dB and 65 dB at low frequencies are obtained for 10 and 20 vol% of fibers, respectively, for a shield thickness of 1 mm.

An increase of shielding at high frequencies is observed for 20 vol% fibers, suggesting the onset of wave absorption phenomena. Calculating the value of the absorption characteristic frequency f_c (Eq. 14 with $\sigma = 11,000 \text{ S/m}$), one gets 23 MHz which is in agreement with the onset of the EMI absorption effects observed in the measured shielding spectra.

As composite conductivity increases with increasing the stearic acid volume fraction, EMI shielding follows the same path as displayed in Figure 4. In Fig. 4-a is shown the measured shielding of the PP/15 vol% tin particles composites (2mm thickness) with different amounts of stearic acid using the coaxial cell method. The increase in the global shielding with the stearic acid content is substantial. The composite with 15 vol% tin and no fatty acid exhibits no shielding properties whereas the one with 10 vol% stearic acid shows a value of 57 dB at low frequencies and reaches a maximal value of 76 dB at 2 GHz. It is worth reminding the fact that the stearic acid does not have any electrical conduction properties [44]. As before, a drop of shielding in the high frequencies can be observed. For composites with 3, 6, 8 and 10 vol% stearic acid, shielding first increases with increasing frequency due to EM wave absorption phenomenon and then drops. The calculated characteristic absorption frequencies (Eq. 14) match with the onset of the shielding increase with frequency observed in the measured spectra.

The composite shielding effectiveness as a function of the stearic acid volume fraction for 15 vol% and 20 vol% tin particles is displayed in Fig. 4-b and 4-c, for two frequencies: 1 MHz (low frequency where the wave reflection mechanism dominates the shielding) and 2 GHz (high frequency where reflection and absorption are predominant). For both particles concentrations, the shielding increases with the stearic acid volume fraction, at both frequencies. The drop of shielding observed at high frequencies becomes significant starting with a frequency of 2 GHz.

Similarly to the behavior observed for the conductivity, an excess of stearic acid has a negative impact on EMISE. This phenomenon has been investigated and related to changes in the mixing conditions. Mixing shear forces were observed to be dramatically reduced with the excessive 15 vol% stearic acid concentration as indicated by the considerably lowered torque measured during mixing. This lowered mixing shear is expected to lead to a less efficient filler dispersion in the composite material, resulting in lower physical properties. This effect can be attributed to the lubricating properties of stearic acid that can accumulate at the interface between the molten mix and the mixer tank walls [43,49]. The mixing torque values for tin particle-based composites are displayed in Figure S1, page 190, in the Supplementary Information Part.

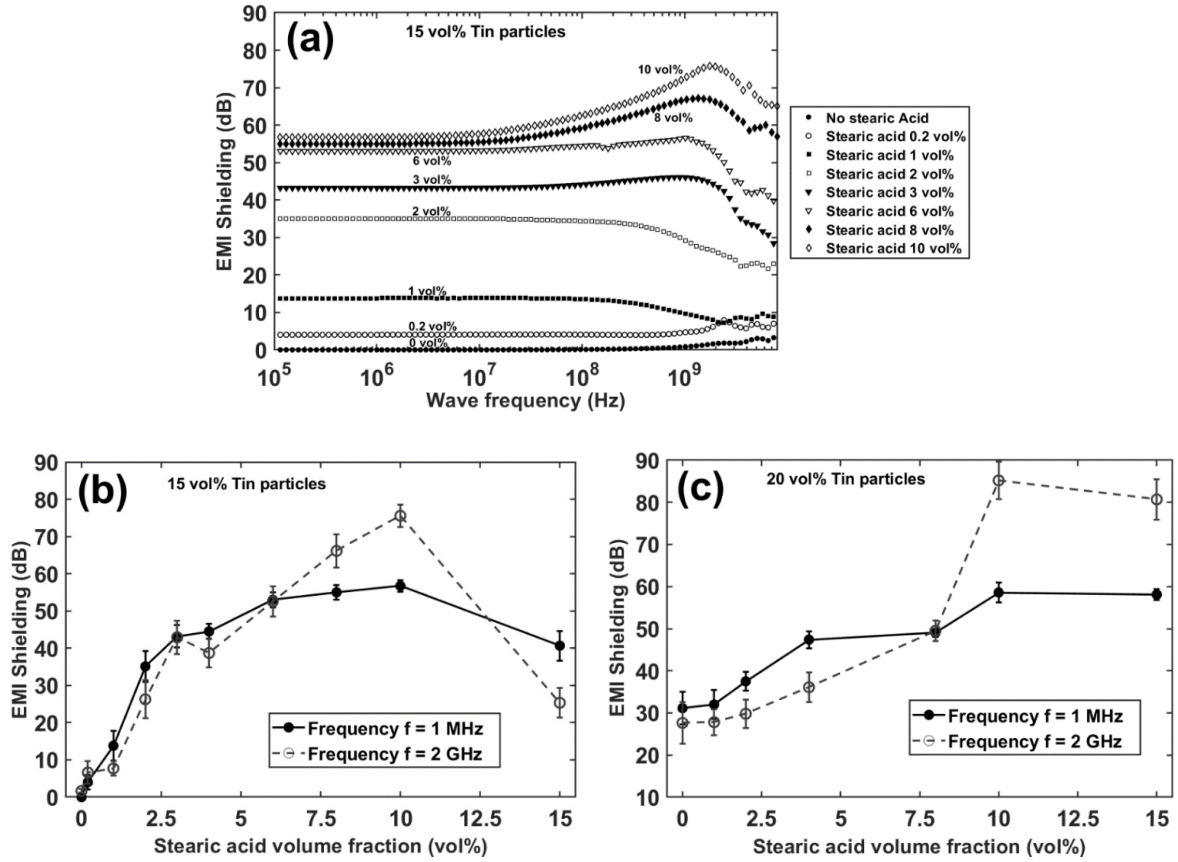


Figure V - 4: Shielding measured in coaxial cell of PP – tin particles with stearic acid for 2 mm-thick samples. (a) As a function of frequency for different stearic acid volume fraction at 15 vol% particles volume fraction. (b) As a function of stearic acid volume fraction at frequencies $f = 1$ MHz and $f = 2$ GHz for 15 vol% particles volume fraction. (c) Same as before for 20 vol% particles volume fraction.

As displayed in Figure 5, similar observations can be made concerning Ag-coated glass fiber-based composites: the addition of stearic acid has a positive impact on the shielding for 10 vol% fibers. Indeed, EMI shielding increases from 40 to 49 dB at 1 MHz and from 29.5 to 63 dB at 2 GHz when adding 2 vol% stearic acid. The increase is particularly significant at high frequencies as the addition of fatty acid seems to mitigate the shielding drop with frequency observed in the composites free of stearic acid and favor the shielding increase due to absorption. The characteristic absorption frequencies f_c (Eq. 14) match well the shielding increase observed in the measured spectra with increasing frequency. The shielding as a function of the stearic acid volume fraction at 1 MHz and 2 GHz for 8, 10 and 15 vol% microfibers is displayed in Fig. 5-b and 5-c.

Similarly to tin particles based composites, shielding increases with increasing the stearic acid concentration, reaching the top value of 88 dB at 2 GHz for the 15 vol% fibers / 4 vol% stearic acid composite at 1mm thickness. While the high frequency shielding value is lower than the low frequency

one at low stearic acid concentrations because of the shielding drop with frequency, this tendency reverses in the presence of the fatty acid. For the three fiber concentrations, an optimal stearic acid concentration is observed (2 vol% for 8 and 10 vol% fibers, 4 vol% for 20 vol% fibers) and seems roughly proportional to the fiber content: the optimal stearic acid concentration appears to be about 2 vol% stearic acid per 10 vol% fibers. Above this optimal concentration, the composite shielding properties start to decrease. Like tin particles composites, the composite mixing shear (related to the mixer measured torque) is observed to decrease dramatically at 4 vol% stearic acid compared to lower concentrations. The torques measured for PP/silver-coated glass fibers/stearic acid composites are shown in Figure S2, page 190, in the Supplementary Information Part. EMI shielding properties and electrical conductivity of PP composites with and without stearic acid are listed in Table 3, for other filler concentrations.

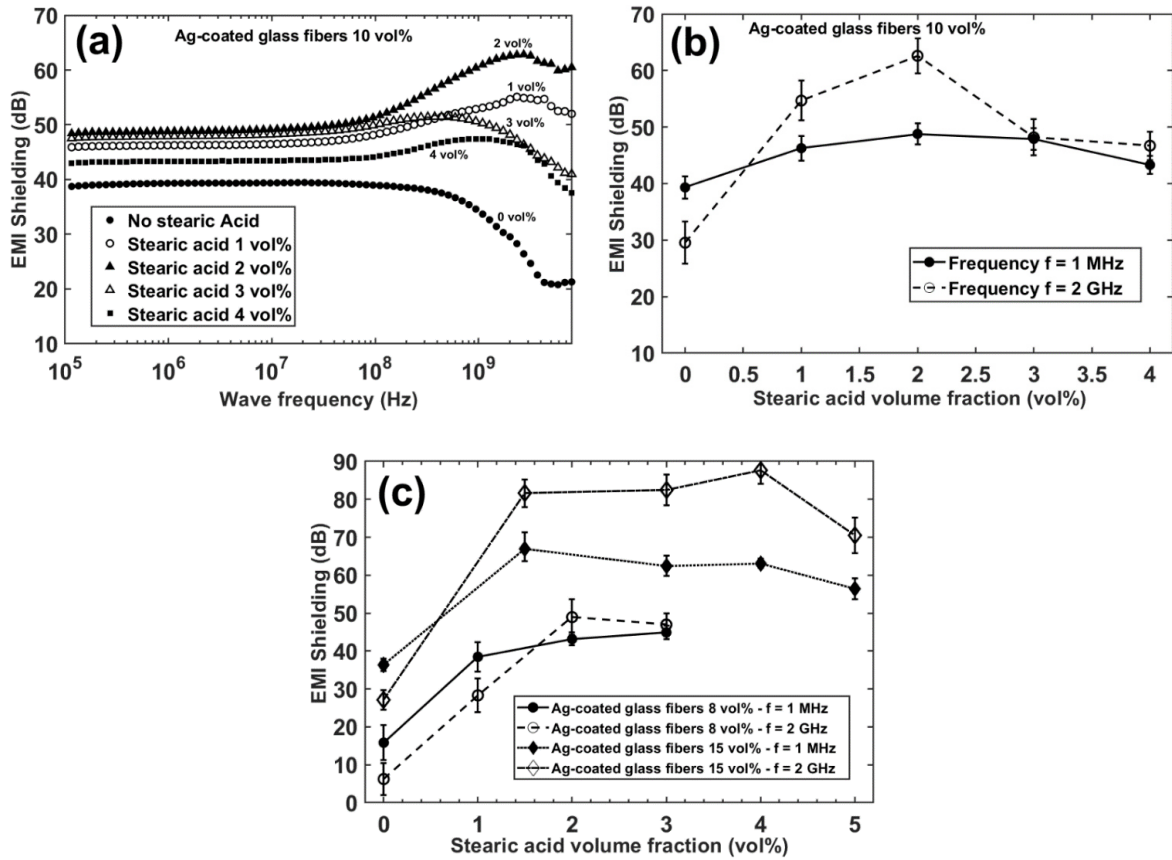


Figure V - 5: Shielding measured in coaxial cell of PP – Ag-coated glass fibers with stearic acid for 1 mm-thick samples. (a) As a function of frequency for different stearic acid volume fraction at 10 vol% particles volume fraction. (b) As a function of stearic acid volume fraction at frequencies $f = 1$ MHz and $f = 2$ GHz for 10 vol% microfibers. (c) Same as before for 8 and 15 vol% microfibers.

Table V - 3: Measured electrical conductivity and EMI shielding of PP composites with and without stearic acid. The EMI shielding samples of tin particles composites are 2mm-thick and the composites prepared with the Ag-coated glass microfibers are 1mm-thick.

Filler	Filler vol%	Stearic acid vol%	Electrical conductivity (S/m)	EMI shielding at 1 MHz (dB)	EMI shielding at 2 GHz (dB)
<i>Tin particles</i>	25	0	430 ± 20	43 ± 2	45 ± 2
		5	3600 ± 200	60 ± 3	65 ± 3
	30	0	870 ± 50	47 ± 2	42 ± 2
		6	19700 ± 700	74 ± 4	90 ± 5
<i>Ag-coated glass fibers</i>	5	0	3.1 ± 2	2.2 ± 1	1.1 ± 0.6
		1	100 ± 70	18 ± 3	9 ± 2
	20	0	11000 ± 1000	63 ± 2	84 ± 4
		4	19000 ± 1000	69 ± 2	91 ± 4

These observations are similar to the previously presented results, pointing out an increase of conductivity and shielding effectiveness with the addition of stearic acid. Top values of 90 and 91 dB are reached with 30 %vol tin particles composite (2mm thickness) and with 20 vol% Ag-coated glass fibers composite (1 mm thickness), respectively.

c. EMI shielding properties of PP composites measured in waveguides

EMI shielding properties of the two composite materials measured from 8.2 to 18 GHz using the waveguide method are displayed in Figure 6. The experimental results of the two waveguides (8.2 – 12.4 GHz and 12.4 – 18 GHz) are concatenated and displayed in the same graphs. The EMI shielding measured using waveguides as a function of frequency for the composites with 15 vol% tin particles with different stearic acid concentrations is presented in Fig. 6-a. Unlike the previous results measured with the coaxial cell, shielding without stearic acid is not zero, but close to an average of 20 dB for a 2mm thickness. As indicated also in Fig. 6-b, the stearic acid concentrations leading to larger increases of EMI shielding at 12 GHz seem to be situated in the range between 2 and 6 vol%. As discussed before, shielding decreases at higher fatty acid concentrations. For composites with 20 vol% tin particles, a monotonic increase of shielding with the stearic acid volume fraction is noted, with no decrease at high fractions. This phenomenon was also observed in the coaxial cell and can be related to the fact that, contrary to the composite at 15 vol% of particles, the composite at 20%vol is already well percolated without the presence of stearic acid. The impact of the addition of fatty acid on the

composite electromagnetic properties becomes thus less important at higher particles concentrations. The addition of stearic acid turns out to be a powerful tool to obtain higher shielding properties at limited filler loading in composite materials filled with metal fillers.

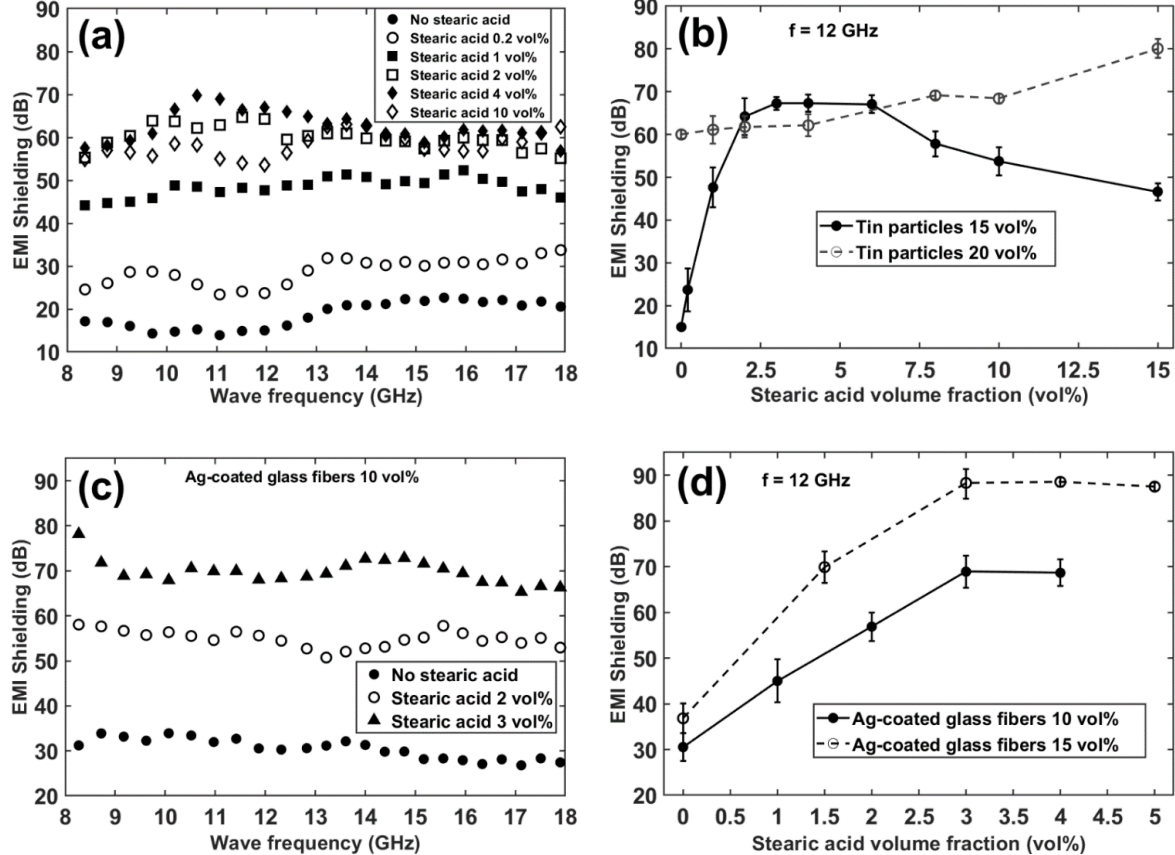


Figure V - 6: Shielding measured in waveguides for PP – tin particles and PP – Ag-coated composites. (a) As a function of frequency for different stearic acid volume fraction at 15 vol% particles. Sample thickness is 2 mm. (b) As a function of stearic acid volume fraction at frequency $f = 12$ GHz for 15 and 20 vol% particles. (c) As a function of frequency for different stearic acid volume fraction at 10 vol% fibers. Sample thickness is 1 mm. (d) As a function of stearic acid volume fraction at frequency $f = 12$ GHz for 10 and 15 vol% fibers.

The EMI shielding properties of the PP/Ag-coated glass fibers/stearic acid composites are shown in Fig. 6-c and 6-d. At 10 vol% fibers, the optimal stearic acid concentration is reached at 3 vol% giving a shielding value as high as 70 dB at 12 GHz and 1mm thickness. The optimal concentration seems to be 3 vol% stearic acid for 15 vol% fibers. Above these optimal concentrations, EMI shielding does not decrease nor increase. A top value as high as 88 dB is reached by the 15 vol% fibers particles with 3 vol% stearic acid. The stearic acid turns out to have a substantial positive impact on the

conductivity and EMI shielding properties of PP composites. The existence of an optimal fatty acid concentration, or concentration range, is observed: 6 – 10 vol% and 10 vol% stearic acid for 15 and 20 vol% tin particles respectively (about 1 vol% stearic acid per 2 vol% tin particles). For fibers-based composite materials, the optimal stearic acid concentrations are 2 – 3 vol% stearic acid for 10 vol% microfibers and 3 vol% stearic acid for 15 vol% microfibers (about 1 vol% per 5 vol% microfibers).

Conductivities and EMI shielding properties of the composites are listed in Table 4 and compared with other composites found in the literature. The composites investigated in our study rank among the most effective materials for shielding and conductivity. The PP/10 vol% Ag-coated glass fibers/3 vol% stearic acid composite exhibits the highest value of EMI shielding at 8.2 GHz for the 1mm thickness. Olivero and Radford studied silver-coated glass fibers-based composites and measured a shielding effectiveness of 51 dB at 19 vol% fibers and 1.6 mm thickness [40].

Table V - 4: Conductivity and EMI shielding properties in the X-band at 8.2 GHz of polymer composites found in the literature.

Polymer matrix	Filler	Filler content	σ (S/m)	EMI sample thickness (mm)	EMI shielding (dB)	Ref.
PP	Tin particles*	15 vol%	2600	2	67	Our work
PP	Ag-coated glass fibers*	10 vol%	2200	1	70	Our work
PC / ABS	Carbon Fibers	20 phr	1050	2	40	[8]
PP	CNT	10 vol%	580	1	58	[10]
PU	Graphene	20 wt%	830	1.5	61	[68]
PP	Stainless steel fibers	1.5 vol%	0.1	3.1	40	[14]
Epoxy	MXenes	15 wt%	100	2	41	[22]
UHMWPE	Ni particles	2.58 vol%	2650	2	52	[16]
EMA / EOC	Cu nanowires	15 wt%	1000	1	45	[18]
PDMS	Liquid eGaN	8.43 vol%	40 000	3	50	[20]
PDMS	Ag-PVP nanowires	0.26 vol%	1400	2	70	[38]
Epoxy	Ag-coated glass spheres	19 vol%	-	1.6	64	[40]
Epoxy	Ag-coated glass fibers	19 vol%	-	1.6	51	[40]
PLA	Ag-coated PLA fibers	5.8 vol%	254	1.5	49	[41]

*with stearic acid

Our materials also display a low density (below 1.3 g.cm⁻³), becoming thus comparable to carbon filler-based composites. Furthermore, enhanced mechanical properties compared to CNT-based composites are obtained with an elongation at break equal to 12.3% compared to 3.8% for CNT-based composite, both at 10 vol% filler loading. Density and tensile mechanical properties are displayed in Table S1 and Figure S3, page 191, in the SI Part. Thus, high conductive and shielding properties combined with low density and good mechanical properties make the PP/silver-coated glass fibers/stearic acid composite a material of choice for high performance shielding applications where light materials are demanded, such as for instance in the automotive or aeronautics industries.

d. Morphology of composites

The microscale morphology of the two composite materials was investigated using optical microscopy in order to unravel the important changes in the electromagnetic properties with the addition of stearic acid. Optical images are shown in Figure 7. Using the microtome cutter, slices of 20 and 50 µm in thickness could be prepared and observed. Microscopic images taken on 20µm-thick composite layers for the composite with 15 vol% tin particles with no stearic acid and with 6 vol% stearic acid are displayed in Fig. 7-a and 7-b. This stearic acid concentration was chosen as it gives among the best increase in electromagnetic properties. The difference of morphology is striking: with no stearic acid, the tin particles are well dispersed in the PP matrix with little to no particle percolation. With the addition of stearic acid, the particles are aggregated with aggregate sizes comprised between 100 and 300 µm in diameter. Areas between the aggregates – ranging from 100 µm to 400 µm in size – are relatively free of particles and constitute the polymer domains.

At first glance, there seem to be few contacts between the aggregates, but a closer look at Fig. 7-d presenting a thicker 50 µm layer indicates multiple contacts between the aggregates. These multiple contacts form a 3D network, explaining the conductive nature of this composite. The same observation made on stearic acid free composite shows again few to no particle-particle contacts. The addition of stearic acid to the composites with tin particles has thus the effect of aggregating the particles, favoring particles percolation on the composite macroscale and improving thereby the electrical conductivity as well as the shielding properties. The observed morphologies can be readily related to the measured conductivity and shielding properties of the investigated materials. Filler segregation is well known to improve electrical and shielding properties for a given filler concentration [29–31,58]. However, a multiple steps experimental procedure is often required to get composites

with segregated fillers. In this work, composites with aggregated filler showing enhanced electromagnetic properties are readily obtained by adding stearic acid, which is a cost-effective approach for industrial scale composite manufacturing.

Another effect of the addition of stearic acid to tin particle composites is particle-particle lubrication. Comparing Fig. 7-a and Fig. 7-b, the presence of multiple small particles of a few microns in diameter among dispersed particles of 10 μm and larger diameters in the composite free of stearic acid can be observed. The smaller particles might have been formed by erosion due to particle-particle contacts during mixing, since these small particles are much less present in the composite made with stearic acid.

This lubrication effect of stearic acid is also visible in the torque measured during mixing (Figure S2, page 190) with a lower torque for the composites with stearic acid and the absence of great torque variations suggesting eroding particle-particle contacts in the absence of the fatty acid [43,49].

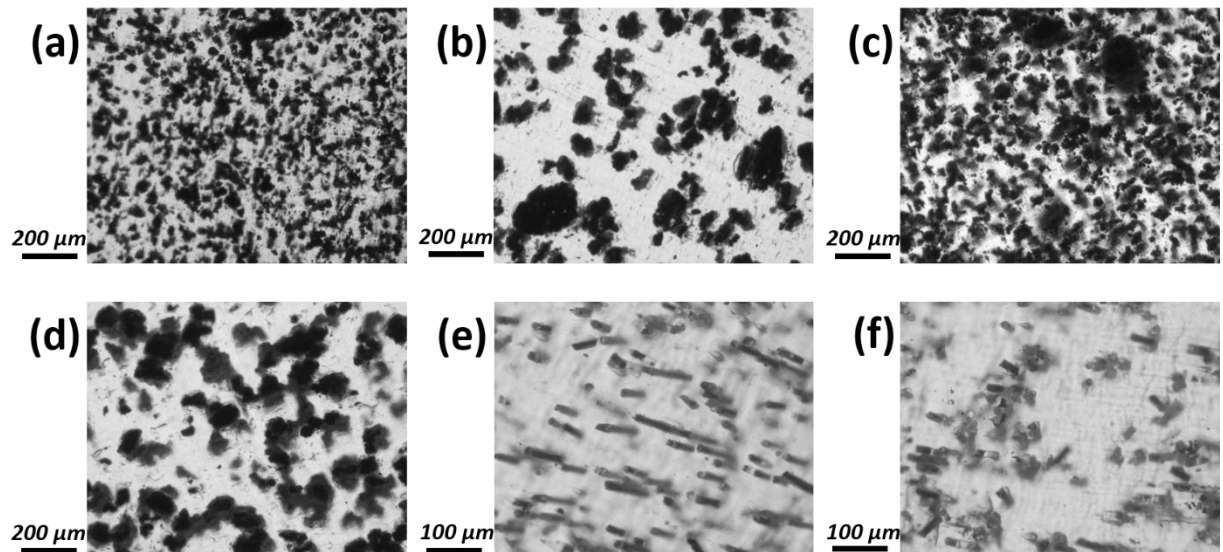


Figure V - 7: Optical microscopy images of PP/tin particles and PP/Ag-coated glass fibers.
 (a) 15 vol% tin particles, 20 μm -thick sample, x10 magnification. (b) Same as before with 6 vol% stearic acid. (c) 15 vol% tin particles, 50 μm -thick sample, x10 magnification. (d) Same as before with 6 vol% stearic acid. (e) 10 vol% Ag-coated glass fibers, 20 μm -thick sample, x20 magnification.
 (f) Same as before with 3 vol% stearic acid.

The morphologies of the PP/Ag-coated glass fibers without stearic acid and with 3 vol% stearic acid (for 20 μm thick composite layer) are shown in Fig. 7-e and 7-f. This stearic acid concentration was chosen as it brings the highest increase in the electromagnetic shielding properties of our composite

materials. A clear change in the composite morphology can also be observed with Ag-coated microfibers, well dispersed for composites free of stearic acid and aggregated in the presence of the stearic acid. The aggregate sizes of Ag-coated microfibers range from 100 to 300 μm with fiber-free polymer domains of equivalent sizes. The morphology difference is less striking than with the tin particles but can be related as well to the improved electrical and shielding properties in the presence of stearic acid.

e. Mechanism of stearic acid action on composite morphology and properties

A mechanism to explain the effect of the presence of stearic acid on the morphology and the properties of the PP/tin particles composites is presented in Fig. 8. For the composite fabrication, PP and stearic acid are introduced in the mixer first, at 190°C. Once they are molten, tin microparticles are introduced in the tank as well. In the first step (Figure 8), liquid drops of stearic acid (having a melting point of 69-70°C) and solid tin particles are dispersed in the molten polymer matrix. Under mixing shear forces, the stearic acid comes in contact with tin particles and reacts with their surface, forming a surface layer of tin stearate on the tin particles. In the second state, the stearic acid being only partially miscible in the molten PP matrix [69] and with the presence of a bonded layer of fatty acid on the particles, stearic acid/tin particles domains are formed. Then, mixing shear forces lead to the aggregation of these domains. Bigger domains are thus formed and stabilized by the surface bonds formed between the stearic acid and tin and by the immiscibility of stearic acid in the PP matrix. A consequence of this aggregation is the tin particles percolation. The next step not shown in the scheme presented in Figure 8 is the improved electrical percolation of these bigger stearic acid/tin particles domains, resulting in improved macroscale composite conductivity and shielding properties. This mechanism will be demonstrated in the following sections of the current study, based on analysis by infrared spectroscopy, contact angle, interfacial tension and infrared transmission microscopy.

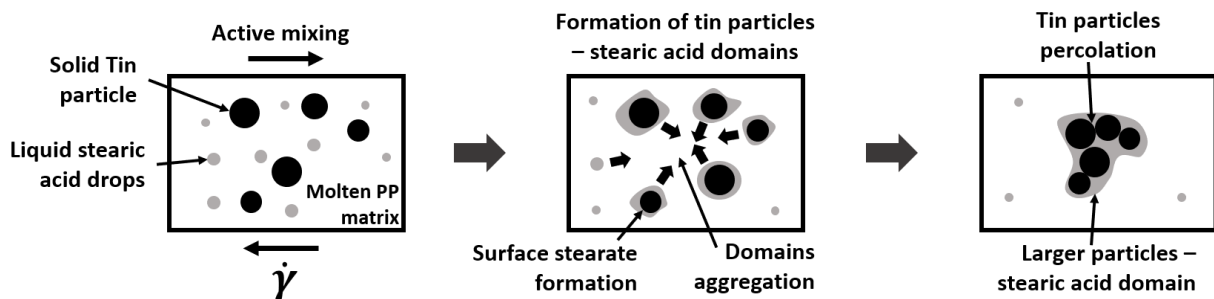


Figure V - 8: Proposed mechanism for the effect of stearic acid during mixing on the final composite morphology. First state: solid tin particles and liquid stearic drops are dispersed in molten PP matrix.

Second state: stearic acid reacts with the surface of tin particles and forms particle/stearic acid domains. Mixing shear forces drive the domain to aggregate. Surface forces stabilize the aggregates.

Third state: Bigger particles/stearic acid domains are formed and reunite several particles that percolate. The same driving forces as before then lead to the global percolation of bigger aggregates.

f. Infrared spectroscopy of tin particles or silver-coated glass fibers mixes with stearic acid

To investigate the reactivity of stearic acid with the metal fillers used in the current study, the fatty acid was directly mixed with the tin particles or with the Ag-coated glass microfibers at 100°C. The infrared spectra of pure tin particles, pure Ag-coated glass fibers, pure stearic acid and of 50/50 vol% blends of these compounds are displayed in Figure 9. For the stearic acid spectrum, the peaks observed at 2916 and 2850 cm⁻¹ can be attributed to C-H single bond vibrations. The peaks at 1710, 1470 and 1300 cm⁻¹ are attributed to C=O carboxyl double bond, CH₂ and CH₃ (rocking and bending modes), and C-O carboxyl single bond, respectively. A very wide, medium intensity absorption band between 2500 and 3500 cm⁻¹ can be attributed to the acid O-H bond. Tin particles and Ag-coated glass fibers show high absorbance in the whole spectral range. The presence of surface oxide O-H bonds is characterized by the presence of a wide, high intensity band between 3400 and 3600 cm⁻¹. This band results from the unsaturated bonds on the metal surface [70,71]. The infrared spectra of stearic acid blends with the two metal fillers show the appearance of a novel peak at 1644 and 1637 cm⁻¹ for tin particles and silver-coated glass fibers, respectively. These new peaks are due to the formation of a metal-stearate complex on the metal surfaces. The reaction of stearic acid on mineral and metal surfaces has been reported multiple times in the past [48,72,73], and the following chemical equation with metal atoms M can be proposed:



A covalent bond is formed through the exchange of acid H⁺ of the stearic acid, leading to the formation of a water molecule. The presence of the covalently bonded heavy metal atoms shifts the absorption wavenumber of the nearby carboxyl double bond C=O, resulting in the observed new peaks. This chemical equation is a simplification of the chemical interaction between stearic acid and the metal surfaces as Lim et al. suggested, for instance, that the bond can be monodentate (one oxygen of the fatty acid carboxyl group interacts with one metal atom), bidentate (the two oxygens interact with the metal atom) or bridging (the two oxygens interact with two different metal atoms) [73]. Thus, as the liquid stearic acid and the metal fillers are mixed with the molten PP matrix, a covalently bonded layer of stearic acid forms on the filler metal surfaces.

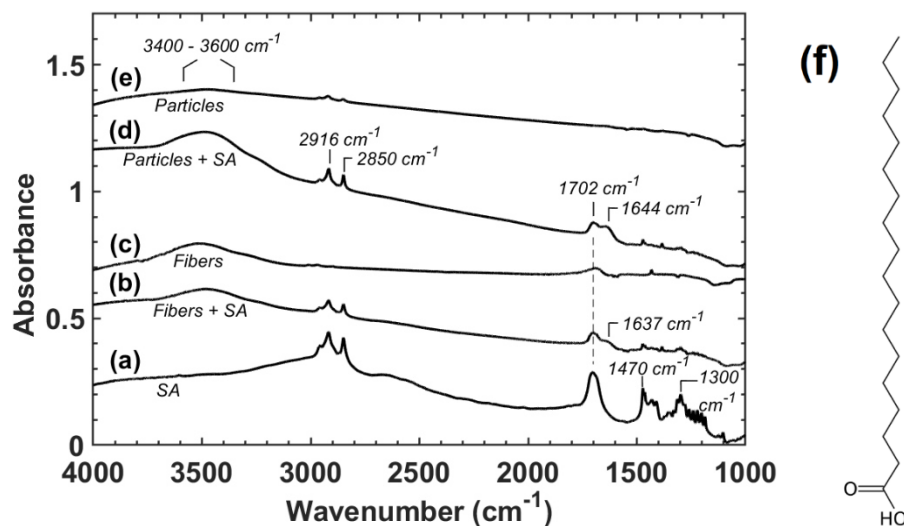


Figure V - 9: Transmission infrared spectroscopy spectra of tin particles and Ag-coated glass fibers and their blends with stearic acid. The blends are made at 100°C. (a) Pure stearic acid, (b) 50/50 vol% blend of fibers with stearic acid, (c) pure fibers, (d) 50/50 vol% blend of tin particles with stearic acid and (e) pure particles. (f) Stearic acid chemical structure.

g. Metal fillers surface properties modification with stearic acid

To characterize the effect of stearic acid on the metal filler surface properties, the water contact angle method was used on stearic acid/tin particles blends and stearic acid/Ag-coated glass microfibers blends. The value of the water contact angle is related to the surface property of materials: the surface is hydrophilic if the angle is lower than 90° and hydrophobic if the angle is greater than 90°. The results are shown in Figure 10. The low angle values of pure tin particles and pure Ag-coated glass

fibers (39° and 18° , respectively) indicate the hydrophilic nature of the metal surfaces due to the presence of metal oxide [74]. On contrary, the water contact angle of pure stearic acid is equal to 101° , corresponding to the hydrophobic nature of the fatty acid. All the blends display hydrophobic contact angle values, even at low concentrations of stearic acid. Thus, the effect of stearic acid on metal fillers surface properties is radical, changing their hydrophilic nature into a hydrophobic one. The water contact angles values higher than the one of stearic acid – in particular for the microfibers – is due to the surface roughness that is known to increase the apparent water contact angle [75].

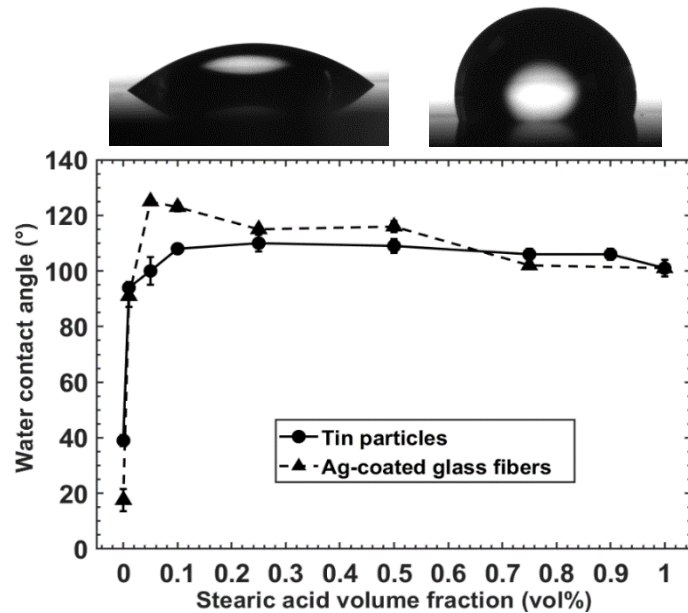


Figure V - 10: Water droplet contact angle on blends of tin particles or Ag-coated glass fibers with stearic acid as a function of the stearic acid volume fraction. Mixing was made at 100°C . Image of the water droplet for pure tin particles (left) and pure stearic acid (right) are shown.

Since surface properties of fillers are converging to the ones of the stearic acid even at low fatty acid concentrations, this indicates that stearic acid rapidly covers the fillers surface entirely. Fatty acid concentration to achieve a monolayer covering the fillers surface can be calculated using the following formula [48]:

$$c_{SA} = e \times SSA \times \rho_{SA} \quad (17)$$

The weight concentration of adsorbed stearic acid relative to the filler surface is c_{SA} , the thickness of the absorbed layer is e , the specific surface area of the fillers is SSA . The latter can be estimated to $18 \text{ m}^2/\text{kg}$ for tin particles and $95 \text{ m}^2/\text{kg}$ for Ag-coated glass fibers, by taking into account

the filler dimensions. ρ_{SA} is the density of the stearic acid. The length of a carbon-carbon single bond is approximately 1.54 Å which gives up the approximate length for the stearic acid molecule (Fig. 9-f). A value of 2.2 nm is obtained, by taking into consideration the bent atomic bonds (109.54°) and the carboxyl head. Hence, calculating the concentration of absorbed stearic acid for a monolayer leads to relative filler weight concentrations of 0.0037 wt% for tin particles and 0.020 wt% for Ag-coated glass microfibers. These values can be converted to relative volume concentrations, leading to 0.03 vol% for tin particles and 0.06 vol% for Ag-coated microfibers. These values are in agreement with our experimental results since the water contact angle starts to change at 0.01 vol% stearic acid and reaches the fatty acid value for 0.05 vol%. In PP composites, stearic acid concentration is such that at least one monolayer is formed and covers the filler surface.

h. Interfacial tension theoretical analysis of the tertiary PP – metal filler – stearic acid mixes

The interfacial tension between two liquids or a solid and a liquid characterizes the affinity between the two compounds and their ability to mix and interact with each other. From values of the surface tension, the interfacial tension can be estimated theoretically using the Owens, Wendt and Wu equations [76,77]:

$$\gamma_{12} = \gamma_1 + \gamma_2 - \frac{4\cdot\gamma_1^d\cdot\gamma_2^d}{\gamma_1^d + \gamma_2^d} - \frac{4\cdot\gamma_1^p\cdot\gamma_2^p}{\gamma_1^p + \gamma_2^p} \quad (18)$$

$$\gamma_{12} = \gamma_1 + \gamma_2 - 2 \cdot \sqrt{\gamma_1^d \cdot \gamma_2^d} - \frac{4\cdot\gamma_1^p\cdot\gamma_2^p}{\gamma_1^p + \gamma_2^p} \quad (19)$$

γ_{12} is the interfacial tension between compound 1 and 2, and γ_1 and γ_2 are the surface tensions of compound 1 and 2, respectively. Exponents d and p indicates the dispersive or polar component of the surface tension. Eq. 18 is the harmonic-mean equation fitted for interfaces between organic liquids and organic polymers, and Eq. 19 is the geometric-harmonic-mean equation fitted for the interface between high- and low-energy phases such as metals and organic polymers [77]. Elias et al. reported the surface tension of PP 7060 and its temperature dependence using the Guggenheim relation [78,79]. At 190°C, the surface tension of this polymer in the molten state is 20 mN/m, without the polar component. At the same temperature, the surface tension of the liquid stearic acid is 19.2 mN/m.

As reported in the literature, the polar component can be considered negligible [44,80,81]. Using Eq. 18 fitted for organic liquids and polymers, a theoretical prediction of the interfacial tension between PP 7060 and stearic acid at 190°C gives the value of 0.02 mN/m. These two compounds have thus a good affinity at the mixing temperature, explaining the easy dispersion of stearic acid drops in the molten polymer and the stabilization of tin particles/stearic acid domains in the polymer matrix.

As for the interaction between the stearic acid and the fillers metal surfaces, pure metals are known to exhibit high values for the surface tension, such as 570 mN/m for pure tin at 190°C [82]. However, with the oxidation of the metal surface, large drops of surface tensions have been observed [83–85], suggesting a more favorable affinity of the filler metal surfaces with stearic acid. This reduced metal surface tension is also evident considering the low water contact angle values of tin particles and Ag-coated glass fibers. The actual surface tension values at room temperature seem thus to be close to the one of water (73 mN/m). Hence, stearic acid can wet the metal surface of the fillers and then form a covalently bonded layer of fatty acid on the whole metal surface. The consequence is the increased affinity between the metal surfaces covered with bonded stearic acid and the other fatty acid molecules. The formation of metal fillers/liquid stearic acid domain is then favored and the low PP/stearic acid interfacial tension results in the good compatibility of the molten polymer with these domains, preventing the phenomena of complete phase demixing or particle aggregations.

i. Infrared transmission microscopy on composites

The 20 μm -thick layers prepared by microtoming were analyzed using an infrared transmission microscope. In the case of PP/tin particles/stearic acid composites, the areas with a high concentration of particles (particles domains) are well separated from the areas with no particles (polymer domains). This enables one to measure the infrared spectra of these two different domains with a 20x20 μm^2 surface infrared beam and investigate local variations in the concentrations of stearic acid (Fig. 8). The measured zones and the resulting spectra are displayed in Fig. 11-a and 11-b, respectively, for PP/15 vol% tin particles without stearic acid and for PP/15 vol% tin particles with 6 vol% stearic acid. Intense peaks related to PP are visible in all spectra in the 1300-1500 cm^{-1} and 2800-3000 cm^{-1} zones. For the composites free of stearic acid, the polymer domain spectra were measured in areas with fewer tin particles.

The absorption in the particle domains is higher than the absorption corresponding to polymer domains, because of the higher absorbance of particles, as noted in the previous infrared

measurements (Fig. 9). The absorption peak of stearic acid at 1710 cm^{-1} (carboxyl C=O double bond) is visible for composites made with the fatty acid but not visible for the composites free of stearic acid. Metal stearate absorption peak is not visible because of its too low concentration. Stearic acid is present in both polymer and particles domains.

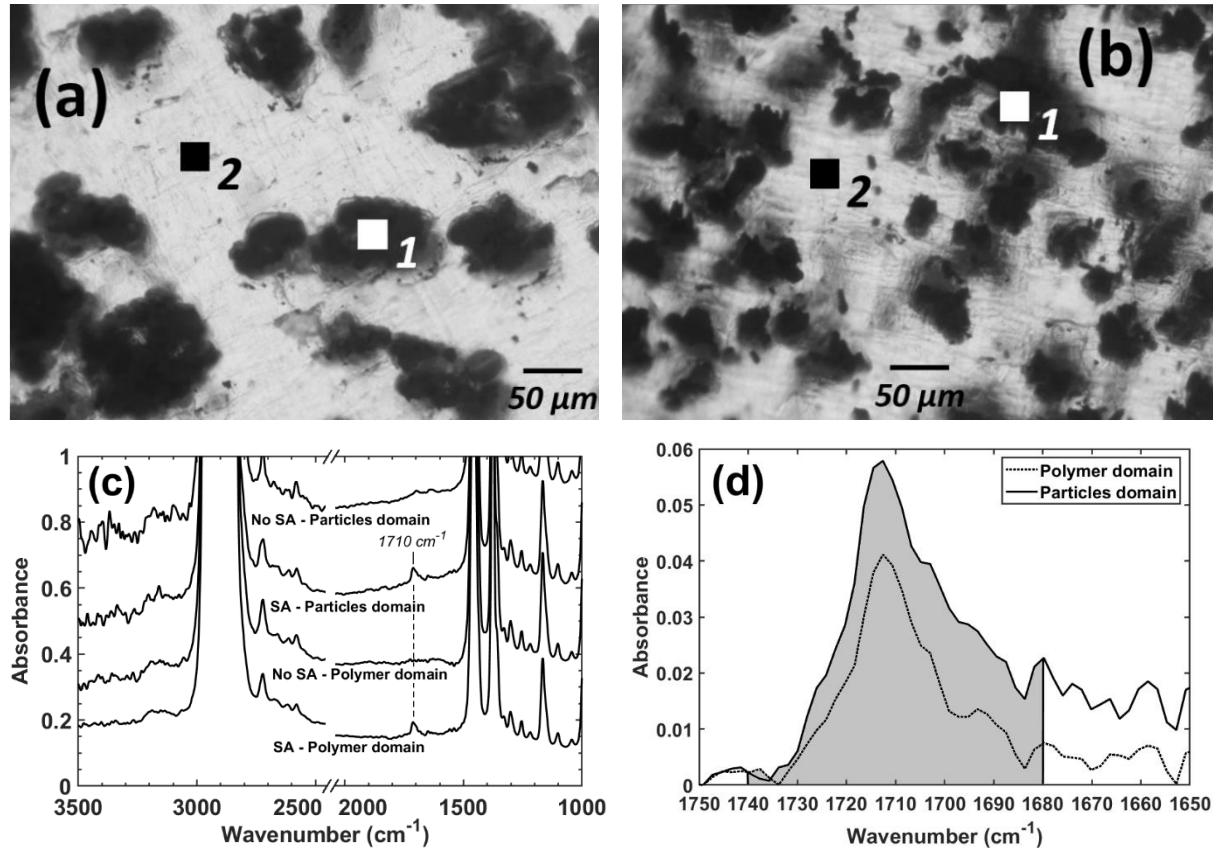


Figure V - 11: Transmission infrared microscopy of PP/tin particles composites with and without stearic acid. (a) Optical microscopy image of PP/15 vol% tin particles/6 vol% stearic acid. The squares are the $20\times20\text{ }\mu\text{m}^2$ areas of the infrared measurement: the white square (1) is the measurement of a tin particle domain and the black square (2) is the measurement of a polymer matrix domain. (b) Same as before without stearic acid. (c) Infrared spectra of the investigated domains corresponding to PP/15 vol% tin particles without and with 6 vol% stearic acid. (c) Close-up on the peak attributed to the stearic acid and comparison between polymer and particles domains for the composite containing stearic acid. Grey area with a baseline correction is used to compare the stearic acid content between the two different domains. Results are listed in Table 5.

To investigate the variations of concentration between the two domain types, the spectral area under the absorbance curves around the stearic acid peak was measured using a baseline correction (Fig. 11-c). Measured spectral areas are listed in Table 5. For tin particles composites with 1 and 6 vol% stearic acid, and Ag-coated glass fibers with 2 vol% stearic acid, the area under the

absorbance curve around the peak corresponding to the stearic acid is larger in the filler domains, with a significant relative variation by 39% to 86%. Absorbance is related to the absorbing group concentration, exhibiting a linear dependence expressed by the Beer-Lambert law. Hence, stearic acid concentration is higher in filler domains compared to polymer domains by about 39% to 86%, giving a strong support to our proposed mechanism (Fig. 8). For the fibers-based composite with 4 vol% stearic acid, no difference in the stearic acid concentration was observed between the two domain types. This can be related to the reduced conductivity and shielding properties of this composite compared to the composites prepared with lower stearic acid concentrations. The stearic acid excess does not interact with the fibers and is homogeneously dispersed in the composite, which explains the infrared results as well as the lower mixing shear related to a poor filler dispersion and degraded physical properties.

Table V - 5: Spectral area of filler domains and polymer domains, as described in Figure 11. The excess in filler domain is the ratio of the filler domain spectral area over the area of the polymer domain, expressed in percentage.

	Filler volume fraction (vol%)	Stearic acid volume fraction (vol%)	Filler domain spectral area (cm)	Polymer domain spectral area (cm)	Excess in filler domain
<i>Tin particles composite 1</i>	15	1	1,4 ± 0,2	0,8 ± 0,1	+ 86 %
<i>Tin particles composite 2</i>	15	6	3,6 ± 0,2	2,6 ± 0,2	+ 39 %
<i>Fibers composite 1</i>	10	2	6,0 ± 0,8	3,8 ± 0,5	+ 56 %
<i>Fibers composite 2</i>	10	4	8,4 ± 1,0	8,7 ± 1,3	- 4 %

A process experiment showing the favored interactions of stearic acid with tin particles over the ones with PP was also carried out. A delayed introduction of stearic acid into the pure PP matrix showed poor mixing between the PP matrix and the stearic acid with a lower mixing torque but not in the presence of the metal particles that tend to keep the fatty acid in the blend. Results are presented in Figure S4, page 192, in the Supplementary Information Part. The use of a different filler treating method by stearic acid [86], the use of other thermoplastic resins and of a stearic acid analogous molecule [87,88] (ethylene bis(stearamide)) showed no significant differences of composite shielding properties. Results are presented in Figures S5 and S6, page 192-193, in the SI Part. This highlights the universal character of the proposed mechanism describing the impact of fatty acids or other analogous molecules on the morphology and shielding properties of composites filled with metal fillers.

4. Conclusion

Polypropylene-based conductive composite materials have been prepared by melt mixing using two types of metal fillers (tin microparticles or hybrid silver-coated glass microfibers). Their shielding properties have been investigated between 0.1 MHz and 18 GHz using two different experimental techniques (coaxial cell method and waveguide method). A substantial enhancement effect of the shielding effectiveness by as much as 50 dB is reported, by a co-segregation effect induced by the addition of stearic acid. This enhancement effect, originating from a drastic change in the composite morphology from a homogeneous to a heterogeneous filler distribution, is accompanied by a lowering effect of the percolation threshold (from 14.7 vol% to 6.9 vol% for tin microparticles and from 3.95 vol% to 2.9 vol% for Ag-coated glass microfibers). The co-segregated morphology observed in the presence of the stearic acid leads to composite materials with shielding effectiveness values as high as 90 dB at 2 mm thickness (for tin microparticles) and 91 dB at 1 mm thickness (for Ag-coated glass microfibers). The optimal stearic acid concentration for a maximum shielding effectiveness was determined for both types of composite materials. Furthermore, for PP/Ag-coated glass microfibers composites, low density values and good mechanical properties are obtained. Our data have been compared to results obtained in the scientific literature, ranking the shielding performance of our composite among the highest reported values. Our finding could represent thus a powerful approach for increasing the shielding effectiveness of composite materials filled with metal fillers with lower percolation thresholds, good mechanical properties and low density values, for potential applications in various domains requiring high shielding effectiveness and material lightness.

References

- [1] Thomassin, J.-M., C. Jérôme, T. Pardoen, C. Bailly, I. Huynen and C. Detrembleur. "Polymer/carbon based composites as electromagnetic interference (EMI) shielding materials," *Materials Science and Engineering: R: Reports* **74**, 211–232 (2013).
- [2] Wanasinghe, D., F. Aslani, G. Ma and D. Habibi. "Review of Polymer Composites with Diverse Nanofillers for Electromagnetic Interference Shielding," *Nanomaterials* **10**, 541 (2020).
- [3] Wanasinghe, D. and F. Aslani. "A review on recent advancement of electromagnetic interference shielding novel metallic materials and processes," *Composites Part B: Engineering* **176**, 107207 (2019).
- [4] Schultz, R. B., V. C. Plantz and D. R. Brush. "Shielding theory and practice," *IEEE Transactions on electromagnetic compatibility* **30**, 187–201 (1988).
- [5] Sudha, J. D., S. Sivakala, K. Patel and P. Radhakrishnan Nair. "Development of electromagnetic shielding materials from the conductive blends of polystyrene polyaniline-clay nanocomposite," *Composites Part A: Applied Science and Manufacturing* **41**, 1647–1652 (2010).
- [6] Ravindren, R., S. Mondal, P. Bhawal, Shek. M. N. Ali and N. C. Das. "Superior electromagnetic interference shielding effectiveness and low percolation threshold through the preferential distribution of carbon black in the highly flexible polymer blend composites," *Polym. Compos.* **40**, 1404–1418 (2019).
- [7] Zhou, H., Z. Xiao, Y. Wang, X. Hao, Y. Xie, Y. Song, F. Wang and Q. Wang. "Conductive and fire-retardant wood/polyethylene composites based on a continuous honeycomb-like nanoscale carbon black network," *Construction and Building Materials* **233**, 117369 (2020).
- [8] Ryu, S. C., J. Y. Kim, C. Cho and W. N. Kim. "Improvements of the Electrical Conductivity and EMI Shielding Efficiency for the Polycarbonate/ABS/Carbon Fiber Composites Prepared by Pultrusion Process," *Macromol. Res.* **28**, 118–125 (2020).
- [9] Rohini, R. and S. Bose. "Electromagnetic Interference Shielding Materials Derived from Gelation of Multiwall Carbon Nanotubes in Polystyrene/Poly(methyl methacrylate) Blends," *ACS Appl. Mater. Interfaces* **6**, 11302–11310 (2014).
- [10] Lecocq, H., N. Garois, O. Lhost, P.-F. Girard, P. Cassagnau and A. Serghei. "Polypropylene/carbon nanotubes composite materials with enhanced electromagnetic interference shielding performance: Properties and modeling," *Composites Part B: Engineering* **189**, 107866 (2020).
- [11] Lan, C., M. Guo, C. Li, Y. Qiu, Y. Ma and J. Sun. "Axial Alignment of Carbon Nanotubes on Fibers To Enable Highly Conductive Fabrics for Electromagnetic Interference Shielding," *ACS Appl. Mater. Interfaces* **12**, 7477–7485 (2020).
- [12] Gao, W., N. Zhao, T. Yu, J. Xi, A. Mao, M. Yuan, H. Bai and C. Gao. "High-efficiency electromagnetic interference shielding realized in nacre-mimetic graphene/polymer composite with extremely low graphene loading," *Carbon* **157**, 570–577 (2020).
- [13] Hamidinejad, M., B. Zhao, A. Zandieh, N. Moghimian, T. Filleter and C. B. Park. "Enhanced Electrical and Electromagnetic Interference Shielding Properties of Polymer–Graphene Nanoplatelet Composites Fabricated via Supercritical-Fluid Treatment and Physical Foaming," *ACS Appl. Mater. Interfaces* **10**, 30752–30761 (2018).
- [14] Ameli, A., M. Nofar, S. Wang and C. B. Park. "Lightweight Polypropylene/Stainless-Steel Fiber Composite Foams with Low Percolation for Efficient Electromagnetic Interference Shielding," *ACS Appl. Mater. Interfaces* **6**, 11091–11100 (2014).
- [15] Dravid, S. V., S. D. Bhosale, S. Datar and R. K. Goyal. "Nickel Nanoparticle-Filled High-Performance Polymeric Nanocomposites for EMI Shielding Applications," *Journal of Elec Materi* **49**, 1630–1637 (2020).

- [16] Duan, H., Y. Xu, D.-X. Yan, Y. Yang, G. Zhao and Y. Liu. "Ultrahigh molecular weight polyethylene composites with segregated nickel conductive network for highly efficient electromagnetic interference shielding," *Materials Letters* **209**, 353–356 (2017).
- [17] Gargama, H., A. K. Thakur and S. K. Chaturvedi. "Polyvinylidene fluoride/nanocrystalline iron composite materials for EMI shielding and absorption applications," *Journal of Alloys and Compounds* **654**, 209–215 (2016).
- [18] Ravindren, R., S. Mondal, K. Nath and N. C. Das. "Prediction of electrical conductivity, double percolation limit and electromagnetic interference shielding effectiveness of copper nanowire filled flexible polymer blend nanocomposites," *Composites Part B: Engineering* **164**, 559–569 (2019).
- [19] Gao, Y.-N., Y. Wang, T.-N. Yue, Y.-X. Weng and M. Wang. "Multifunctional cotton non-woven fabrics coated with silver nanoparticles and polymers for antibacterial, superhydrophobic and high performance microwave shielding," *Journal of Colloid and Interface Science* **582**, 112–123 (2021).
- [20] Wang, Z., J. Ren, R. Liu, X. Sun, D. Huang, W. Xu, J. Jiang, K. Ma and Y. Liu. "Three dimensional core-shell structured liquid metal/elastomer composite via coaxial direct ink writing for electromagnetic interference shielding," *Composites Part A: Applied Science and Manufacturing* **136**, 105957 (2020).
- [21] Shahzad, F., M. Alhabeb, C. B. Hatter, B. Anasori, S. Man Hong, C. M. Koo and Y. Gogotsi. "Electromagnetic interference shielding with 2D transition metal carbides (MXenes)," *Science* **353**, 1137–1140 (2016).
- [22] Wang, L., L. Chen, P. Song, C. Liang, Y. Lu, H. Qiu, Y. Zhang, J. Kong and J. Gu. "Fabrication on the annealed Ti₃C₂Tx MXene/Epoxy nanocomposites for electromagnetic interference shielding application," *Composites Part B: Engineering* **171**, 111–118 (2019).
- [23] Li, L., Y. Cao, X. Liu, J. Wang, Y. Yang and W. Wang. "Multifunctional MXene-Based Fireproof Electromagnetic Shielding Films with Exceptional Anisotropic Heat Dissipation Capability and Joule Heating Performance," *ACS Appl. Mater. Interfaces* **12**, 27350–27360 (2020).
- [24] Mural, P. K. S., S. P. Pawar, S. Jayanthi, G. Madras, A. K. Sood and S. Bose. "Engineering Nanostructures by Decorating Magnetic Nanoparticles onto Graphene Oxide Sheets to Shield Electromagnetic Radiations," *ACS Appl. Mater. Interfaces* **7**, 16266–16278 (2015).
- [25] Lalan, V. and S. Ganesanpotti. "Broadband Electromagnetic Response and Enhanced Microwave Absorption in Carbon Black and Magnetic Fe₃O₄ Nanoparticles Reinforced Polyvinylidenefluoride Composites," *Journal of Elec Materi* **49**, 1666–1676 (2020).
- [26] Ju, J., T. Kuang, X. Ke, M. Zeng, Z. Chen, S. Zhang and X. Peng. "Lightweight multifunctional polypropylene/carbon nanotubes/carbon black nanocomposite foams with segregated structure, ultralow percolation threshold and enhanced electromagnetic interference shielding performance," *Composites Science and Technology* **193**, 108116 (2020).
- [27] Raagulan, K., R. Braveenth, L. Ro Lee, J. Lee, B. Kim, J. Moon, S. Lee and K. Chai. "Fabrication of Flexible, Lightweight, Magnetic Mushroom Gills and Coral-Like MXene–Carbon Nanotube Nanocomposites for EMI Shielding Application," *Nanomaterials* **9**, 519 (2019).
- [28] Wang, G., L. Wang, L. H. Mark, V. Shaayegan, G. Wang, H. Li, G. Zhao and C. B. Park. "Ultralow-Threshold and Lightweight Biodegradable Porous PLA/MWCNT with Segregated Conductive Networks for High-Performance Thermal Insulation and Electromagnetic Interference Shielding Applications," *ACS Appl. Mater. Interfaces* **10**, 1195–1203 (2018).
- [29] Yuan, D., H. Guo, K. Ke and I. Manas-Zloczower. "Recyclable conductive epoxy composites with segregated filler network structure for EMI shielding and strain sensing," *Composites Part A: Applied Science and Manufacturing* **132**, 105837 (2020).
- [30] Zhang, Y.-P., C.-G. Zhou, W.-J. Sun, T. Wang, L.-C. Jia, D.-X. Yan and Z.-M. Li. "Injection molding of segregated carbon nanotube/polypropylene composite with enhanced electromagnetic interference shielding and mechanical performance," *Composites Science and Technology* **197**, 108253 (2020).

- [31] Ren, F., Z. Li, L. Xu, Z. Sun, P. Ren, D. Yan and Z. Li. "Large-scale preparation of segregated PLA/carbon nanotube composite with high efficient electromagnetic interference shielding and favourable mechanical properties," *Composites Part B: Engineering* **155**, 405–413 (2018).
- [32] Sharif, F., M. Arjmand, A. A. Moud, U. Sundararaj and E. P. L. Roberts. "Segregated Hybrid Poly(methyl methacrylate)/Graphene/Magnetite Nanocomposites for Electromagnetic Interference Shielding," *ACS Appl. Mater. Interfaces* **9**, 14171–14179 (2017).
- [33] Wang, Y.-Y., Z.-H. Zhou, C.-G. Zhou, W.-J. Sun, J.-F. Gao, K. Dai, D.-X. Yan and Z.-M. Li. "Lightweight and Robust Carbon Nanotube/Polyimide Foam for Efficient and Heat-Resistant Electromagnetic Interference Shielding and Microwave Absorption," *ACS Appl. Mater. Interfaces* **12**, 8704–8712 (2020).
- [34] Yang, Z., Y. Zhang and B. Wen. "Enhanced electromagnetic interference shielding capability in bamboo fiber@polyaniline composites through microwave reflection cavity design," *Composites Science and Technology* **178**, 41–49 (2019).
- [35] Ghosh, S., S. Ganguly, P. Das, T. K. Das, M. Bose, N. K. Singha, A. K. Das and N. Ch. Das. "Fabrication of Reduced Graphene Oxide/Silver Nanoparticles Decorated Conductive Cotton Fabric for High Performing Electromagnetic Interference Shielding and Antibacterial Application," *Fibers Polym* **20**, 1161–1171 (2019).
- [36] Wang, R., H. Yang, J. Wang and F. Li. "The electromagnetic interference shielding of silicone rubber filled with nickel coated carbon fiber," *Polymer Testing* **38**, 53–56 (2014).
- [37] Buch, A. "Pure metals properties: A scientific and technical handbook" (1999).
- [38] Zeng, Z., W. Li, N. Wu, S. Zhao and X. Lu. "Polymer-Assisted Fabrication of Silver Nanowire Cellular Monoliths: Toward Hydrophobic and Ultraflexible High-Performance Electromagnetic Interference Shielding Materials," *ACS Appl. Mater. Interfaces* **12**, 38584–38592 (2020).
- [39] Tan, Y.-J., J. Li, Y. Gao, J. Li, S. Guo and M. Wang. "A facile approach to fabricating silver-coated cotton fiber non-woven fabrics for ultrahigh electromagnetic interference shielding," *Applied Surface Science* **458**, 236–244 (2018).
- [40] Olivero, D. A. and D. W. Radford. "A multiple percolation approach to EMI shielding composites incorporating conductive fillets," *Journal of Reinforced Plastics and Composites* **17**, 674–690 (1998).
- [41] Zhang, K., H.-O. Yu, K.-X. Yu, Y. Gao, M. Wang, J. Li and S. Guo. "A facile approach to constructing efficiently segregated conductive networks in poly(lactic acid)/silver nanocomposites via silver plating on microfibers for electromagnetic interference shielding," *Composites Science and Technology* **156**, 136–143 (2018).
- [42] Hatzikiriakos, S. G., I. B. Kazatchkov and D. Vlassopoulos. "Interfacial phenomena in the capillary extrusion of metallocene polyethylenes," *Journal of Rheology* **41**, 1299–1316 (1997).
- [43] Fisch, M. and R. Bacaloglu. "Study of additive compatibility with poly(vinyl chloride) (PVC). 2: Dynamic mechanical analysis of PVC lubrication by stearic acid and its derivatives," *J Vinyl Addit Technol* **4**, 4–11 (1998).
- [44] Anneken, D. J., S. Both, R. Christoph, G. Fieg, U. Steinberger and A. Westfechtel. "Fatty Acids," in *Ullmann's Encyclopedia of Industrial Chemistry* (ed. Wiley-VCH Verlag GmbH & Co. KGaA, 2006)
- [45] Nhan, H. N., M. Jean-Louis and W. Jean-Luc. "Modeling of Electromagnetic Shielding Effectiveness of Multilayer Conducting Composites in the Microwave Band," in *2006 First International Conference on Communications and Electronics* 482–485 (IEEE, 2006). doi:10.1109/CCE.2006.350874.
- [46] Sun, J., W. Wang and Q. Yue. "Review on Microwave-Matter Interaction Fundamentals and Efficient Microwave-Associated Heating Strategies," *Materials* **9**, 231 (2016).
- [47] Kirkpatrick, S. "Percolation and Conduction," *Rev. Mod. Phys.* **45**, 574–588 (1973).
- [48] Auscher, M. C., R. Fulchiron, N. Fougerouse, T. Périé and P. Cassagnau. "Zirconia based feedstocks: Influence of particle surface modification on the rheological properties," *Ceramics International* **43**, 16950–16956 (2017).
- [49] Osman, M. A., A. Atallah, T. Schweizer and H. C. Öttinger. "Particle–particle and particle-matrix interactions in calcite filled high-density polyethylene—steady shear," *Journal of Rheology* **48**, 1167–1184 (2004).

- [50] Si, Y., Z. Guo and W. Liu. "A Robust Epoxy Resins @ Stearic Acid-Mg(OH)₂ Micro nanosheet Superhydrophobic Omnipotent Protective Coating for Real-Life Applications," *ACS Appl. Mater. Interfaces* **8**, 16511–16520 (2016).
- [51] Patti, A., H. Lecocq, A. Serghei, D. Acierno and P. Cassagnau. "The universal usefulness of stearic acid as surface modifier: applications to the polymer formulations and composite processing," *Journal of Industrial and Engineering Chemistry* **96**, 1–33 (2021).
- [52] Wei, B., L. zhang and S. Yang. "Polymer composites with expanded graphite network with superior thermal conductivity and electromagnetic interference shielding performance," *Chemical Engineering Journal* **404**, 126437 (2021).
- [53] Iqbal, M. Z., G. M. Mamoor, T. Bashir, M. S. Irfan and M. B. Manzoor. "A study on polystyrene - metal powder conductive composites," *Journal of Chemical Engineering* **25**, 4 (2010).
- [54] Nguyen, D. M., T. N. Vu, T. M. L. Nguyen, T. D. Nguyen, C. N. H. Thuc, Q. B. Bui, J. Colin and P. Perré. "Synergistic Influences of Stearic Acid Coating and Recycled PET Microfibers on the Enhanced Properties of Composite Materials," *Materials* **13**, 1461 (2020).
- [55] Yi, Z., J. Yang, X. Liu, L. Mao, L. Cui and Y. Liu. "Enhanced mechanical properties of poly(lactic acid) composites with ultrathin nanosheets of MXene modified by stearic acid," *J Appl Polym Sci* **137**, 48621 (2020).
- [56] Xiong, C., Z. Zhou, W. Xu, H. Hu, Y. Zhang and L. Dong. "Polyurethane/carbon black composites with high positive temperature coefficient and low critical transformation temperature," *Carbon* **43**, 1788–1792 (2005).
- [57] Vanga-Bouanga, C., T. F. Heid, M. F. Frechette and E. David. "Influence of interface on the dielectric response, electrical and thermal conductivity of high density polyethylene based composites," in *2015 IEEE Conference on Electrical Insulation and Dielectric Phenomena (CEIDP)* 709–712 (IEEE, 2015). doi:10.1109/CEIDP.2015.7352138.
- [58] Wang, H., K. Zheng, X. Zhang, T. Du, C. Xiao, X. Ding, C. Bao, L. Chen and X. Tian. "Segregated poly(vinylidene fluoride)/MWCNTs composites for high-performance electromagnetic interference shielding," *Composites Part A: Applied Science and Manufacturing* **90**, 606–613 (2016).
- [59] Yu, C., Y. S. Kim, D. Kim and J. C. Grunlan. "Thermoelectric Behavior of Segregated-Network Polymer Nanocomposites," *Nano Lett.* **8**, 4428–4432 (2008).
- [60] Lee, S. H., S. Yu, F. Shahzad, J. P. Hong, W. N. Kim, C. Park, S. M. Hong and C. M. Koo. "Highly anisotropic Cu oblate ellipsoids incorporated polymer composites with excellent performance for broadband electromagnetic interference shielding," *Composites Science and Technology* **144**, 57–62 (2017).
- [61] Jung, J., H. Lee, I. Ha, H. Cho, K. K. Kim, J. Kwon, P. Won, S. Hong and S. H. Ko. "Highly Stretchable and Transparent Electromagnetic Interference Shielding Film Based on Silver Nanowire Percolation Network for Wearable Electronics Applications," *ACS Appl. Mater. Interfaces* **9**, 44609–44616 (2017).
- [62] Oh, H.-J., V.-D. Dao and H.-S. Choi. "Electromagnetic shielding effectiveness of a thin silver layer deposited onto PET film via atmospheric pressure plasma reduction," *Applied Surface Science* **435**, 7–15 (2018).
- [63] Xu, Z. and H. Hao. "Electromagnetic interference shielding effectiveness of aluminum foams with different porosity," *Journal of Alloys and Compounds* **617**, 207–213 (2014).
- [64] Lu, Y., Q. Liang and W. Li. "Fabrication of copper/modal fabric composites through electroless plating process for electromagnetic interference shielding," *Materials Chemistry and Physics* **140**, 553–558 (2013).
- [65] Lu, Y., Q. Liang and L. Xue. "Electroless nickel deposition on silane modified bamboo fabric through silver, copper or nickel activation," *Surface and Coatings Technology* **206**, 3639–3644 (2012).
- [66] Dou, Z., G. Wu, X. Huang, D. Sun and L. Jiang. "Electromagnetic shielding effectiveness of aluminum alloy–fly ash composites," *Composites Part A: Applied Science and Manufacturing* **38**, 186–191 (2007).
- [67] Wu, G., X. Huang, Z. Dou, S. Chen and L. Jiang. "Electromagnetic interfering shielding of aluminum alloy–cenospheres composite," *J Mater Sci* **42**, 2633–2636 (2007).

- [68] Li, Y., J. Liu, S. Wang, L. Zhang and B. Shen. "Self-templating graphene network composites by flame carbonization for excellent electromagnetic interference shielding," *Composites Part B: Engineering* **182**, 107615 (2020).
- [69] Broda, J., C. Slusarczyk, J. Fabia and A. Demsar. "Formation and properties of polypropylene/stearic acid composite fibers," *Textile Research Journal* **86**, 64–71 (2016).
- [70] Socrates, G. *"Infrared and Raman Characteristic Group Frequencies: Tables and Charts"* (John Wiley & Sons, 2004).
- [71] Lin, C., B. Wang, Y. Cheng and C. Wang. "Influence of stearic acid on the structure and rheological behavior of injection-molded ZTA suspensions," *Mater Sci-Pol* **31**, 36–42 (2013).
- [72] Dong, Z., Y. Wan, S. Yang, C. Qi and J. Zhang. "Enhanced wear resistance of sol-gel TiO₂ film on a carbon steel in unlubricated sliding against steel ball by stearic acid modification," *J Sol-Gel Sci Technol* **66**, 460–465 (2013).
- [73] Lim, M. S. *et al.* "Adsorption and Desorption of Stearic Acid Self-Assembled Monolayers on Aluminum Oxide," *Langmuir* **23**, 2444–2452 (2007).
- [74] Kenney, J. T., W. P. Townsend and J. A. Emerson. "Tin and iron hydrous oxide deposits on polyethylene, teflon, and paraffin," *Journal of Colloid and Interface Science* **42**, 589–596 (1973).
- [75] Wenzel, R. N. "Resistance of solid surfaces to wetting by water," *Ind. Eng. Chem.* **28**, 988–994 (1936).
- [76] Owens, D. K. and R. C. Wendt. "Estimation of the surface free energy of polymers," *J. Appl. Polym. Sci.* **13**, 1741–1747 (1969).
- [77] Wu, S. "Interfacial and Surface Tensions of Polymers," *Journal of Macromolecular Science, Part C: Polymer Reviews* **10**, 1–73 (1974).
- [78] Elias, L., F. Fenouillot, J. C. Majeste and Ph. Cassagnau. "Morphology and rheology of immiscible polymer blends filled with silica nanoparticles," *Polymer* **48**, 6029–6040 (2007).
- [79] Guggenheim, E. A. "The Principle of Corresponding States," *The Journal of Chemical Physics* **13**, 253–261 (1945).
- [80] Zdziennicka, A., K. Szymczyk, B. Jańczuk, R. Longwic and P. Sander. "Surface, Volumetric, and Wetting Properties of Oleic, Linoleic, and Linolenic Acids with Regards to Application of Canola Oil in Diesel Engines," *Applied Sciences* **9**, 3445 (2019).
- [81] Ferfis, J. L. "The wettability of cellulose film as affected by vapor-phase adsorption of amphipathic molecules," (Lawrence University, 1974).
- [82] Gancarz, T., Z. Moser, W. Gąsior, J. Pstruś and H. Henein. "A Comparison of Surface Tension, Viscosity, and Density of Sn and Sn–Ag Alloys Using Different Measurement Techniques," *Int J Thermophys* **32**, 1210–1233 (2011).
- [83] Fiori, L., E. Ricci and E. Arato. "Dynamic surface tension measurements on molten metal-oxygen systems: model validation on molten tin," *Acta Materialia* **51**, 2873–2890 (2003).
- [84] Lee, J., T. Tanaka, M. Yamamoto and S. Hara. "Effect of Oxygen on Surface Tension of Liquid Ag-Sn Alloys," *Mater. Trans.* **45**, 625–629 (2004).
- [85] Khan, M. R., C. B. Eaker, E. F. Bowden and M. D. Dickey. "Giant and switchable surface activity of liquid metal via surface oxidation," *Proc Natl Acad Sci USA* **111**, 14047–14051 (2014).
- [86] Hernández, Y. *et al.* "Stearic acid as interface modifier and lubricant agent of the system: Polypropylene/calcium carbonate nanoparticles," *Polym Eng Sci* **59**, E279–E285 (2019).
- [87] Nouri, A., P. D. Hodgson and C. Wen. "Study on the Role of Stearic Acid and Ethylene-bis-stearamide on the Mechanical Alloying of a Biomedical Titanium Based Alloy," *Metall and Mat Trans A* **41**, 1409–1420 (2010).
- [88] Pluta, M., J. Bojda, E. Piorkowska, M. Murariu, L. Bonnaud and P. Dubois. "The effect of halloysite nanotubes and N,N'- ethylenbis (stearamide) on the properties of polylactide nanocomposites with amorphous matrix," *Polymer Testing* **61**, 35–45 (2017).

Supplementary information

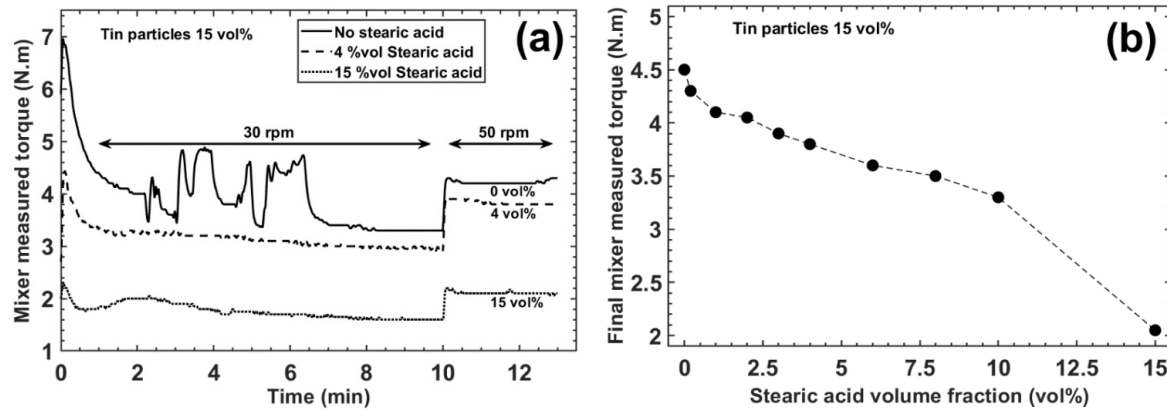


Figure S V - 1: PP - 15 vol% tin particles composite blends with different stearic acid concentrations. (a) Mixer torque as a function of time for composites without stearic acid, and with 4 and 15 vol% stearic acid. The first 10 mins of mixing and the following 3 mins are done with a mixing speed of 30 and 50 rpm respectively, both at 190°C. (b) Final mixer torque measured at $t = 13$ mins as a function of stearic acid volume concentration.

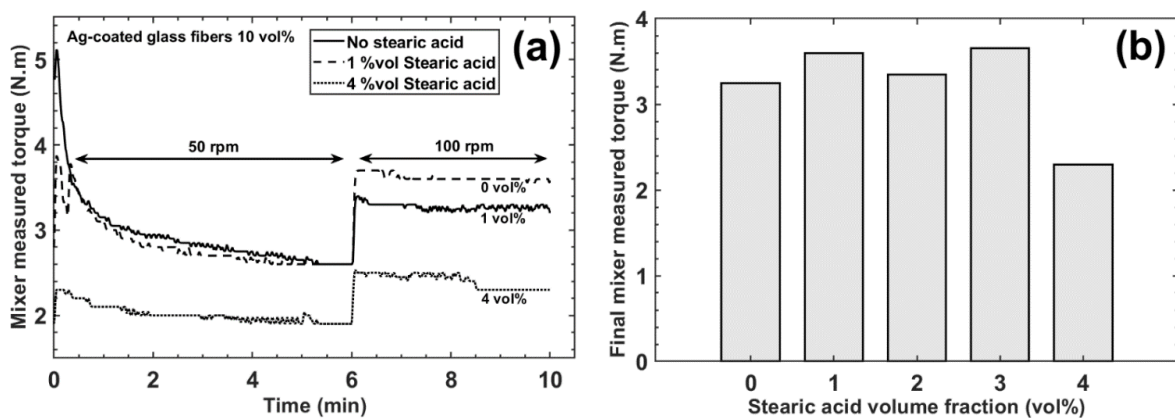


Figure S V - 2: PP – 10 vol% Ag-coated glass fiber composite blends with different stearic acid concentration. (a) Mixer torque as a function of time for composites without stearic acid, and with 1 and 4 vol% stearic acid. The first 6 mins of mixing and the following 4 mins are done with a mixing speed of 50 and 100 rpm respectively, both at 200°C. (b) Final mixer torque measured at $t = 10$ mins as a function of stearic acid volume concentration.

Table S V - 1: Measured PP composites density with different filler volume fraction. Additions of stearic acid leads to small variations of composite densities and thus are not indicated. Density measurements is done by the Archimedean immersion in water method in a Mettler Toledo high precision scale.

Filler	Filler vol%	Measured density
<i>Tin particles</i>	15	1.85 ± 0.03
	20	2.17 ± 0.03
	25	2.48 ± 0.03
	30	2.81 ± 0.04
<i>Ag-coated glass fibers</i>	8	1.04 ± 0.03
	10	1.09 ± 0.02
	15	1.16 ± 0.02
	20	1.25 ± 0.02

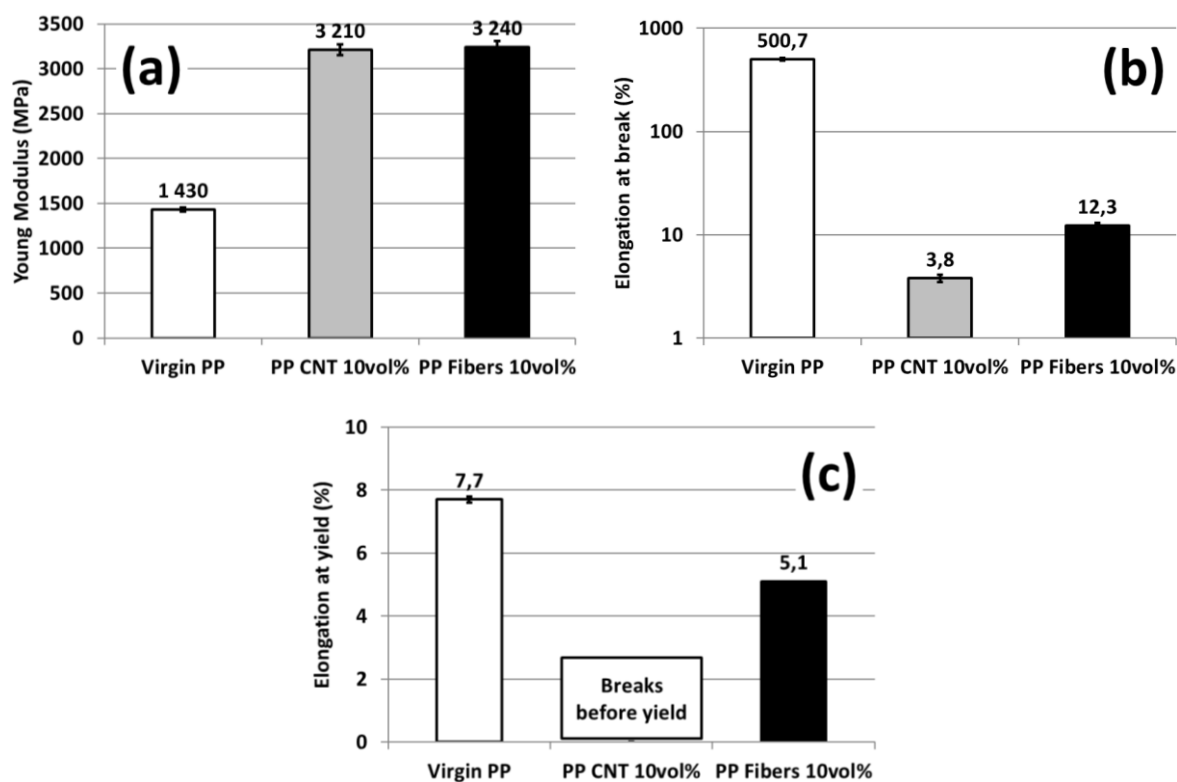


Figure S V - 3: Tensile mechanical properties of PP – 10 vol% silver-coated glass fibers – 2 vol% stearic acid composite compared with PP – 10 vol% CNT composite from a previous study [10] (Chapter III). Standard measurements carried-out on composite injected dog bones. (a) Young modulus measured at 1mm/min elongation speed and low deformation. (b) Elongation at break measured at 10 mm/min. (c) Elongation at yield measured at 10 mm/min.

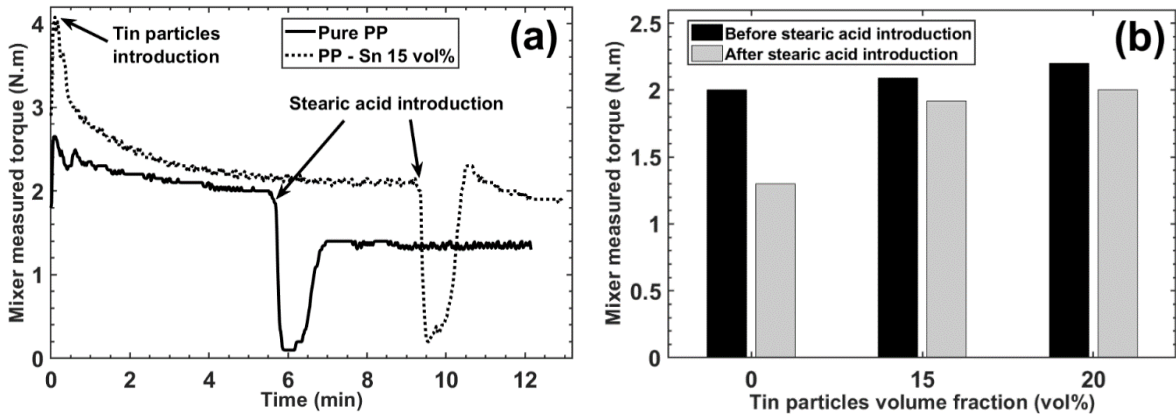


Figure S V - 4: Delayed introduction of stearic acid during pure PP or PP – tin particles composites mixing. (a) Mixer measured torque as a function of time. Stearic acid is introduced once torque of the initial blend is stabilized. Tank is filled to half of its volume, temperature is $T = 190^\circ\text{C}$ and mixing speed is 50 rpm. (b) Stabilized mixer torque before and after stearic acid introduction for pure PP and PP – tin particles composites with 15 and 20 vol% particles.

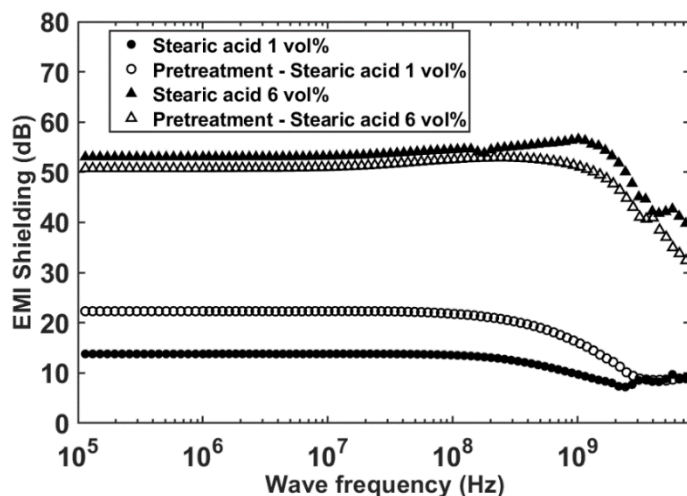


Figure S V - 5: Influence of tin particles pretreatment by stearic acid on shielding properties in PP composites with 15 vol% particles (2mm thickness). Two concentration of stearic acid are investigated. Instead of being introduced in molten PP and stearic acid in the mixer tank, tin particles are treated by stearic acid in an oven at 100°C for 10 mins before being introduced in molten PP.

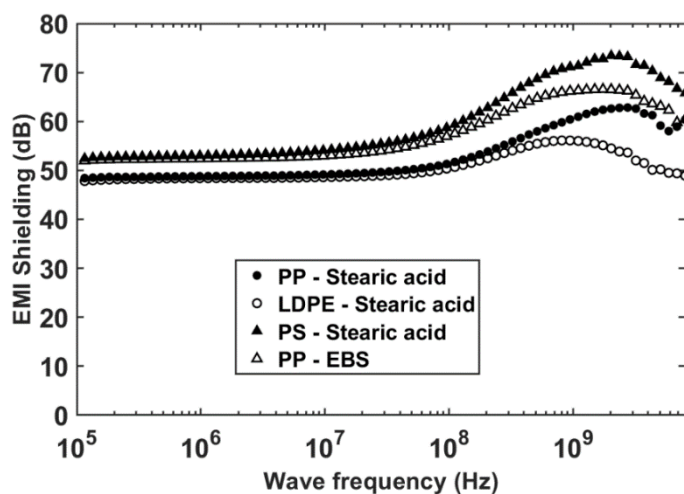


Figure S V - 6: Influence of the use of other thermoplastic matrices and the use of an analogous stearic acid molecule on shielding properties in composites with 10 vol% Ag-coated glass fibers (1mm thickness). Volume fraction of stearic acid is 2 vol% and ethylene bis(stearamide) (EBS) is 4 vol% to account for double molar mass. PP = polypropylene (reference), LDPE = low density polyethylene, PS = polystyrene.

Chapter VI. Theoretical modeling of EMI shielding properties of composite materials filled with metal fillers

Chapter VI. Theoretical modeling of EMI shielding properties of composite materials filled with metal fillers

Abstract

In this study we developed a novel EMI shielding theoretical model suited for composite materials filled with metal fillers. Based on the self-inductance component of the metal electrical conductivity, this model predicts a drop of shielding effectiveness above a characteristic frequency. The model could effectively fit experimental shielding effectiveness of PP composites filled with tin particles and Ag-coated glass fibers. The developed theoretical model was also found to correctly describe the experimental shielding of numerous composite materials filled with metal fillers reported in the literature. The origin of the decrease in the shielding effectiveness of metal based composite materials at high frequencies, frequently reported in the experimental data available in the literature, is thus finally unraveled and theoretically described. Three “universal” shapes for the electromagnetic shielding curves are proposed, based on the interrelation between two characteristic frequencies: the characteristic frequency of the absorption effects and the characteristic frequency of inductance effects. Our study provides thus a general frame summarizing all possible scenarios for understanding the behavior of the shielding effectiveness of composite materials in dependence on frequency.

Keywords: EMI shielding, theoretical modelling, metal filler, inductive effects

Reformatted version of to-be-submitted paper

Revealing the impact of the inductive impedance on the electromagnetic interference shielding effectiveness of composite materials filled with metal filler: new theoretical approach vs. experimental investigations

Hubert Lecocq¹, Olivier Lhost², Philippe Cassagnau², Anatoli Serghei²

¹*Institut des Matériaux Polymères, Université de Lyon, 69622 Villeurbanne, France*

²*TOTAL Research and Technology Feluy, C 7181, Feluy, Belgium*

1. Introduction

Theoretical predictions and modeling of physical properties of materials have the great advantage of cost and time savings. With a reliable and robust theoretical model, one can design a material or a device without the cost and time required to fabricate and test multiple samples. This is particularly the case for designing large structures such as ships or aircrafts where the industry cannot afford to make and test multiple versions of the vehicle. The same approach turns out to be highly effective for developing functional materials. In the field of EMI shielding, for instance, theoretical predictions and modeling are very useful to optimize the placement of shields in a complex electronic device or in in-vehicle systems. This requires knowing the shielding behavior of the shield material when changing the shield thickness, the wave frequency and the distance from the wave source for instance. Several studies dealt with modeling and predictions of EMI shielding properties of composite materials as presented in Chapter I [1–7]. In carbon nanotubes (CNT) or graphene based composite materials, Xia et al. developed a theoretical model capable of effectively predicting shielding effectiveness from wave frequency, sample thickness, filler intrinsic physical properties and filler distribution in the polymer matrix based on the effective medium theory and electric charge transport phenomena [4,6].

As described in detail in Chapter III, EMI shielding of a homogeneous and isotropic material depends on its electrical conductivity, the incident wave frequency and the shield thickness (and

eventually its magnetic permeability if the material possesses magnetic properties). This model predicts an increase of shielding effectiveness with the increase of any of these parameters. Concerning incident wave frequency, two regimes can be distinguished. Below the characteristic absorption frequency – which depends on conductivity and thickness – the shielding effectiveness is constant with frequency but increases rapidly above the same characteristic frequency. Such behavior, however, was not observed in composite materials filled with metal particles (tin particles and silver-coated glass fibers). A drop in the shielding effectiveness, or a brief increase followed by a drop, was noted at the high frequencies (above 100 MHz). This drop of shielding effectiveness at high frequencies is in contradiction with the predictions of the cited theoretical model (described in Chapter III), and was observed in numerous studies on composite materials filled with metal fillers [8–15]. Hypothesis of frequency independent, homogeneous and isotropic material properties are then not met. Hot compression molding of our samples and optical microscopy observations did not reveal any particular orientation of the fillers in the polymer matrix (tin particles and silver-coated glass fibers-based composites in Chapter V), the isotropic hypothesis of the model remaining therefore fulfilled. The homogeneous hypothesis does not seem to be questioned either, as the EM wave wavelengths used in the study (10^5 Hz to 18 GHz frequency which corresponds to wavelength ranging from 3 km to 1.7 cm) are very large compared to the length-scale of the composite filler heterogeneities ($\approx 100 \mu\text{m}$ at most). The only hypothesis that does not seem to be fulfilled is whether or not the physical properties of the material are constant in dependence on the wave frequency.

In this work we develop a novel theoretical model that takes into account a frequency dependent conductivity function that originates from the onset of inductive effects. The frequency dependence arises thus from the inductive component of the metal material conductivity (self-inductance). The new parameter in this model is the characteristic inductive frequency f_i : below this frequency, inductance effects are weak and conductivity is constant, but above this frequency, conductivity decreases due to inductive effects. Influence of this parameter as well as of the incident wave frequency, DC electrical conductivity and shield thickness on the shielding effectiveness will be analyzed in detail. Our approach allows us to effectively predict the EMI shielding properties of PP – tin particles or Ag-coated glass fibers composites, both exhibiting important inductive effects at high frequencies. Furthermore, the ability to successfully fit shielding properties of numerous other composite materials filled with metal fillers found in the literature highlights the strength and the relevance of this novel EMI shielding theoretical model. Our study provides thus a general frame that gives evidence for three “universal” shielding curves, resuming thereby all possible scenarios in understanding the shielding behavior of composite materials in dependence on frequency.

2. EMI shielding theoretical model with an inductive component of conductivity

a. Frequency dependance of metal material conductivity

The electrical conductivity is a physical parameter derived from the measurement of the electrical impedance. For metal materials, both these parameters do not show a constant behavior with the applied frequency, especially in the high frequency range, due to reactive (inductive) effects. This is shown for instance in Figure 1, where the real and imaginary parts as well as absolute value of the impedance of a 4m-long 0.95mm-diameter tin wire are displayed. Real part Z' is the resistive part of the impedance and imaginary part Z'' is the reactive part of the impedance (in our particular case, it is the self-inductance). Z' is constant equal to 0.66Ω with frequency up to 1 MHz and starts to increase at higher frequencies. Using this impedance value, the conductivity of the tin wire can be calculated, giving $8.54 \times 10^6 \text{ S/m}$. The high frequency increase observed in Z' is due to skin-effects. Z'' increases linearly with frequency (typically the expected response for an inductive impedance), being negligible compared to Z' below 22 kHz and dominant compared to Z' above the same frequency. Thus, the absolute value of impedance is dominated by Z' below 22 kHz, hence constant, and by Z'' above 22 kHz, hence increasing with frequency. Impedance, defined as a complex number, can be expressed as:

$$Z^* = Z' - j \cdot Z'' = \frac{l}{\sigma_0 \pi r^2} - j \cdot \frac{\omega}{\omega_0} \quad (1)$$

Wire length, radius and DC conductivity are respectively l , r and σ_0 . This DC conductivity is constant with frequency as it is solely related to charge bearer mobility. The electric field pulsation is ω ($\omega = 2\pi f$) and ω_0 is a characteristic frequency associated with inductive effects in the wire. This typical frequency behavior of a metal material was observed in other studies [16–18].

Thus, wire conductivity which is inversely proportional to absolute value of impedance is not constant and is expected to drop with increasing frequency as the electrical impedance rises up. To take into account this frequency dependence of the metal conductivity, the following expression is proposed:

$$\sigma^* = \frac{\sigma_0}{1 + j \cdot \frac{f}{f_i}} \quad (2)$$

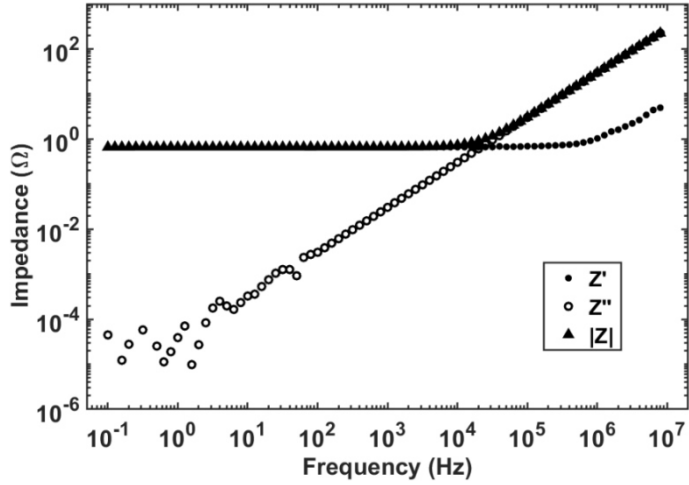


Figure VI - 1: Real part, imaginary part and absolute value of tin wire as a function of the frequency of the applied electric field. Wire length is 4m, diameter is 0.95mm. Voltage was set to 0.2 V.

The incident wave frequency is f and f_i is the characteristic frequency where the contribution of the inductive impedance starts to overcome the resistive impedance. Within this framework, the composite material is considered as a network of resistive/inductive cells as shown in Figure 2-a. With this representation, composite conductivity is constant at low frequency below the characteristic frequency ($R/2\pi L$) as coils in Fig. 2-a behave as short-circuit. Above the same characteristic frequency, coils start to oppose current flow and composite conductivity decreases which is analog to the behavior of metal materials (impedance increases and shielding effectiveness decreases with increasing frequency). Theoretical predictions of a composite material conductivity with an inductive component with different inductive characteristic frequencies f_i are presented in Figure 2-b. Compared to the constant conductivity case, conductivity indeed decreases above a certain frequency which is coherent with the increase of impedance. Equation 2 is actually analog to a first order electronic filter. Thus, when $f=f_i$, $|\sigma^*| = \sigma_0/\sqrt{2}$ with σ_0 corresponding to the low frequency conductivity plateau value. The characteristic frequency f_i corresponds hence to the beginning of the conductivity drop.

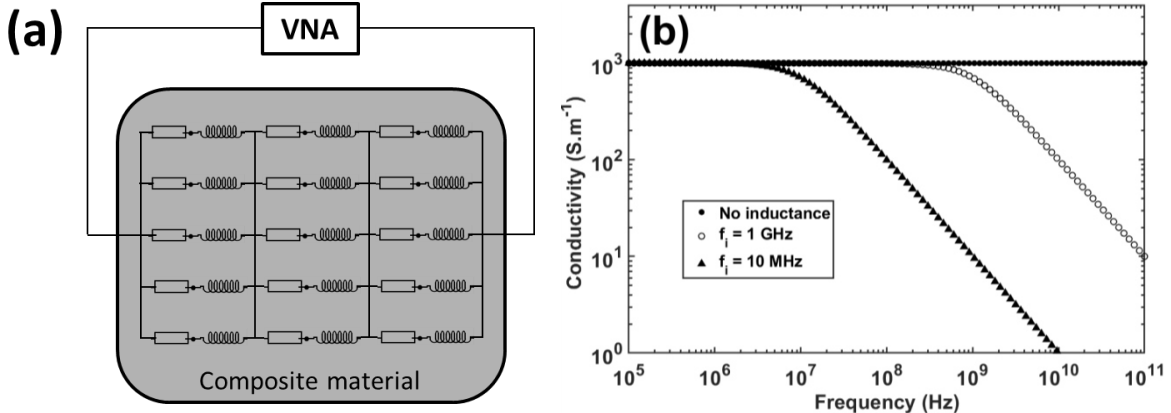


Figure VI - 2: Frequency dependence of composite material conductivity due to inductive effects.
(a) Composite material schematized as a network of resistive/inductive cells. (b) Theoretical predictions of the frequency variations of composite conductivity at different inductance characteristic frequency parameters.

b. EMI shielding theoretical model and parameters influence on shielding effectiveness

This model is based on the homogeneous and isotropic theoretical model developed in Chapter III, but with taking into account a frequency dependent conductivity. The EMI shielding effectiveness is defined as [1]:

$$SE = -10 \log_{10} \left(\frac{P_t}{P_i} \right) = -20 \log_{10} \left(\frac{E_t}{E_i} \right) = -20 \log_{10} \left(\frac{H_t}{H_i} \right) \quad (3)$$

$$SE_T = SE_A + SE_R + SE_M \quad (4)$$

$$SE_A = 20 \cdot \frac{d}{\delta} \cdot \log_{10}(e) \quad (5)$$

$$SE_R = -20 \cdot \log \left(\left| \frac{4Z_0Z}{(Z+Z_0)^2} \right| \right) \quad (6)$$

$$SE_M = 20 \cdot \log \left(\left| 1 - \left(\frac{Z-Z_0}{Z+Z_0} e^{-d/\delta} \right)^2 \right| \right) \quad (7)$$

$$Z = \frac{E}{H} = \sqrt{\frac{\mu^*}{\epsilon^*}} = \sqrt{\frac{j\omega\mu'}{\sigma+j\omega\epsilon'}} \quad (8)$$

$$\delta = \sqrt{\frac{2}{\mu\omega\sigma}} = \sqrt{\frac{1}{\mu\pi f\sigma}} \quad (9)$$

$$f_c = \frac{1}{\pi\mu\sigma d^2} \quad (10)$$

SE_T , SE_A , SE_R and SE_M are respectively the total, absorption, single reflection and multiple internal reflections shielding effectiveness. The incident wave frequency and shield thickness are f and d respectively. Material conductivity, dielectric permittivity (real part) and magnetic permeability (real part) are respectively σ , ϵ' and μ' . Z , Z_0 , δ and f_c are respectively the material wave impedance, the air wave impedance (377Ω), the material skin depth and the absorption characteristic frequency, and were described in detail in Chapter I and III. According to the theoretical model described in these chapters, the shielding effectiveness is constant below f_c and increases rapidly above f_c . The three relevant parameters that have a significant influence on shielding are f , d and σ . The increase of any of these three parameters leads to an increase in the shielding effectiveness (above f_c for f).

The novel theoretical model proposed in the current chapter was developed to take into consideration inductive effects specific to metal materials. This was done by combining Eqs. 4-7 with a frequency dependent conductivity given by Eq. 2, and taking into account one more parameter, f_i , the characteristic frequency of inductive effects. The drop of conductivity above f_i due to inductive effect leads to a drop of shielding effectiveness compared to the constant conductivity case. In Figure 3 three typical shielding curves predicted by our new theoretical approach are displayed. The curve shape depends on the relative position of the two characteristic frequencies: the characteristic frequency for absorption effects f_c and the one for inductive effects f_i . If there are no inductive effects – that is if f_i is well above the studied frequency range – the curves shapes correspond to the homogeneous and isotropic theoretical model described in Chapter III. Shielding is constant below f_c and depends on shield conductivity and thickness. Above f_c , shielding increases rapidly with increasing frequency. The higher the sample conductivity and thickness are, the lower f_c is leading to absorption effects that takes place earlier. This case is represented in Fig. 3-a for a 1mm-thick sample with different conductivity values (σ_0). If f_i is in the studied frequency range and inferior to f_c , as frequency increases the sample conductivity drops before the intervention of absorption leading to a shielding drop as represented in Fig. 3-b for a 1mm-thick sample with a DC conductivity of 100 S.m^{-1} . One can also see that for the sample with the lowest f_i (10^7 and 10^8 Hz), shielding finally drops to a value close to zero but not for the sample with $f_i = 10^9$ Hz that reaches a high frequency shielding plateau. In this high frequency range, the conductivity drop is actually exactly compensated by the intervention of the absorption shielding phenomenon. Indeed, if $f \gg f_i$ then $|\sigma^*| \approx \frac{\sigma_0 \cdot f_i}{f}$ and then $\delta \approx (\pi \cdot \mu' \cdot \sigma_0 \cdot f_i)^{-1/2}$ which is a constant. For $f \gg f_c$, wave absorption is the dominant shielding mechanism and according to Eq. 5, since δ is a constant, shielding is constant. This is the case for the considered sample where the plateau is reached above 2×10^{10} Hz which is much greater than $f_i = 10^9$ Hz and $f_c = 2.5 \times 10^9$ Hz.

For the other curves, the high frequency plateau value has a value close to zero because sample conductivity dropped too much before the intervention of the absorption ($f_c = 2.5 \times 10^9$ Hz).

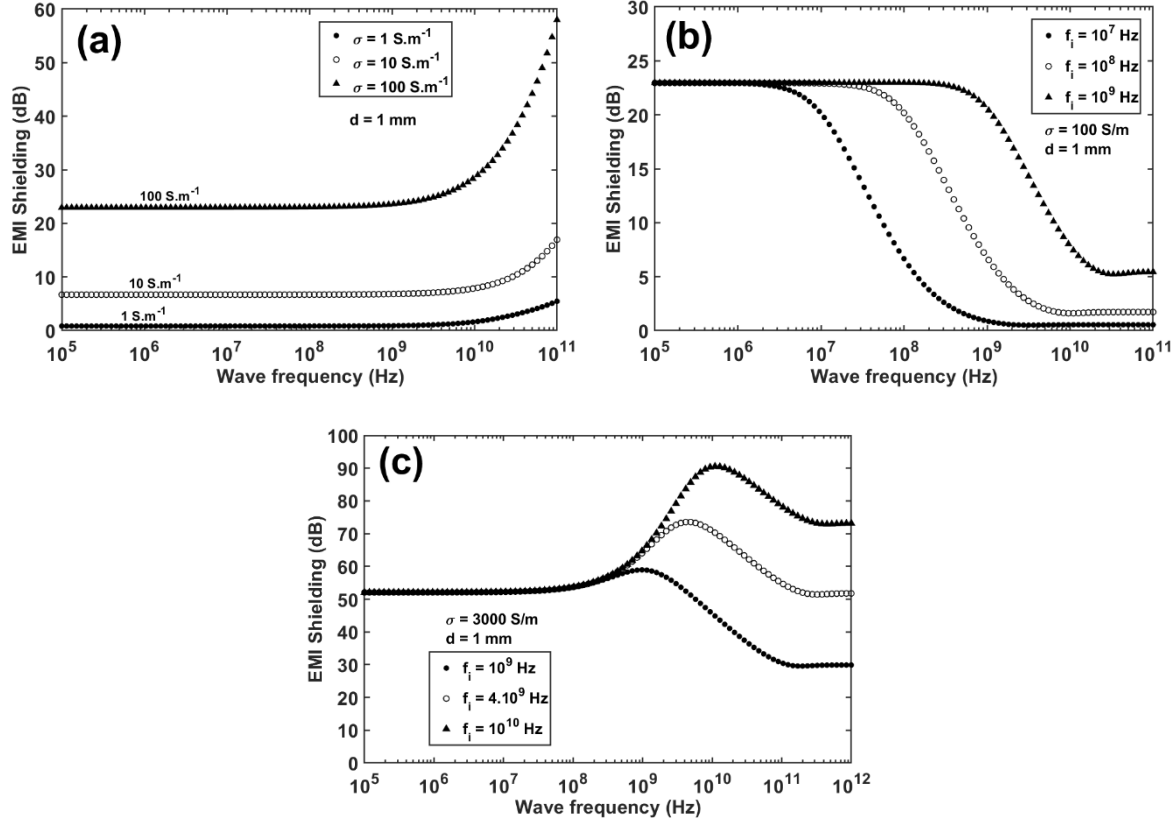


Figure VI - 3: The three typical shielding curves predicted by our theoretical model. (a) case 1: f_i is well above studied frequency range with no inductive effects. (b) case 2: f_i is inferior to f_c which leads to a shielding drop above the inductance frequency. (c) case 3: f_i is superior to f_c and in the studied frequency range which leads to an increase of shielding due to absorption followed by a decrease due to inductive effects.

The last type of curves corresponds to the case where f_i is in the studied frequency range but higher than f_c . This case is displayed in Fig. 3-c with a 1mm-thick sample with a DC conductivity of 3000 S.m^{-1} , which corresponds to an absorption critical frequency of $f_c = 8.4 \times 10^7$ Hz. Above this characteristic frequency, an increase in the shielding effectiveness is observed. As frequency rises up and reaches the inductance characteristic frequency, sample conductivity drops. This stops the rapid shielding increase due to absorption. Shielding effectiveness reaches a maximum and decreases. As previously described, it then reaches a plateau when the skin depth δ becomes a constant. The closer f_i is to f_c , the lower is the frequency where the shielding maximal value is reached, as the conductivity drop takes place earlier in frequency.

The shielding effectiveness of samples with a constant characteristic inductive frequency $f_i = 1$ GHz, and different DC conductivities and shield thicknesses is shown in Figure 4. Upon varying the characteristic frequency f_i , the shape of the shielding curves changes, according to the value of the DC conductivity and thickness. In both cases, the increase of one of these parameters lead to an increase of the low frequency shielding plateau as explained in Chapter III. This also leads to a decrease of the characteristic absorption frequency f_c . In Fig. 4-a, f_c is equal to respectively 25 GHz, 2.5 GHz, 250 MHz and 50 MHz for DC conductivity values of 10, 100, 1000 and 5000 S.m⁻¹. The first two samples then have a f_c superior to f_i which corresponds to previous case 2 (Fig. 3-b) with a shielding drop and no absorption. The two other samples have their f_c equal or inferior to f_i with corresponds to previous case 3 (Fig. 3-c) with an increasing then decreasing shielding effectiveness with frequency. The same observations can be made on Fig. 4-b with the variation of sample thickness. Characteristic absorption frequencies are respectively 250 GHz, 2.5 GHz, 100 MHz and 11 MHz for shielding thicknesses of 0.1, 1, 5 and 15 mm. The changes of curve shapes are more important with the variation of the shield thickness as f_c is inversely proportional to the thickness squared compared to an inversely proportional relationship to conductivity.

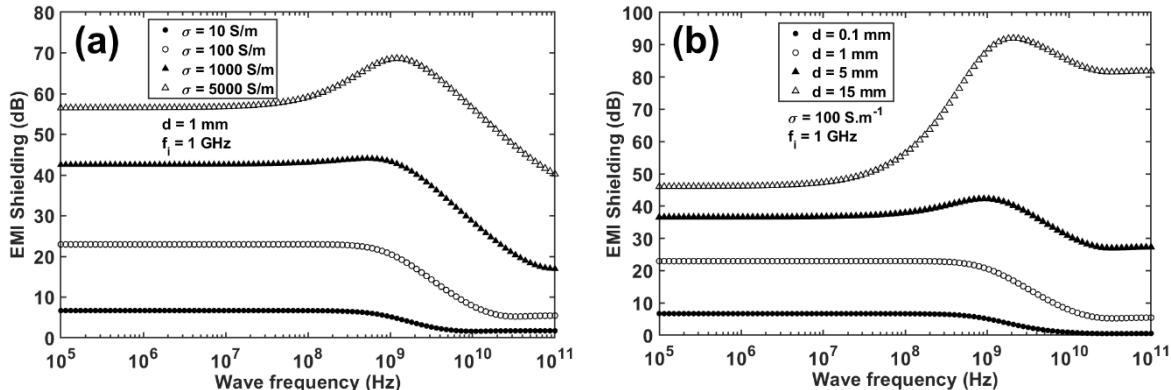


Figure VI - 4: Shielding effectiveness of different samples with a constant characteristic inductive frequency $f_i = 1$ GHz, and varying DC conductivity σ_0 (a) or shield thickness d (b).

Calculating the second derivative of the shielding versus frequency curves, we can assess whether the shielding maximal value – reflecting the competition between absorption and inductance effects – is reached at the exact frequency f_i . That could enable one to easily identify this parameter on an experimental curve. This scaling law study is presented in Figure 5. For a sample of 1mm thickness, 2000 S.m⁻¹ DC conductivity and inductance frequency set to $f_i = 1$ GHz, the position of the negative peak observed in the second derivative – that marks the transition from an increasing to a decreasing shielding – is reached at a frequency close to f_i (Fig. 5-a). The same calculation was done

with different samples (σ_0 and d) and for different values of f_i . The frequency position of the negative peak detected in the second derivative is displayed in Fig. 5-b, in dependence on the characteristic frequency f_i of inductance effects for different values of σ_0 and d . The two frequencies are very close (dots close to the unity-slope linear law) with f_{2nd} slightly greater than f_i . The gap seems to widen a little as f_i increases and is smaller for material 1 ($\sigma_0 = 100 \text{ S/m}$, $d = 1\text{mm}$) compared to the other materials (higher σ_0 or d). The maximal reached ratio between the two frequencies is 1.35 which is still a small difference. Thus, the smaller f_i , σ_0 or d are, the closer the two frequencies are, but the difference is still small for higher parameters. One can thus have a good estimation of f_i taking the frequency at which the maximal shielding value is reached. In the case where there is no maximum – when shielding simply decreases – the frequency at which the shielding decrease starts is a good estimation of f_i . For a more precise determination, calculation of the second derivative and determination of the frequency position of the negative peak will give out f_i as previously shown.

The introduction of an inductive component to sample conductivity leads thus to a decrease of EMI shielding compared to the constant conductivity case. The shielding decrease as a function of frequency depends on the relative position of the absorption characteristic frequency f_c (which depends on sample DC conductivity σ_0 and thickness d) and the inductance characteristic frequency f_i . For $f_c > f_i$, shielding effectiveness will drop above f_i because of inductance effects and reach a plateau. For $f_c < f_i$, shielding will first increase above f_c because of absorption, then decrease above f_i because of inductance and finally reach a plateau.

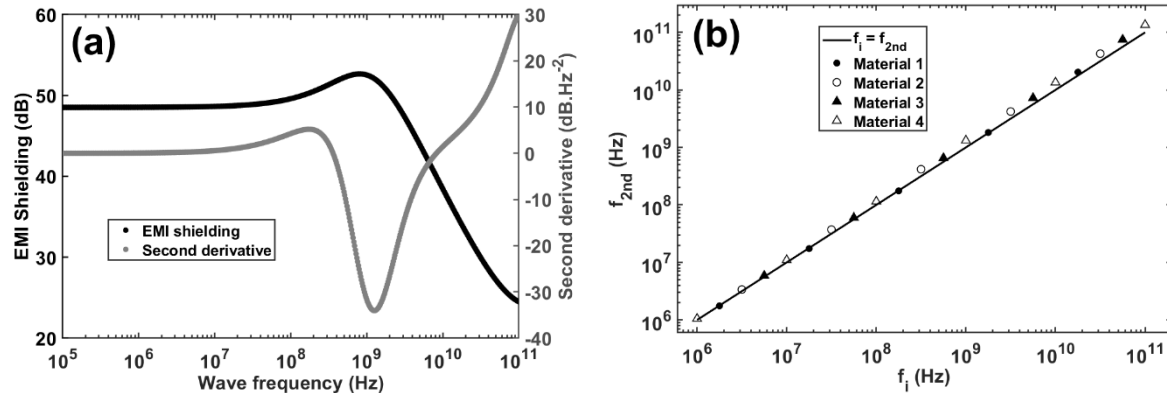


Figure VI - 5: Inductance frequency scaling law. (a) Shielding versus frequency and second derivative for a sample of 1mm thickness, 2000 S.m⁻¹ DC conductivity and inductance frequency $f_i = 1 \text{ GHz}$. The second extrema of the derivative is reached at $f = 1.26 \times 10^9 \text{ Hz}$. (b) Second derivative extrema frequency f_{2nd} as defined before in function of f_i for different materials. Material 1: $\sigma_0 = 100 \text{ S/m}$, $d = 1\text{mm}$; 2: $\sigma_0 = 1000 \text{ S/m}$, $d = 1\text{mm}$; 3: $\sigma_0 = 5000 \text{ S/m}$, $d = 1\text{mm}$, 4: $\sigma_0 = 100 \text{ S/m}$, $d = 15\text{mm}$.

3. Application of the inductive component theoretical model to metal filler-based composite materials

a. Modeling of shielding effectiveness of studied tin particles and Ag-coated glass fibers PP composites

By taking into account the characteristic inductance frequency f_i , the shielding effectiveness of composite materials with metal fillers as a function of frequency (Data presented in Chapter V) can be fitted effectively. Sample thickness and DC conductivity were experimentally measured (Figure V – 1, page 163, and V – 2, page 166). The experimental shielding effectiveness measured in coaxial cell of PP composites loaded with two concentrations of tin particles (a) and in the presence of stearic acid (b) is presented in Figure 6 with the corresponding fitted curves according to our inductance theoretical model. The theoretical fit is good and corresponds to a coefficient R^2 close to 1. The theoretical model correctly predicts the low frequency shielding plateau and the drop of shielding effectiveness observed with these materials. For the 15 vol% tin particles with 10 vol% stearic acid composite material (Fig. 6-b), the model correctly predicts the increase of shielding due to absorption and the following shielding drop due to inductance effects. The fit parameters f_i are quite close to one another, situated between 100 MHz and 1 GHz. The high frequency shielding plateau predicted by the theoretical model (where absorption compensates conductivity drop) is not observed as it is probably situated in higher frequencies, out of the measured frequency range.

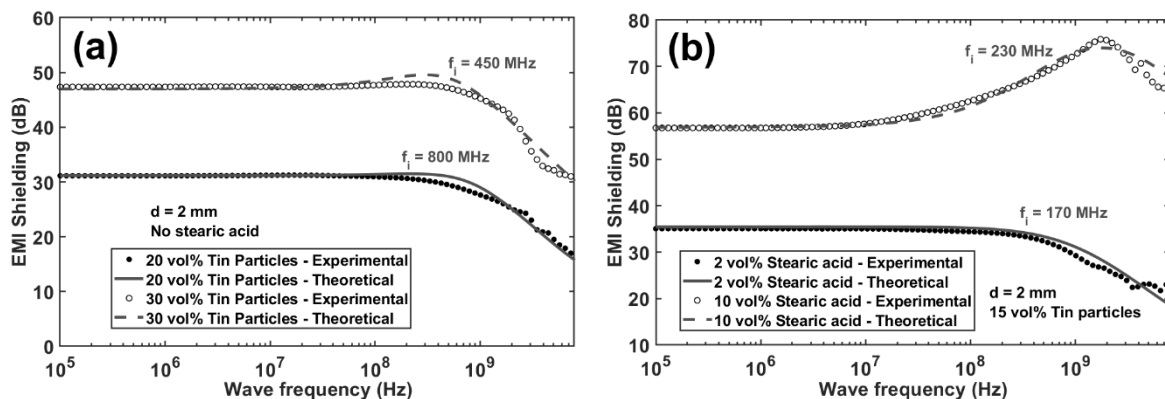


Figure VI - 6: Experimental shielding effectiveness in function of frequency of tin particles-based composite materials. Experimental data are fitted with the inductance component theoretical model. Fitting parameter f_i is indicated. Sample thickness is 2mm. (a) Two concentrations of tin particles. (b) 15 vol% tin particles with two concentrations of stearic acid.

Within the same framework, the experimental shielding measured in coaxial cell of Ag-coated glass fibers-based composite materials are presented in Figure 7 and compared to the fitted theoretical curves. Again, the theoretical fit is good, with a coefficient R^2 close to 1. The model correctly predicts the low frequency shielding plateau, the shielding increase because of absorption and the shielding drop because of inductance effects. One can notice a slight deviation from the theoretical prediction between 100 MHz and 2 GHz for the 10 vol% fibers with 2 vol% stearic acid sample (Fig. 7-b). The fitting parameter f_i ranges from 100 MHz to 1 GHz, except the previously cited sample that gives a value of f_i of 3 GHz.

We can then show in the following that the experimental shielding of studied metal fillers-based composite that could not be fitted with the theoretical model described in Chapter III can be fitted with the present theoretical approach that takes into account inductive effects. The self-inductance of metal fillers in the composite is thus non-negligible and leads to a decrease in shielding compared to the case of non-inductive fillers (CNT, Chapter III).

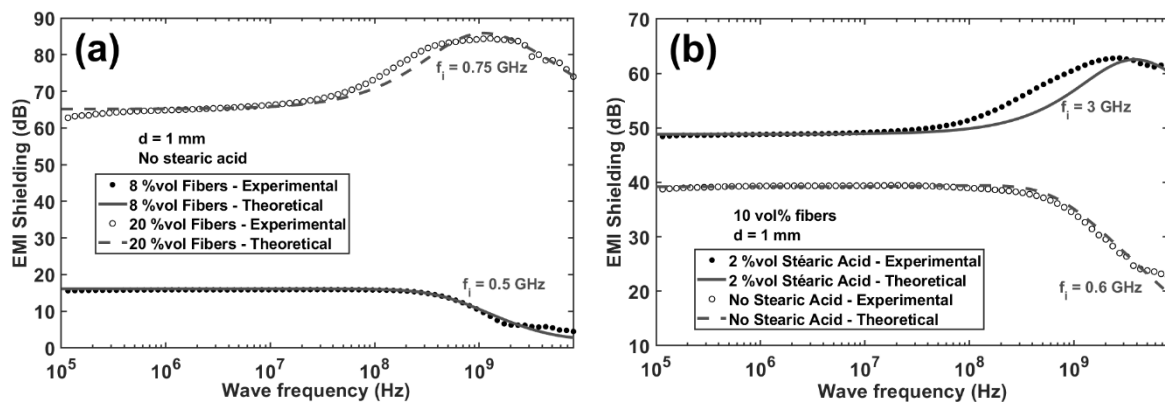


Figure VI - 7: Experimental shielding effectiveness in function of frequency of Ag-coated glass fibers-based composites. Experimental data are fitted with the inductance component theoretical model.

*Fitting parameter f_i is indicated. Sample thickness is 1mm. (a) Two concentrations of fibers.
(b) 10 vol% fibers with two concentrations of stearic acid.*

b. Fitting of metal-filler based composite shielding from the literature

Many other studies reported in the literature reveal a decreasing shielding with frequency on composite materials filled with metal fillers. In order to generalize our theoretical approach, the shielding effectiveness of those composite materials has been predicted according to Eqs. 2 & 4 and compared to the experimental results. Reported materials and experimental shielding as well as theoretical predictions are listed in Table 1. Using the DC conductivity reported in the cited studies,

the experimental shielding curves were fitted with the inductance component theoretical model. The model correctly predicts the shielding drop with frequency. Fitting coefficient R^2 close to 1 are obtained and can be related to the very small deviations between the experimental and the theoretically predicted values of shielding (typically less than 2 dB). This proves once again the ability of the inductance based theoretical model to fit and predict shielding of a large range of metal filler-based composite materials. Some of the cited work did not report the value of the DC conductivity, therefore the experimental shielding curves were fitted adjusting both DC conductivity σ_0 and characteristic frequency f_i parameters (indicated by a *).

Characteristic frequencies ranging from 40 to 400 MHz are obtained by fitting experimental data from the literature. These values are quite close to the values obtained with our composite materials. Only one study from the presented list shows a fitting frequency f_i equal to 0.15 MHz but is obtained on a composite material whose matrix is pure Aluminum which is quite different from a polymer matrix. The obtained fitting frequency f_i parameters of our composite materials as well as the ones reported in the literature are represented in function of their associated DC conductivity in Figure 8. For tin particles-based composites, conductivity values range from 10 to 20,000 S.m⁻¹ and f_i from 100 MHz to 1 GHz (particle concentrations from 15 to 30 vol% with and without stearic acid). Most of the points seems to be situated between 200 MHz and 1 GHz and the highest conductivity point is situated at $f_i = 100$ MHz. For Ag-coated glass fiber-based composites, conductivities are situated in the same range as before but frequency parameters are slightly higher, ranging from 400 MHz to 3 GHz. Points from the literature studies have similar conductivity values compared to our composites but with lower inductance frequency parameters. Thus, the points with conductivity values higher than 10⁵ S.m⁻¹ have a frequency parameter situated between 40 and 70 MHz. The general trend that can be perceived from our composites and literature data points is a slight decrease of the fitting frequency parameter f_i with increasing material DC conductivity. This decrease seems to depend on the used metal filler as it is more marked with tin particles-based composite and literature composite than with Ag-coated glass fibers-based composites. This decrease is however small (approximately one decade) if we take into consideration the variation of the DC conductivity by 5 to 6 decades.

The developed theoretical model with an inductive component then displays a great potential to predicting the shielding effectiveness of metal filler-based composite materials. Its key-point is related to the self-inductance of metal materials which can display a decreasing conductivity as frequency increases. The shielding properties of our studied composites based on tin particles and Ag-coated glass fibers, as well as of composite materials from the scientific literature, could be effectively predicted by taking into account the characteristic inductance frequency parameter.

Table VI - 1: Reported experimental and theoretically predicted shielding effectiveness of metal fillers-based composite materials from our study and studies from the literature. Considered wave frequencies are the extrema of the work studied frequency range.

Matrix	Filler	Filler content	Thickness (mm)	Conductivity (S/m)	Frequency 1	Experimental shielding (dB)	Theoretical prediction (dB)	Frequency 2	Experimental shielding (dB)	Theoretical prediction (dB)	Theoretical inductance frequency (MHz)	Ref.
PP	Tin particle	20 vol%	2	140	1 MHz	31.1	31.1	8 GHz	17	16.4	800	Our work
PP	Ag-coated glass fiber	10 vol%	1	850	1 MHz	39.3	39.2	8 GHz	22.5	20.5	600	Our work
Bamboo fibers	Ag/Ni coating	-	1	3100*	100 MHz	53.8	53.75	1 GHz	49.55	49.6	400	[13]
Aluminum	Cenosphere	40 vol%	2	7.6×10^6	100 MHz	90	88	1,5 GHz	63	64.5	0.15	[15]
Modal fabrics	Ag/Cu coating	36 wt%	1	2350*	100 MHz	50.5	50.5	1 GHz	40.3	40.25	240	[12]
Aluminum foam	-	7 vol% ^a	10	600*	200 MHz	67.5	65	1,8 GHz	46	47,7	70	[11]
PC	Cu ellipsoid	7 vol%	0,5	7.8×10^4	300 kHz	72	74	12 GHz	30	30	41	[8]
		15 vol%	0,5	4.2×10^5	300 kHz	80	85	12 GHz	60	60	70	[8]
PET	Ag coating	-	0,001	1.3×10^7	45 MHz	61	60	1 GHz	36	36.5	50	[10]

^a Foam with 93 vol% porosity, * conductivity also as fitting parameter.

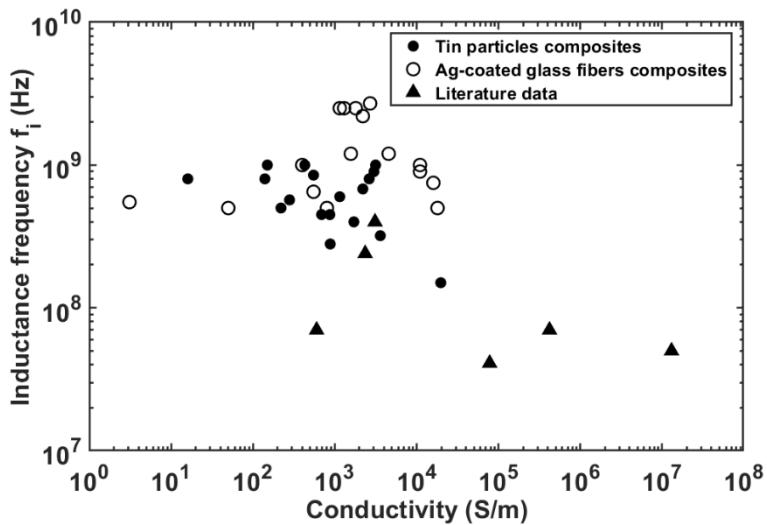


Figure VI - 8: Obtained fitting inductance frequency parameter as a function of composite DC conductivity. Data from this study and from the scientific literature.

4. Theoretical model limits and development perspectives

The developed theoretical model is limited to composite materials prepared using fillers displaying a self-induction behavior such as metal particles. Composite homogeneity and isotropy hypothesis must also be respected as the theoretical model might not work if the fillers have a non-random orientation or if the characteristic length-scale of the material heterogeneities becomes too close to the EM wave wavelength.

In the present framework, the obtained characteristic inductance frequency parameters f_i have not been analyzed in dependence on the distribution of fillers in the polymer matrix, as this analysis would require extensive investigations of the composite morphology, which was out-of-the-scope of the present work.

Besides the inductive component, some other contributions, not yet taken into account, could also play a role, leading to deviations between the experimental and the theoretical curves. This seems to be the case with some of our composites as displayed in Figure 9. For the 15 vol% Ag-coated glass fibers composite with 3 vol% stearic acid, there is a deviation between experimental and theoretically predicted shielding effectiveness between 10 MHz and 1 GHz. The sample exhibits a higher shielding effectiveness than predicted by the theoretical model. It seems that absorption, which increases shielding with increasing frequency, shows up earlier in frequency than theoretically predicted (thus a lower f_c). In this frequency range, the sample conductivity then seems to be higher than the sample DC

conductivity. A solution to improve the fit would be to increase the DC conductivity parameter σ_0 as it would decrease f_c and absorption would start earlier in frequency. Using the frequency independent, homogeneous and isotropic model with constant conductivity (Eq. 4 – 7, no inductive component), we can determine the corresponding composite conductivity associated to each experimental point (grey triangles on Fig. 9). According to theoretical predictions, the composite conductivity would show a constant value in the low frequencies and a decreasing value in the high frequencies. However, in the 10 MHz – 1 GHz frequency range, composite conductivity increases compared to the constant low frequency value. This increase is then counterbalanced by the inductive effects and leads to a decreasing conductivity as predicted. This conductivity increase in the cited frequency range is linked to the observed shielding deviation between experiment and theory as it was not predicted by the theoretical model. Thus, there seem to be another component to composite conductivity in addition to the inductance component.

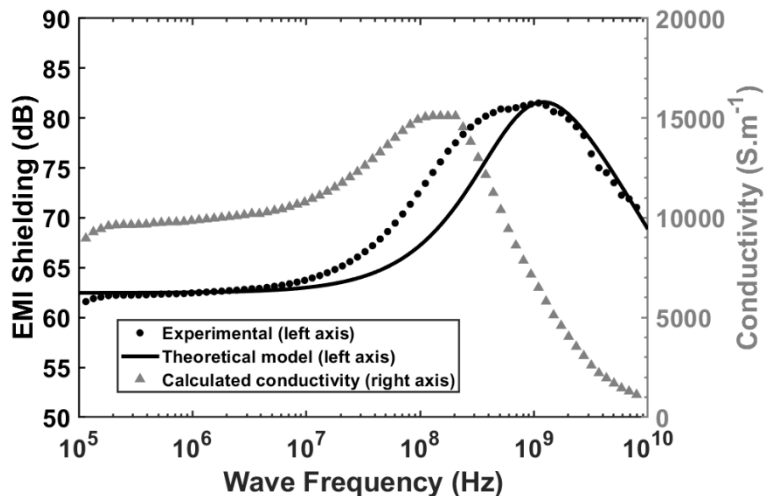


Figure VI - 9: Experimental and theoretically predicted EMI shielding in function of wave frequency of the 15 vol% Ag-coated glass fibers composite with 3 vol% stearic acid (black dots and line). Measurement done in coaxial cell. Calculated conductivity (grey triangles) is obtained from the experimental shielding using the homogeneous and isotropic theoretical model without the inductive component (Eq. 4 – 7).

One possible way of improving the developed theoretical model would be to identify this additional component to composite conductivity. This can be potentially carried-out by considering an additional capacitive component as reported in the literature [4,6]. The presence of micro or nanocapacitors in the composite material due to fillers that are close one to another but not in contact (and also transferring currents through tunneling effects) can be linked to an increasing composite conductivity with wave frequency. This hypothesis could work with the previously considered

composite (Fig. 9) as composite conductivity seems to increase with wave frequency, with nevertheless a preponderant inductive component. The RL network representation of the composite (Fig. 2-a) would have to be change in a RLC network of appropriate structure. This has not been, nevertheless, the subject of the current work since our study deals with metal particles where a more dominant inductive effect is expected. For other type of fillers (such as for instance carbon-based), however, a better theoretical description might be reached by considering a RLC network.

Another possible way of improving the theoretical model would be to add a mesh component. In the previous chapter V on the study of tin particles and Ag-coated glass fibers-based composite materials, optical observations of the composite showed a segregated structure on some of the samples (in particular in the presence of stearic acid). The composite material then looks like a metal mesh. EMI shielding properties of a metal mesh is different from the ones of the same metal bulk, and are the subject of many studies [19–21]. Thus, adding a mesh component to our EMI shielding theoretical model could lead to a potential refining of the theoretical predictions.

5. Conclusion

Based on the self-inductance component of the metal conductivity, we developed a novel EMI shielding theoretical model suited for metal filler-based composite materials. This model takes as hypothesis homogeneity and isotropy of the material, and a representation of the composite as a RL network with a decreasing composite conductivity with frequency. This model predicts a decrease of EMI shielding effectiveness above a set characteristic inductance frequency f_i . According to the relative position of f_i and the characteristic absorption frequency f_c , three universal curve shapes were identified. If f_i is higher than f_c and above the studied frequency range, the characteristic curve shape of the frequency independent, homogeneous and isotropic EMI shielding model are observed with a constant shielding effectiveness below f_c and an increasing one above f_c . If $f_i < f_c$, shielding is constant below f_i and rapidly decreases above it. Shielding then reaches a high frequency constant value where absorption counterbalances inductive effects. Lastly, if $f_i > f_c$, shielding increases above f_c from the low frequency plateau and then decreases once frequency gets superior to f_i , shielding effectiveness reaching a maximum value at a frequency close to f_i .

Taking the experimentally measured DC conductivity and analyzing the characteristic inductance frequency f_i parameter, the experimental shielding effectiveness of studied PP composite

materials filled with tin particles or Ag-coated glass fibers and stearic acid could be successfully fitted, with typical determination coefficients R^2 close to 1. The theoretical model was also found to be able to successfully fit experimental shielding of metal filler-based composite materials from numerous other studies reported in the literature. Rather small variations of the fitting parameter f_i were observed, situated in most of the cases between 100 MHz and 1 GHz.

A small deviation between experimental and theoretically predicted shielding effectiveness for some of the studied samples, suggesting an additional capacitive component to composite conductivity. This lays ground for possible improvements of the developed theoretical model. Moreover, linking the characteristic inductance frequency f_i to composite material characteristics, such as filler intrinsic properties, concentration and dispersion, would strengthen the model theoretical bases and enables one to predict composite experimental shielding without fitting the data.

References

- [1] Schultz, R. B., V. C. Plantz and D. R. Brush. "Shielding theory and practice," *IEEE Trans. Electromagn. Compat.* **30**, 187–201 (1988).
- [2] Nhan, H. N., M. Jean-Louis and W. Jean-Luc. "Modeling of Electromagnetic Shielding Effectiveness of Multilayer Conducting Composites in the Microwave Band," in *2006 First International Conference on Communications and Electronics* 482–485 (IEEE, 2006). doi:10.1109/CCE.2006.350874.
- [3] Al-Saleh, M. H. and U. Sundararaj. "Electromagnetic interference shielding mechanisms of CNT/polymer composites," *Carbon* **47**, 1738–1746 (2009).
- [4] Xia, X., Y. Wang, Z. Zhong and G. J. Weng. "A theory of electrical conductivity, dielectric constant, and electromagnetic interference shielding for lightweight graphene composite foams," *J Appl Phys* **120**, 085102 (2016).
- [5] Peng, Z., J. Peng, Y. Peng and J. Wang. "Complex conductivity and permittivity of single wall carbon nanotubes/polymer composite at microwave frequencies: A theoretical estimation," *Sci. Bull.* **53**, 3497–3504 (2008).
- [6] Xia, X., A. D. Mazzeo, Z. Zhong and G. J. Weng. "An X-band theory of electromagnetic interference shielding for graphene-polymer nanocomposites," *J Appl Phys* **122**, 025104 (2017).
- [7] Nasouri, K., A. M. Shoushtari and M. R. M. Mojtabahedi. "Theoretical and experimental studies on EMI shielding mechanisms of multi-walled carbon nanotubes reinforced high performance composite nanofibers," *J. Polym. Res.* **23**, 71 (2016).
- [8] Lee, S. H., S. Yu, F. Shahzad, J. P. Hong, W. N. Kim, C. Park, S. M. Hong and C. M. Koo. "Highly anisotropic Cu oblate ellipsoids incorporated polymer composites with excellent performance for broadband electromagnetic interference shielding," *Compos. Sci. Technol.* **144**, 57–62 (2017).

- [9] Jung, J., H. Lee, I. Ha, H. Cho, K. K. Kim, J. Kwon, P. Won, S. Hong and S. H. Ko. "Highly Stretchable and Transparent Electromagnetic Interference Shielding Film Based on Silver Nanowire Percolation Network for Wearable Electronics Applications," *ACS Appl. Mater. Interfaces* **9**, 44609–44616 (2017).
- [10] Oh, H.-J., V.-D. Dao and H.-S. Choi. "Electromagnetic shielding effectiveness of a thin silver layer deposited onto PET film via atmospheric pressure plasma reduction," *Appl. Surf. Sci.* **435**, 7–15 (2018).
- [11] Xu, Z. and H. Hao. "Electromagnetic interference shielding effectiveness of aluminum foams with different porosity," *J. Alloys Compd.* **617**, 207–213 (2014).
- [12] Lu, Y., Q. Liang and W. Li. "Fabrication of copper/modal fabric composites through electroless plating process for electromagnetic interference shielding," *Mater. Chem. Phys.* **140**, 553–558 (2013).
- [13] Lu, Y., Q. Liang and L. Xue. "Electroless nickel deposition on silane modified bamboo fabric through silver, copper or nickel activation," *Surf. Coat. Technol.* **206**, 3639–3644 (2012).
- [14] Dou, Z., G. Wu, X. Huang, D. Sun and L. Jiang. "Electromagnetic shielding effectiveness of aluminum alloy–fly ash composites," *Compos. Part Appl. Sci. Manuf.* **38**, 186–191 (2007).
- [15] Wu, G., X. Huang, Z. Dou, S. Chen and L. Jiang. "Electromagnetic interfering shielding of aluminum alloy–cenospheres composite," *J. Mater. Sci.* **42**, 2633–2636 (2007).
- [16] Steinberg, K., M. Scheffler and M. Dressel. "Microwave inductance of thin metal strips," *J. Appl. Phys.* **108**, 096102 (2010).
- [17] Pendry, J. B., A. J. Holden, W. J. Stewart and I. Youngs. "Extremely Low Frequency Plasmons in Metallic Mesostructures," *Phys. Rev. Lett.* **76**, 4773–4776 (1996).
- [18] Huerta-Chua, J. and R. S. Murphy-Arteaga. "A Modified Model for the Self Inductance of Metal Lines on Si," in *IEEE International Workshop Series on Signal Integrity and high-speed interconnects* 111–114 (IEEE, 2009). doi:10.1109/IMWS.2009.4814920.
- [19] Jacoby, K. T., M. W. Pieratt, J. I. Halman and K. A. Ramsey. "Predicted and measured EMI shielding effectiveness of a metallic mesh coating on a sapphire window over a broad frequency range," in *SPIE Defense, Security, and Sensing* 73020X (2009). doi:10.1117/12.818200.
- [20] Wang, H., Z. Lu and J. Tan. "Generation of uniform diffraction pattern and high EMI shielding performance by metallic mesh composed of ring and rotated sub-ring arrays," *Opt. Express* **24**, 22989 (2016).
- [21] Wang, H., Z. Lu, Y. Liu, J. Tan, L. Ma and S. Lin. "Double-layer interlaced nested multi-ring array metallic mesh for high-performance transparent electromagnetic interference shielding," *Opt. Lett.* **42**, 1620 (2017).

General Conclusion and Outlooks

GENERAL CONCLUSION AND OUTLOOKS

This project is in-line with the current trends, addressing the problematic of electromagnetic pollution and greenhouse gas emissions reduction thanks to lightened structures. The developed composite materials meet and even surpass the project objectives of EMI shielding while conserving a low density and good mechanical properties. The best candidate that constitutes the silver-coated glass fibers-based composite allies a low material density like the CNT-based composite (which exhibited an insufficient electrical conductivity and large changes in its mechanical properties) with high shielding properties like the tin particles-based composite (which presented a large density value). The addition of stearic acid to the metal fillers-based composite material led to even higher values of shielding effectiveness. Thus, one of the best options with a reasonable filler concentration is the PP composite filled with 10 vol% Ag-coated glass fibers and 3 vol% stearic acid which showed for a 1mm thickness great values of EMI shielding effectiveness of 50 dB at 1 & 100 MHz, and 70 dB at 8 & 10 GHz with minor changes of mechanical properties, meeting the project goals. All the studied composite materials are listed in the recapitulative table below with their respective advantages and drawbacks.

Recapitulative table of studied composite materials in these works, their advantages (green) and limits (red)

CNT	Liquid metal	Tin particles – Stearic acid	Ag-coated glass fibers – Stearic acid
40 dB Shielding	Incompatible with molten PP	More than 40 dB	More than 40 dB
Density < 1.5	No shielding	Density >> 1.5	Density < 1.5
Drop in mechanical properties		Drop in mechanical properties	Mechanical properties close to pure PP
Shaping difficulties		Tacky samples	Cost of filler

The CNT-based composite materials, though not displaying properties as good as metal fillers-based materials, exhibited decent EMI shielding properties and enabled us to develop a first theoretical model based on the hypotheses of frequency independent properties, homogeneous and isotropic materials. This theoretical model was very useful in identifying and understanding the relevant parameters and physical mechanisms of EMI shielding. Three main shielding mechanisms were pinpointed and their evolutions with the relevant parameters (wave frequency, shield thickness and conductivity) well understood: they are the single reflection, the wave absorption and the multiple internal reflections. Shielding effectiveness was found to be constant with frequency under the

absorption characteristic frequency and to increase rapidly above this frequency. The model revealed a minimum required conductivity of 600 S.m^{-1} to achieve the set project objectives, value barely reached by the most concentrated CNT composite. Those composites can still be useful to shielding applications if CNT concentration is not too high (4 – 7 vol% for minor change of mechanical properties and processibility) and if shield thickness is increased such for structural parts. On the contrary, we showed the impossibility of directly mixing liquid metal with molten PP in the hope of obtaining a metal percolated network. The measured viscosity ratio ($< 10^{-6}$) and interfacial tension (350 mN.m^{-1}) certify the incompatibility of these two materials. This study however led to a premiere: the measurement of interfacial tension between a molten polymer and a liquid metal. An important contribution to liquid metal-based composite materials that have many applications in micro-electronics, flexible electronics, 3D printing and potentially EMI shielding.

The understanding and modeling of involved physical phenomena in our experimental results were capital in these works. Thus, the effect of stearic acid on the metal fillers-based composite material morphology could be figured out using different physicochemical measurements. A mechanism of surface reaction of the fatty acid of fillers surface and favored aggregation of filler-stearic acid domains was identified and linked to the enhanced electrical conductivity and EMI shielding properties of the considered composite materials. The use of metal fillers gave us the opportunity to improve our shielding theoretical model as deviations were observed between its predictions and the experimental results. Self-inductance properties of the metal filler were considered and composite conductivity was not defined as frequency independent anymore. The identification of the right additional physical phenomenon at play enabled us to correctly predict the shielding properties of our metal fillers-based composite materials as well as the ones from the literature. This study thus brings a substantial contribution to composite material processing science and to composite materials EMI shielding theoretical modeling.

Many interesting subjects still remain to study. Development and industrialization of the PP – silver-coated glass fibers – stearic acid composite material is the next step towards commercialization. A more extensive production scale-up study (in extrusion) is required. As observed with CNT-based composites, the effects of injection molding on the EMI shielding properties of fibers-based composite must be analyzed prior mass production. Does a low conductivity layer form on sample surface with injection molding, as observed with CNT-based composites, and does it affect sample EMI shielding properties? Studies on the fibers-based composite material can also be pursued. Adding other fillers or polymer matrices to the composite can lead to improvement of particular properties such as choc

or UV resistance, flame retardation or increased EMI shielding properties at constant fiber concentration (such as with polymer mix fillers segregation).

Theoretical modeling of (complex) composite materials is a perpetual quest as each composite type can require a different modeling strategy and model corrections must be frequently done. Concerning the metal filler-based composite theoretical model, the characteristic inductance frequency parameter remains to be linked to filler and matrix intrinsic properties as well as to the filler distribution in the polymer. Model corrections could be required such as the addition of a capacitive component shifting the representation of the material from a RL network to a RLC network. Considering the segregated structure of the metal fillers-based composite material in presence of stearic acid, a mesh shielding component could also be added to refine the model predictions.

The rapid development of remote communications requiring EMI shielding protections and the demand for lighter materials are among the greater challenges of nowadays. To address these challenges, the contribution of the research carried-out in this study is of importance in many aspects. We highlighted the great benefit of using hybrid metal fillers associated with a dispersing agent to reach great shielding properties. Our works also greatly contributed to the development of the complex but of great interest theoretical modelling of composite materials.

ANNEXE: LIST OF ABBREVIATIONS AND SYMBOLS

ABS	Acrylonitrile butadiene styrene polymer
CB	Carbon black
CNT, NTC	Carbon nanotubes, Nanotubes de carbone
CPC	Conductive polymer composite
dB	Decibel(s)
DC	Direct current / courant continu
EM	Electromagnetic / Électromagnétique
EMA	Ethylene methyl acrylate copolymer
EMI	Electromagnetic interference(s)
EMISE	Electromagnetic interference shielding effectiveness
EOC	Ethylene octene copolymer
Eq.	Equation
Eqs.	Equations
Fig.	Figure
Figs.	Figures
GO	Graphene oxide
LDPE	Low density polyethylene
MFI	Melt flow index
MWCNT	Multi wall carbon nanotubes
PA	Polyamide
PANI	Polyaniline
PC	Polycarbonate
PDMS	Polydimethylsiloxane
PE	Polyethylene
PEK	Polyetherketone
PLA	Polylactic acid
PMMA	Poly(methyl methacrylate)
PP	Polypropylene
PS	Polystyrene
PU	Polyurethane
PVDF	Polyvinylidene fluoride
RDDM	Retraction of a deformed drop method
RFID	Radiofrequency identification
rGO	Reduced graphene oxide

SA	Stearic acid
SE	Shielding effectiveness
SEM	Scanning electron microscopy
SWCNT	Single wall carbon nanotubes
UHMWPE	Ultra high molecular weight polyethylene
UV	Ultraviolet
VNA	Vectorial network analyzer

α	Characteristic factor of wave absorption
B	Magnetic field (induced)
c	Speed of light in a vacuum
C_a	Capillary number
d	Sample thickness
D	Deformation parameter
D_e	Deborah number
δ	Skin depth
E	Electric field
$E_{t,I}$	Amplitude of the transmitted, incident wave electric field
f	Wave frequency
f_c	Characteristic absorption frequency
f_i	Characteristic inductance frequency
φ	Volume fraction
φ_c	Percolation threshold (in volume fraction)
ϵ	Dielectric permittivity
ϵ'	Real part of dielectric permittivity
ϵ''	Imaginary part of dielectric permittivity
ϵ_0	Dielectric permittivity of vacuum
ϵ_r	Relative to vacuum dielectric permittivity
η_d	Dispersed phase viscosity
η_{eq}	Equivalent viscosity
η_m	Matrix viscosity
G'	Storage modulus
G''	Loss modulus
γ_{12}	Interfacial tension
H	Magnetic field
$H_{t,I}$	Amplitude of the transmitted, incident wave magnetic field
j	Imaginary number $\sqrt{-1}$

L	Length
λ	Wavelength
μ	Magnetic permeability
μ'	Real part of magnetic permeability
μ''	Imaginary part of magnetic permeability
μ_0	Magnetic permeability of vacuum
μ_r	Relative to vacuum magnetic permeability
ω	Wave pulsation
p	Viscosity ratio
P	Wave power
$P_{t,I}$	Power of the transmitted, incident wave
r	Radius
R	Electrical resistance
RL	Resistor-Inductor electrical circuit or network
RLC	Resistor-Inductor-Capacitor circuit of network
R_0	Initial droplet radius
R^2	Determination parameter squared
$S_{11,12,22,21}$	Scattering parameter
SE_A	Absorption shielding effectiveness
SE_M	Multiple internal reflections shielding effectiveness
SE_R	Simple reflection shielding effectiveness
SE_T	Total shielding effectiveness
σ	Electrical conductivity
t	Time
T	Temperature
T_m	Melting temperature
τ_d	Drop relaxation characteristic time
θ	Angle
vol%, %vol	Percent volume fraction, pourcentage volumique
Z	Wave impedance
Z'	Resistive part of the impedance
Z''	Reactive (inductive) part of the impedance
Z_0	Wave impedance in open air
wt%, %m	Weight volume fraction, pourcentage massique

Abstract

In this work we present the development of a polymer composite material with electromagnetic interference shielding properties. The project objective is set to a shielding effectiveness of at least 40 dB for a film thickness of 1mm over a broad frequency range spanning from 100 MHz to 10 GHz that includes many applications which can be found in consumer electronics or connected cars. Composite material density and mechanical properties are expected to remain as close as possible to the pure polymer matrix. No study found in the literature complies with all these specifications, highlighting the challenge of such a research project. Understanding the physical mechanisms of shielding in polymer composite materials is also an issue of this work.

In the project, we first focused on the study of carbon fillers-based composite materials that displayed good but not satisfying shielding properties due to limited electrical conductivity. Development of a first theoretical model enabled us to identify the relevant composite properties for shielding and oriented our attention on composites filled with metal fillers. The high density of this kind of fillers however required a low concentration in the composite materials and strategies to lower fillers electrical percolation. Liquid metal revealed to be incompatible with molten polymer because of high values of interfacial tension and viscosity ratio. A hybrid filler of moderate density but high conductivity was found to be the best candidate. The addition of fatty acid led to improved shielding properties that reached and surpassed the set objectives. The unexpected effect of the fatty acid on material morphology was identified and explained, and composites shielding properties could be successfully modeled. Thus, this work has significantly contributed to the development of novel polymer composite materials for shielding applications, to the processing of these materials and to the understanding of shielding physics.

Keywords: Electromagnetic shielding, Composite materials, Theoretical modeling, Electrical conductivity

Résumé

Ces travaux portent sur le développement d'un matériau composite polymère aux propriétés de blindage électromagnétique. L'objectif du projet est une valeur d'efficacité de blindage de 40 dB à 1mm d'épaisseur dans une large gamme de fréquence s'étalant de 100 MHz à 10 GHz et incluant de nombreuses applications dans l'électronique nomade ou les voitures connectées. La densité du matériau et ses propriétés mécaniques doivent demeurer proches de celles de la matrice pure. Aucune étude de la littérature scientifique ne remplit toutes ces conditions à la fois, soulignant le défi posé par ce projet de recherche. Comprendre la physique du blindage électromagnétique des matériaux composites est également une problématique importante de ces travaux.

Le début de ces travaux s'est concentré sur l'étude de composites à base de charges carbonées qui ont présenté de bonnes propriétés de blindage mais insuffisantes pour le projet en raison de leur conductivité électrique limitée. Le développement parallèle d'un premier modèle théorique nous a permis d'identifier les paramètres pertinents au blindage et nous a ainsi orienté vers l'étude de composites à base de charges métalliques. La densité élevée de ce type de charges nécessite cependant de limiter leur concentration dans le matériau et donc de développer des stratégies pour abaisser leur seuil de percolation électrique. Le métal à l'état liquide s'est avéré incompatible avec le polymère fondu en raison des valeurs trop importantes de tension interfaciale et de rapport de viscosité. Le meilleur candidat est une charge hybride de densité modérée et de haute conductivité, associée à un acide gras permettant au composite de dépasser les objectifs de blindage fixés. Ainsi, ces travaux contribuent de façon significative au développement de nouveaux matériaux composites aux propriétés de blindage électromagnétique et à leur mise en œuvre, ainsi qu'à la compréhension de la physique du blindage dans les matériaux composites.

Mots clefs : Blindage électromagnétique, Matériaux composites, Modélisation, Conductivité électrique

Adresse du laboratoire de recherche

Laboratoire Ingénierie des Matériaux Polymères (IMP) – UMR 5223 – Site Lyon 1
15 Boulevard André Latarjet 69100 Villeurbanne
FRANCE
Tél : 04.72.44.81.58.